Light Activatable Nanosystems for Drug Delivery

Doctorate of Philosophy
University of Edinburgh

2023

Paige Amber Shaw

Lay Summary

Polymers hold the key to overcome significant drawbacks in therapeutics, with the possibility of increasing the bioavailability of drugs, increasing their solubility, improving circulation time, and unlocking biological targeting to reduce off-site toxicity.

Herein, a number of different applications of polymers for drug delivery are reported. The difficulties faced by polymers to be uptaken by cells was addressed and a new method for improving and measuring polymer cell uptake was developed. The benefits of light responsive polymeric-prodrug conjugates were explored by integrating coumarin-camptothecin monomers into a water soluble polymeric backbone. Finally, highly efficient light sensitive drug loaded nanoparticles were established, utilising the biocompatibility and stability afforded by polyethylene glycol poly-L-lactide diblock copolymers.

Abstract

Polymers are showing great promise in advancing the field of “Smart Medicines”, the area on which this PhD thesis is focused. The contents of this thesis explore the versatility of light in combination with polymeric systems to achieve selective drug delivery in three ways: using light to monitor cell uptake, the release of drugs from a polymeric backbone, and drug release via nanoparticle cleavage.

The first project includes the modification of RAFT agents to enable the controlled synthesis of size-defined monodisperse polymers with defined end-groups. Here, modifications included fluorophores and lysine-based cell-penetrating peptides. The modified RAFT agents then allowed for the synthesis of polymer chains that were fluorescently “tagged” and demonstrated enhanced cell uptake due to the cell penetrating peptide attached. The polymers showed high biocompatibility and were found to be localised inside endosomes within cells. This work demonstrates the first use of RAFT agents modified with both a fluorophore and cell-penetrating peptide, which endows both a tracking ability and high cell uptake. It allowed for polymer uptake to be measured quantitatively using fluorescence to compare the cellular uptake abilities of three different length cell-penetrating peptides.

The second route explored within the PhD thesis was light-mediated drug release. Here two approaches were taken:

(i). Drug attachment along a polymeric backbone with drug release facilitated by photo-cleavage. Here, the water insoluble chemotherapy agent camptothecin was conjugated to a coumarin methacrylate monomer via a light cleavable bond, rendering the camptothecin 'inactive'. The coumarin camptothecin monomer was then co-polymerised with the water soluble N,N-dimethyl acrylamide (DMA) to yield a water soluble, light cleavable, camptothecin containing polymer. The light sensitivity of the polymer under 365 nm light was validated in solution and in vitro. Biological testing showed high biocompatibility of the polymer under dark conditions, with the polymer showing high levels of toxicity following irradiation. This work demonstrates the versatility of polymers to be used for selective cell-killing, but also their ability to enhance the water solubility of typically 'difficult to formulate' chemotherapy drugs.

(ii). Integrating a light responsive coumarin moiety containing two orthogonal functional groups in between the two blocks of an amphiphilic block copolymer comprised of polyethylene glycol (PEG) and poly-L-lactide (PLA). Such photo-cleavable amphiphilic polymers were used to form light-sensitive nanoparticles, with the ability to encapsulate drugs within their core. Here the chemotherapy drug doxorubicin was encapsulated and consequently liberated by illumination under 365 nm light. Nanoparticles were found to release over 60 % of encapsulated drug after only 2 minutes of light irradiation. In vitro results validated the novel strategy, showing high biocompatibility under dark conditions and selective toxicity upon irradiation.

In summary the developed polymer systems showed promise as drug delivery agents by demonstrating good biocompatibility, trackability, high cell uptake, improved drug solubility, controlled drug activation, and selective drug delivery.

Contents

Declaration of Authorship

The research detailed within this thesis has been performed by the author in the duration of the PhD studentship between the dates of September 2018 and December 2022 under the supervision of Professor Mark Bradley, School of Chemistry, University of Edinburgh. The work, data, analysis, and interpretation presented here are those of the author unless explicitly stated. Where published work has been consulted or referred to in the text, the source has been clearly cited. This work has not been submitted for any other degrees or professional qualifications.

Parts of the work presented herein have been published as such:

- Shaw, P, A. Forsyth, E. Haseeb, F. Yang, S. Bradley, M. and Klausen, M. *Frontiers in Chemistry*, 2022, **10**, 921354.
- Shaw, P. A. Klausen, M. Lilienkampf, A. Bradley, M. Fluorophore-tagged poly-Lysine RAFT agents: Controlled synthesis of trackable cell-penetrating polymers, *ACS Macro Letters*. Submitted.

Signed:

Paige Shaw

Date: 25/05/2023

Acknowledgements

Thank you from the bottom of my heart to Professor Mark Bradley for the past 4.5 years of support and guidance . Coming to do a PhD in organic chemistry group as a physicist was no easy task, but Mark ensured I not only had everything I needed to learn, but also embraced the background knowledge I brought along to make me feel valued and included, while also having the space to learn and grow. The OPTIMA programme he led will influence the rest of my life going forward and has given me a multidisciplinary background in innovation, research, and business that has already led me to have opportunities I would never have dreamt of. Thank you to Dr Annamaria Lilienkampf for your guidance and support navigating the publication world. Thank you to my OPTIMA cohort, we have shared many challenges and laughs together along the way. Thank you especially to Layla Mathieson who has been an amazing friend from the first day we met when we fought on the floor of laser quest.

Thank you to Paul Cowling and Sonia Rehman who took me under their wing from day one to train me to be the chemist I am today. I hold our time together very dear and will look back on it often. Thank you to the Bradley group, the old and the new, I have shared more laughs than I can count, and you are all considered friends for life. Do not hesitate if you ever need a couch to stay on or an ear to listen. Thank you finally to Dr Maxime Klausen, from acquaintance, to friend, to now life partner. I will be eternally grateful for your help guidance and love, both in the lab and outside of it.

I am coming out from this experience not only a much better scientist but also with confidence and friendships that will last a life time, thank you everyone.

Abbreviations

AIBN	2,2’-Azobis(2-methylpropionitrile)
BSA	Bovine serum albumin
Boc	Tert-butyloxycarbonyl
CMC	Critical Micelle Concentration
CPP	Cell Penetrating Peptide
DCC	N,N'-Dicyclohexylcarbodiimide
DCM	Dichloromethane
Dde	N -[1-(4,4-dimethyl-2,6-dioxocyclohex-1-ylidene)ethyl]
DDMAT	2-(Dodecylthiocarbonothioylthio)-2-methylpropionic acid
DIC	N, N′-Diisopropylcarbodiimide
DIPEA	N,N-Diisopropylethylamine
DLS	Dynamic light scattering
DMA	Dimethyl Acrylamide
DMAP	*N,N*-Dimethylaminopyridine
DMEM	Dulbecco's Modified Eagle Medium
DMF	*N,N*-Dimethylformamide
DMFDMA	*N,N*-Dimethylformamide dimethylacetal
DMSO	Dimethylsulfoxide
Dox	Doxorubicin HCl
EDC	1-Ethyl-3-(3-dimethylaminopropyl)carbodiimide
EDTA	Ethylenediaminetetraacetic acid
EPR	Enhanced permeability and retention
EtOAc	Ethyl Acetate

FA	Formic Acid
FBS	Foetal bovine serum
Fmoc	9-Fluorenylmethyloxycarbonyl
GPC	Gel Permeation Chromotography
HPLC	High-performance liquid chromatography
HRMS	High Resolution Mass Spectrometry
LCMS	Liquid Chromatography Mass Spectrometry
Ms	Methylsulphonic
MTT	3-(4,5-Dimethylthiazol-2-yl)-2,5-diphenyltetrazolium bromide
MW	Microwave
Mw	Molecular Weight
OXYMA	Ethyl cyanohydroxyiminoacetate
PBS	Phosphate Buffered Saline
PCL	Polycaprolactone
PDI	Polydispersity Index
PEG	Polyethylene glycol
PLA	Poly-L-Lactic Acid
RAFT	Reversible Addition−Fragmentation chain-Transfer
SD	Standard Deviation
TEM	Transmission electron microscopy
TFA	Trifluoroacetic Acid
THF	Tetrahydrofuran
TIS	Triisopropylsilane
UV-Vis	Ultraviolet-Visible Spectroscopy
W/o/W	Water in oil in water emulsion method

1 Light Activatable Nanosystems for Drug Delivery

1.1 Polymer Applications in Chemotherapy

Significant progress is being achieved in world-wide efforts to develop novel and efficient therapeutics, with the Food and Drug Administration (FDA) currently approving 49 drugs each year on average (**Figure 1**) [1]. Cancer drugs dominate such approvals, of which a large proportion consist of drugs categorised as ‘small molecules’. Although cancer has been at the forefront of research priorities over the last century, much work is still left to be done to not only improve current treatment efficacy, but also to minimise harmful side effects that lead many patients to withdraw from treatment altogether. According to the World Health Organisation (WHO), cancer is the second leading cause of death, resulting in 10 million deaths in 2020 alone (1/6 of all deaths worldwide)[2]. As half the Earth’s population will develop some form of cancer within their lifetime, it is evident that innovative treatments methods need to be developed to impact these statistics.

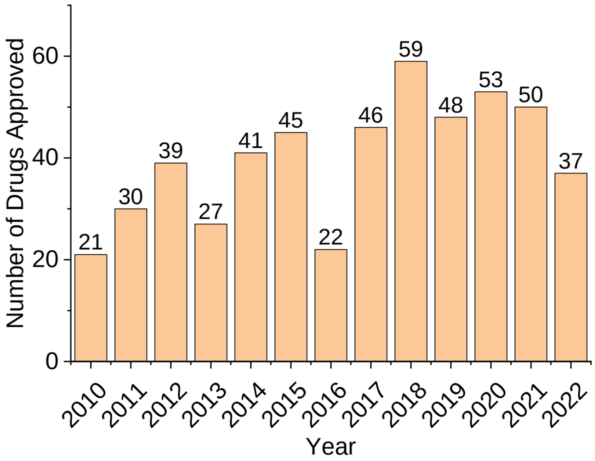

Figure 1: Number of drugs approved by the FDA between 2010 – 2022. Data taken from ‘2022 FDA Approvals’ published in Nature Reviews Drug Discovery[1].

Offsite toxicity presents significant drawbacks in chemotherapy delivery as a drugs presence affects the whole body and not only the cancerous sites. This means that lower drug dosages must be given, limiting cancer killing efficiency, as well as inflicting patients with painful and potentially fatal side effects. A study investigating the cause of deaths in patients receiving chemotherapy over a 30 day period, found that 7.5 % of deaths occurred due to chemotherapy toxicity, as opposed to being cancer-related[3]. If valid, the implications of these findings on deaths caused by off-site toxicity of chemotherapy would be tremendous when considering world-wide cancer statistics. Therefore, it is paramount that novel solutions to minimise the toxicity of chemotherapy agents are found.

1.1.1 Polymer Background

Polymers are long chain molecules made up of several hundred covalently bonded repeating units (monomers) and have molar masses of typically $>10^2$ g/mol [4]. Many of the properties of polymers depend on the degree of polymerisation (DP_n) and the molecular weight (M_n) of the polymer. The degree of polymerisation is given by the total number of monomers bonded together to form a polymer (**Equation 1**).

Equation 1: $$DP_n = M_n/M_0$$

Where M_n is the number average molecular weight of a polymer chain, and M_0 is the molecular weight of a monomer unit.

Due to the nature of polymerisation techniques, natural variation occurs within a polymer's size and composition. As a result, polymers usually consist of mixtures of macromolecules with similar structures but carrying differing molecular weights and degrees of polymerisation. Therefore, DP_n and M_n are given as average values. The measurement of the molecular weight distribution of a polymer is known as the polydispersity index, PDI (**Equation 2**), where a PDI of 1 indicates a given polymer has chains that are all exactly equal in length[5].

Equation 2: $$PDI = M_w/M_n$$

Where M_w is the weight average molecular weight and M_n is the number average molecular weight.

The properties of polymers vary greatly depending on their chain lengths and composition, with the ability to control mechanical toughness, melting transition temperatures, viscosities, solubility, and biocompatibility[6]. Polymers can be from either natural or synthetic origin and can have a broad range of morphologies including linear, cross-linked, branched and dendritic. Polymers can also be classified depending on the types and patterns of monomers they are comprised of[7]. Homopolymers are comprised of one type of monomer and polymers comprised of two or three types of monomers are known as binary and ternary copolymers, respectively. The order in which the monomers reside in the chain can also result in alternating, statistic, block, and graft copolymers.

To achieve polymerisation in which the resulting molecular weight of the polymer is controlled, either step-growth reactions or chain-growth reactions can be performed.

Step growth polymerisation reactions involve the step-by-step covalent bonding of monomers using conventional organic reactions[8]. Discreet and independent reactions are performed to bond monomers together to form condensation polymers or addition polymers. For this process, both monomer units and intermediate molecules must have two functional groups within their structure to allow for polymerisation to occur. Should three or more functional groups be present, cross-linked and branched polymers can form as a result.

Chain growth, or addition polymerisation features the use of activated species, also known as initiators, or other molecules with active centres[9]. Monomers become reactive due to the presence of these species with an active centre which then causes monomer addition to occur, the resulting bonded monomer species are also reactive and cause further bonding with monomers, thus creating polymers. The reactive monomer species are formed from either radical creating compounds which cause homolytic bond scission to occur, or from ionic molecules. Monomers are added until an ideal length is achieved and then the growth is suspended by a termination or chain transfer step. Reversible addition fragmentation termination (RAFT) polymerisation is an example of such reactions and has grown in recent years due to the high control over polymer synthesis it affords [10]. The control of molecular weight, PDI, and polymer architecture can also be achieved with other synthesis methods such as anionic, cationic, or group transfer polymerisation methods but such techniques can only be applied to a limited number of monomer choices and require stringent reaction conditions. RAFT polymerisation allows for advanced architectures to be obtained in living polymerizations, while also maintaining the robust reaction conditions and diverse monomer selection of conventional free radical polymerisations. RAFT polymerisation also provides a platform for enabling polymer end group modification, making it a highly versatile and controllable polymerisation technique.

1.1.2 Polymer Nanoparticles for Drug Delivery

Polymers present an attractive alternative to current treatments as they are able to conjugate, absorb, and encapsulate a variety of therapeutics including peptides, nucleic acids, antibodies, and small molecules. In doing so, such therapeutic agents can have their water solubility, circulation time, and overall bioavailability increased [11, 12]. By increasing the solubility, novel therapeutics previously shelved from biological application would have the potential to be explored as viable chemotherapy candidates. By providing protection of the therapeutic agents from the harsh biological environment, they are able to avoid unwanted immune responses leading to longer biological half-lives, enhancing their circulation times in the blood.

The solubility control of polymers can be exploited to fabricate diblock co-polymers with varying polarity along the polymeric backbone[13]. In doing so, hydrophobic interactions arise due to such polymers being present in aqueous media and results in the formation of nanoparticles that are able to encapsulate drugs. Drugs within such nanoparticles then have enhanced solubility and a ‘shield’ from the biological environment. Nanoparticles also have the ability to be selectively uptaken by cancer cells compared to healthy cells due to the enhanced-permeability and retention (EPR) effect[14]. The EPR effect arises due to the anatomical and pathophysiological differences between cancerous and normal tissue. Large gaps exist between endothelial cells in tumour blood vessels meaning tumour tissues selectively uptake large molecules such as nanoparticles and other macromolecules.

Depending on polymer composition and synthesis methods, polymers can be used to form polymersomes[15], dendrimers[16], and micelles[17], that vary in their shape, size, and loading ability (hydrophilic vs hydrophobic cores). Common polymer compositions used for nanoparticle synthesis include poly-ethylene glycol (PEG)[18], poly-L-lactide (PLA)[19], polycaprolactone (PCL)[20], poly D,L-lactic-co-glycolic acid (PLGA)[21], and poly-methyl methacrylate (PMMA)[22]. Genexol-PM® is an injectable micelle formulation of the typically highly-toxic and insoluble chemotherapy agent paclitaxel, consisting of PEG and poly(D,L-lactic acid) (PDLA) for breast cancer treatment[23]. PEG is often selected as a hydrophilic block due to its ability to avoid detection by the immune system while also providing stability of the nanoparticles in water. Poly-lactides are often used as hydrophobic blocks due to their biodegradability and ability to provide a site for drug binding within the nanoparticles. PEG-PLA diblock copolymer nanoparticles are a common selection for nanoparticle synthesis; in which a drug would become encapsulated by PLA in the centre, or ‘core’, of the nanoparticle, and PEG would remain on the outside, providing a stabilising non-fouling ‘corona’ (**Figure 2**)[24, 25].

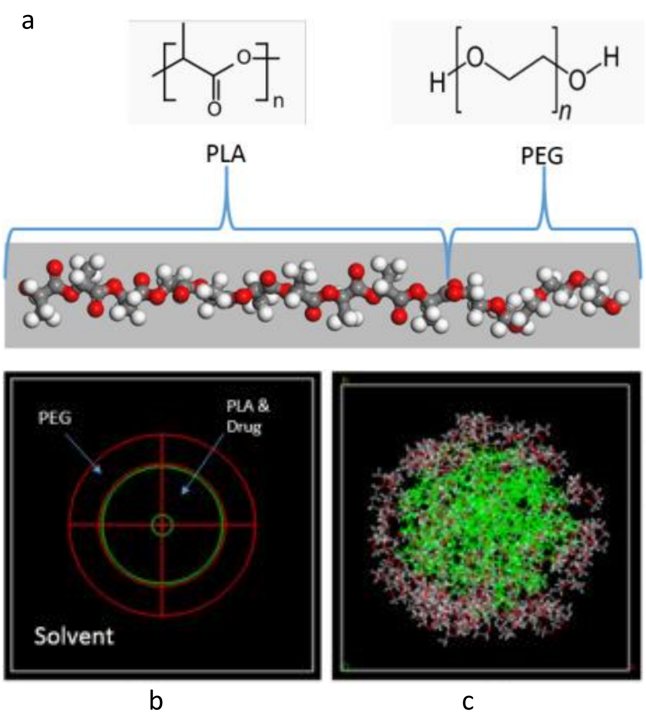

Figure 2: a) PEG-PLA copolymer chain model and monomer repeating units. b) Regions of a drug encapsulated PEG-PLA nanoparticles. c) Atomistic nanoparticle modelling of PEG-PLA drug loaded nanoparticle. Recreated from Meunier *et al.*[25] with permission from Elsevier.

Other examples of polymer nanoparticles, their applications and composition are illustrated in **Table 1**.

Table 1: Examples of polymer nanoparticles and their biological applications.

Polymers	Formulated Drug/ Bioactive Compound	Application	Ref.
PCL, PLA, PLGA	Coumarin-6	Drug delivery, theragnostics, bioimaging	20
PLGA	Fenofibrate	Neovascular age-related macular degeneration, diabetic retinopathy	26
PCL-PEG-PCL	Paclitaxel	Lung cancer	27
PLGA, PCL	Ciprofloxacin	Tissue regeneration, anti-inflammatory activity	28
PLGA-PEG	Paclitaxel	breast, pancreatic and brain cancer	27

As well as tuning the size and chemical composition of polymeric nanoparticles, the surface corona can also be ‘decorated’ with targetting moeities such as peptides, antibodies, and amino acids to enable cancer targetting and detection[29-31]. Nanoparticles have a host of cancer related applications. They have been used to detect cancer biomarkers and cancer cells directly by modifying their surface with amino acids, monoclonal antibodies, and peptides, known as ‘active targetting’ to target, cell surface proteins, ciculating tumour cells and proteins (**Figure 3**) [32]. The native environment of the body and tumours can also be exploted for ‘passive targetting’, utilising PEG to avoid the immune system, pH sensitivity due to the acidic environment of cancer cells, and the EPR effect to selectively deliver cargos.[33].

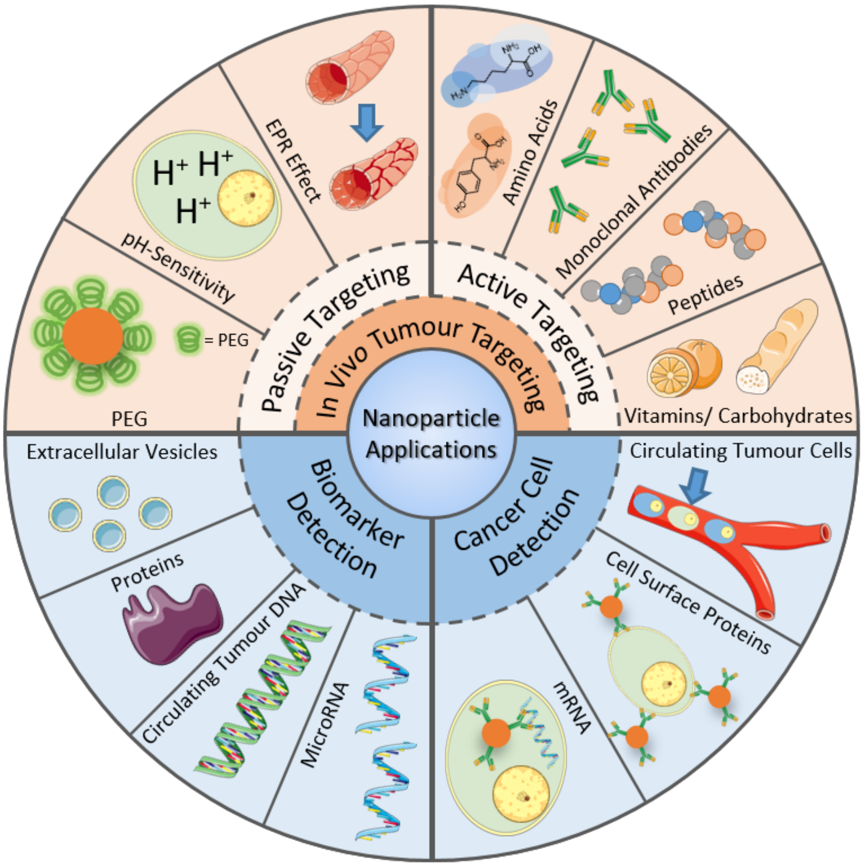

Figure 3: Schematic illustration of cancer-related applications of nanoparticles. Image adapted from Dessale *et al.*[32] and Yao *et al.*[33].

1.2 Light Responsive Materials in Medicine

Despite the great chemical flexibility and tunability that polymer nanoparticles afford, the controlled on-demand release of encapsulated drugs at a target still remains a challenge[34]. Smart materials that respond to an internal or external trigger offer a promising approach to conventional drug delivery methods; which for nanoparticles often relies on diffusion of drugs from the nanoparticle due to osmotic pressure, meaning off-site toxicity can occur[35]. Biological phenomena give rise to local triggers such as pH, enzymes, and redox/ionic conditions, whereas external triggers consist of a more ‘on-demand’ solution, utilising triggers such as light, temperature, and ultrasound.

1.2.1 Light for Anti-Cancer Applications

Light provides a reliable, highly controlled external stimulus for diagnosis and treatment in the forms of imaging and targeted delivery[36]. The benefit of using light as an external stimulus is the accuracy it affords both in terms of location and intensity, benefits that internal stimuli, temperature, and ultrasound don’t possess in the same capacity. As well as this, the wavelength-dependent spectral properties of biological tissues are well understood, giving rise to ‘biological optical transparency windows’ in which high light penetration can be achieved within the body[37]. The absorption coefficient of light describes the proportion of photons that will be absorbed by a certain type of material or biological tissue. Whole blood (oxygenated (HbO_2) and deoxygenated (Hb)) and fat possess much higher absorption coefficients at lower wavelengths. By shifting the wavelength of light further into the red and infrared (IR) greater tissue penetration can be achieved, making these wavelengths more preferable for internal biological applications (**Figure 4**).

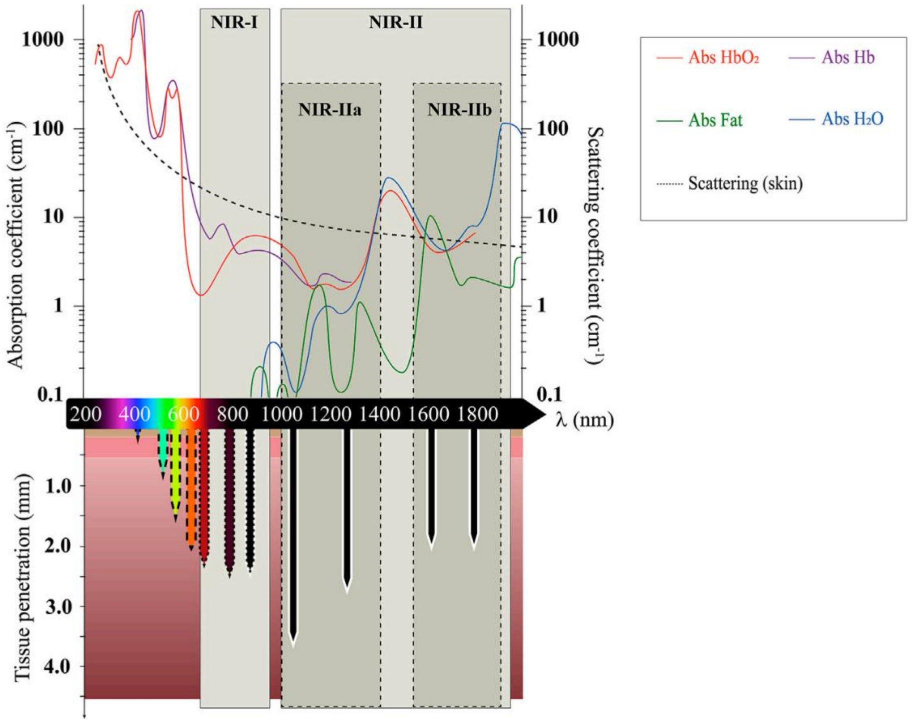

Figure 4: Absorption and scattering coefficients of *in vivo* chromophores, tissues, and water over the visible and IR wavelengths (200–2000 nm) with corresponding tissue penetration [38].

In vivo imaging and drug delivery applications using light arise due to the interaction that molecules have with light, giving rise to useful properties such as fluorescence and photocleavage. The response generated by photons incident on a molecule is dependent on their chemical structure and environment and the subsequent energetic pathways that occur are best described using a Jablonski diagram (**Figure 5**)[39].

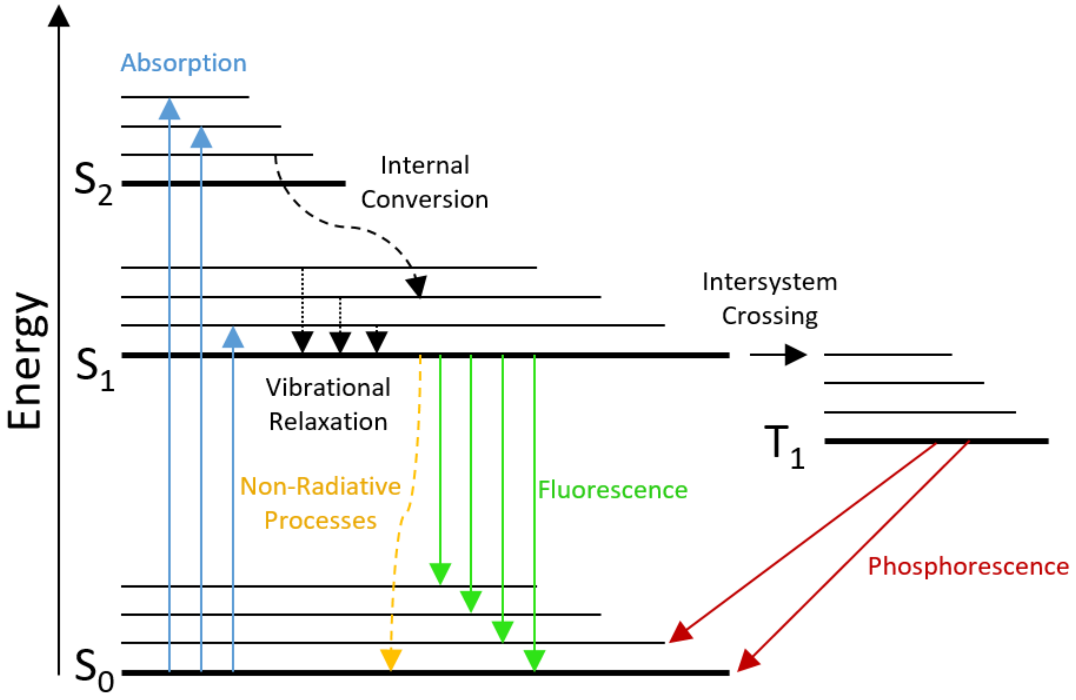

Figure 5: Jablonski diagram of the photophysical mechanisms within a molecule after irradiation with incident photons.

Once a molecule absorbs an incident photon, a ground-state (S_0) electron will be promoted to an excited state[40]. The electron will then usually relax back down to the lowest energy level of the first excited singlet state (S_1) where it will then either drop back down to the ground state by emitting a photon (fluorescence) or by another non-radiative process (e.g. heat, vibration). Electrons can also move horizontally energetically from an excited state into the triplet state by intersystem crossing (S_1 to T_1), in which case the electron will eventually relax back down to the ground state in the form of photon release (phosphorescence) or non-radiative process including reactive oxygen species generation.

For *in vivo* imaging applications, molecules are designed that optimise electron relaxation via fluorescence, making brighter, more efficient fluorophores[41]. Photocleavage occurs through non-radiative decay, either from S_1 or T_1, and molecules with optimum cleaving potential are designed with this in mind[42]. Fluorescence and photocleavage efficiencies can be improved by design considerations that minimise unwanted forms of emission. The quantum yield (Φ) of a compound is a measure of the photo-responsive efficiency of a molecule. It defines the likelihood of a desired event (in this case fluorescence or photocleavage) occurring and is measured by the rate at which an event occurs per photon absorbed. For example, the fluorescence Φ_f of commonly used fluorophores Cy5 (PBS, 620 nm), fluorescein (0.1 M NaOH, 496 nm), and rhodamine B (H_2O, 514 nm) are 27 %, 95 %, and 31 %, respectively[43-45]. Uncaging (photocleavage) Φ_u values are typically lower and are dependant not only on the chromophore, but also on the leaving group[46]. Examples of commonly used uncaging chromophores include coumarins, nitrobenzyls, and BODIPYs.

As well as the Φ, the absorbance wavelength of a chromophore should be considered for *in vivo* applications[38]. As light penetrates tissue better at wavelengths of >600 nm, molecules that absorb within this spectral range would also need to be used. However, the synthesis of such long-wavelength absorbing chromophores is often complex, and yields bulky, high molecular weight compounds that aren't water soluble and are therefore limited in their biological applications. A way to overcome this is through the use of two-photon absorption (2PA), first theoretically described by Maria Göpper-Mayer in 1929. 2PA relies on the near-simultaneous absorption of two photons using the combined energy to generate an electronic transition from S_0 to an excited state (**Figure 6**). Electrons under 2PA undergo a two-step process firstly being excited to a 'virtual state' (**Figure 6**, dashed line), which then, subject to a further photon being incident on the molecule within the attosecond timescale (usually achieved by femto-second pulsed lasers), will be further promoted to a singlet excited state. The overall impact of this method means that a molecule that typically absorbs at ~400 nm in one-photon, that holds the benefits of simple synthesis, high quantum yields, and water solubility, can absorb at ~800 nm using 2PA and will therefore be able to be excited at high tissue depths at this wavelength. Further information on two photon absorption can be found in my review article titled 'Two-Photon Absorption: An Open Door to the NIR-II Biological Window' authored during my PhD which can be found in the Appendix[38].

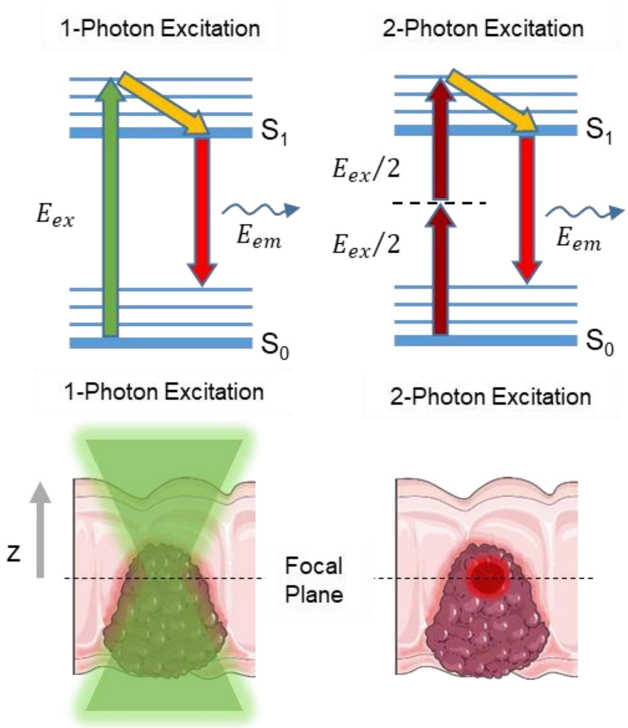

Figure 6: One (Right) and two (Left) photon absorption and emission processes[38].

Due to the nature of the 2PA process requiring two incident photons, the irradiation area is therefore limited to a femto-litre sized volume, where photon absorption will not occur above or below the focal point of incident light. This property allows for high levels of control by exploiting precise molecular excitation to achieve superior drug delivery and imaging applications. By enabling highly precise excitation, photo-cleavable drugs can be delivered with high accuracy, minimising off-site toxicity. High contrast images can be achieved by exciting fluorophores in a select location, preventing nearby auto fluorescence. Photobleaching of chromophores can also be minimised using this method, as well as minimising phototoxicity often associated with irradiating tissue at shorter wavelengths. Overall, by using 2PA small, easily synthesised, and water soluble chromophores can be used for *in vivo* drug delivery and imaging applications with unique benefits.

1.2.2 Examples of Light Activatable Nanocarriers

The past decades have seen an increase in organic nanosystems designed for photo responsive cargo release of both small and large molecules. Systems explored include proteins[47], peptides[48], microgels[49], DNA[50], and polymer nanoparticles[51]. Cargos investigated include chlorambucil[52], fluorouracil[53], camptothecin[53], doxorubicin[54], and tamoxifen[55].

DNA and proteins are often selected as carriers due to high biocompatibility and biodegradability due to them being naturally occurring organic materials. For example, Tan *et al.* developed a light responsive chemotherapy delivery system in which DNA was conjugated to camptothecin to yield amphiphilic nanoparticles that utilised a UV responsive 2-nitrobenzyl ether moiety to yield a decapped drug core, leading to an irreversible self-immolative process causing camptothecin release[56].

An example of red light responsive lipid nanoparticles utilised upconverting nanoparticles to liberate a chemotherapy drug through photolysis[57]. The upconverting nanoparticles were conjugated to a coumarin-based photocleavable linker, typically photocleaving under UV/blue light, to make photolysis possible using deep red excitation (**Figure 7**).

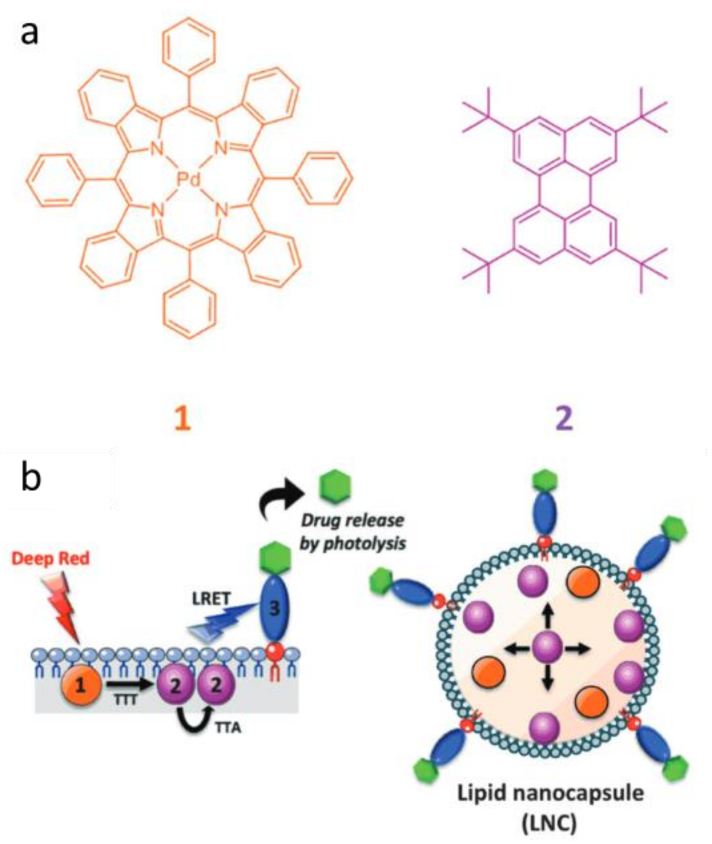

Figure 7: Formulation and of the upconverting nanoparticles. a) Chemical structures of the photosensitizer ‘PdTPBP’ (1) and the emitter TBPe (2). b) Design of light-activable nanoparticles: upconversion facilitating compounds (1) and (2) are integrated in the core nanoparticle and the caged drug is anchored at its surface allowing efficient deep-red light upconversion-assisted photolysis[57]. Reproduced with permissions from John Wiley and Sons.

Polymer nanoparticles hold unique benefits due to their structural versatility which gives them the ability to mimic structures and physical properties of native plasma lipoproteins that form biological carriers, allowing their applications as drug delivery candidates[58]. A common approach for the fabrication of red-shifted light sensitive polymeric nanoparticles is often through a secondary trigger such as ROS or in combination with inorganic substrates. For example, Wei *et al.* developed a light-activatable chemotherapy delivery system using protoporphyrin conjugated polymer micelles[59]. Reactive oxygen species (ROS) generation occurred through the photoconversion of protoporphyrin triggered by red light irradiation, resulting in the disassociation of apatinib and doxorubicin loaded micelles, successfully delivering the cargo. PEG-stearamine conjugates were also used to form doxorubicin loaded light-activatable micelles using a combination of a ROS responsive thioketal linker and the photosensitizer pherophorbide A for site-specific synergistic photodynamic-chemotherapy applications [60]. Another approach was achieved by Lyu *et al.* in which photoliable semiconducting polymer nanotransducers were synthesised for photo-triggered gene-editing. PEI brushes, $^1O_2$ generating backbones and $^1O_2$ sensitive linkers were combined with NIR irradiation triggering the decomposition of gene vectors leading to the release of CRISPR/Cas9 plasmids for efficient *in vivo* gene editing[61].

Many solutions have been developed to overcome the issues surrounding targeted drug delivery, however issues still exist with stability, complex synthesis, and lack of efficiency. No light-responsive drug delivery system has currently been approved by the FDA, indicating there is further work to be done to find novel solutions.

2 Aims and Objectives

Light and polymers present benefits in drug delivery applications, both uniquely allowing for biological selectivity and higher localised dosing of medicinal agents. However, there has been less research performed on systems combining the two technologies synergistically, which, if successful, could provide unique solutions within various fields of medicine. In my PhD, a number of different chemical approaches, primarily for anti-cancer and drug delivery applications, were undertaken.

Polymer RAFT agent modification was explored to achieve controlled cellular uptake of size-controlled polymer structures, holding possible application as polymeric systems for drug delivery. Polymer end group modification was achieved by attaching a RAFT agent in addition to poly-Lysine residues that constitute a cell penetrating peptide that facilitate increased polymer cell uptake. Fluorophore conjugation to the RAFT agent would also allow polymer cell uptake to be evaluated and enable intracellular imaging.

Light responsive drug caged coumarin monomers were explored with the monomer being caged with the hydrophobic anticancer drug camptothecin. The monomer was randomly polymerised within a hydrophilic chain, thereby improving the solubility of the drug, while also allowing it to be selectively released upon irradiation.

Finally, hydrophilic (PEG) and hydrophobic (PLA) polymer chains were joined using a light cleavable coumarin moiety. These amphiphilic polymers were used to encapsulate the anticancer drug doxorubicin to yield light responsive cancer killing nanoparticles.

3 RAFT Agent Modification for Increased Polymer Cell Uptake

RAFT agents facilitate controlled radical polymer chain growth, allowing for size control and low PDI's to be achieved in polymer synthesis. Commonly used RAFT agents include thiocarbonylthio compounds such as dithioesters[62], dithiocarbamates[63], trithiocarbonates[64], and xanthates[65]. A RAFT's typical structure has variable R and Z groups as shown in **Figure 8**.

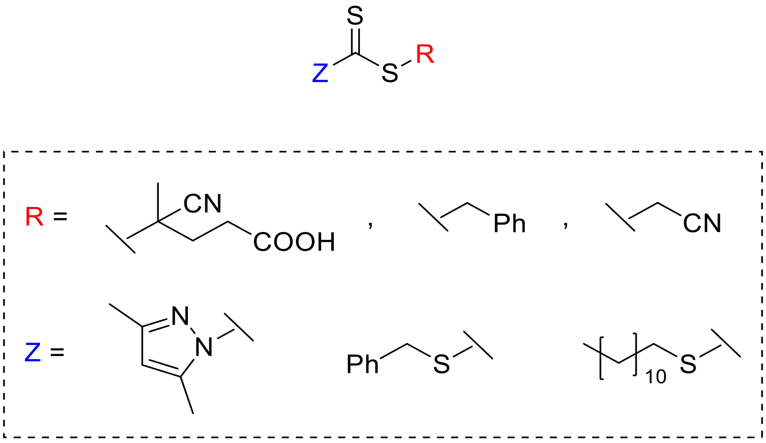

Figure 8: Generic structure of a class of RAFT agents and examples of variable groups.

Due to the mechanism of RAFT polymerisation, and the proportions of reactants contained in the polymerisation reactions (low concentrations of RAFT agent with even lower concentrations of initiator) the R group will be the resulting end group of the majority of the polymer chains (**Figure 9**), whereas the Z group will only be attached to a small proportion of polymer chains that are 'dead' upon termination[10]. By modifying the RAFT agent in the R position, controlled polymer end group modification can be achieved.

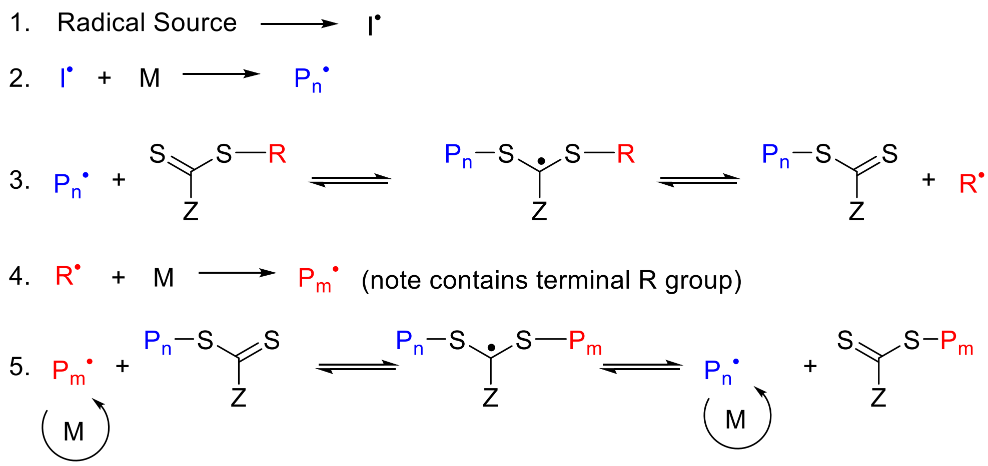

Figure 9: Proposed mechanism of RAFT polymerisation. A radical source I$^{\bullet}$ is introduced to a monomer that begins to grow and propagate. Resulting radical chains $P_n^{\bullet}$ attack the RAFT agent, and the R group is liberated as a radical which then begins propagating with the surrounding monomer, forming chains $P_m^{\bullet}$. Chains $P_m^{\bullet}$ and $P_n^{\bullet}$ reversibly attach to the RAFT agent (dead chains) or grow when liberated (propagating chains).

One of the major problems within drug development is the innate water-solubility issues that many drugs possess. Indeed, many highly effective chemotherapy agents such as Doxorubicin, Camptothecin, and Paclitaxel are all limited in their used due to their low hydrophilicity[66]. Polymer systems have a multitude of applications within drug delivery, one being improved drug solubility. However, cellular uptake by polymers is often limited, lowering their overall bioavailability. Drug delivery using polymers often relies on self-assembly (e.g. formation of nanoparticles) to exploit high endocytosis rates of macromolecules. If the bioavailability and uptake of polymers could be increased, without the requirement of self-assembly that places restrictive design considerations, their applications within drug delivery would be vastly expanded. By utilising polymers for drug delivery via the covalent attachment of drugs onto the polymeric backbones, many applications of polymers could be exploited such as increased drug loading, improved solubility, and target specificity.

Peptides hold the potential for improving the bioavailability of polymers as specific peptides have the ability to penetrate through cell membranes, target specific cell types (e.g cancer by the RGD peptide), and are easily synthesized by solid-phase methods.[67] Cell penetrating peptides (CPP) such as Transportan 10,[68] Penetratin,[69] and the TAT peptide[70] are commonly used to facilitate translocation across a cell membrane; with simpler structures such as poly-Lysine,[71-73] and poly-Arginine[74] also able to achieve similar outcomes. Peptide‒polymer conjugates, with their dual combination of components, provide materials with unique properties.[75] The advantages of each building block, synergistically combined, generates materials with high functional group densities due to the polymer chain and selective biological activity (arising from the peptide), whilst retaining their abilities to tune solubility and topology. The ability to allow multidrug loading across the polymer/peptide chain could make them ideal vectors for therapeutic and diagnostic applications.[76, 77]

A polymer's cellular uptake and localisation is typically evaluated via the use of fluorescent tags, either by conjugation of fluorophores onto the end-groups post-polymerisation[78-82], or by co-polymerisation of fluorescent monomers [81, 83]. However, post-polymerisation tagging can lead to difficulties in achieving complete conjugation of the fluorophore which leads to complex purification to separate successfully conjugated polymers. Polymerising fluorescent monomers results in polymers with varying levels of fluorophores within each polymer chain, which again can hinder analysis and quantification of cellular uptake.

Conjugating a fluorophore directly onto a peptide-RAFT agent would provide a high level of control by ensuring that each polymer chain carries only a single fluorophore, allowing for accurate comparisons of cell uptake between different polymer samples, and would overcome many of the aforementioned limitations. Within this work the design and synthesis of RAFT agents incorporating both a fluorophore and a CPP were achieved, allowing for the synthesis of fluorescently-tagged *N,N*-dimethylacrylamide (DMA) polymer–peptide conjugates for improved cellular uptake applications.

3.1 Lysine RAFT Agent Synthesis

The peptide was conjugated as the RAFT agents “R group” to ensure one peptide per polymer chain. This was important to ensure consistency within the polymer-peptides, and also to allow for direct comparison across samples in which the peptide had been altered. 5,6-Carboxyfluorescein ($\lambda_{Ex/Em} = 495/517$ nm) (CF) was selected as the fluorophore due to its easy functionalisation, low toxicity, and absence of interference with the peptides biological function.[84] For the cellular delivery moiety, L-Lysine residues, which are positively charged at physiological pH, were incorporated onto the RAFT agent to facilitate transport across negatively charged cell membranes. However, high charge density can result in cell toxicity,[85] with positively charged molecules being associated with membrane disruption, leading to apoptosis. Therefore, poly-Lysine chains of varying lengths were explored to ensure optimum cellular uptake while also minimising toxicity and cell death. Three fluorescein-tagged RAFT agents **1**–**3**, containing either 3, 5, or 7 lysines, respectively, were synthesised using solid-phase methods, as shown in **Scheme 1**.

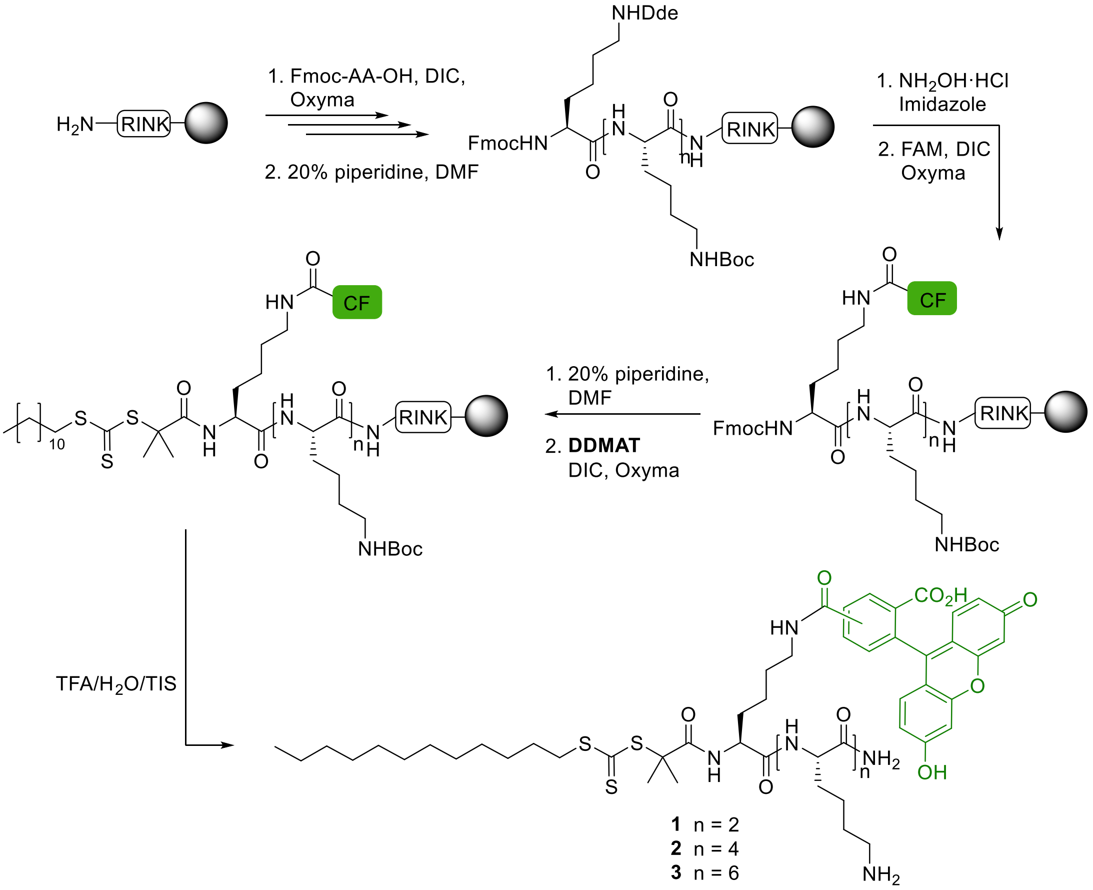

Scheme 1. Solid-phase synthesis of the fluorescein-tagged lysine RAFT agents **1**–**3** containing 3, 5, and 7 L-Lysine residues.

The peptide polymer conjugates were designed to contain the peptide attached to the RAFT agent as the R group, to ensure complete functionalisation of the resulting polymers. The RAFT agent selected contained a radical stabilising dimethyl unit to direct polymerisation. The peptide RAFT analysis were synthesised on solid-phase to allow for high purity peptides and easy reaction monitoring. The carboxyfluorescein fluorophore was conjugated to the L-Lysine residue side chain located closest to the RAFT agent, to ensure a consistent conjugation position on all peptide-RAFT agents.

Peptide synthesis was achieved by sequential Fmoc-Lys(Boc)-OH coupling onto an aminomethyl polystyrene resin, bearing a Rink-amide linker, using Oxyma and DIC as a coupling mixture until the desired peptide length was obtained (**Scheme 1**). Observing a yellow solution via a Kaiser test verified complete conjugation of the free amines on the resin[86]. In the presence of small amounts of primary amines, the Kaiser test will produce a deep blue colour, indicating a peptide coupling is incomplete. Ensuring complete peptide coupling is vital to prevent the formation of incomplete peptide chains, which can decrease yield and complicate purification due to the presence of other different peptide compositions.

Between each coupling step, a solution of 20 % piperidine in DMF was used to cleave the terminal Fmoc groups to allow for the generation of the free amine. It is important to note that the longer the peptide, the more difficult sequential couplings of the lysine residues became; with the final step of the synthesis of **3** containing 7 lysines, requiring 3 repeated coupling attempts before complete conjugation was observed. The final lysine residue coupled for each of the three peptides was Fmoc-Lys(Dde)-OH. The Dde protected side chain allowed for the orthogonal deprotection of its ε-amino group, while retaining the Boc groups on all the other lysine residues. This allowed for the selective coupling of CF onto a single lysine side chain. The Dde group was selectively removed by a mixture of hydroxylamine hydrochloride and imidazole, followed by coupling of CF[87]. The mixed isomer version of the carboxyfluorescein was used as large quantities were required as multiple repeated couplings had to be performed before the coupling was completed. However, later this was found to cause issues with the purification as separation of the isomers of the CF conjugated peptide occurred, which then made it difficult to ensure the same proportions of each isomer were in **1**-**3**.

Finally, 2-(dodecylthiocarbonothioylthio)-2-methylpropionic acid (**DDMAT**), a carboxylic acid terminated trithiocarbonate RAFT agent, was conjugated onto the amino-terminus of the peptide. This RAFT agent was found to be highly compatible with solid-phase synthesis and full completion of the coupling was found from the Kaiser test after just one coupling step under identical conditions as used for the lysine residues. Cleavage off the resin and peptide deprotection using a mixture of TFA:H_2O:TIS (90:5:5, *v/v/v*) proceeded cleanly without any side-reactions between the RAFT agent and the reducing agent triisopropylsilane (TIS). The peptide-RAFT agents **1**–**3** were obtained in >99 % purity after purification, and fully characterised via NMR, HRMS, and HPLC. The optimisation of the preparative-HPLC method found that the separation of the impurities from the peptides **1**-**3** occurred best in a solvent mixture of Methanol (0.1 % TFA) and H_2O (0.1 % TFA). Other solvent mixtures explored were, Acetonitrile (0.1 % TFA) with H_2O (0.1 % TFA), Methanol (0.1 % FA) with H_2O (0.1 % FA), and Acetonitrile (0.1 % FA) with H_2O (0.1 % FA). The major impurity found occurred from the incomplete deprotection of the Dde group, likely due to the deprotection not being performed for long enough, leading to a proportion of the cleaved peptide containing Dde in place of the CF. This was also found to be size dependant with **3** containing approximately 20 % of the impurity, whereas **1** contained around 5 %. However, successful removal of the impurities was achieved using the preparative-HPLC method.

3.2 Control RAFT Agent Synthesis

A CF-tagged ‘control’ RAFT agent without any lysine residues was also synthesised. A control RAFT agent would allow for comparison of the polymers of cell uptake with the cell penetrating peptide polymers. As a first attempt, a control RAFT agent **7** was synthesised as reported by Zhang *et al.* using click chemistry using 5,6-carboxyfluorescein **CF**, as opposed to 5-carboxyfluorecein as reported (**Scheme 2**)[88]. Carboxyfluorescein was first functionalised with a propargylamine linker **4** to make a ‘clickable’ 5,6-carboxyfluorescein **5**. **5** was then conjugated to the RAFT agent **6** to yield **CF-RAFT 7**. However, following synthesis, the RAFT agent **7** was found not to polymerise under the same conditions as **1**-**3**, with the reactions terminating prior to completion. This was likely caused by residual copper in the carboxyfluorescein conjugated RAFT agent **7**, due to the click chemistry approach. Copper is a known radical scavenger[89] and could potentially quench the polymerisation (radical) reaction and prevent efficient chain extension.

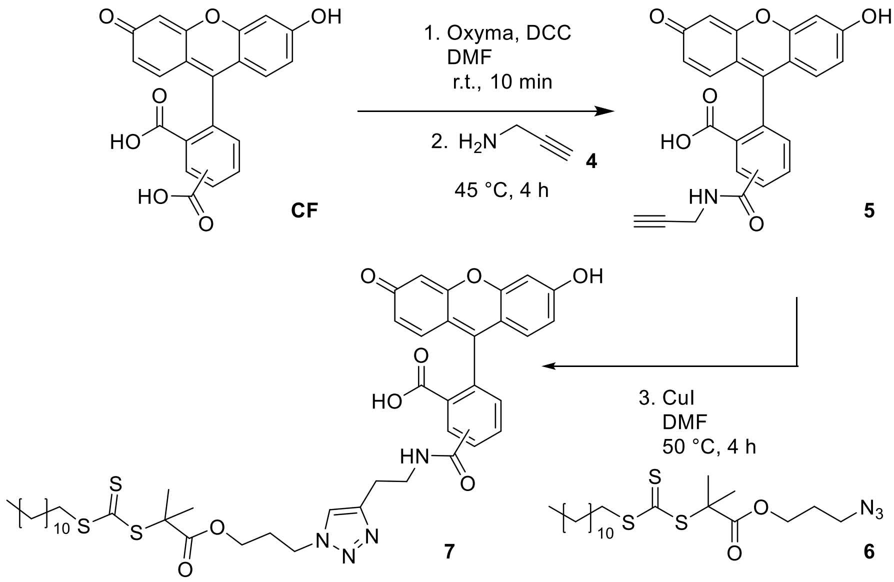

Scheme 2: Initial synthesis of the control RAFT agent **7**[88].

An alternative method was established to synthesise the control RAFT agent without the requirement of click-chemistry. The fluorescein-tagged control RAFT agent **9** without any lysine residues was synthesised in three steps with amide coupling between **CF** and a **DDMAT** RAFT agent derivative functionalised with a diaminoethane spacer (**Scheme 3**).

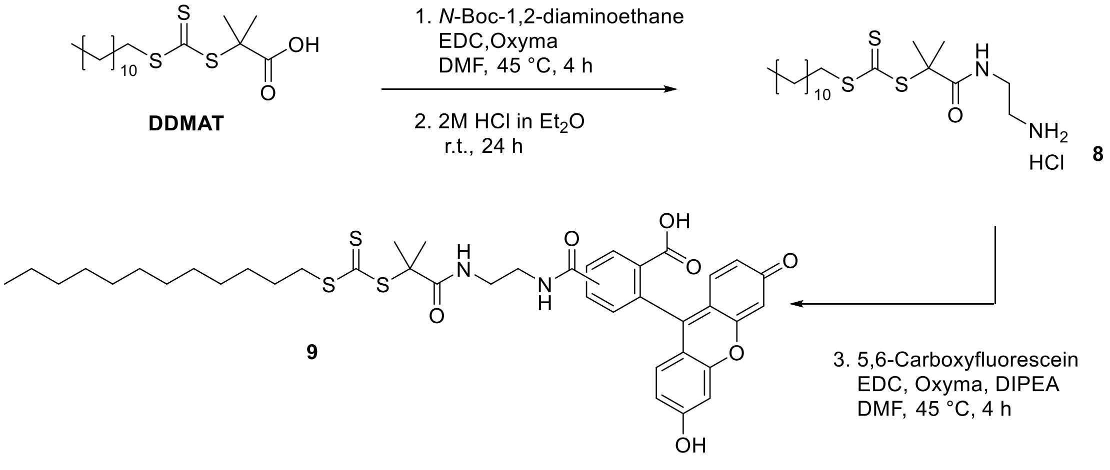

Scheme 3: Synthesis of the control RAFT-agent **9** without lysines.

9 was designed to contain both 5,6-carboxyfluorescin **4**, and the same RAFT agent as the Lysine-containing RAFT agents **1-3** (**DDMAT)**. HCl in diethyl ether cleaved the Boc groups and the resulting compound **8** precipitated, giving a pure product that required no further purification, that was conjugated with **CF** to give **9**.

3.3 Polymer Synthesis and Characterisation

Following the synthesis of the 4 RAFT agents, DMA was selected as the monomer to form the polymer chains due to its compatibility with the unconjugated RAFT agent, speed of polymerisation, and reportedly low PDIs of resulting polymers made via RAFT polymerisation. Polydimethyl acrylamide (PDMA) also benefits from high biocompatibility, and stability towards hydrolysis.[90] Here, target polymer lengths of 7.5 kDa and 50 kDa were selected to span the molecular weight range and challenge the peptide delivery systems. Short polymers are less likely to be toxic and have higher initial uptake,[78] while larger polymers (>40 kDa) have been shown to have higher long term accumulation in tumours.[91] As each polymer chain would only be attached to one fluorophore, exploring short polymers also has the benefit of increased brightness which would more easily facilitate detailed analysis of intracellular polymer localisation. DMA was polymerised with RAFT agents **1**, **2**, **3**, and **9** under similar conditions using AIBN as an initiator. Polymerisation solutions were prepared in Dioxane:D_2O at a ratio of 9:1 at concentrations of ~0.7 M and reactions were performed under argon at 70 °C for ~4 hours. Quenching in liquid nitrogen under air at ~95 % monomer conversion yielded highly size-controlled and low PDI ~7.5 kDa polymers **3Lys-PDMA-7.5k**,

5Lys-PDMA-7.5k, **7Lys-PDMA-7.5k**, and **0Lys-PDMA-7.5k**, and ~50 kDa polymers **3Lys-PDMA-50k**, **5Lys-PDMA-50k**, **7Lys-PDMA-50k**, and **0Lys-PDMA-50k** (**Table 2**). After 4 hours of reaction time, samples of the reaction mixture were taken using a degassed needle for ^{1}H NMR analysis to determine monomer conversion. Samples were prepared in deuterated DMSO and all polymer samples showed similar conversion rates after 4 hours with around 95 % monomer-polymer conversion. As RAFT polymerisation reactions approach 100 % monomer conversion, the risk of polymer chains terminating each other increases, which can lead to poor PDI's that would render the polymers incomparable for their applications in this project. Therefore, all polymer samples were quenched at 4.5 hours to minimise this risk.

Polymers were purified using precipitation in diethyl ether, washed twice by dissolving in MeOH and precipitating, followed by dialysis. Dialysis was performed to ensure the removal of any unreacted RAFT agents that wouldn't be removed by precipitation. If any unreacted compound **1**, **2**, **3**, or **9** was left within the polymer samples, the resulting cell uptake measurements would be inaccurate as it would mean the concentrations of fluorescein in the samples would be invalid. As RAFTs **1-3** were soluble in water, the free RAFT agent could be separated from the resulting polymers via dialysis. **9** was ether soluble, and thus readily separated from its resulting polymers via a polymer precipitation step.

Table 2: Synthesis and characterisation of fluorescently-tagged, lysine–PDMA polymers synthesised using the RAFT agents **1**, **2**, **3**, and **9**.

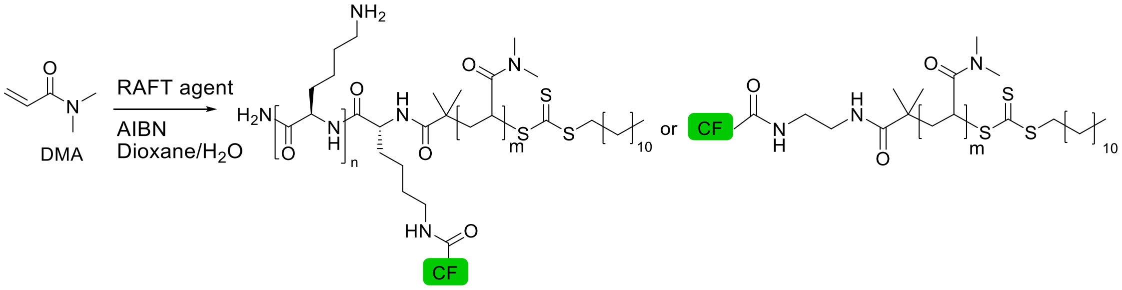

RAFT agent	Polymer	n	Conv. [%][a]	Theor. size[b]	M_w [Da] (^{1}H NMR)	M_w [Da][c] (GPC)	PDI
1	**3Lys-PDMA-7.5k**	3	97	8308	8229	7937	1.1
2	**5Lys-PDMA-7.5k**	5	98	8638	8477	8050	1.4
3	**7Lys-PDMA-7.5k**	7	97	8819	8761	10276	1.3
9	**0Lys-PDMA-7.5k**	–	96	7818	7663	6211	1.2
1	**3Lys-PDMA-50k**	3	97	49155	53292	49041	1.3
2	**5Lys-PDMA-50k**	5	98	49907	51581	47397	1.3
3	**7Lys-PDMA-50k**	7	98	50163	52328	51943	1.3
9	**0Lys-PDMA-50k**	–	96	48318	48714	46037	1.3

[a] Monomer conversion determined by ^{1}H NMR. [b] Based on monomer conversion and the mass of the RAFT agent added. [c] Determined by GPC using DMF with 0.1% LiBr as eluent and PMMA as reference standards. The polymer size discrepancies in the GPC analyses can be attributed to the charge differences between the polymers, causing interactions both within the GPC column and inter-molecular interactions and discrepancies arising from the polymer reference used [92, 93].

The RAFT agents **1**, **2**, **3**, and **9** polymerised at a similar rate to the unmodified **DDMAT**, indicating that the addition of the fluorophore or the peptide did not inhibit the rate of radical transfer. This was initially a concern due to the increasing amount of free amines on the peptide backbone potentially causing the radical transfer to quench. Following synthesis, the polymer sizes were determined by ^{1}H NMR (polymer backbone resonances were integrated relative to the RAFT's terminal CH_3 groups)(**Figure 10**), and GPC (**Figure 11**). Determination of the final monomer conversion (^{1}H NMR) allowed the calculation of the theoretical molecular weights as a percentage of the initial target molecular weight (i.e. 7.5 kDa and 50 kDa) to which is added the mass of the RAFT agents. The ^{1}H NMR and GPC data verified the polymer chain lengths as being 7.5 kDa and 50 kDa, validating that the polymerisations occurred under controlled conditions and via the RAFT mechanism.

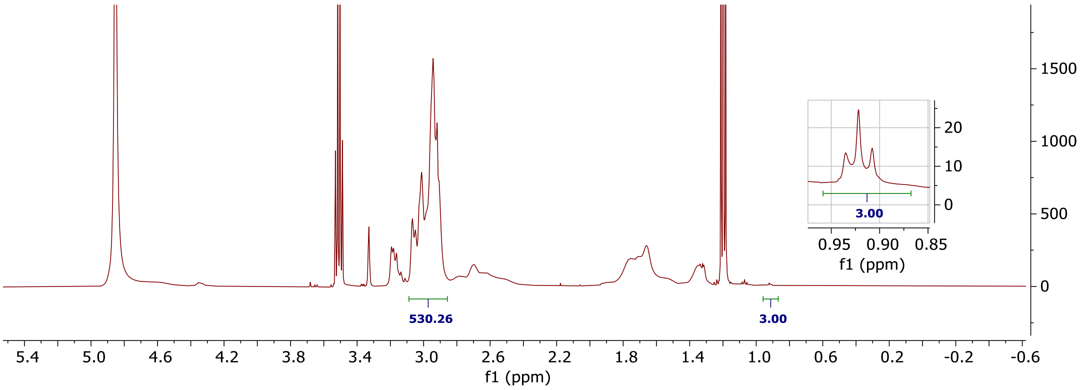

Figure 10: Determination of the size of **3Lys-PDMA-7.5k** by ^{1}H NMR spectroscopy. The resonance at 2.85–3.10 ppm (PDMA chain) is integrated with respect to the triplet at 0.92 ppm (terminal CH_3 on the RAFT agent) to calculate the polymer M_w. The same method was applied for the size determination of all the polymers.

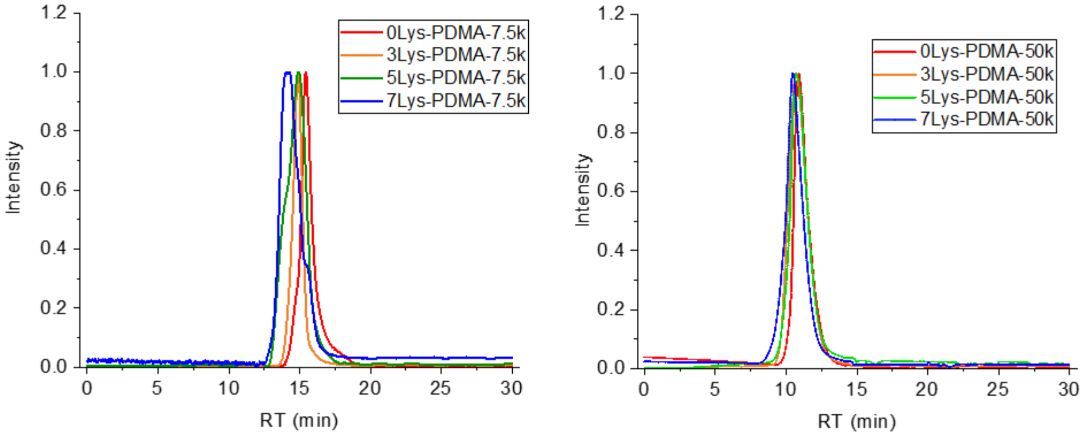

Figure 11: GPC traces of 7.5 kDa and 50 kDa lysine–PDMA polymers.

The GPC traces showed consistency with the desired polymer lengths, with peaks appearing at similar retention times, yielding molecular weight values close to 7.5 kDa and 50 kDa when calibrated to PMMA standards. However, more variation can be seen amongst the low Mw polymers with a pattern emerging of the longer the peptide on the polymer, the shorter the retention time. This occurs despite the polymers being quenched at very similar monomer conversion levels, which should indicate only small discrepancies between molecular weights. However, the proportional molecular weight change due to the peptide is much greater for the shorter polymers which would affect the retention time to a greater degree. The columns in the GPC system in which the polymers flow down are also susceptible to interactions and should ideally be ran in an ‘interaction free system’[94], as repulsive or attractive forces arising between the sample and stationary phase will cause peak shifting to occur, where the more highly charged sample will cause a bigger peak shift. This would explain the pattern seen for **7Lys-PDMA-7.5k** having a higher molecular weight value than anticipated as it is more positively charged.

Polymer PDI’s were all relatively low, indicating low polymer size dispersity that should allow for comparison between polymer samples. Low PDI’s also indicate that the polymerisation occurred via the RAFT agent instead of undergoing free-radical polymerisation, in which case the PDI would be much higher. This indicates that the RAFT agent should be present at the end of each polymer chain.Polymers were characterised by fluorescence spectroscopy, with polymers of the same size showing similar fluorescence intensities (**Figure 12**). This validates the polymers contained the “peptide-carboxyfluorescein RAFT” unit and that they are of a similar size.

The size differences between the 7.5 kDa and the 50 kDa Mw polymers could also be validated by the fluorescence intensity of the polymers. As each polymer chain contains exactly one fluorophore the size difference can be validated as the shorter polymers have an approximately 6.50 × brighter fluorescence at any given concentration, as would be expected (when taking into account the size differences of the polymers which is a factor of 6.66).

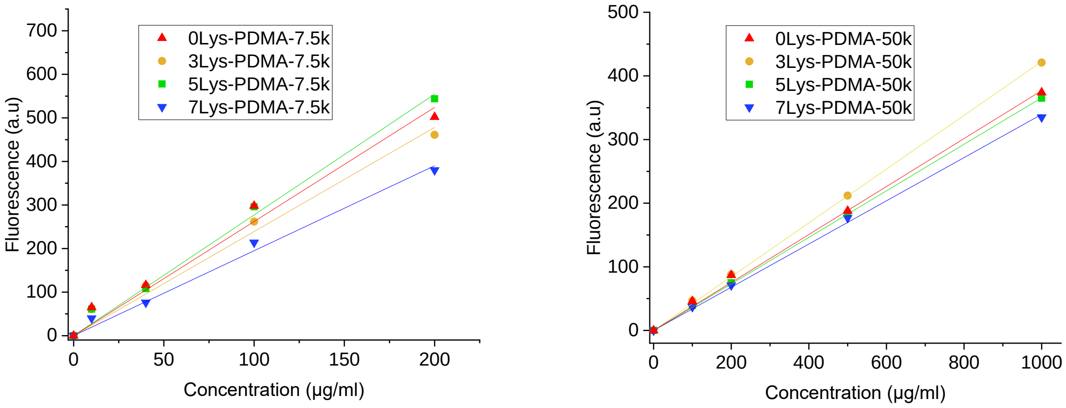

Figure 12: Concentration dependence of fluorescence ($\lambda_{Ex/Em}$ = 480/520 nm) of the 7.5 and 50 kDa polymers in PBS (prepared by serial dilution of 2 mg/ml stock solution).

3.4 *In vitro* Studies

To validate the polymers for biological applications their biocompatibility with cells was studied. For this, the MTT assay was selected for validation of cell toxicity as a rapid colourmetric assay. In this assay an estimate of the viable cell number is given by the dehydrogenase activity found in living cells reducing the tetrazolium ring in the MTT reagent (3-(4,5-dimethylthazolk-2-yl)-2,5-diphenyl tetrazolium bromide), causing a colour change from yellow to deep purple. Therefore, by reading the absorbance at 570 nm, quantification of the cell viability can be made. The MTT assay was selected in this case due to its ease of use and also the absorbance wavelength used was compatible with the fluorophore as their absorbance spectra do not overlap. HeLa cells were used as they are rapidly growing (doubling every 24 hours), making them ideal for testing. Cells were incubated with different concentrations of the polymers (5-1000 μg/ml) for 24 hours and the MTT assay was then performed to assess cell viability (**Figure 13**). Both the low and high molecular weight polymers showed no cell toxicity, even at very high concentrations (400 mg/ml and 1000 μg/ml, respectively) (**Figure 13a,** and **b**). This was further validated by the analysis of variance (Anova- Single Factor) yielding p values of less than 0.05 for all data points, indicating no significant difference between the cell viability of the control cells and the cells incubated with polymers.

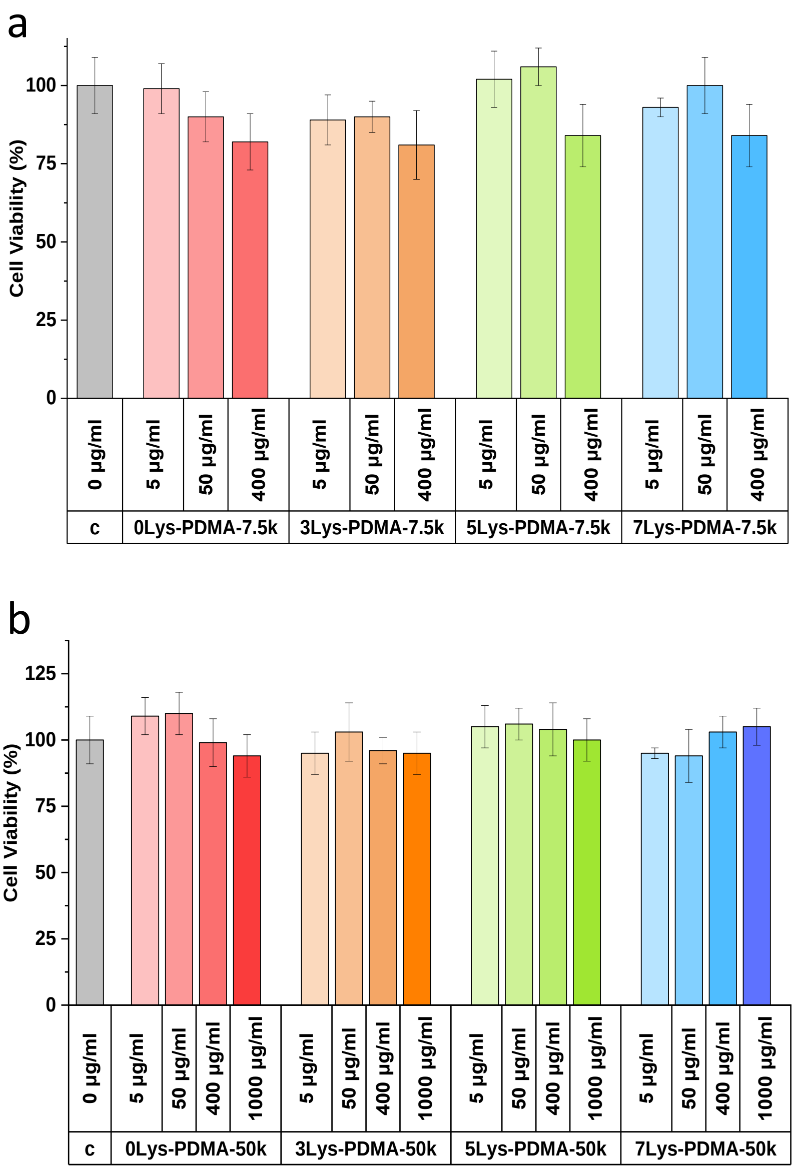

Figure 13: The cell viability (MTT assay) of HeLa cells after incubation with 7.5 kDa (5 – 400 µg/ml, 24 h) and 50 kDa polymers (5 – 1000 µg/ml, 24 h). c = control. Values are mean ± SD, n = 3, $p > 0.05$.

To evaluate cellular uptake efficiency, HeLa cells were plated and left to grow overnight. Cells were incubated with the 7.5 kDa and 50 kDa polymers (50 µg/ml) in complete media for 24 hours and analysed by flow cytometry (**Figure 14**). A 50 µg/ml concentration was selected after biocompatibility validation via an MTT assay.

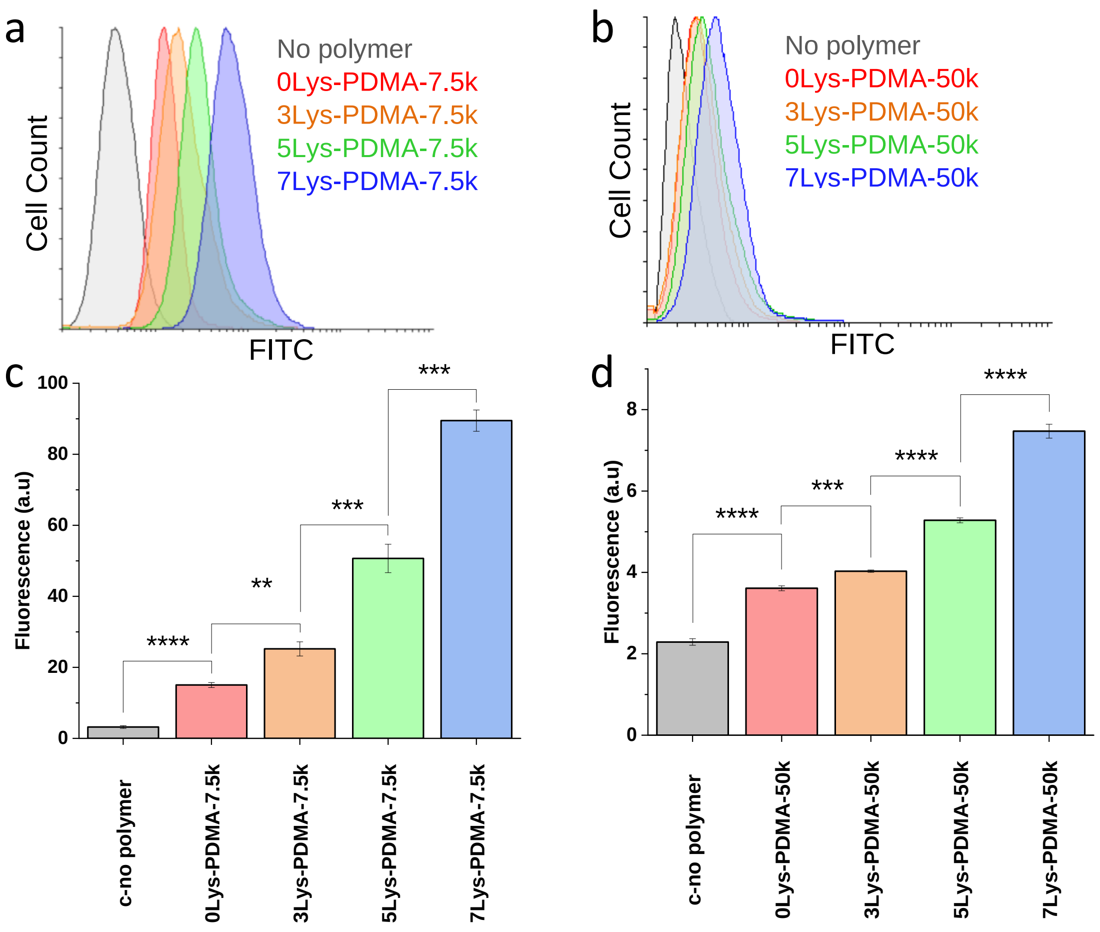

Figure 14: Flow cytometry histograms showing increase in the cellular uptake of both the a) 7.5 kDa and the b) 50 kDa polymers on the fluorescein isothiocyanate (FITC) channel (green, $\lambda_{Ex} = 488$ nm, $\lambda_{Em} = 530/30$ nm) compared to the corresponding control polymer without lysine and cells alone. Graphical data showing the cellular uptake of c) 7.5 kDa and d) 50 kDa polymers as measured by flow cytometry. The cells were incubated with the polymers at 50 µg/ml for 24 h. Values are mean ± SD, n = 3, ** = $p \leq 0.01$, *** = $p \leq 0.001$, **** = $p \leq 0.0001$.

The lysine chain length had a large impact on polymer uptake, with longer lysine chains resulting in higher polymer uptake with 1.7, 3.4, and 6.0-fold increased uptake for the **3Lys-PDMA-7.5k**, **3Lys-PDMA-7.5k**, and **7Lys-PDMA-7.5k**, respectively, compared to the control polymer **0Lys-PDMA-7.5k**. The 50 kDa polymers (**3Lys-PDMA-50k**, **5Lys-PDMA-50k**, **7Lys-PDMA-50k**) also showed increased uptake, although less significant (1.1, 1.5, and 2.1-fold increase in fluorescence compared to **0Lys-PDMA-7.5k**) likely due to both relatively lower brightness of the polymers per unit mass, and the higher uptake of the shorter polymers.

Cell uptake and localisation of the PDMA polymers was evaluated using confocal microscopy (**Figure 15a**) and the corresponding brightness was quantified (**Figure 15b**). HeLa cells were incubated with 200 µg/ml of the 7.5 kDa polymers for 24 h and stained with Hoechst 33342 nuclear stain. All images were taken under identical optical parameters and processed in the same way to allow for comparisons to be made between polymer samples. A large increase in fluorescence intensity can be seen for the **7Lys-PDMA-7.5k** polymers compared to the control polymer with the fluorescence intensity indicating that the level of cell uptake was proportional to the number of lysine residues.

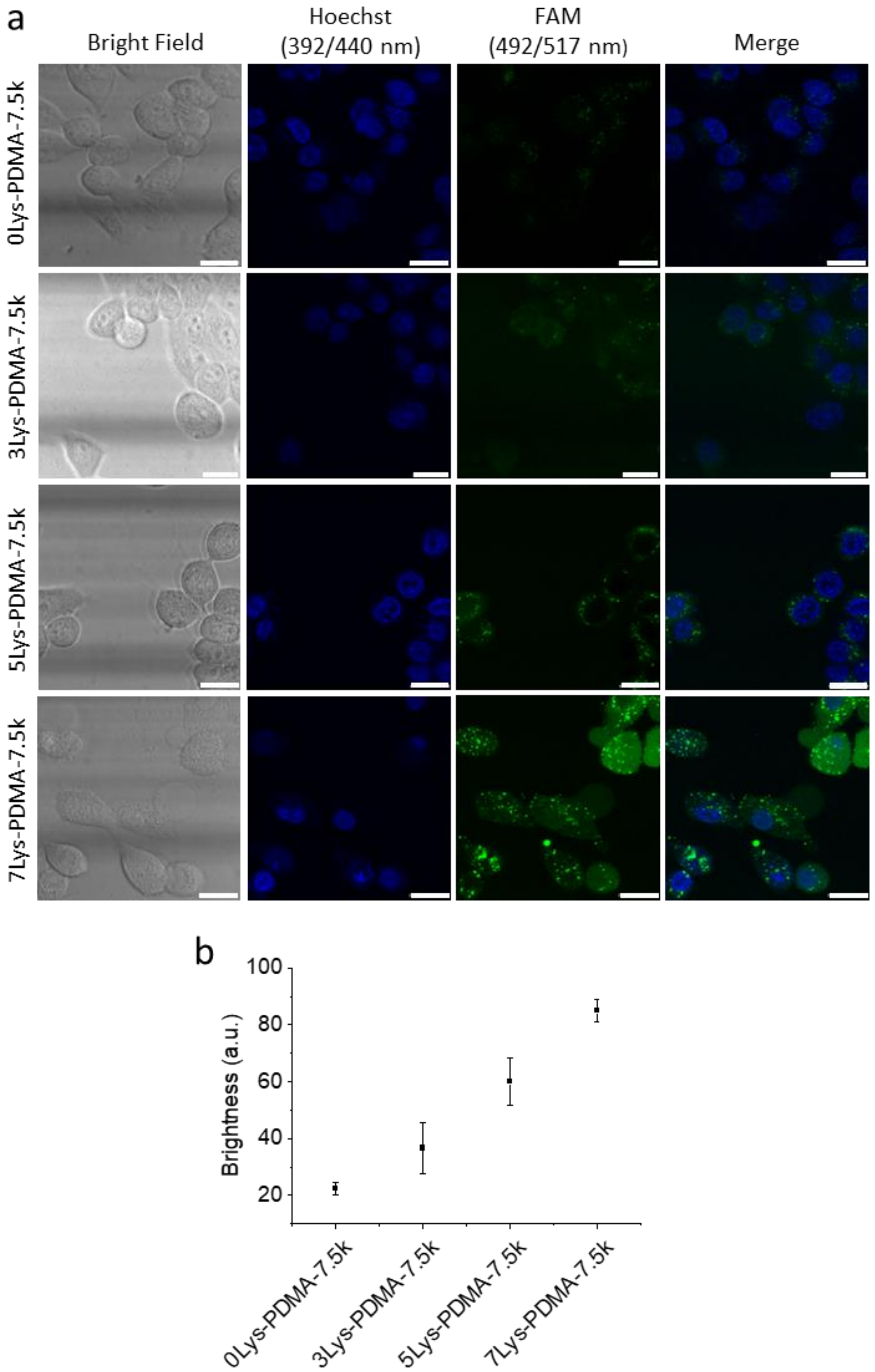

Figure 15: a) Confocal microscopy images of HeLa cells after incubation with 200 µg/ml (24 h) of 7.5 kDa polymers (FAM channel, $\lambda_{Ex/Em}$ = 492/517 nm). Cells were co-stained with Hoechst 33342 nuclear stain ($\lambda_{Ex/Em}$ = 392/440 nm). Scale bar = 20 µm. b) Associated brightness of confocal images. Values are mean ± SD, n = 3.

Finally, possible endosomal localisation of the polymers was explored due to reports that poly-Lysine moieties enter cells via non-specific adsorptive endocytosis.[95] Endosomal uptake was shown by co-staining cells with the endosomal stain CellLight™ Early Endosomes-RFP (**Figure 16**). CellLight™ reagents exploit the BacMem technology utilising insect cell viruses acting as a gene delivery platform to deliver fluorescent protein-signal peptide fusions. CellLight™ Early Endosomes-RFP labels early endosomes with red fluorescent protein that would be able to determine polymeric cell uptake via endocytosis, and co-localisation.

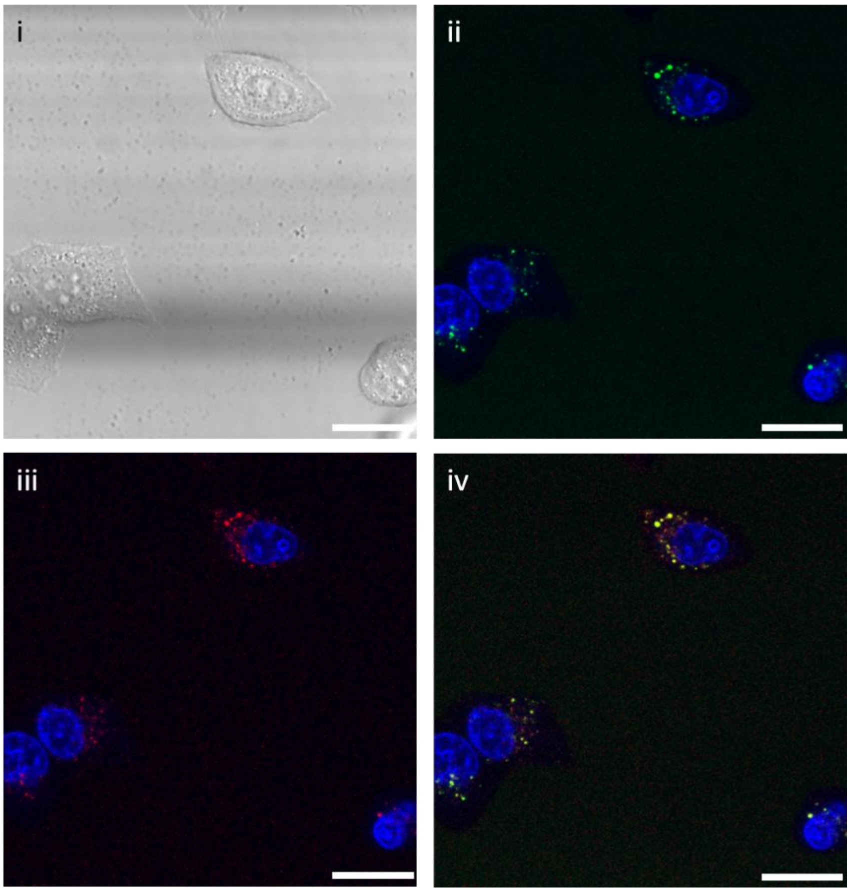

Figure 16. Confocal microscopy images of HeLa cells showing colocalization of the polymer with endosomes. HeLa cells were incubated with 5Lys-PDMA-7.5k (200 µg/ml, 24 h), co-stained with Hoechst 33342 nuclear stain ($\lambda_{Ex/Em}$ = 392/440 nm) and with CellLight™ early Endosomes-RFP, BacMam 2.0 (ThermoFisher) for early endosomes ($\lambda_{Ex/Em}$ = 555/584 nm). Scale bar = 20 µm.

Microscopy images confirmed the polymer uptake was via endocytosis by the co-localisation of both the CellLight™ Early Endosomes-RFP and the polymers overlapping. Therefore, polymers have entered the cells through the expected pathway.

3.5 Conclusion

In summary, size-controlled lysine–PDMA polymers were prepared by controlled polymerisation using fluorescently-tagged lysine-based RAFT agents prepared entirely by solid-phase synthesis. A 6-fold increase in polymer cell uptake was achieved as a result of adding lysine residues as an end group to the polymer chains, and these lysine-based RAFT agents can therefore be used as a strategy to deliver polymer vehicles inside cells for therapeutic and diagnostic applications. These novel RAFT agents could become useful tools to tackle the challenge of drug bioavailability and to develop enhanced therapies. Peptides conjugated to a RAFT agent is highly novel and powerful and it allows peptides with targeting activities to be attached to size controlled polymers with high efficiency.

4 Light Responsive Polymer Drug Release

Polymers hold unique benefits within drug delivery, potentially allowing high drug loading densities and promoting solubility. Coumarin is a molecule with light sensitive properties (both one- and two-photon) that when combined with polymers, would allow for the synthesis of light-cleavable systems that hold great potential for drug delivery[96].

4.1 Coumarin Monomer Synthesis

Integrating drugs conjugated to light responsive monomers into a hydrophilic polymeric backbone, would not only allow for improved drug solubility, but also allow for selective, targeted drug delivery. To facilitate this, a coumarin based monomer was synthesised, with the ambition of using it for two-photon release, according to a 3-step process shown in **Scheme 4**.

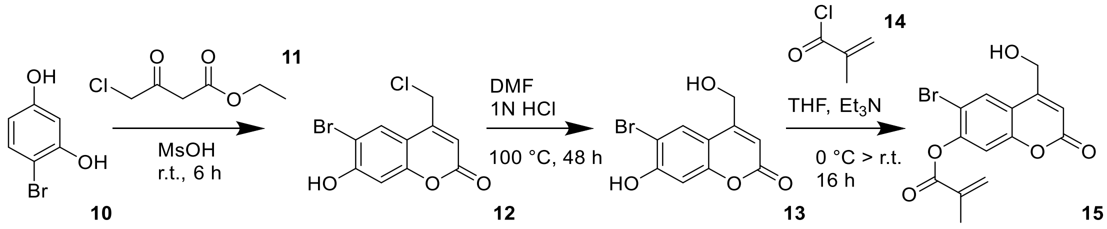

Scheme 4: Synthetic pathway to the coumarin monomer (**15**).

The first step was a cyclisation of ethyl 4-chloroacetoacetate **11** onto 4-bromoresorcinol **10**, with the product **12** obtained with a 72 % yield. The second step was hydrolysis involving the heating of **12** in a mixture of hydrochloric acid in DMF over two days, giving **13** in a 67 % yield. The third step involved the slow addition of methacryloyl chloride **14** into a basic solution of **13**, resulting in the monofunctionlised coumarin monomer product (**15**) and a difunctionalised by-product. This, along with other by-products resulted in a yield of 38 % after purification using column chromatography. This monomer was initially selected from the literature as it described a structure that was light cleavable according to **Scheme 5**[97].

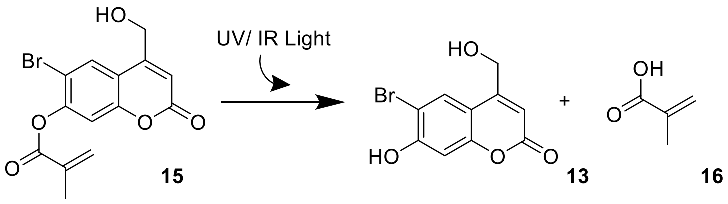

Scheme 5: The reported photocleavage of compound **15** when irradiated with light. Cleavage was indicated to occur at the ester bond to yield **13** and methacrylic acid **16**[97].

4.2 Coumarin Monomer Polymerisation

The coumarin monomer **15** was reported to cleave under UV light irradiation (365 nm) or under two-photon irradiation at ~700 nm. By shifting the cleavage conditions into the near infra-red NIR spectral range under two-photon irradiation, higher tissue penetration, lower tissue damage, and more precise drug release could be achieved. As such, a drug delivery system based on incorporating the coumarin monomers into a diblock copolymers was designed (**Figure 17**).

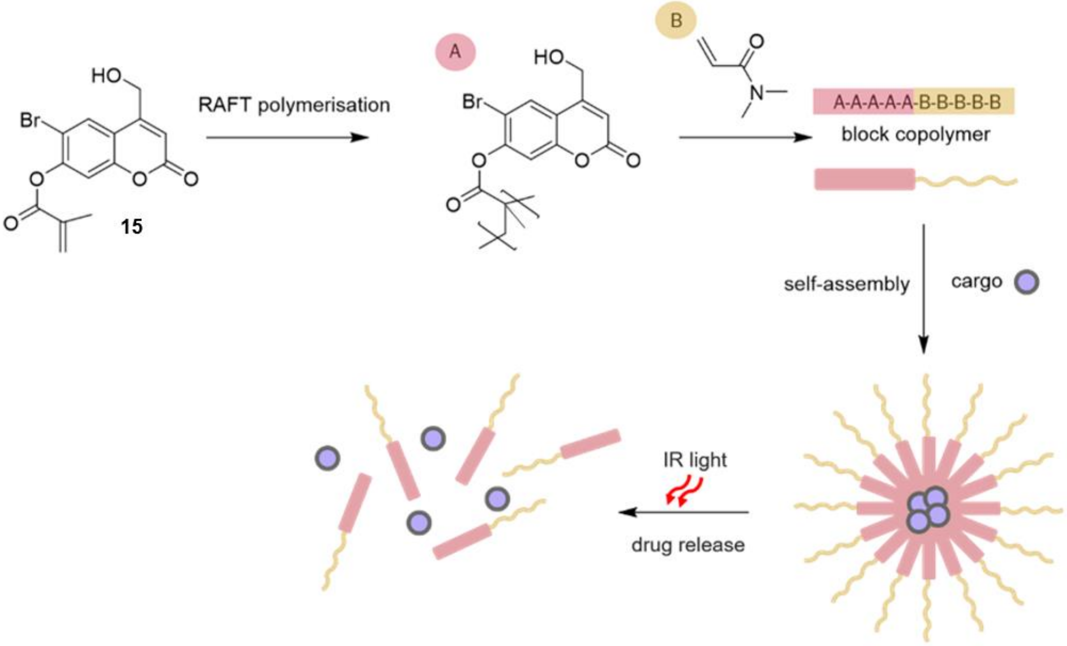

Figure 17: The generation of light cleavable nanoparticles encapsulating a cargo. The light responsive coumarin monomer **18** synthesised would undergo RAFT polymerisation to form a hydrophobic polymer (block A). Dimethylacrylamide polymerisation would add a hydrophilic block B to the polymer. An amphiphilic block copolymer with the structure A-A-A-B-B-B (when exposed to an aqueous environment at concentrations above the critical micelle concentration) would self-assemble in the presence of hydrophobic cargo (purple), into nanoparticles encapsulating the cargo. Once exposed to light, the coumarin moiety would react and disassociate from the methacrylate-based backbone of polymer A, decreasing of the hydrophobicity of the block. The nanoparticles would then break down due to the decrease in hydrophobic forces, releasing the cargo.

4.2.1 Coumarin Random Copolymers

For validation, **15** was first polymerised within a random copolymer with DMA acting as a water soluble monomer, using AIBN, and the RAFT agent 2-[[(butylthio)thioxomethyl]thio]-propanoic acid. Polymerisations were performed in a mixture of dioxane and D_2O (9:1), under argon with a ratio of AIBN:RAFT of 0.2:1, before being quenched in liquid nitrogen while exposed to air. Three polymerisation reactions with ratios of **15**:DMA, with respect to the RAFT agent, of 4:40 (**CM-DMA-1**), 4:80 (**CM-DMA-2),** and 4:120 (**CM-DMA-3**), were carried out.

Different ratios of DMA to **15** were explored to determine which monomer composition would result in a water soluble polymer. Water solubility was a desired property as it would allow for irradiation experiments to be performed in an aqueous environment that more closely emulates that of *in vivo* experiments. Polymer samples **CM-DMA-2** and **CM-DMA-3** containing less than 5 % **15** were fully water soluble, making them suitable for irradiation experiments. However, the polymer sample with ~10 % **CM-DMA-1** became insoluble in water, meaning that the maximum amount of coumarin monomer in the polymer was between 5-10 % before the polymer becomes insoluble. Polymer samples were also analysed via GPC to determine their size and PDI (**Figure 18**)

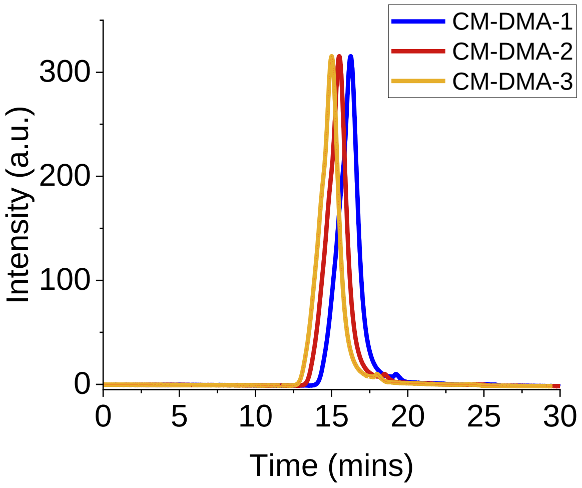

Figure 18: GPC chromatogram of **15** and DMA containing random copolymers, **CM-DMA-1**, **CM-DMA-2**, and **CM-DMA-3**.

As expected, polymers sizes corresponded very closely to the theoretical values based on the reaction conditions (**Table 3**). PDI values were also low (<1.5), indicating that the polymerisation occurred via RAFT and the polymers had a low size dispersity.

Table 3: Monomers ratios used in the random copolymerisation reactions of **15** with DMA, with resulting polymer sizes and water solubility. (Molar ratios of AIBN:RAFT were 0.2:1 with respect to DMA and **15** ratios in the table)

Polymer	**15**	DMA	Theoretical Size [Da][a]	Mw [Da] (GPC)[b]	PDI	Solubility in water (Y/N)
CM-DMA-1	4	40	5594	5595	1.37	N
CM-DMA-2	4	80	9594	9638	1.42	Y
CM-DMA-3	4	120	13594	13743	1.47	Y

[a] Based on monomer components and the mass of the RAFT agent. [b] Determined by GPC using DMF with 0.1% LiBr as eluent and PMMA as reference standards.

4.2.2 Coumarin Diblock Copolymers

Diblock copolymers of DMA:**15** were also synthesised to facilitate light responsive nanoparticles. Different monomer ratios were explored to facilitate nanoparticles with different morphologies. To synthesise the diblocks copolymers, a RAFT agent was first polymerised with the desired ratio of DMA using AIBN as an initiator, at 70 ºC under argon. The reaction was quenched in liquid nitrogen under air and purified via precipitation in diethyl ether. The diblock was then continued by polymerising the DMA polymers with the desired ratios of monomer **15**, under the same conditions and quenched and purified in the same way. Three polymers were synthesised using different ratios of **15** and DMA to vary the hydrophilicity of the diblock, and also to vary the size of the resulting polymers. The size and PDI of the diblock polymers was assessed using GPC where the expected molecular weights and low PDIs were confirmed (**Table 4**, **Figure 19**).

Table 4: Monomers used in the diblock copolymer polymerisation reactions, theoretical and measured size, PDI, and polymer design properties. Molar ratios of AIBN:RAFT were 0.2:1 with respect to DMA and **15** in the table)

Polymer	**15**	DMA	Theoretical Size [Da][a]	Mw [Da] (GPC)[b]	PDI	Property
CM-DMA-4	10	20	6168	6146	1.36	Short
CM-DMA-5	50	100	27188	29957	1.64	Long
CM-DMA-6	20	220	29018	30563	1.60	Long, more hydrophilic

[a] Based on monomer components and the mass of the RAFT agent. [b] Determined by GPC using DMF with 0.1% LiBr as eluent and PMMA as reference standards.

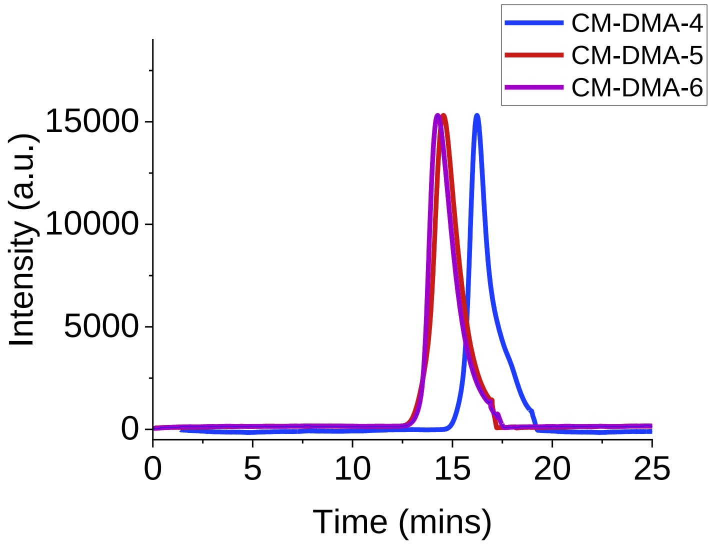

Figure 19: GPC chromatogram of **15** and DMA containing diblock copolymers

4.3 Coumarin Nanoparticle Synthesis

To form nanoparticles from diblock copolymers **CM-DMA-4**, **CM-DMA-5**, and **CM-DMA-6**, the nanoprecipitation method was used. Polymers were dissolved in a water miscible solvent and added dropwise to a larger volume of water to encourage nanoparticles to form. Here, 6 mg of each polymer was dissolved in DMF (200 µL) this solution was added dropwise to H_2O (800 µL) under stirring. To purify the nanoparticles dialysis was performed over 24 hours.

TEM and DLS was performed to analyse the morphology of the nanoparticles generated (**Table 5**) (**Figure 20**).

Table 5: Nanoparticle characterisation of polymers **CM-DMA-4**, **CM-DMA-5**, and **CM-DMA-6** in water.

Polymer	Nanoparticle Diameter [nm] (DLS)	PDI (DLS)	Nanoparticle Diameter [nm] (TEM)	Error (SD) [nm] (TEM)
CM-DMA-4	60	0.279	22	6
CM-DMA-5	408	0.475	504	224
CM-DMA-6	82	0.220	54	20

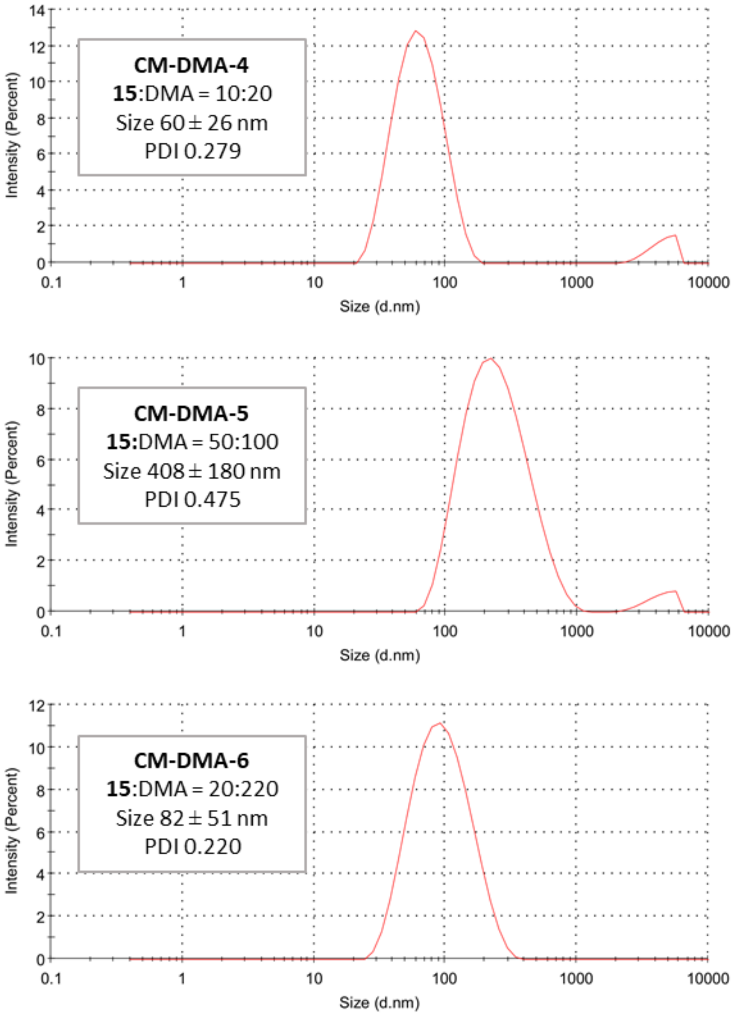

Figure 20: DLS of nanoparticles formed from **15**-DMA diblock polymers, in H_2O.

DLS results showed that the monomer composition of the polymers had a large impact on the resulting nanoparticle size and their PDIs. The shorter polymer **CM-DMA-4** resulted in the smallest nanoparticles, as was to be expected as a shorter polymer is likely to also result in nanoparticles with a smaller diameter. Interestingly the ratio of **15**:DMA also had a large impact on nanoparticle size. Polymers **CM-DMA-5** and **CM-DMA-6** had similar molecular weights but where **CM-DMA-6** contained a higher proportion of **15**. **CM-DMA-5** nanoparticles were much larger in diameter and PDI. This is likely due to the combination of longer hydrophobic chains and shorter hydrophilic chains causing more instability in the nanoparticle due to entropy, making them more likely to aggregate, leading to higher PDIs. TEM was also performed to assess the morphology of the nanoparticles (**Figure 21**).

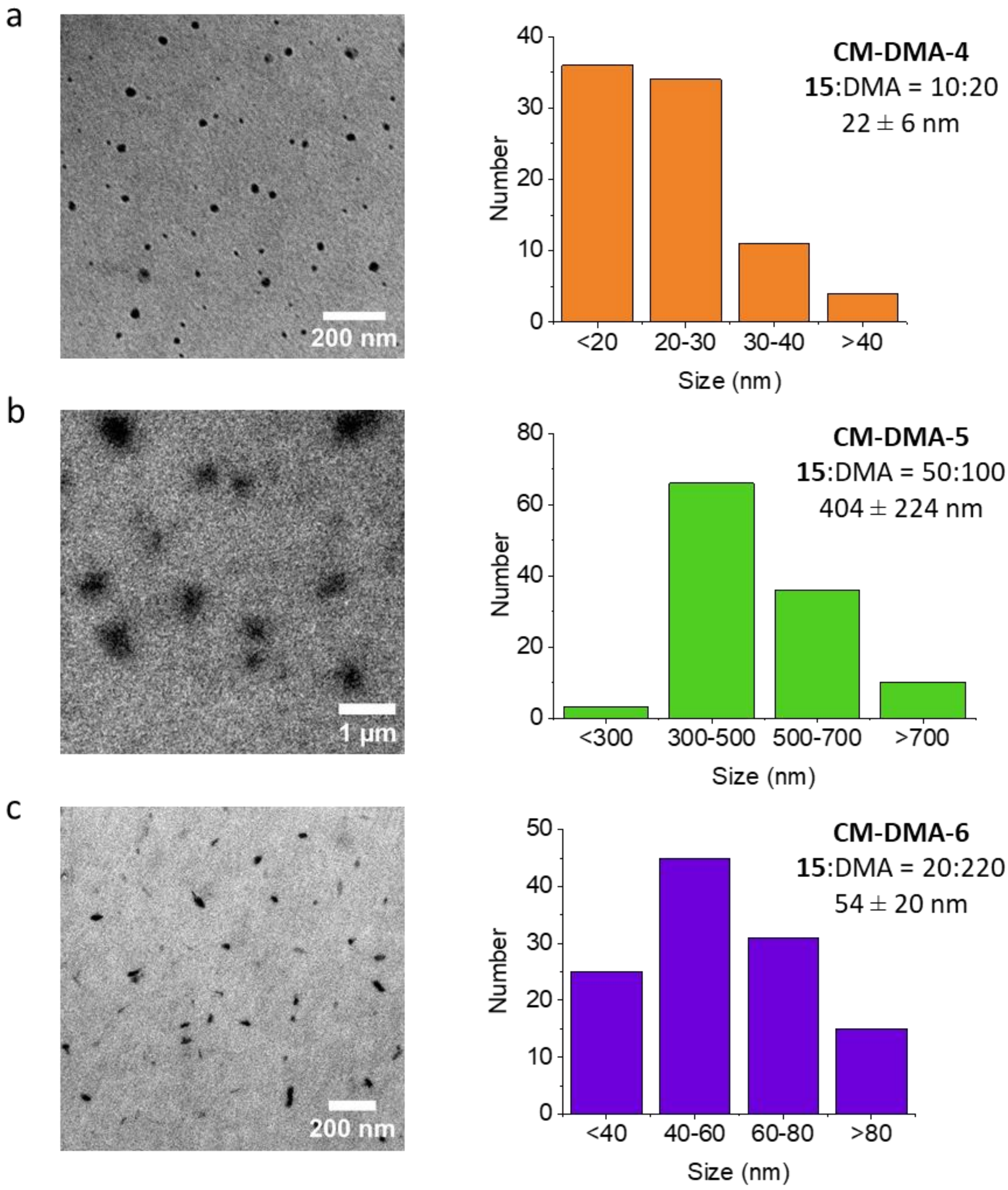

Figure 21: TEM images of morphology and corresponding size dispersity of nanoparticles. a) **CM-DMA-4**. b) **CM-DMA-5**. c) **CM-DMA-6**.

TEM confirmed the findings from the GPC results, with more monodisperse samples being seen from **CM-DMA-4**. As these nanoparticles were the most homogenous in terms of shape, size and PDI, they were selected for testing under irradiation.

To validate the light sensitivity of the nanoparticles, an experiment was designed to assess cargo release under light to quantify nanoparticle cleavage. Nanoparticles were fabricated using polymer **CM-DMA-4** encapsulating Rhodamine B. Nanoparticles were fabricated as before but with Rhodamine B being added to the polymer in DMF. Nanoparticles were then purified using dialysis against deionised water (15,000 Mw cut off) over 3 days, until the water was clear.

4.4 Light Responsivity of Coumarin

A series of experiments were designed to explore the light sensitivity of the coumarin moiety. As the coumarin monomer **15** was poorly water soluble, the light sensitivity was tested on the compound in mixtures of organic solvents using NMR and HPLC. To test the coumarin in aqueous conditions polymer **CM-DMA-2** was used containing **15**:DMA in a 4:80 ratio as this polymer contained the highest amount of light cleavable **15** while also remaining water soluble. The polymers were evaluated using NMR and absorbance spectrometry to assess cleavage. Finally, nanoparticle cleavage was evaluated by assessing cargo release from rhodamine containing nanoparticles fabricated from **CM-DMA-4**.

4.4.1 Coumarin Monomer

The light-sensitivity of the monomer was evaluated using HPLC (**Figure 22**) after 365 nm irradiation over 60 minutes. The degradation was assessed via HPLC (retention time of 4.65 minutes for **15**). Peaks were expected to appear at 3.20 minutes, indicating the release of compound **13** as the cleavage occurs. After 60 minutes no signs of cleavage were observed, with the area under the peak remaining constant (**Figure 22a**) and no new peaks appeared (**Figure 22b** and **c**).

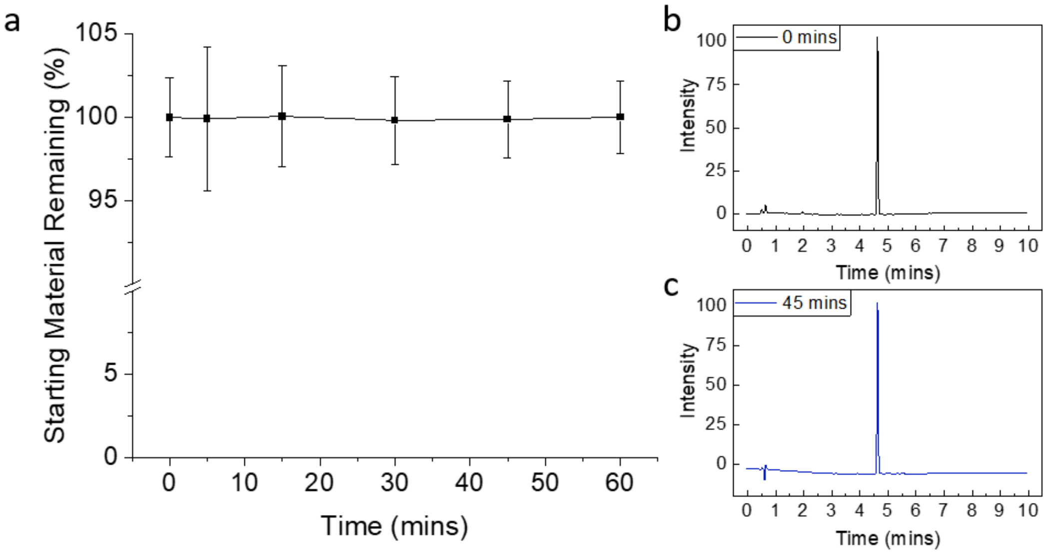

Figure 22: a) Percentage of compound **15** remaining following 365 nm irradiation over 60 minutes. Samples were analysed via HPLC (282 nm, eluting with acetonitrile (0.1% FA) and water (0.1% FA). Values are mean ± SD, n = 2. b) HPLC trace of **15** at t = 0. c) HPLC trace of **15** after 45 minutes of 365 nm irradiation.

To further validate these results, an experiment was carried out using ^{1}H NMR. A sample of compound **15** was dissolved in DMSO-d_6 (2 mg/ml) and ^{1}H-NMR spectra were collected before and after the irradiation (sample was irradiated under 365 nm light in a quartz cuvette under stirring for 180 minutes). Following irradiation, no change could be seen (**Figure 23a** and **b**). Note that the water content in the sample increased during the course of the experiment due to the hygroscopicity of the DMSO-*d*6. This is also the likely cause of the proton of the hydroxyl group no longer being visible following irradiation.

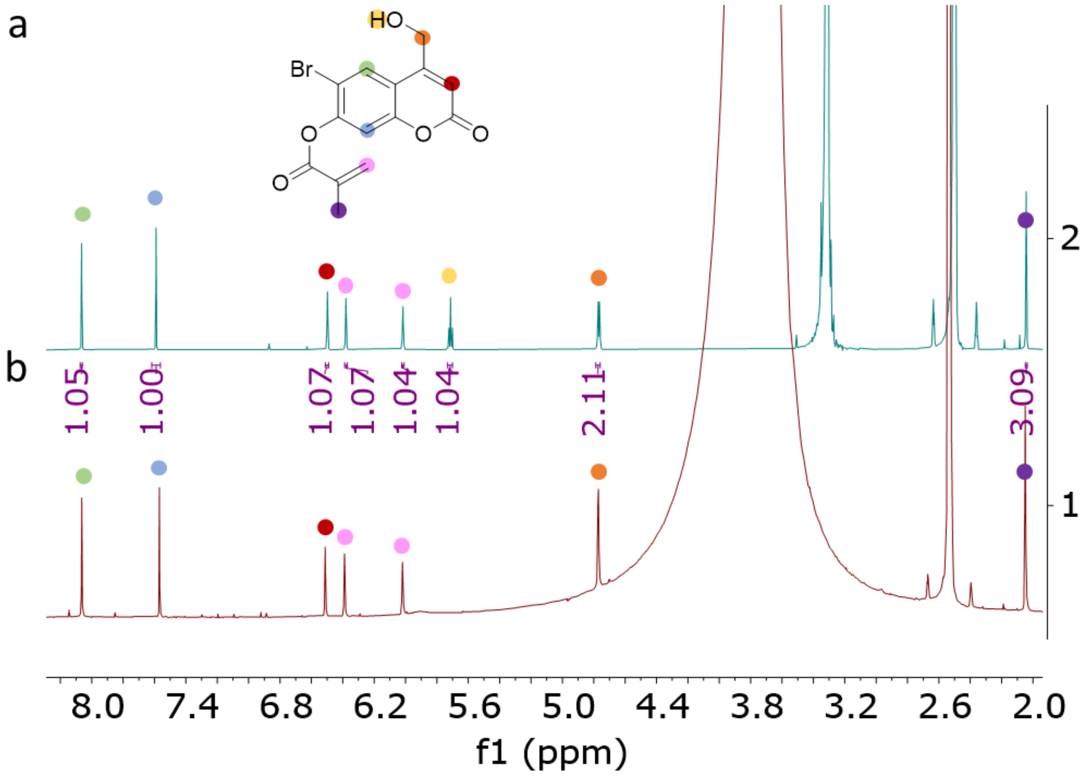

Figure 23: 1H-NMR Spectra of compound **18** in DMSO-*d*6. a) Prior to irradiation. b) After 180 minutes of 365 nm irradiation.

4.4.2 Coumarin Random Copolymer

A rationale for the cleavage of **15** not occurring could be due to the high percentage of organic solvent required to solubilise the coumarin monomer. Water is speculated to be involved in the cleavage mechanisms of coumarin-4-yl methyl esters, and therefore could affect cleavage rates if not present in high enough quantities[98]. Therefore, the water soluble random copolymer **CM-DMA-2** was irradiated in aqueous conditions to validate the light sensitivity of the coumarin moiety. This experiment was performed to validate an identical experiment performed in the literature in which this coumarin moiety was reported to be light cleavable[97]. In this experiment the authors irradiated a similar hydrophilic polymer in aqueous conditions and showed that the broad peaks from 6.5-8.5 ppm in the ^{1}H-NMR spectrum corresponding to the polymerised coumarin monomer disappears under 365 nm irradiation. The synthesised **CM-DMA-2** would cleave according to **Scheme 6**, with the residual coumarin moiety **13** being water soluble. The broad NMR peaks corresponding to the coumarin along the polymer chain would not be expected to disappear completely, but to decrease, and narrow peaks corresponding to the non-polymerised coumarin should appear.

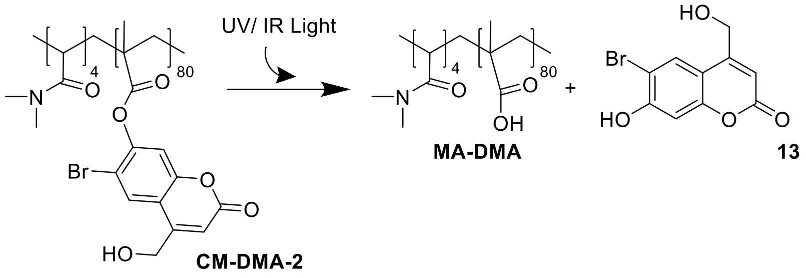

Scheme 6: Cleavage of the coumarin **13** from the backbone of the polymer **CM-DMA-2** under UV light.

However, following 30 minutes of 365 nm irradiation, no change could be seen (**Figure 24)**, and integrations remained constant (within the 5 % error margin of NMR spectra), indicating that no cleavage occurred.

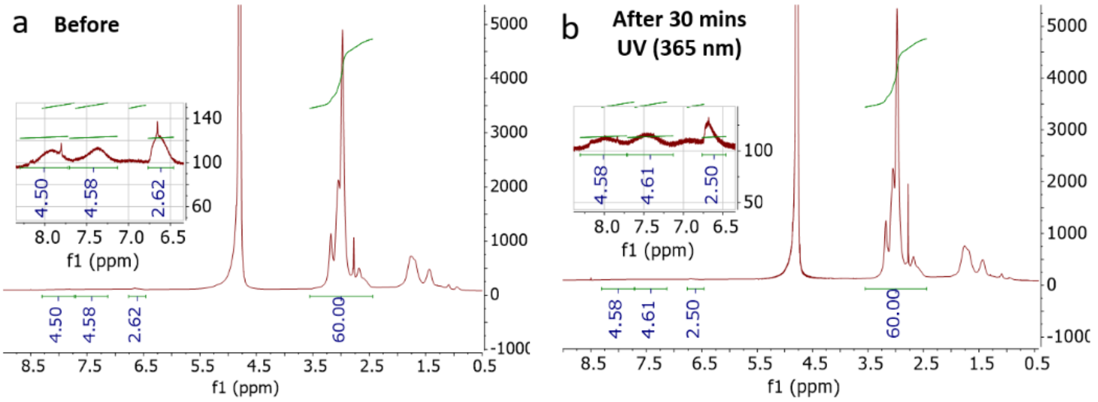

Figure 24: ^{1}H-NMR spectra of **CM-DMA-2** in D_2O. Peaks between 2.44-3.55 ppm correspond to the backbone of the poly-DMA, integrated to 60 to represent 6 protons, and 6.5-8.5 ppm correspond to the polymerised-compound **15**. a) Before irradiation, showing the integration of the coumarin peaks with respect to the poly-DMA backbone. b) After 30 minutes of 365 nm irradiation, showing the same ratios of integration, indicating no cleavage occurred.

To ensure that the problem was not due to lack of sensitivity in the NMR, another approach was taken. Before and after polymer **CM-DMA-2** was irradiated, absorbance spectra were acquired to investigate if cleavage occurred. Coumarin **13** with a free hydroxyl at position-7 has a more red-shifted absorbance spectra compared to that with the methacrylate moiety attached **15** (**Figure 25a** and **b**). Note, analysis were performed in MeOH due to the lack of water solubility of **15**. Following cleavage, a shift in the absorbance peak of the polymer should occur from ~320 nm to ~ 365 nm. However, following irradiation, no change could be seen, indicating no cleavage of the coumarin from the polymer.

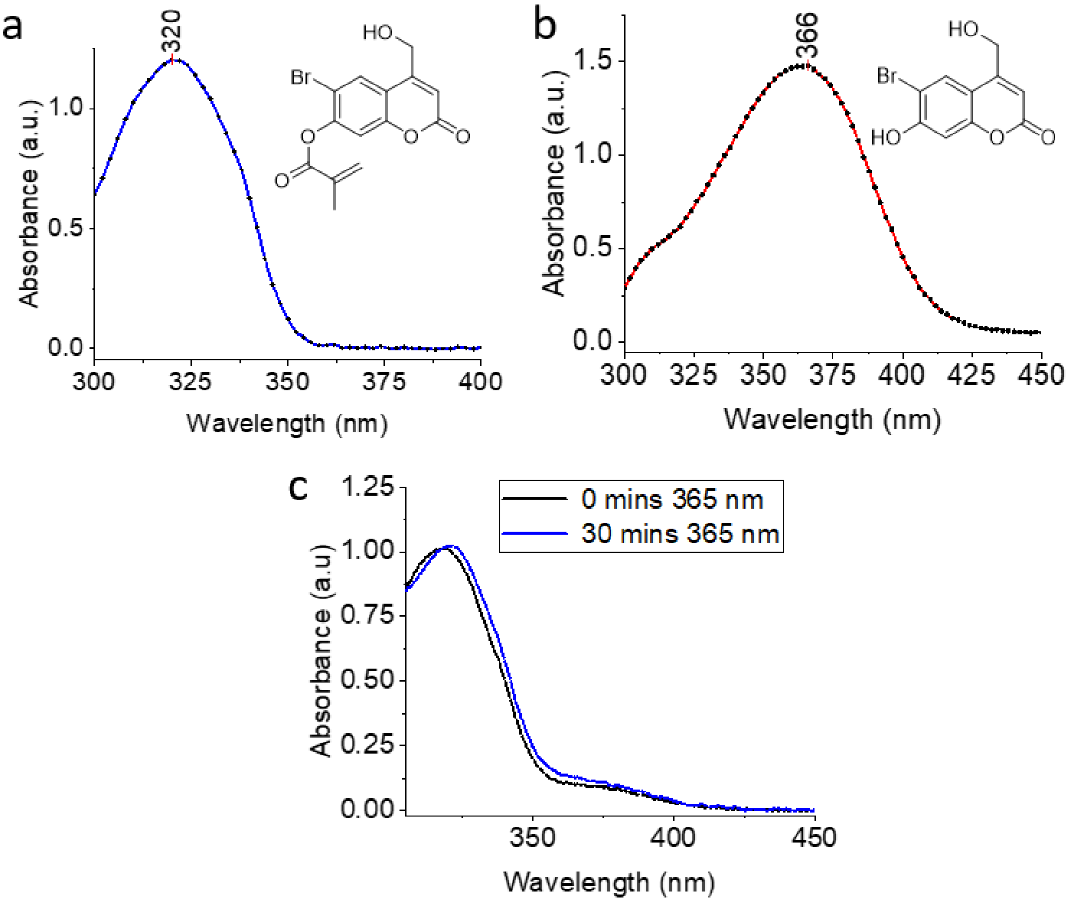

Figure 25: a) Absorbance spectrum of **15** in MeOH. b) Absorbance spectra of **13** in MeOH. c) Absorbance spectra of **CM-DMA-2** before and after 30 minutes of irradiation under 365 nm.

4.4.3 Coumarin Nanoparticles

To investigate the release profile of nanoparticles under 365 nm light, Rhodamine B loaded nanoparticles fabricated using **CM-DMA-4** were used. Nanoparticles were irradiated under 365 nm light and the fluorescence signal was measured (540 nm λ_{ex}, 570 nm λ_{em}) (release of rhodamine would be expected by the uncaging of the coumarin, and would result in an increase in the fluorescence signal). However, no rhodamine was released from the nanoparticles following irradiation (**Figure 26a**).

To determine that rhodamine could be released from the nanoparticles a sample of nanoparticles was heated. Heating nanoparticles leads to the polymers dissociating from each other and a cargo being released. The nanoparticles were heated to 70 °C for 60 minutes and samples were taken at given time points and the fluorescence was analysed. The rhodamine was found to release from the nanoparticles during heating, validating that the nanoparticles contained the cargo, but were not releasing the cargo under 365 nm irradiation (**Figure 26b**).

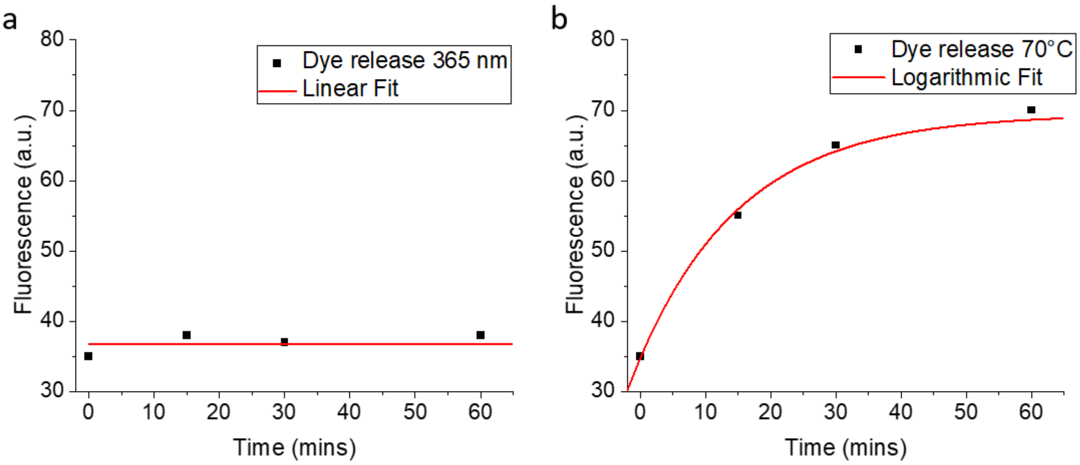

Figure 26: Fluorescence signal intensity (540 nm λ_{ex}, 570 nm λ_{em}) of Rhodamine B showing a) Rhodamine B release from nanoparticles over 60 minutes of 365 nm irradiation. b) Rhodamine B release from nanoparticles over 60 minutes of heating at 70 °C.

Upon further analysis of the literature, there was only one report of position 7 being used on the coumarin allowing light-cleavage[97]. It was therefore deemed unlikely that this position on the coumarin was light-sensitive, and the literature was in error.

4.5 Coumarin-Camptothecin Monomer Synthesis

After validating the lack of UV light sensitivity of compound **15** as a monomer, polymer, and as nanoparticles, a new approach to utilising the monomer for drug release was developed. After establishing that the 7- position was not photoactive as reported, a system in which the well-reported photoactive 4- position on the coumarin was utilised to facilitate drug release (**Figure 27**).

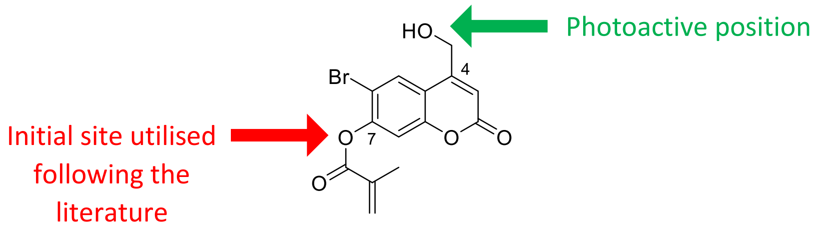

Figure 27: The supposed photoactive position 7 on the coumarin **15** as reported in the literature and the actual photo active position 4[97].

Moving forward, the project utilised the well-reported photoactive position 4 (**Figure 27**, green) and exploited the newly-established photo stability of the methacrylate in position 7 (**Figure 27**, red). The mechanism for the photocleavage is demonstrated in **Scheme 7** and arises due to the 'Zimmerman meta-effect' causing electron redistribution as a result of photon absorption, thus resulting in photo-sensitivity at position 4.

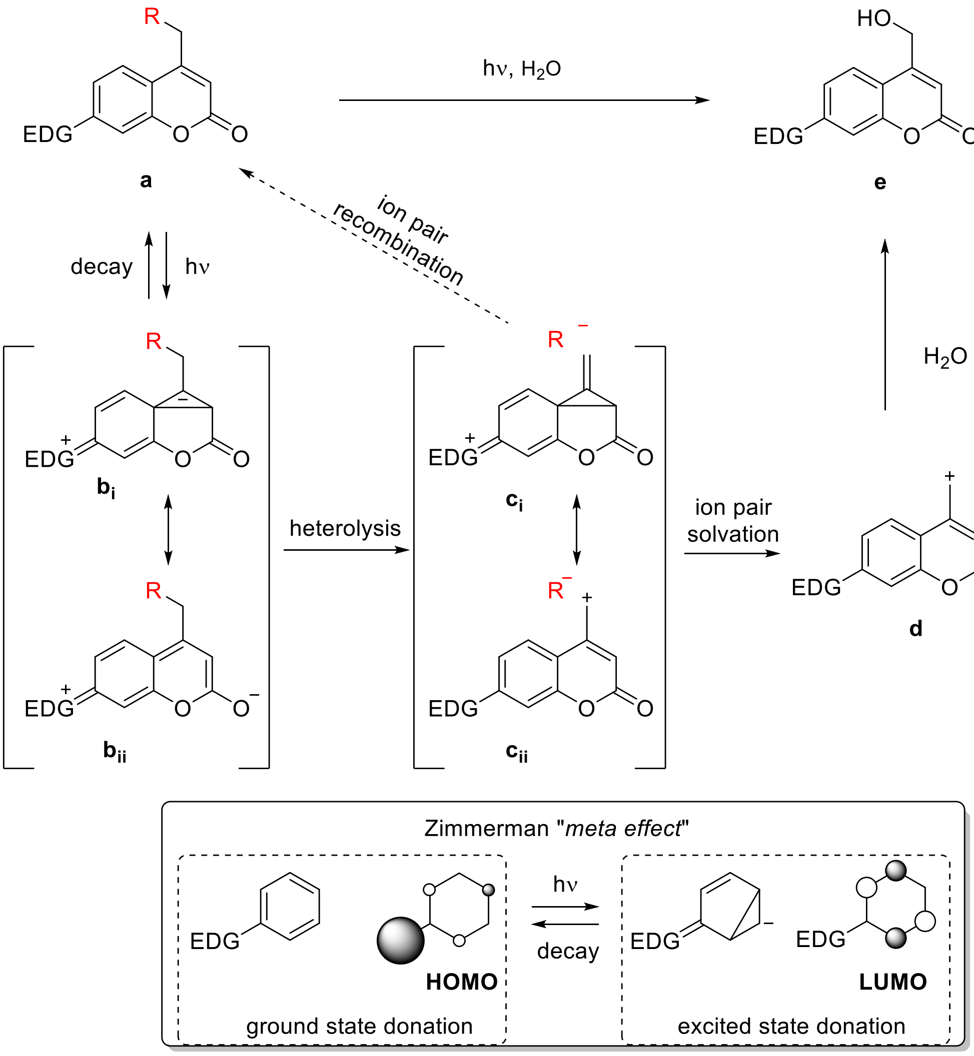

Scheme 7: Mechanism of photocleavage of coumarin arising from the Zimmerman meta-effect. EDG =electron donating group.

For the new design, a highly toxic hydrophobic anti-cancer drug was conjugated onto coumarin **15** in the photoactive position 4 that was then polymerised within a hydrophilic polymer to yield a water soluble polymer with a light cleavable drug attached.

Camptothecin (**CPT**) was selected as the chemotherapy agent due to its very poor water solubility and very high toxicity. **CPT** targets topisomerase that is over expressed in many cancers, resulting in DNA damage and cell apoptosis. The drug cannot be given via classic delivery methods of high doses of drug over intermittent time frames due to the high levels of toxicity, and therefore must be given at lower doses which reduces cancer killing efficiency and drives resistance[99]. Caging the coumarin moiety **15** to the **CPT's** active site renders the drug inactive as long as it is caged. When exposed to light in selective biological sites, the drug will be uncaged and become active. The project will therefore develop a selectively targeting, water soluble solution to delivering **CPT** into cancer cells.

CPT was conjugated to the coumarin monomer **15** in a one-step synthesis using triphosgene and DMAP in DCM. The **CPT**-coumarin monomer **17** was purified using column chromatography (**Scheme 8**).

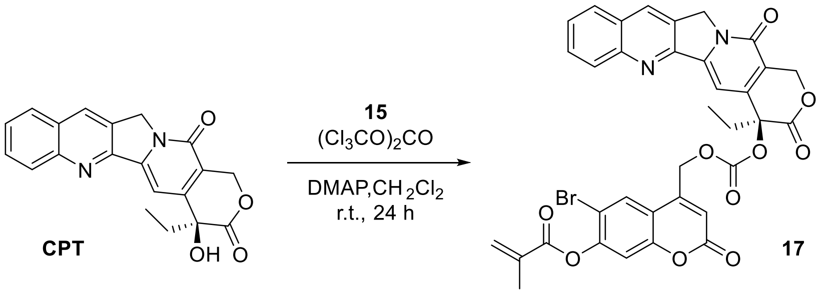

Scheme 8: Synthesis of **17** via conjugation of **CPT** to coumarin monomer **15**.

The light sensitive monomer **17** was then polymerised to give **CM-CD-DMA** as a water soluble polymer by random RAFT copolymerisation with DMA. The monomer ratio of 2:100 of **17**:DMA was selected for the polymerisation conditions for two reasons. The first reason was to include enough DMA to ensure water solubility of the polymer, to permit biological testing. The second was to incorporate enough **CPT**-Coumarin **17** into the polymer **CM-CD-DMA** when considering the IC50 of **CPT** in HeLa (5-10 µM), but also factoring in the typical polymeric doses in cell experiments (up to 1 mg/ml polymer for HeLa) [100-103]. The polymerisation was performed in a mixture of dioxane and D_2O in a 90:10 ratio using AIBN as an initiator under argon (**Table 6**), and the polymer was characterised using NMR and GPC to validate the size and structure of the polymer.

Table 6: Synthesis and characterisation of the light sensitive **CPT** releasing water soluble polymer **CM-CD-DMA**.

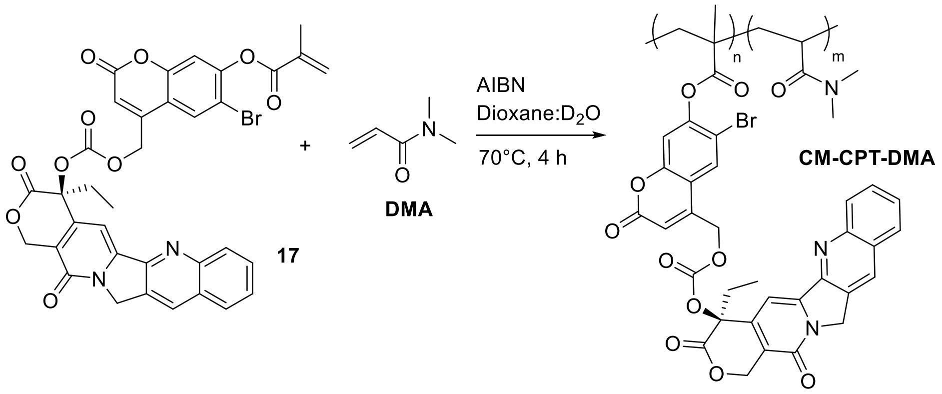

Polymer	**17**	**DMA**	AIBN	RAFT	Theoretical Size [Da][a]	Mw [Da] (GPC)[b]	PDI
CM-CPT-DMA	2	100	0.1	1	11704	11997	1.29

[a] Based on monomer components and the mass of the RAFT agent. [b] Determined by GPC using DMF with 0.1% LiBr as eluent and PMMA as reference standards.

4.6 Light Responsivity of Coumarin-Camptothecin

4.6.1 Coumarin-Camptothecin Monomer

17 under 365 nm irradiation should cleave according to **Scheme 9**.

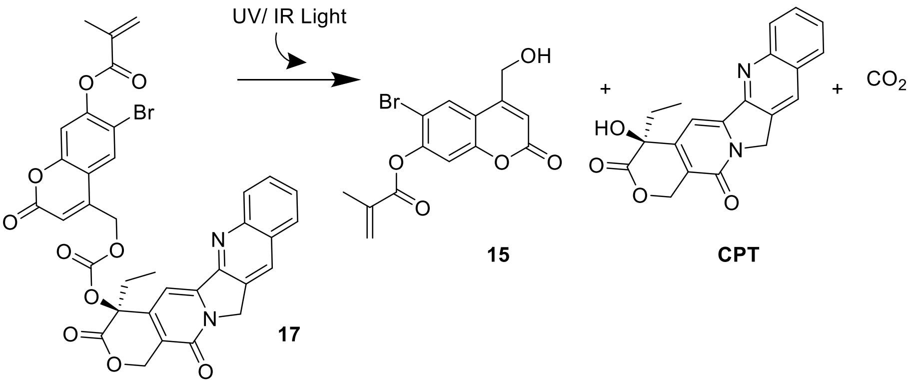

Scheme 9: Photocleavage of **CPT**-coumarin monomer **17**.

HPLC was used to assess the cleavage efficiency of **CPT** from **17**. A 100 µM solution of **17** was irradiated at 365 nm for 60 seconds and samples were taken and analysed via HPLC, to evaluate cleavage rate (**Figure 28**).

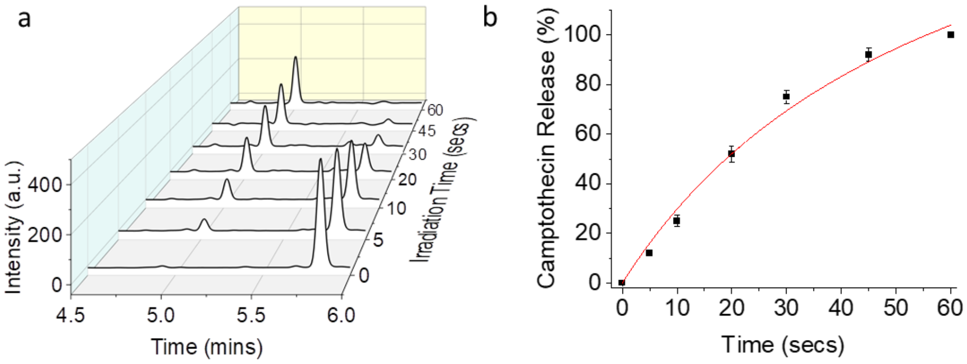

Figure 28: **CPT** release from **17** during 365 nm irradiation in a 50:50 mixture of H_2O:Acetonitrile. a) HPLC traces at 310 nm, shows intensity, retention time (mins), and irradiation time (secs). **17** t_R = 5.82 min, **CPT** t_R = 5.02 min b) **CPT** release under irradiation via peak integration. Values are mean ± SD, n = 3.

During the cleavage the peak at 5.82 min (**17**) decreased, while the peak at 5.02 min (**CPT**) increased, indicating drug release. The cleavage rate of **17** occurred very quickly, achieving 100 % cleavage of **CPT** after only 60 seconds of irradiation. To investigate the efficiency of cleavage a kinetic follow-up was performed to determine the photochemical quantum yield of the uncaging reaction (Φ_u), given by **Equation 3**.

Equation 3: $$\Phi_u = (I\sigma^{\lambda}t_{90\%})^{-1}$$

Where I is irradiation intensity expressed in einstein·cm^2·s^{-1}, σ^{λ} is the decadic extinction coefficient at the excitation wavelength λ ($\varepsilon^{\lambda} \times 10^3$, where ε is the extinction coefficient) in cm^2·mol^{-1}, and $t_{90\%}$ is the irradiation time for 90 % photolysis conversion, given in seconds.

This method relies on using a reference (potassium ferrioxalate) of which the optical properties are well reported to determine I of the 365 nm light source used. Actinometry was then be performed to determine the Φ_u of **17**. I was determined according to a method reported by Suzuki *et al.* in which a 0.006 M Potassium ferrioxalate was mixed with 1,10-phenanthroline both before and after a 5 second 365 nm irradiation[104]. The absorbance spectra were acquired, and the absorbance of the Fe^{2+} ion complex at 510 nm measured (**Figure 29**).

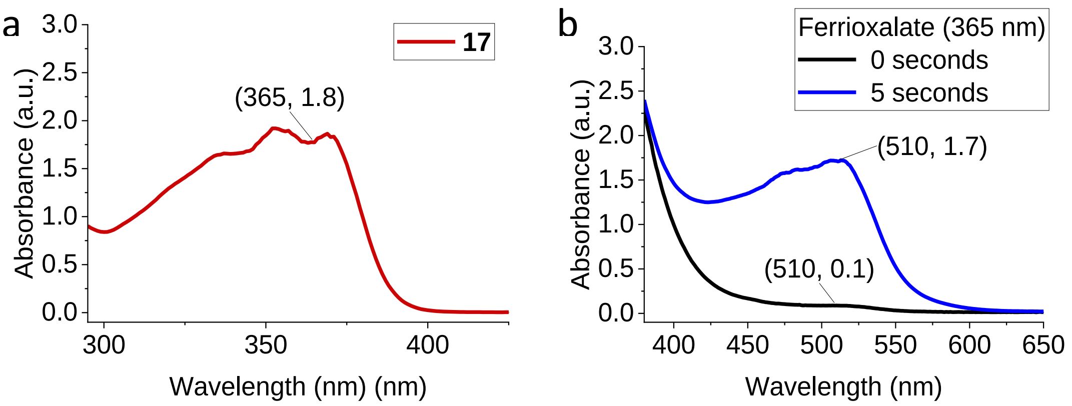

Figure 29: a) Absorbance spectrum of **17**. Absorbance at 365 nm used to determine ε^{λ} and therefore σ^{λ}. b) Absorbance spectra of potassium ferrioxalate and 1,10-phenanthroline mixture before and after 5 seconds of 365 nm irradiation.

Total irradiation intensity I of the 365 nm light source was calculated to be 5.55×10^{-8} einstein·cm^{2}·s^{-1}, $t_{90\%}$ was measured to be 45 seconds, and ε^{365} was measured to be 1.8×10^{4} l·mol^{-1}·cm^{-1}. The quantum yield of Φ_{u} was therefore determined to be 2.2 % of **17**, which is in range for similar coumarin uncagers[96].

4.6.2 Coumarin-Camptothecin Polymer

To verify the light sensitivity of the polymer HPLC and LCMS were used, with the cleavage products as shown in **Scheme 10**. NMR was limited by lack of clear visualisation of the polymer structure surrounding the **CPT**-coumarin conjugate, and GPC could not be used due to lack of sensitivity in detecting small mass differences (>2 % of the polymer chain by mass was **17**).

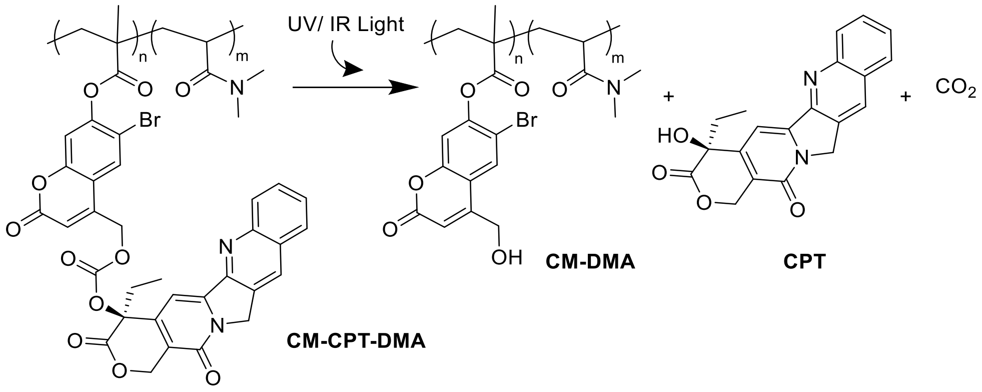

Scheme 10: Photocleavage of the water soluble photosensitive **CPT** containing polymer **CM-CPT-DMA**.

The HPLC (495 nm) showed a broad peak at 5.33 minutes indicating the **CPT** conjugated to the backbone (**Figure 30a**). But as the polymer was irradiated under 365 nm light, the **CPT** detached from the backbone **CM-DMA** and a narrow peak began appearing at 4.75 minutes that proceeded to increase in intensity with irradiation time (**Figure 30b-d**). To confirm this peak corresponded to **CPT**, the same samples were analysed by LCMS. As shown in **Figure 31**, the mass of **CPT** could not be seen at t = 0 of **CM-CPT-DMA** prior to irradiation (**Figure 31a**), but after just 15 seconds of irradiation the mass (349.9 g/mol) could be observed (**Figure 31b**), corresponding to **CPT**.

The **CM-CPT-DMA** polymer was irradiated under 365 nm light while stirring and samples were taken after cleavage times between 0 mins - 15 mins. To quantify the cleavage rate, the peak height difference of the two peaks at 5.33 and 4.75 minutes were measured, corresponding to camptothecin remaining on the backbone and cleaved **CPT**, respectively. The cleavage of the polymer resulted in the broad polymer peak shown in the HPLC trace decreasing, while the narrow free **CPT** emerged and continue to increase with irradiation. Calculation of the percentage of cleavage, based on a concentration curve of **CPT** (**Figure 30f**), showed the cleavage reached 82 % after 3 minutes of irradiation (**Figure 30e**). For this reason, for the biological experiments, an irradiation time of 2 minutes was selected to optimise cleavage while minimising cell damage under 365 nm irradiation.

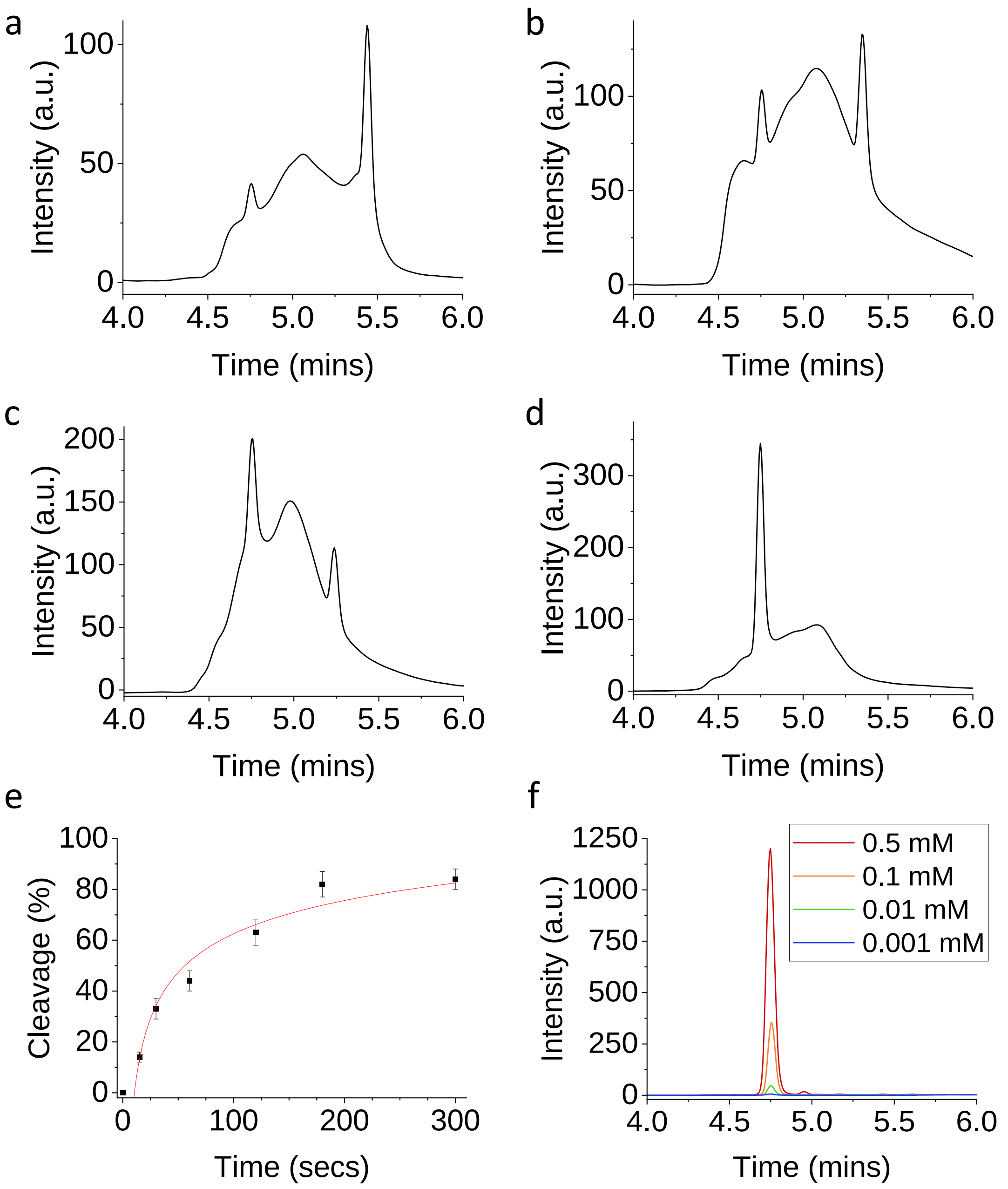

Figure 30: HPLC analysis of the cleavage of **CPT** under 365 nm from **CM-CPT-DMA** (2 mg/ml) in acetonitrile:H_2O 50:50. a) HPLC t = 0. b) HPLC t = 15 seconds. c) HPLC t = 30 seconds. d) HPLC t = 180 seconds e) cleavage percentage of the **CPT** from the backbone of the polymer. Values are mean ± SD, n = 3. f) HPLC calibration of free **CPT**. Eluting with acetonitrile and H_2O (both containing 0.1 % FA) with 20 µl injection volumes.

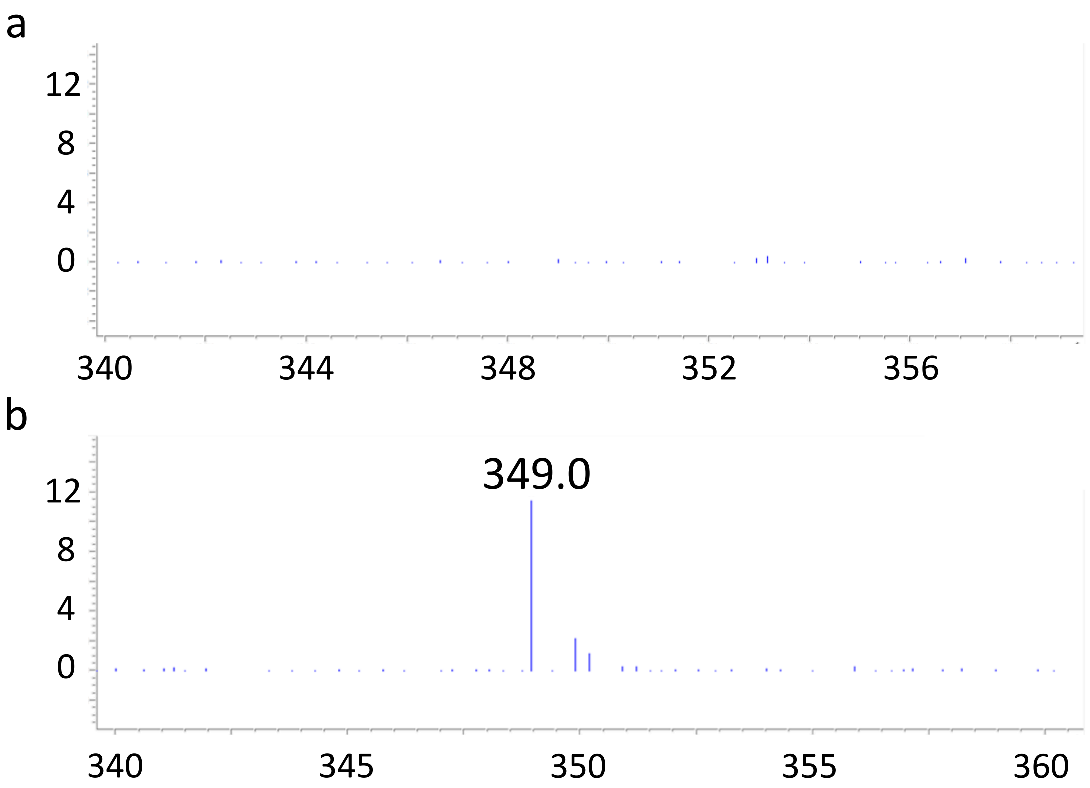

Figure 31: LCMS mass spectra of the **CM-CPT-DMA** polymer before and after irradiation. LCMS eluted with a gradient over 10 minutes in acetonitrile: water (both containing 0.1 % FA). Mass spectra were acquired from the region on the spectra corresponding to the **CM-CPT-DMA** polymer (4.75 minutes). a) t = 0 showing no free **CPT** was present in the solution prior to irradiation. b) Mass spectra showing the presence of **CPT** after 15 minutes of irradiation under 365 nm light.

4.7 *In vitro* Studies

To validate the biological applications of the polymer, a study was performed by incubating HeLa cells with the polymer and irradiation at 365 nm. HeLa cells were incubated with the polymer **CM-CPT-DMA** in complete media for 24 hours at concentrations of 6.75 µg/ml, 12.5 µg/ml, 25 µg/ml, 50 µg/ml, 100 µg/ml, and 250 µg/ml (corresponding to concentrations of **CPT** of 0.375 µM, 0.75 µM, 1.5 µM, 3 µM, 6 μM, and 15 μM, respectively). Cells were then either placed in the dark or irradiated (365 nm) for 2 minutes. 4 hours later an MTT assay was performed to assess cell toxicity (**Figure 32**). Cells were also imaged under bright field to assess cell morphology following exposure to the polymer and UV light (**Figure 33**).

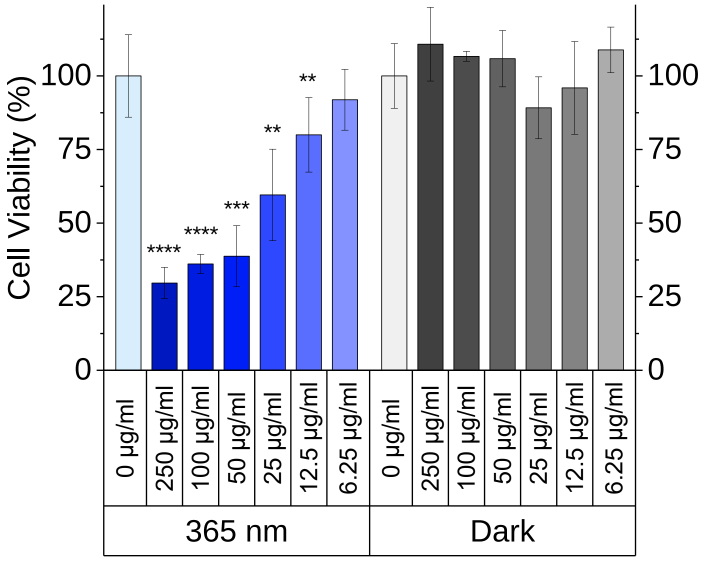

Figure 32: Cell viability of HeLa cells following exposure to varying concentrations of the **CPT** containing polymer, **CM-CPT-DMA** (either kept in the dark or following a 2-minute 365 nm irradiation). Values are mean ± SD, n = 3, ** = $p \leq 0.01$, *** = $p \leq 0.001$, **** = $p \leq 0.0001$.

CM-CPT-DMA showed no toxicity in the dark, indicating biocompatibility. However, 4 hours after the cells were exposed to the active drug **CPT** (generation via irradiation of the polymer) high levels of toxicity were seen, validating it as a selective drug delivery system. Both the 100 μg/ml and 250 μg/ml concentrations showed similar levels of toxicity after 4 hours. This is likely due to this being the maximum level of cell death possible over this time frame irrespective of the amount of drug released, attributed to a saturation of the drug in the cell death pathway.

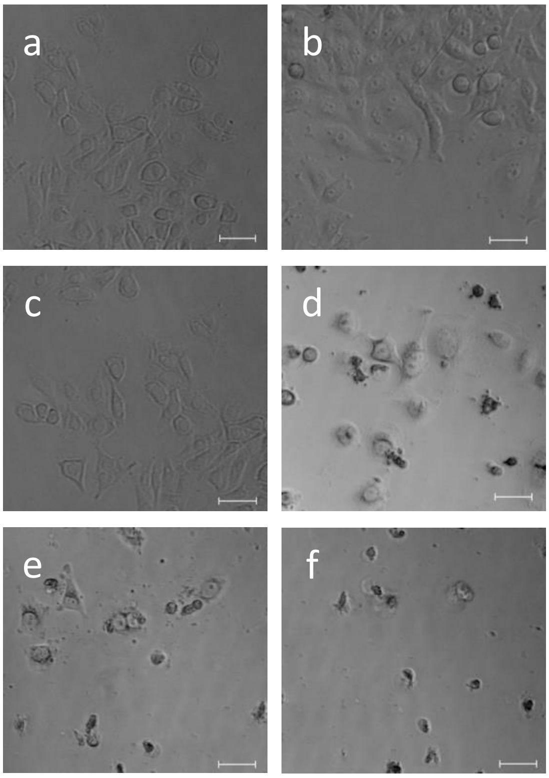

Figure 33: HeLa cell morphology under bright field microscopy when incubated with **CM-CPT-DMA**. Scale bar = 50 µm. a) control cells, non-irradiated. b) control cells, 2 mins 365 nm irradiation. c) 250 µg/ml **CM-CPT-DMA**, non-irradiated. d) 25 µg/ml **CM-CPT-DMA**, 2 mins 365 nm irradiation. e) 100 µg/ml **CM-CPT-DMA**, 2 mins 365 nm irradiation. f) 250 µg/ml **CM-CPT-DMA**, 2 mins 365 nm irradiation.

The cell morphology was also in accordance with the MTT assay results. Control samples of healthy Hela cells, irradiated HeLa cells, and cells containing the highest concentration of the polymer and kept in the dark, all showed a similar morphology indicating healthy cells (**Figure 33a-c**). The cells were elongated indicating adhesion to the well-plate and can be seen in various stages of mitosis, indicating live cells. Samples containing between 25 - 250 µg/ml of **CM-CPT-DMA** polymer that have undergone irradiation showed differing amounts of cell death (**Figure 33d-f**), as indicated by dark round cells, and cells with an uneven border indicating cells in differing states of apoptosis.

4.8 Conclusion

Coumarin monomer **15** previously reported as being light cleavable under 365 nm was synthesised and incorporated into polymers and nanoparticles. Following experimentation under 365 nm irradiation, the monomer **15** was shown to be stable and therefore did not cleave as reported. A different approach was taken to use the monomer to fabricate a fully water soluble light sensitive camptothecin drug delivery polymer **CM-CPT-DMA**, by conjugating the camptothecin to the light sensitive 4 position on the coumarin **15**. The cleavage of the camptothecin from polymer **CM-CPT-DMA** was validated and the cleavage rate was successfully measured, with 82 % cleavage being achieved within 3 minutes of exposure to 365 nm light. The polymer's biological applications were then validated in HeLa cells, showing highly effective cell death after only 4 hours of exposure to camptothecin. The polymer without irradiation was shown to be biocompatible, with no cell death being observed even when incubating with a high concentration of the polymer (250 μg/ml).

5 Light Responsive Doxorubicin Delivery Nanoparticles

Within medicine, nanoparticle drug delivery holds many unique benefits, with the major one being in improving bioavailability. This can be accomplished by improving drug solubility that would allow higher concentrations of the drug to be used. Higher concentrations can also be facilitated as nanoparticles protect the drug and naturally accumulate more in tumour cells over healthy cells due to the EPR effect[91]. However, drug delivery via nanoparticle encapsulation still lacks precision as drug release is often dependent on diffusion of the drug from the core, delivering the drug around the body as the nanoparticles circulate *in vivo*. For this reason, light activatable drug loaded nanoparticles were developed as a potential solution.

Following the work in chapter 4, a new approach was taken to design light sensitive nanoparticles while considering the light sensitive position of coumarin and the optimisation of cleavage efficiency (**Figure 34**). PEG and PLA were selected as the hydrophilic and hydrophobic blocks, respectively, due to the reports of biocompatibility, low cost, and well-established roles within nanoparticle fabrication[105-107]. PEG facilitates immune response resistance, and PLA enables stability and drug loading. Coumarin was selected as the light sensitive moiety due to its simple synthesis and its two photon absorption properties. Photosensitive coumarin was strategically placed between the PEG and PLA blocks to enable high yields of polymer from minimum amounts of synthesised coumarin, but also to optimise resulting nanoparticle cleavage efficiency. The coumarin was attached to the PEG covalently in a non-light-cleavable position to minimise toxicity as the PEG will increase the hydrophilicity of the coumarin. The PLA was attached to the coumarin via the light-sensitive position to enable both blocks to be separated from each other when exposed to light, thus decreasing the hydrophobic force and breaking the nanoparticle open. By only having one coumarin moiety per polymer chain, it is likely that only minimal cleavage would be required from the PLA to disrupt the whole nanoparticle structure to facilitate drug release. Doxorubicin was selected as the cargo as a frequently reported chemotherapy agent often loaded into PEG-PLA nanoparticles, providing a good framework for comparison.

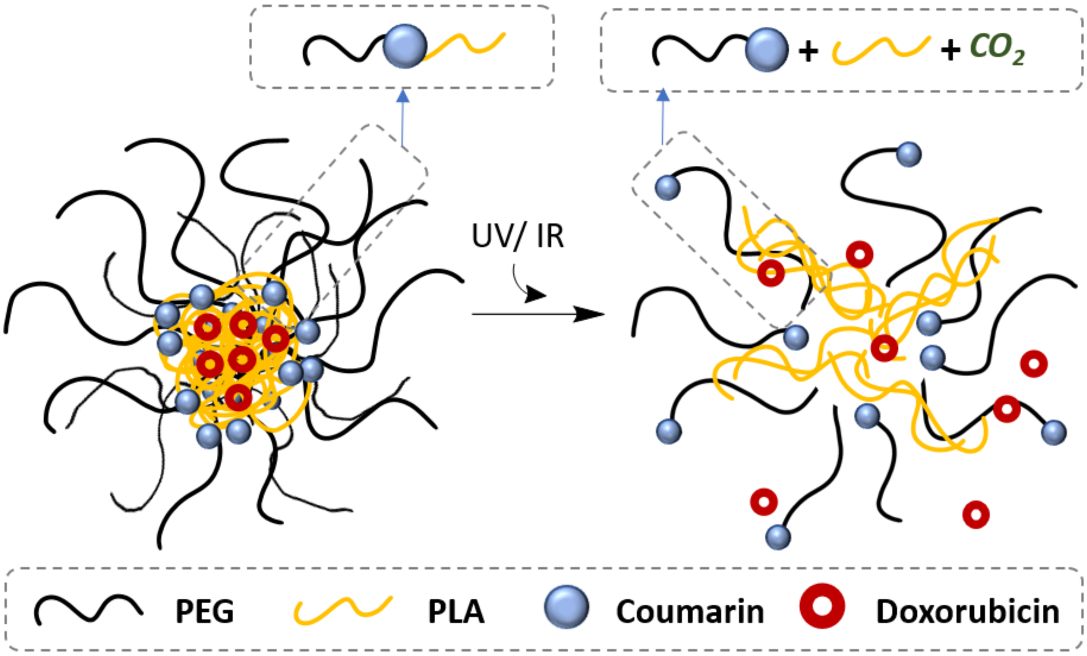

Figure 34: PEG-PLA Doxorubicin loaded nanoparticles. A light sensitive coumarin moiety is covalently bonded between the PEG and the PLA polymer chain. By irradiating the nanoparticles with either UV (one photon) or with IR (two-photon), the PLA chain cleaves from the PEG-coumarin resulting in the nanoparticle opening, thus releasing the doxorubicin cargo.

5.1 Photosensitive Difunctionalised Coumarin

To design the coumarin moiety, an amino coumarin was selected due to its peak absorbance around 380 nm, making it more compatible with the 365 nm light source and a more viable candidate for 2-photon cleavage[108]. The coumarin was designed to have two compatible functional groups to which a PEG and a PLA could be orthogonally attached to avoid mixtures of polymers containing two PEG or two PLA polymers. These functional groups were chosen to be an azide, to facilitate click chemistry for the non-light sensitive bond, and a simple alcohol to facilitate a carbamate or carbonate bond that would be compatible with light cleavage. The designed molecule and synthetic pathway are shown in **Scheme 11**.

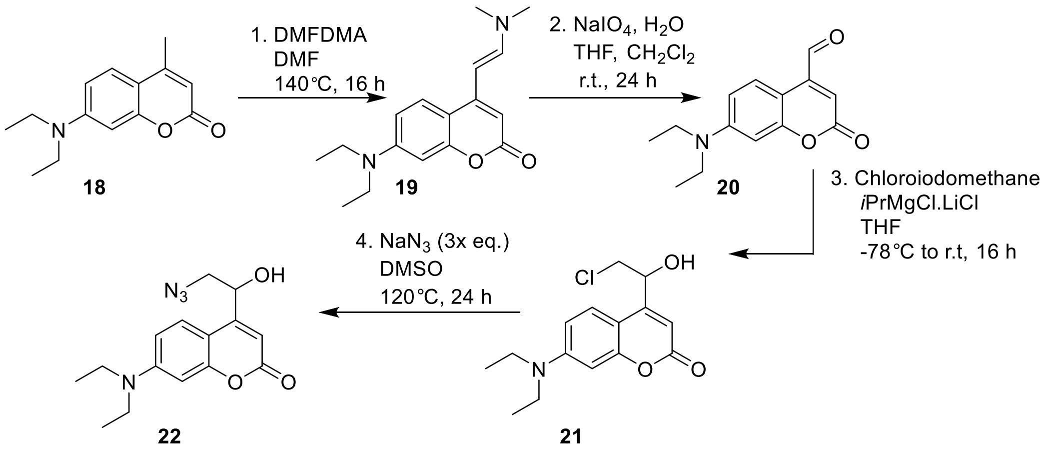

Scheme 11: Four step synthesis to yield di-functional conjugatable coumarin **22**.

The first two steps of the synthesis are well reported and yielded an amino-coumarin with an aldehyde functional group **20**. To facilitate the azide group incorporation, a chlorinated 'arm' was introduced on the benzylic position by Grignard reaction onto the aldehyde, yielding compound **21**. This chlorine on the newly conjugated 'arm' was then displaced by an azide using high temperature and sodium azide, however this occurred with low yields. Although each of step 2-4 required column chromatography, the small quantities of product synthesised proved to be ample due to the PEG and PLA polymer's high molecular weights.

Following synthesis, the final product **22** was fully characterised using ^{1}H NMR, ^{13}C NMR, HPLC, and HRMS. To ensure that the conjugation didn't alter the optical properties of the coumarin from the reported values (that could alter the required wavelengths for cleavage) absorbance and fluorescence spectroscopy were performed (**Figure 35**)[109]. The absorbance and fluorescence peak wavelengths were validated to be 382 nm and 446 nm, respectively.

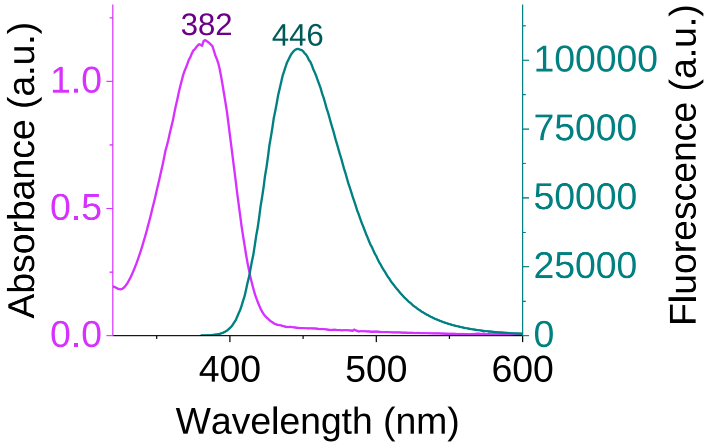

Figure 35: Absorbance and fluorescence spectra of **22** in DCM.

When considering the molecular weights of the desired PEG and PLA polymers to optimise nanoparticle synthesis, literature well documents the arising nanoparticle characteristics[110]. For nanoparticles in which the cargo is to be delivered quickly, shorter PLA chains combined with longer PEG chains should be selected as the minimised hydrophobic force means nanoparticles are less robust and the cargo therefore more quickly diffuses out of the structure. Conversely, more stable nanoparticles hold cargo over longer periods of time and longer PLA chains allow this. For this reason, a PEG polymer with an alkyne termination (5000 Mw, **PEG5-Alkyne**), was purchased along with two PLA polymers (5000 Mw and 20,000 Mw, **PLA5-OH** and **PLA20-OH**, respectively). Due to the intended light-sensitive nature of the nanoparticles, theoretically the **PEG5-Alkyne** paired with the **PLA20-OH** as a diblock would be the most fitting as diffusion from the core of the nanoparticle would to be minimised. A **PEG5-Alkyne** and **PLA5-OH** polymer surrounding the coumarin was also made to compare these theoretical beliefs and also to investigate differences in morphology, drug loading, and drug release.

5.2 Coumarin-Polymer Conjugation

5.2.1 PEG-Control Linker Click Chemistry

A control linker in the form of commercially available azido-PEG$_3$-Alcohol (**CL**) with the same functional groups as the coumarin was purchased to enable low-cost testing to be performed on a system that wouldn’t be vulnerable to light cleavage. The linker is referred to here as the ‘control linker’ and abbreviated as **CL**.

After attempting the click-chemistry synthesis with **CL** and **PEG5-Alkyne** via the traditional method of using CuI under a nitrogen atmosphere, a facile approach for click-chemistry with temperature stable polymers was found [111]. In this approach, no degassing of the system is required, the copper can be easily removed, and the reaction is completed in minutes (**Scheme 12**).

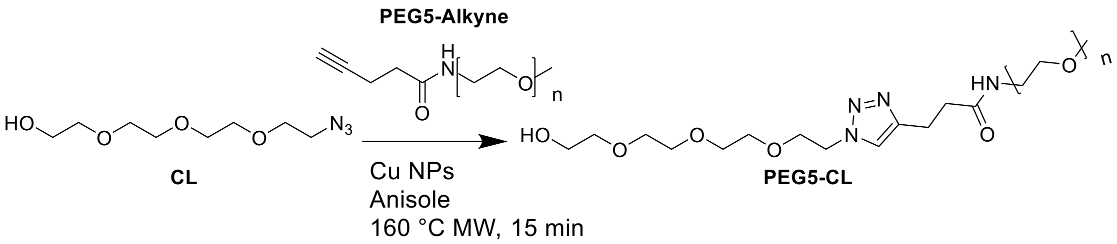

Scheme 12: Click reaction between the control linker **CL** and **PEG5-Alkyne**.

In this reaction, anisole was added to copper nanoparticles (60-80 nm) along with the control linker and **PEG5-Alkyne**. The copper nanoparticles are insoluble in anisole and are therefore able to be centrifuged out of solution following the reaction allowing for the easy removal of copper, a difficulty often faced with click chemistry. The reaction was completed at a high temperature (160 °C) in just 15 minutes under microwave irradiation. The ‘Very High Absorbance’ option was selected on the microwave to minimise localised heating of the copper nanoparticles in the microwave that could prove to be a hazard in a closed system. The solution was centrifuged at 13,000 rpm for 10 minutes and the supernatant removed to separate the nanoparticles. The polymer was cleaned via precipitation into diethyl ether, and the anisole was washed away by redissolving the polymer in methanol and precipitating in diethyl ether three times.

The product of the click reaction between the control linker and **PEG5-Alkyne**, **PEG5-CL**, was confirmed from ^{1}H NMR by confirming a shift in the peaks of the protons on the two carbon atoms adjacent to the alkyne on the **PEG5-Alkyne** polymer (**Figure 36**).

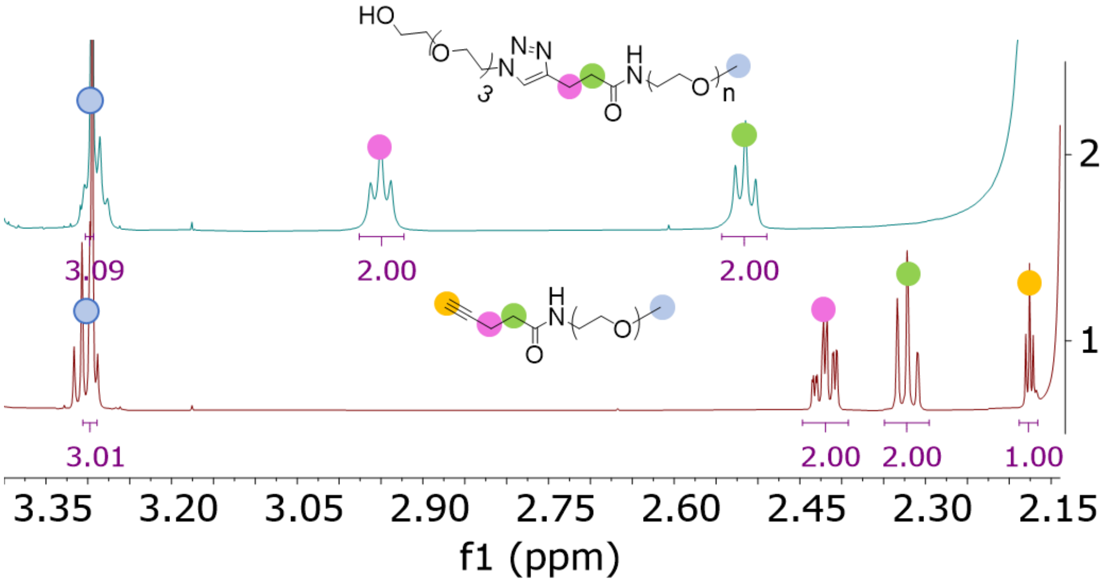

Figure 36: ^{1}H NMR in CD_3CN of the reaction of **PEG5-Alkyne** with the control linker **CL**. (Top) **PEG5-CL**. A shift in the peaks adjacent to the triazole occurs. (Bottom) **PEG5-Alkyne**. Peaks corresponding to the proton on the alkyne unit are shown (2.18 ppm (orange), 2.42 ppm (pink), and 2.32 ppm (green)). Following the reaction, the peak corresponding to the alkyne hydrogen (orange) disappears and the pink and green peaks move to a higher ppm due to the increase in shielding following the formation of the triazole. Peaks in light blue corresponding to the protons on the terminal methoxy group at 3.29 ppm remain unchanged following the reaction.

5.2.2 PEG-Control Linker Activation

Following the confirmation of the click reaction between the **PEG5-Alkyne** and the control linker to form polymer **PEG5-CL**, the next step was to conjugate a hydrophobic PLA block. **PEG5-CL** was reacted with *p*-nitrophenyl chloroformate **23** to activate the alcohol to form **PEG5-CL-Act** (**Scheme 13**).

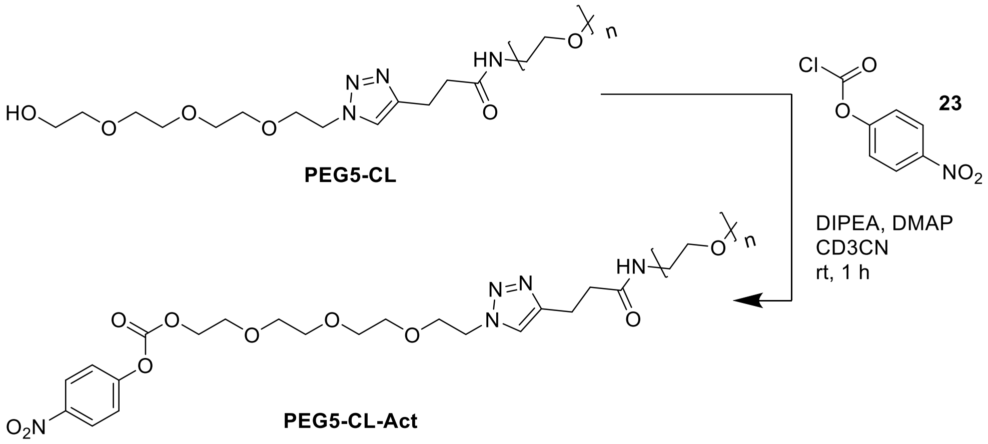

Scheme 13: **PEG5-CL-Act** product formed from the activation of **PEG5-CL** using *p*-nitrophenyl chloroformate **23**.

The reaction was performed in an NMR tube in deuterated degassed acetonitrile under an argon atmosphere. Large excesses of reactants **23**, DIPEA, and DMAP were used to promote the reaction, with any by-products/ unreacted reactants removed by precipitation of the polymer in diethyl ether. After 15 minutes a ^{1}H NMR spectrum was acquired to confirm that the reaction had completed (the protons on the nitrophenyl group were compared to the integrations of the protons on the polymer chain (**Figure 37**). Following synthesis, the **PEG5-CL-Act** polymer was purified by precipitation (diethyl ether ×3). No further purification was performed as the nitrophenyl carbonate is susceptible to hydrolysis. ^{1}H NMR was performed following purification to quantify the conversion to calculate the molar ratios for the next step and assess purity.

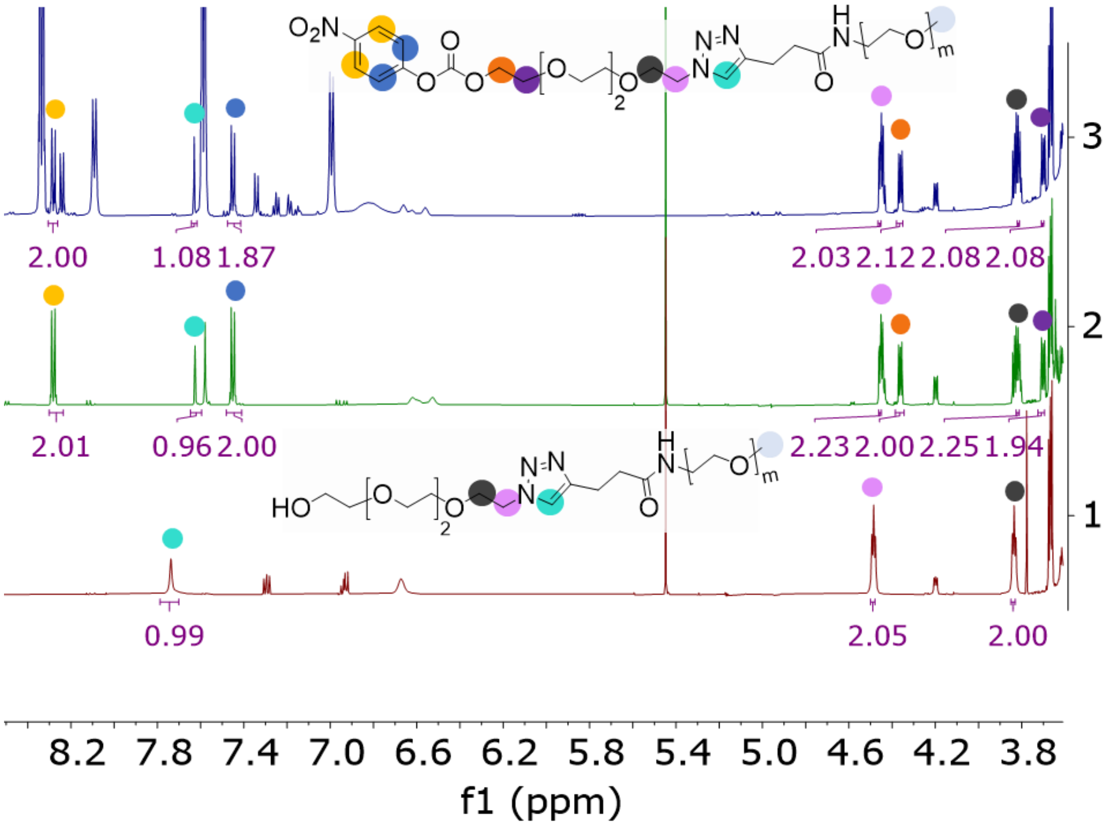

Figure 37: NMR Spectra in CD_3CN of **PEG5-CL-Act** following the generation of the carbonate group onto **PEG5-CL**. (Top) **PEG5-CL-Act** crude in the reaction mixture. Confirmation of reaction completion of **PEG5-CL-Act** was validated by integrating the protons on the nitrophenyl group (yellow and dark blue), with respect to the proton on the triazole (teal) and the four protons on the two methylenes adjacent to the triazole (pink and black). (Middle) **PEG5-CL-Act** following purification, validating the nitrophenyl groups presence on the polymer and the removal of impurities. (Bottom) Starting material **PEG5-CL**.

The next step was to react **PEG5-CL-Act** with **PLA20-OH** and was performed as shown in **Scheme 14**. However, the reaction failed as neither **PEG5-CL-Act** nor the **PLA20-OH** reacted and peaks in the ^{1}H NMR spectrum remained the same, even after performing the reaction at higher temperatures under microwave conditions for 4 hours. This was determined to be likely due to the poor nucleophilicity of the alcohol on the **PLA20-OH**. As such, a strategy was adopted to modify the **PLA20-OH** and

PLA5-OH into amines (**PLA5-NH2** and **PLA20-NH2**), respectively, to increase their reactivity.

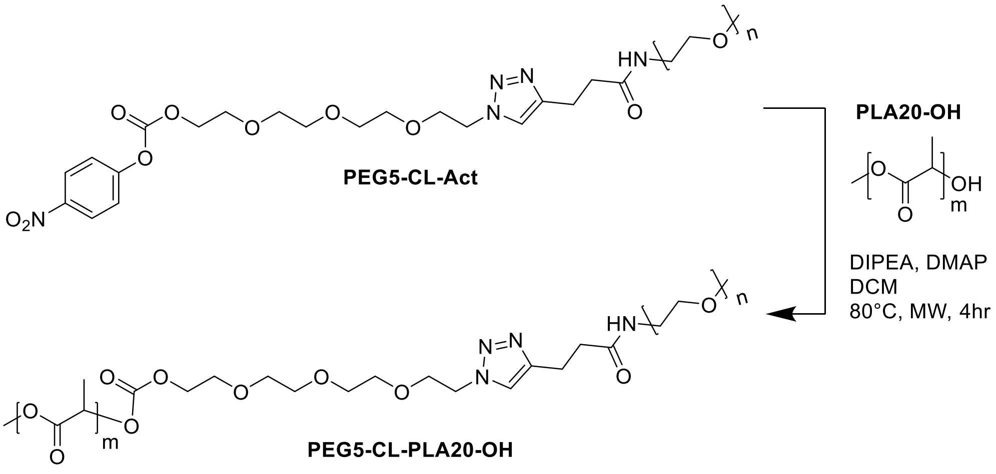

Scheme 14: Attempted reaction between **PEG5-CL-Act** and **PLA20-OH**.

5.2.3 PLA End Group Modification

PLA20-OH with a molecular weight of 20 kDa was initially modified using a mono-terminated Boc protected amine spacer **24** (**Scheme 15**), yielding **PLA20-NH-Boc**. Boc protection was chosen over Fmoc protection as although Fmoc protection is easier to quantify via ^{1}H NMR for the polymers, the base required for deprotection could potentially result in the hydrolysis of the PLA backbone. An ester bond was selected between the **PLA20-OH** and the spacer **24** as although it is not the most biologically resistant, it is a relatively efficient bond to create with the alcohol on the polymer and is also the same as that along the backbone of the PLA and so should tolerate the same environment. The reaction was performed both on a milligram and on a gram scale, proving its scalability. Microwave heating was used to speed up the completion of the reaction as reactions on molecules with high molecular weights

(20 kDa in this case) can suffer from slow reaction speeds due to viscosity and the fact that the functional group of the molecule will be present in low concentrations compared to the size of the molecule[112]. Microwave heating was also required as it allows the boiling point of solvents to be surpassed to further speed up reactions. Thus, DCM was used as the solvent for the esterification despite its low boiling point of 39.6 °C, due to the limited solubility of PLA in other solvents, with microwave heating allowing for a reaction temperature of 85 °C to be achieved. Also, the urea by-product from the reaction is insoluble in DCM and will therefore precipitate out of solution during the reaction, allowing for it to be removed via filtration. By using microwave heating, the reaction was completed and achieved full conversion after 4 hours at 85 °C.

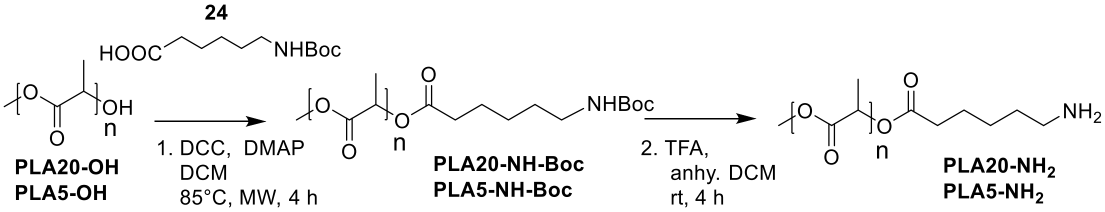

Scheme 15: Modification of the end group of **PLA20-OH** and **PLA5-OH** to **PLA20-NH$_2$** and **PLA5-NH$_2$**, respectively, using carboxylic acid terminated Boc protected amine spacer **24**.

To purify the **PLA20-NH-Boc** the urea was removed by filtration and the polymer was precipitated using diethyl ether and collected by centrifugation. The polymer was further purified by repeating the precipitation in methanol and diethyl ether. The completion of the reaction was confirmed using ^{1}H NMR in deuterated DCM by integrating the peaks corresponding the CH$_3$ at the end of the PLA chain along with the peaks of the protons on the spacer (**Figure 38**). The nine protons corresponding to the Boc group were clearly identified (singlet at 1.41 ppm). The Boc group was removed by stirring the **PLA20-NH-Boc** in a mixture of anhydrous DCM and TFA in a 50:50 ratio at room temperature for 3 hours. The polymer was purified by the aforementioned precipitation method and dried overnight in a vacuum oven at 40 °C to remove residual solvents, yielding **PLA20-NH$_2$** as a white solid. The Boc group removal was validated by ^{1}H NMR.The same procedure was repeated with **PLA5-OH** to modify the end group to yield **PLA5-NH$_2$**.

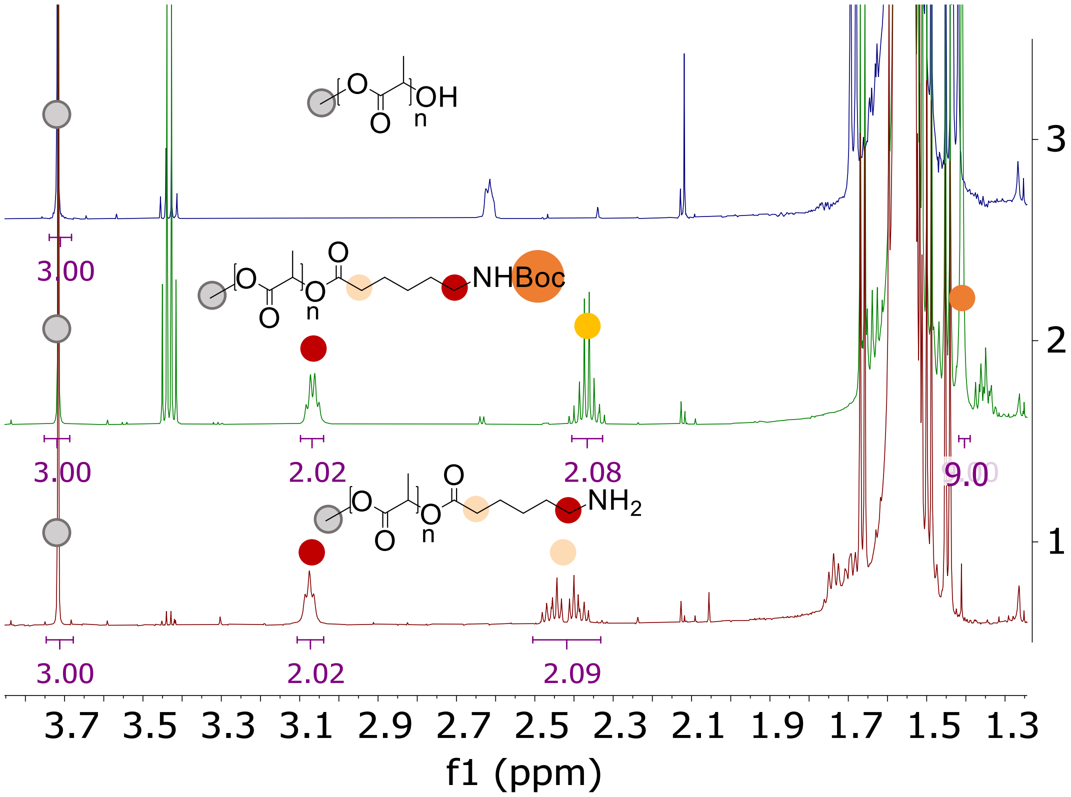

Figure 38: ^{1}H NMR spectra following the end group modification of **PLA20-OH** in DCM-d$_2$. (Top) **PLA20-OH**. The methyl group shown at 3.72 ppm (light blue) and polylactic acid chain at 1.55 ppm. (Middle) **PLA20-NH-Boc**. The methyl group (light grey) at 3.72 ppm integrated as 3 with respect to the NH-Boc spacer protons integrating to (2 x 2H) at 3.07 ppm (maroon) and 2.37 ppm (beige). The Boc group protons integrating to 9 at 1.41 ppm (orange). (Bottom) **PLA20-NH$_2$**. The spacer protons at 3.07 ppm (maroon) and 2.42 ppm (beige) are highlighted. The Boc peak is no longer present following TFA cleavage.

5.2.4 PEG-Control Linker-PLA

To complete the diblock polymer, the activated **PEG5-CL-Act** was reacted with **PLA20-NH2** resulting in the elimination of the nitrophenol yielding **PEG5-CL-PLA20** (**Scheme 16**).

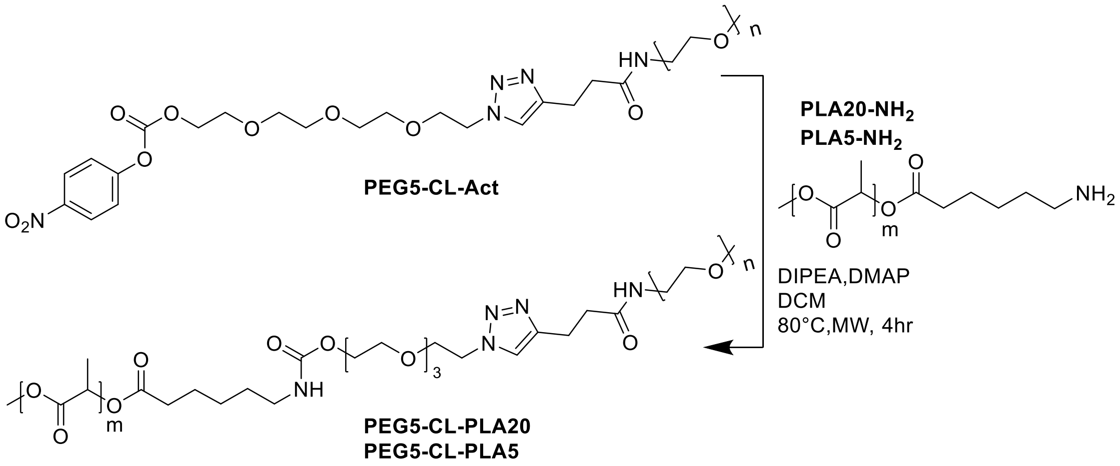

Scheme 16: **PEG5-CL-PLA20** and **PEG5-CL-PLA5** synthesis from **PLA20-NH2** and **PLA20-NH2**, respectively.

The reaction was performed in anhydrous DCM due to solvent compatibility issues between the PEG and PLA. Prior to the reaction, the **PLA20-NH2** was stirred in a solution of DCM containing DIPEA for 10 minutes to neutralise the TFA salt which would prevent the reaction occurring. **PEG5-CL-Act** was added in excess as this could be readily removed during purification. The reaction was performed at 80 °C with microwave heating for 4 hours. The reaction was purified using precipitation in diethyl ether, the polymer was then resuspended in DCM and washed via precipitation in methanol and diethyl ether. By precipitating the polymer in methanol excess **PEG5-CL** (likely no longer activated due to the reaction conditions) was removed, leaving only the pure diblock polymer **PEG5-CL-PLA20**. The diblock polymer had brittle crystalline structure, whereas both the **PEG5-CL-Act** and **PLA20-NH$_2$** precursors had a more chalk-like appearance. Reaction completion was validated using ^{1}H NMR in deuterated DCM (**Figure 39**).

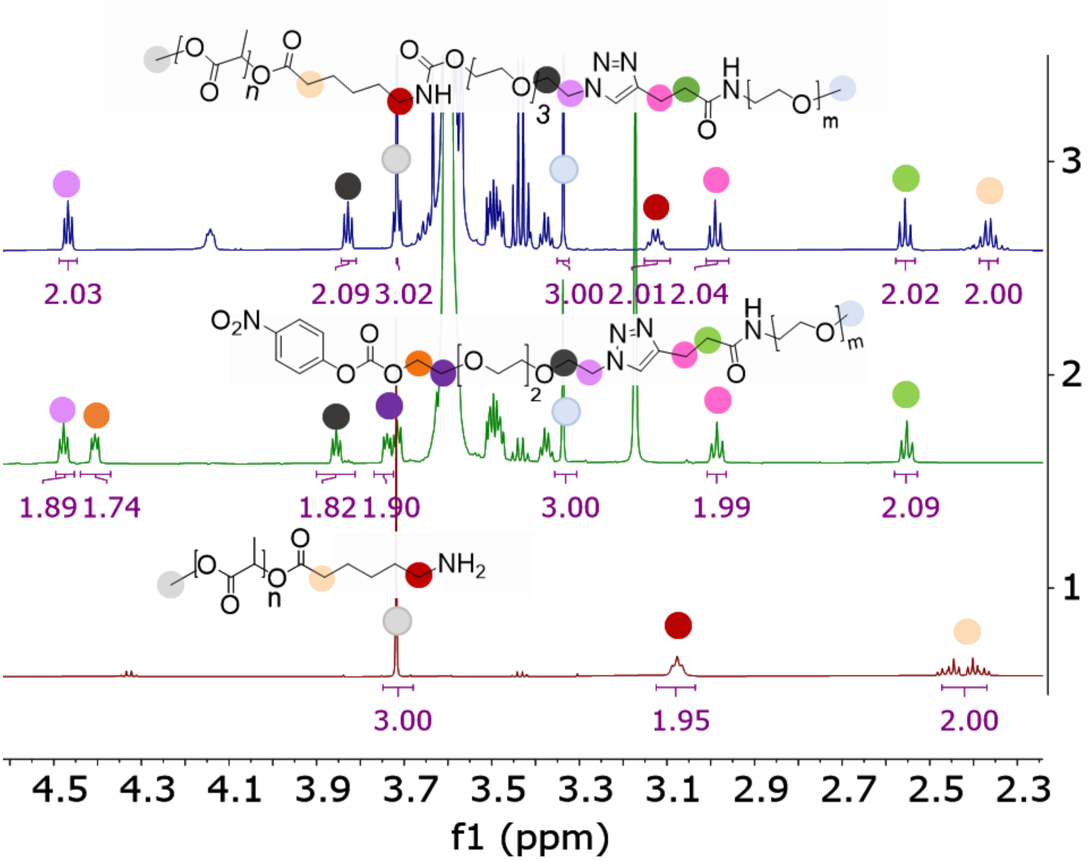

Figure 39: ^{1}H NMR spectra for the validation of the synthesis of the diblock polymer **PEG5-CL-PLA20** in DCM-d$_2$. (Top) **PEG5-CL-PLA20** diblock polymer. (Middle) **PEG5-CL-Act**. (Bottom) **PLA20-NH$_2$**. The diblock was confirmed from peak analysis. The integration of the peaks corresponding to the terminal CH_3 groups of both the PLA and PEG chains (light grey and light blue, respectively) were both equivalent. As the terminal peaks were equivalent, both the PEG and PLA moieties were present in equal amounts, indicating a diblock. Peaks corresponding to other parts of both and PLA and PEG chains are also present with the correct integrations (light purple, black, pink, green, maroon, and beige). The peaks at 4.41 ppm (orange) and 3.77 ppm (purple) from the **PEG5-CL-Act** also shifted following the reaction.

Following the successful reaction with the **PLA20-NH2**, the reaction was also repeated with the **PLA5-NH2** and **PEG5-CL-PLA5**.

5.2.5 PEG-Coumarin Click Chemistry

Following successful synthesis of the diblock polymers **PEG5-CL-PLA5** and **PEG5-CL-PLA20** using the control linker., the same synthesis procedures were used on the coumarin **25**, starting with the click reaction with the 5 kDa molecular weight **PEG5-Alkyne** (**Scheme 17**) to yield '**PEG5-CM**'.

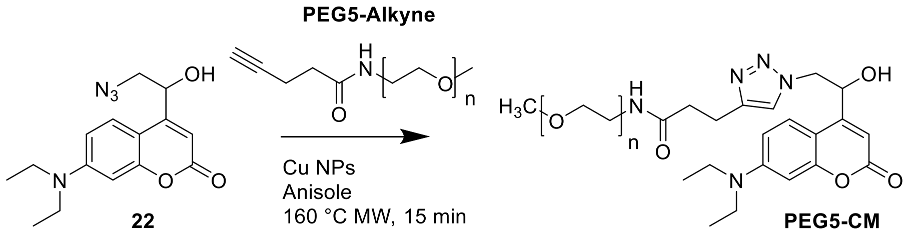

Scheme 17: Click reaction of the azide containing coumarin **22** with **PEG5-Alkyne** to give **PEG5-CM**.

An excess of coumarin-azide **22** with **PEG5-Alkyne** were reacted in anisole with copper nanoparticles microwave heating for 15 minutes. The copper nanoparticles were separated using centrifugation and the polymer was again cleaned using precipitation with diethyl ether. The reaction was validated using ^{1}H NMR (**Figure 40**) as before. The resonance from the protons on the alkyne spacer shift following the reaction and the terminal proton on the alkene disappears as expected.

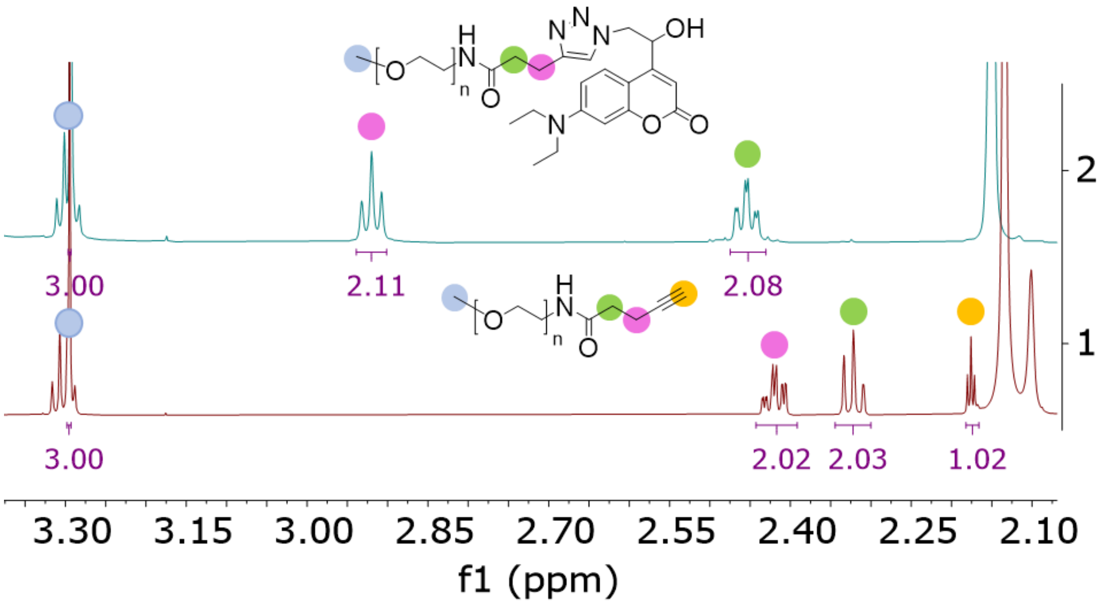

Figure 40: ^{1}H NMR in CD_3CN of (Top) **PEG5-CM**, coumarin-azide **22** clicked to **PEG5-Alkene**. (Bottom) **PEG5-Alkene** starting material.

A colour change was also be observed as the coumarin-azide **22** (dark brown) gave **PEG5-CM** as a light-medium brown solid after purification.

5.2.6 PEG-Coumarin Activation

Following the synthesis of **PEG5-CM**, the alcohol on the coumarin was activated using *p*-nitrophenyl chloroformate **23** (**Scheme 18**) to yield **PEG5-CM-Act**, prior to the reaction with **PLA20-NH$_2$** or **PLA5-NH$_2$**. The reaction was performed in an amber NMR tube to be able to monitor the reaction via ^{1}H NMR, protecting the reaction mixture from light that would result in the nitrophenyl carbonate cleaving from the coumarin on the polymer.

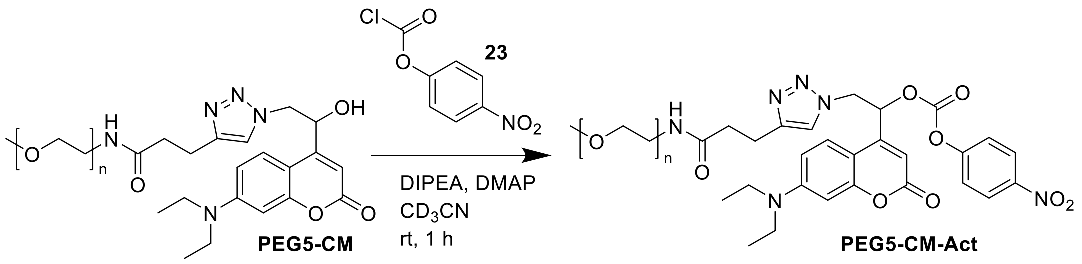

Scheme 18: Synthesis of **PEG5-CM-Act** involving the activation of **PEG5-CM** with nitrophenyl chloroformate **23**.

The reaction was performed under argon in deuterated acetonitrile and inverted for 15 minutes before ^{1}H NMR analysis confirmed the reaction had gone to completion (**Figure 41**). Between 2.5-5 equivalents of reactant (to the **PEG5-CM**) were added to promote the reaction, as the polymer could be easily purified via precipitation and separated from the excess reactants.

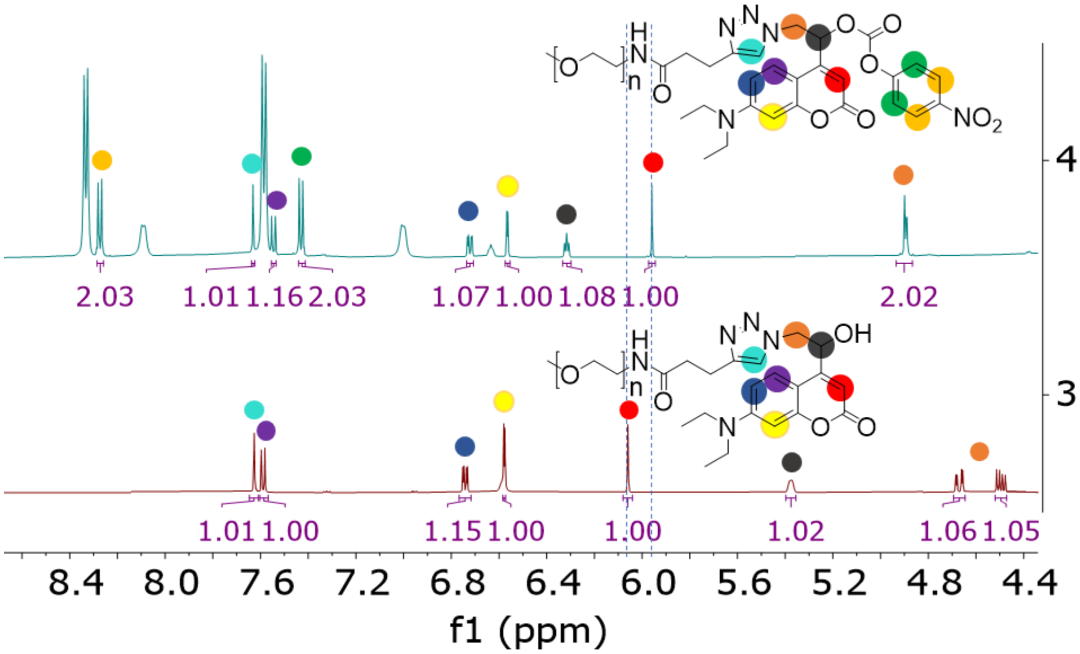

Figure 41: ^{1}H NMR spectra of the synthesis of **PEG5-CM-Act** using *p*-nitrophenyl chloroformate in deuterated acetonitrile. (Top) Reaction mixture indicating 100 % conversion of the starting material into **PEG5-CM-Act** including the peaks from excess *p*-nitrophenyl chloroformate **23** and DMAP. (Bottom) Starting material **PEG5-CM**. The completion of the reaction can be validated by the integration of the nitrophenyl peaks (yellow and green). A clear indication of the conversion percentage is the integral of the red doublet peak indicating the carbon in position 3 (1H) that shifts from 6.06 ppm to 5.96 ppm following the reaction.

The polymer **PEG5-CM-Act** was purified by precipitation using diethyl ether, resuspended in DCM washed two further times. Care was taken from the beginning of this synthesis to minimise light and water exposure to prevent the nitrophenol cleaving from the **PEG5-CM-Act**. This involved ensuring the transfer of solutions was performed as quickly as possible, minimising ambient light (turning lights off where possible) as well as using amberised falcon tubes. To quickly dry the polymer following precipitation a stream of nitrogen gas was passed over the polymer via a needle for 45 minutes until the polymer was visibly dry. The compound was yielded as a light-medium brown solid.

5.2.7 PEG-Coumarin-PLA

The **PEG5-CM-Act** was reacted with **PLA20-NH2** to complete the light sensitive diblock, **PEG5-CM-PLA20**. As the **PEG5-CM-PLA20** polymer and **PLA20-NH2** are insoluble in methanol but the **PEG5-CM** was soluble, an excess of the **PEG5-CM-Act** was used as this could be readily removed and give a pure diblock product. The reaction was performed as shown in **Scheme 19** with microwave heating in anhydrous DCM with DMAP for 4 hours at 85 °C. The microwave tube was wrapped in foil while the reaction solution was being prepared to prevent light exposure.

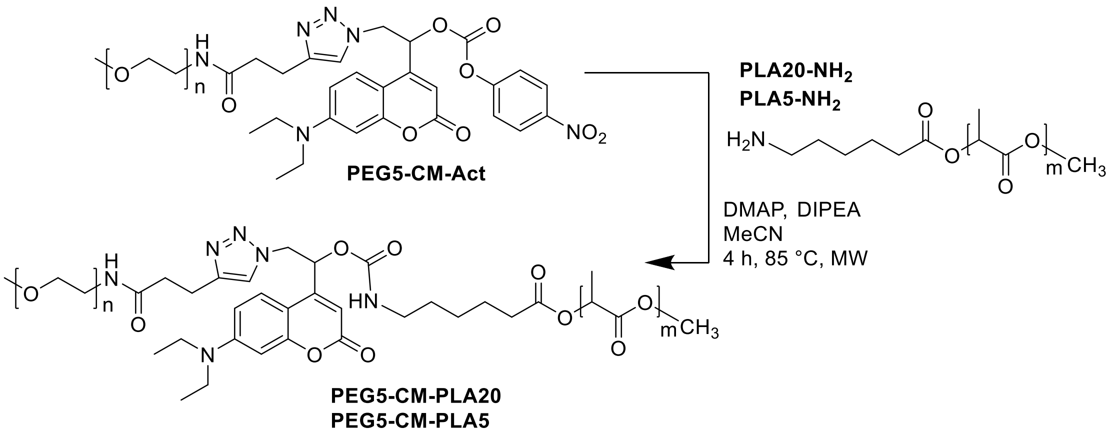

Scheme 19: Synthesis of **PEG5-CM-PLA20** and PEG5-CM-PLA5 from **PLA20-NH2** and **PLA20-NH2**, respectively.

Following the reaction, the solution became yellow indicating the liberation of nitrophenol from the **PEG5-CM-Act**. The purification of the **PEG5-CM-PLA20** polymer was performed in an amberised falcon tube, the polymer was precipitated using diethyl ether, resuspended in DCM, and precipitated using methanol and diethyl ether. The product **PEG5-CM-PLA20** was dried overnight under vacuum at 40 °C. A similar crystalline polymer was yielded to that given using the control linker

(**PEG5-CL-PLA20)**. The polymer conjugation was again validated using ^{1}H NMR in deuterated DCM (**Figure 42**).

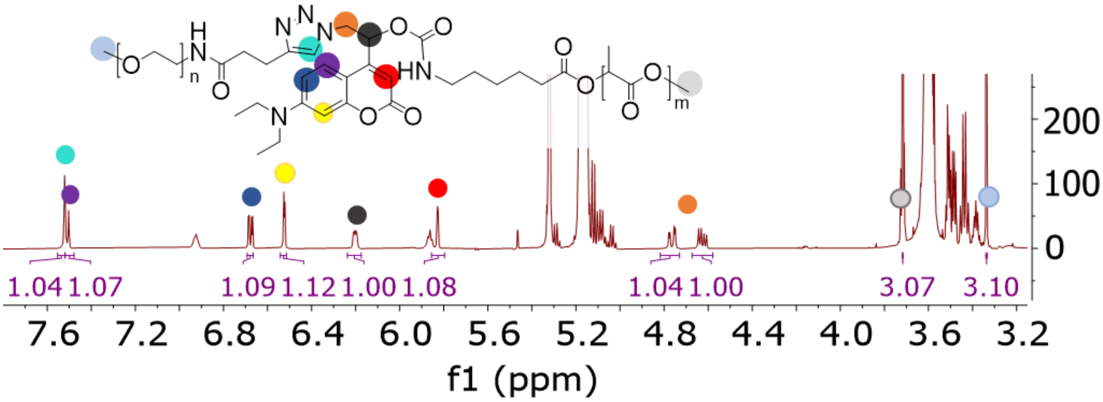

Figure 42: ^{1}H NMR of **PEG5-CM-PLA20** in DCM-d_2. Features indicating the completion of the reaction include the down shifting of the signal from the proton on benzylic carbon (black) compared to the starting material, and the equal integrations of the three protons from the methoxy terminated PEG and PLA chains (light blue and light grey, respectively) (3H).

The NMR confirmed the generation of the **PEG5-CM-PLA20** product, and the synthesis was repeated using the shorter **PLA5-NH$_2$** to yield the product **PEG5-CM-PLA5**.

The absorption of the coumarin following the conjugation with the **PEG5-Alkyne** and **PLA20-NH$_2$** was measured to ensure no change in the optical properties had occurred as this would alter the irradiation wavelength required. No change in the peak position of the absorption spectra was observed (**Figure 43**)..

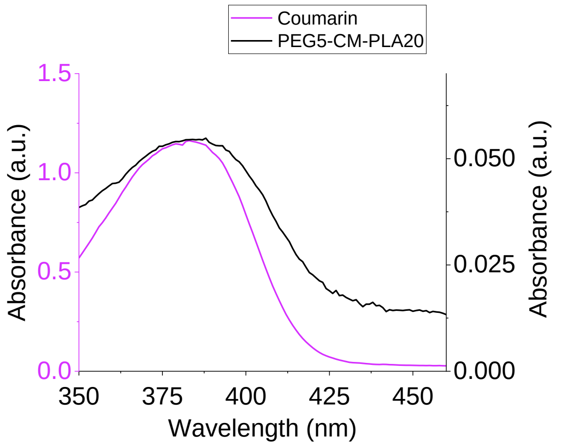

Figure 43: Absorption spectra of the coumarin **22** and coumarin-containing polymer **PEG5-CM-PLA20** in DCM.

5.2.8 GPC Characterisation

To further characterise the synthesised polymers, the polymer samples were evaluated using GPC to assess size, PDI, and validate diblock conjugation (**Table 7**). Samples were dissolved in DMF containing 0.1 % LiBr and ran on the GPC in the same solvent mixture at 60 °C. The molecular weights were calculated by comparison to reference PMMA polymers, and they all were in accordance with their theoretical molecular weights. Extremely low PDI's were also measured, validating the benefits of the synthesis method, and could also lead to equally homogenous nanoparticle fabrication as a result.

Table 7: Showing polymeric content of synthesised polymers and starting materials along with the theoretical molecular weights and molecular weights measured using GPC.

Sample	Contains PEG	Contains PLA	Theoretical Mw [Da][a]	Mw [Da][b] (GPC)	PDI
PEG5-Alkyne	✓		5,000	5,523	1.03
PLA5-OH		✓	5,000	5,617	1.10
PLA5-NH$_2$		✓	5,114	5,805	1.13
PLA20-OH		✓	20,000	21.238	1.12
PLA20-NH$_2$		✓	20,114	21,390	1.07
PEG5-CL	✓		5,219	5,894	1.03
PEG5-CL-PLA5	✓	✓	10,359	10,112	1.11
PEG5-CL-PLA20	✓	✓	25,359	25,320	1.07
PEG5-CM	✓		5,302	5,684	1.03
PEG5-CM-PLA5	✓	✓	10,442	9,936	1.08
PEG5-CM-PLA20	✓	✓	25,442	25,918	1.09

[a] Theoretical molecular weights based on modifications made to commercially bought polymers with pre-determined molecular weights. [b] Determined by GPC using DMF with 0.1% LiBr as eluent and PMMA as reference standards.

The shift in the GPC traces due to the conjugation of the polymers could clearly be seen (**Figure 44**), and low PDIs of the **PLA5-NH$_2$** and **PLA20-NH$_2$** were seen despite the chemical modification of the end group, showing the reaction was successful and didn’t result in any degradation or cross reactions. The peaks between the polymer conjugation synthesis using both **CL** and coumarin **22** were very similar in shape and retention times as expected.

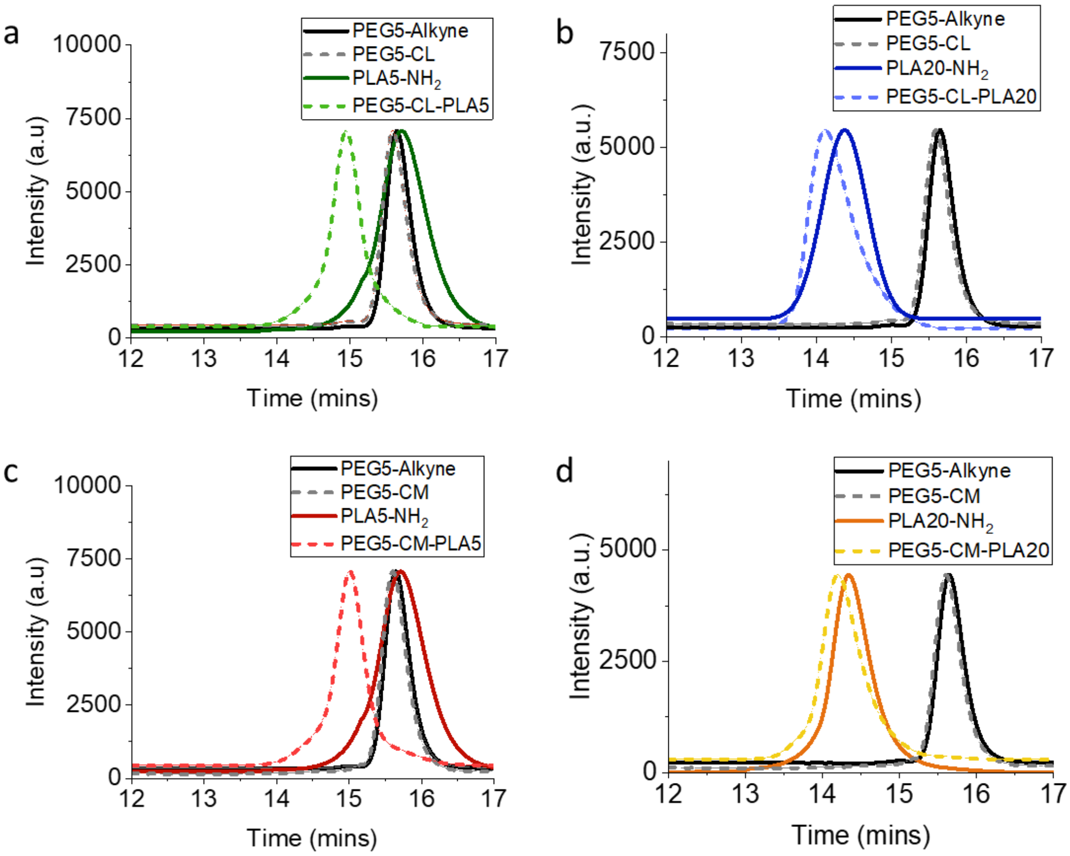

Figure 44: GPC traces (RI channel) of synthesised diblock copolymers a) **PEG5-CL-PLA5**, b) **PEG5-CL-PLA20**, c) **PEG5-CM-PLA5**, and d) **PEG5-CM-PLA20**, along with intermediates **PEG5-CL**, and **PEG5-CM**, and starting materials **PEG5-Alkyne**, **PLA5-NH$_2$**, and **PLA20-NH$_2$**. Samples were ran in DMF with 0.1 % LiBr at 60 °C. Sample data was normalised for clarity.

5.3 Light Sensitive Nanoparticles

PEG-PLA polymers when exposed to an aqueous environment will begin to orientate themselves according to optimal enthalpic and entropic contributions. Hydrophobic PLA chains will come into closer proximity to minimise contact with water, whereas hydrophilic PEG chains will orientate themselves in such a way to optimise contact with water. The orientation of the polymers gives rise to nanoparticles that are able to encapsulate cargo, where the chain lengths and fabrication method can be varied to produce nanoparticles with varying shapes, sizes, and cargo delivery rates. The PEG-Coumarin-PLA diblocks were used to fabricate nanoparticles encapsulating doxorubicin (**Figure 45**).

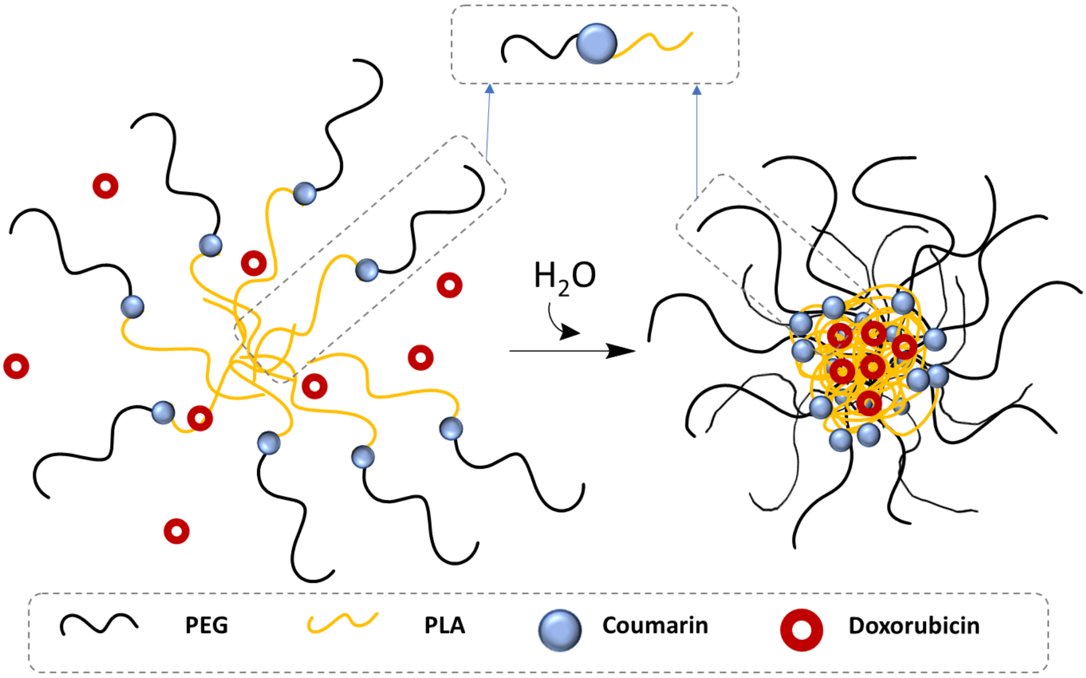

Figure 45 : PEG-Coumarin-PLA nanoparticle formation encapsulating doxorubicin.

5.3.1 Unloaded Nanoparticle Synthesis

Literature reports two main synthesis methods of PEG-PLA containing nanoparticles, the nanoprecipitation method [106, 107, 110, 113], and the water in oil in water emulsion (W/o/W) method [114, 115]. The nanoprecipitation method involves dissolving the polymer in a water soluble solvent such as DMF or acetonitrile, which is then slowly added to a much larger volume of water to drive the formation of nanoparticles. Cargo is added to either the solvent or aqueous phase depending on its solubility and nanoparticles are purified using a method such as dialysis or centrifugation. The W/o/W method involves dissolving the polymer in a water insoluble, volatile solvent such as DCM and mixing it into water using sonication often with an emulsifying agent such as PVA. The nanoparticles are left to form under stirring in an open flask to encourage the DCM to evaporate or the DCM is evaporated under reduced pressure. Purification usually involves centrifugation to remove excess cargo and the majority of the PVA.

From this point only the coumarin containing polymers **PEG5-CM-PLA5** and **PEG5-CM-PLA20** were used in experiments. To investigate the best method for the application of the light sensitive polymers, nanoparticles were made using both the nanoprecipitation and the W/o/W methods from **PEG5-CM-PLA5** and **PEG5-CM-PLA20**.

5.3.1.1 Nanoprecipitation method

5.3.2.1 Synthesis

Polymers **PEG5-CM-PLA5** and **PEG5-CM-PLA20** were dissolved in acetonitrile and added dropwise to deionised water (1:10 ratio) under stirring in amber vials. Flasks remained open under stirring overnight to allow for the evaporation of the acetonitrile. To explore if concentration had an impact on nanoparticle size, final concentrations of 1 mg/ml and 3 mg/ml polymer in water (following acetonitrile evaporation) were used to yield four nanoparticle samples **NP’(5)-1** and **NP’(5)-3**, made from **PEG5-CM-PLA5** at 1 mg/ml and 3 mg/ml, respectively, and **NP’(20)-1** and **NP’(20)-3**, made from **PEG5-CM-PLA20** at 1 mg/ml and 3 mg/ml, respectively. Nanoparticle samples were centrifuged to remove any trace acetonitrile that might have been remaining and also to validate the method for purifying nanoparticles containing cargo. However, upon centrifuging the sample at up to 20,000 rpm at 4 °C for 2 hours, only partial recovery of the nanoparticles was achieved, meaning this method of purification would not be a viable option for purification of the nanoparticles from non-encapsulated cargo.

5.3.1.1.2 DLS Size and Zeta Potential Measurements

Zetasizer measurements were performed on the nanoparticles to assess size as well as hydrodynamic diameter and surface charge (zeta potential) (**Table 8**).

Table 8: Hydrodynamic diameter and zeta potential measurements of nanoparticle samples fabricated using the nanoprecipitation method.

Polymer	Sample Name	Conc. [mg/ml]	Zeta Potential [mV]	Error (SD) [mV]	Diameter [nm]	Error (SD) [nm]	PDI
PEG5-CM-PLA5	**NP’(5)-1**	1	-1.81	0.12	44	18	0.121
PEG5-CM-PLA5	**NP’(5)-3**	3	-2.63	0.03	62	26	0.173
PEG5-CM-PLA20	**NP’(20)-1**	1	-3.69	0.49	61	22	0.183
PEG5-CM-PLA20	**NP’(20)-3**	3	-1.62	0.16	74	31	0.222

Nanoparticles formed from the shorter polymer **PEG5-CM-PLA5** (**NP’(5)-1** and **NP’(5)-3**) were smaller than those fabricated using the longer polymer and also the nanoparticles made at higher concentrations were also larger (**NP’(5)-3** and **NP’(20)-3** compared to **NP’(5)-1** and **NP’(5)-3**) (although the errors could mean that no significant difference was observed). Low PDIs indicate homogeneity that were also be seen in the DLS traces shown in **Figure 46**. Nanoparticles also showed a slightly negative surface charge (zeta potential), which was consistent with the literature on PEG-PLA nanoparticles[110, 115].

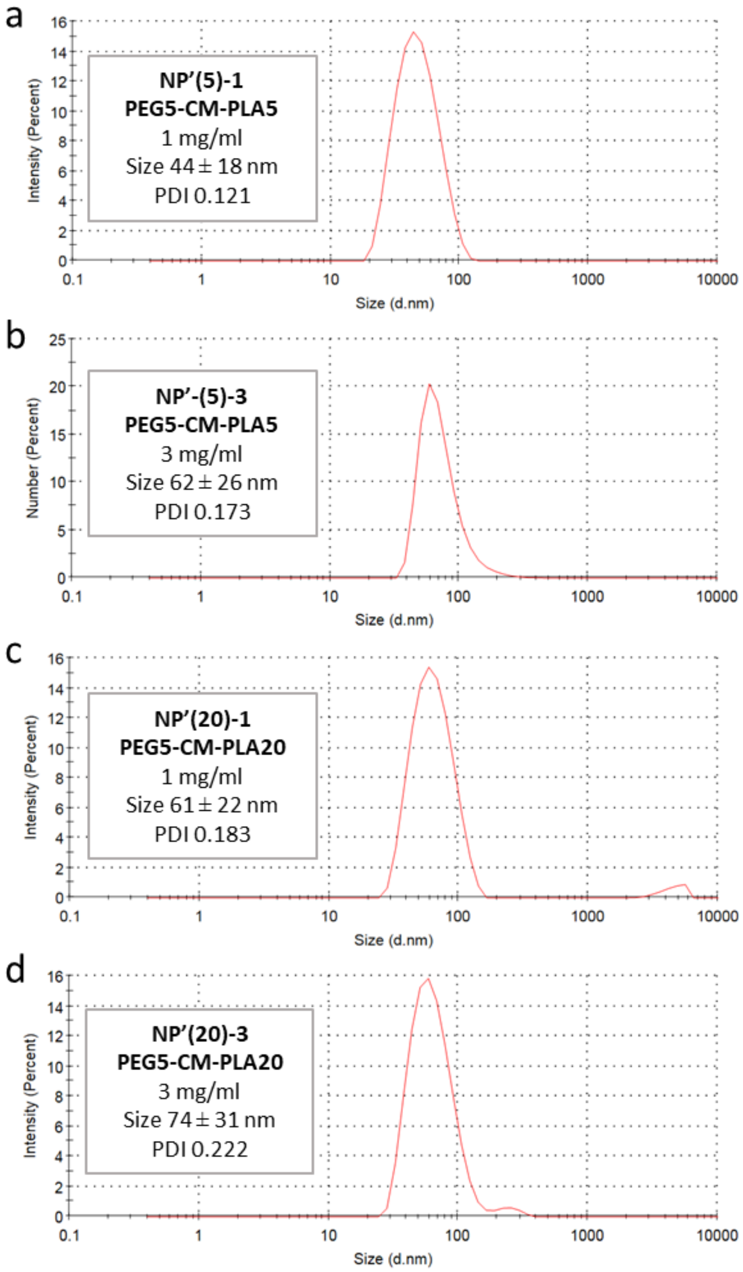

Figure 46: DLS analysis showing the size profiles of the nanoparticle samples in H_2O, prepared using the nanoprecipitation method. A) **NP’(5)-1**. B) **NP’(5)-3**. C) **NP’(20)-1**. D) **NP’(20)-3**.

Following the validation of the size of the nanoparticles, the reason for the nanoparticles failing to centrifuge out of solution is likely their size.

5.3.1.2 W/o/W method

5.3.2.2 Synthesis

Polymer samples **PEG5-CM-PLA5** and **PEG5-CM-PLA5** were dissolved DCM in and 5% PVA w/v in deionised water was added to the DCM. The samples were sonicated until a homogenous emulsion occurred. Further H_2O was added dropwise, to give a total concentration of 0.5 % PVA, and the solution was further sonicated. DCM was evaporated under reduced pressure and samples were stirred overnight. The nanoparticles were centrifuged to remove excess PVA as this could contribute to cell toxicity. Nanoparticles could be retrieved by centrifugation (8,000 rpm for 15 minutes), possibly indicating that the size of the nanoparticles was larger compared to the nanoprecipitation method. Nanoparticles were cleaned twice using centrifugation, and then resuspended in H_2O. Final concentrations of 1 mg/ml and 3 mg/ml of polymers in H_2O was used to yield nanoparticle samples **NP(5)-1**, **NP(5)-3**, **NP(20)-1**, and **NP(20)-3**.

5.3.1.2.2 DLS Size and Zeta Potential Measurements

The hydrodynamic diameter and zeta potential of these nanoparticles were measured using a zetasizer (**Table 9**)(**Figure 47**). As suspected, the nanoparticles fabricated using the W/o/W method were significantly larger than those fabricated using the nanoprecipitation method, allowing for successful pelleting during centrifugation. The nanoparticle size range was also consistent with literature reports [106, 110, 115, 116]. The same pattern of larger nanoparticles resulting from longer polymers and higher concentrations was also observed.

Table 9: Hydrodynamic diameter and zeta potential measurements of nanoparticle samples made using the W/o/W method.

Polymer	Sample	Conc. [mg/ml]	Zeta Potential [mV]	Error (SD) [mV]	Diameter [nm]	Error (SD) [nm]	PDI
PEG5-CM-PLA5	**NP(5)-1**	1	-1.4	0.2	98	57	0.182
PEG5-CM-PLA5	**NP(5)-3**	3	-1.5	0.4	110	56	0.192
PEG5-CM-PLA20	**NP(20)-1**	1	-1.8	0.2	161	48	0.065
PEG5-CM-PLA20	**NP(20)-3**	3	-1.4	0.2	193	43	0.052

Low PDIs were observed in the **PEG5-CM-PLA20** samples with narrower peak shapes shown in **Figure 47c** and **d**. Similar zeta potentials were observed compared to the nanoprecipitation method which was expected due to the similar surface chemistry of the nanoparticle samples.

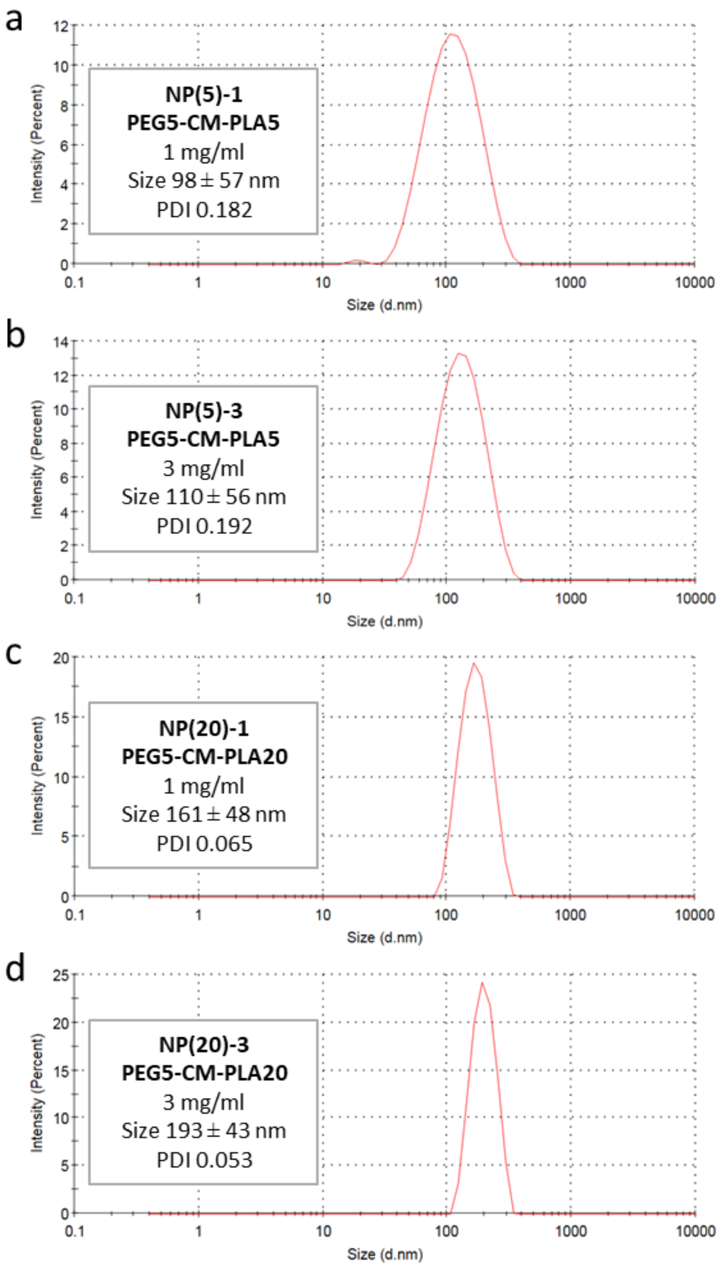

Figure 47: DLS results showing the size profiles of the nanoparticle samples in H_2O, prepared using the W/o/W method. A) **NP(5)-1**. B) **NP(5)-3**. C) **NP(20)-1**. D) **NP(20)-3**.

As the nanoparticles formed using the W/o/W method showed a lower PDI and could be successfully centrifuged, this method was selected to be the method in which to make the light sensitive nanoparticles containing cargo. Centrifugation is beneficial for separating unloaded cargo from light sensitive polymer nanoparticles as although dialysis is possible, the time and methods required could potentially expose the nanoparticles to environmental light sources that could cause premature cargo release and degradation.

5.3.1.2.3 Critical Micelle Concentration

The critical micelle concentration (CMC) of polymers at the concentration in which it becomes energetically favourable for the polymers in solution to form nanoparticles. It is the minimum concentration at which nanoparticles will be formed. To evaluate the critical micelle concentration of **PEG5-CM-PLA5** and **PEG5-CM-PLA20**, Nile Red was used. A dye that is insoluble in water but is fluorescent (655 nm λ_{em}) in a hydrophobic environment. Therefore, by incubating Nile Red with the polymers at different concentrations in water, the CMC can be determined (at the CMC the fluorescence of the Nile Red will start to be observed as the Nile Red is encapsulated in the hydrophobic core of the nanoparticles). A range of concentrations (1 µg/ml - 100 µg/ml) of **NP(5)-3** and **NP(20)-3** were used, prepared from **PEG5-CM-PLA5** and **PEG5-CM-PLA20** fabricated using the W/o/W method. The fluorescence of the samples (520 nm λ_{ex}, 655 nm λ_{em}) was recorded and plotted as shown in **Figure 48**. The concentration at which fluorescence begins to increase is considered the CMC as this is the concentration in which the nanoparticles begin to form, and the Nile Red becomes encapsulated and fluorescent.

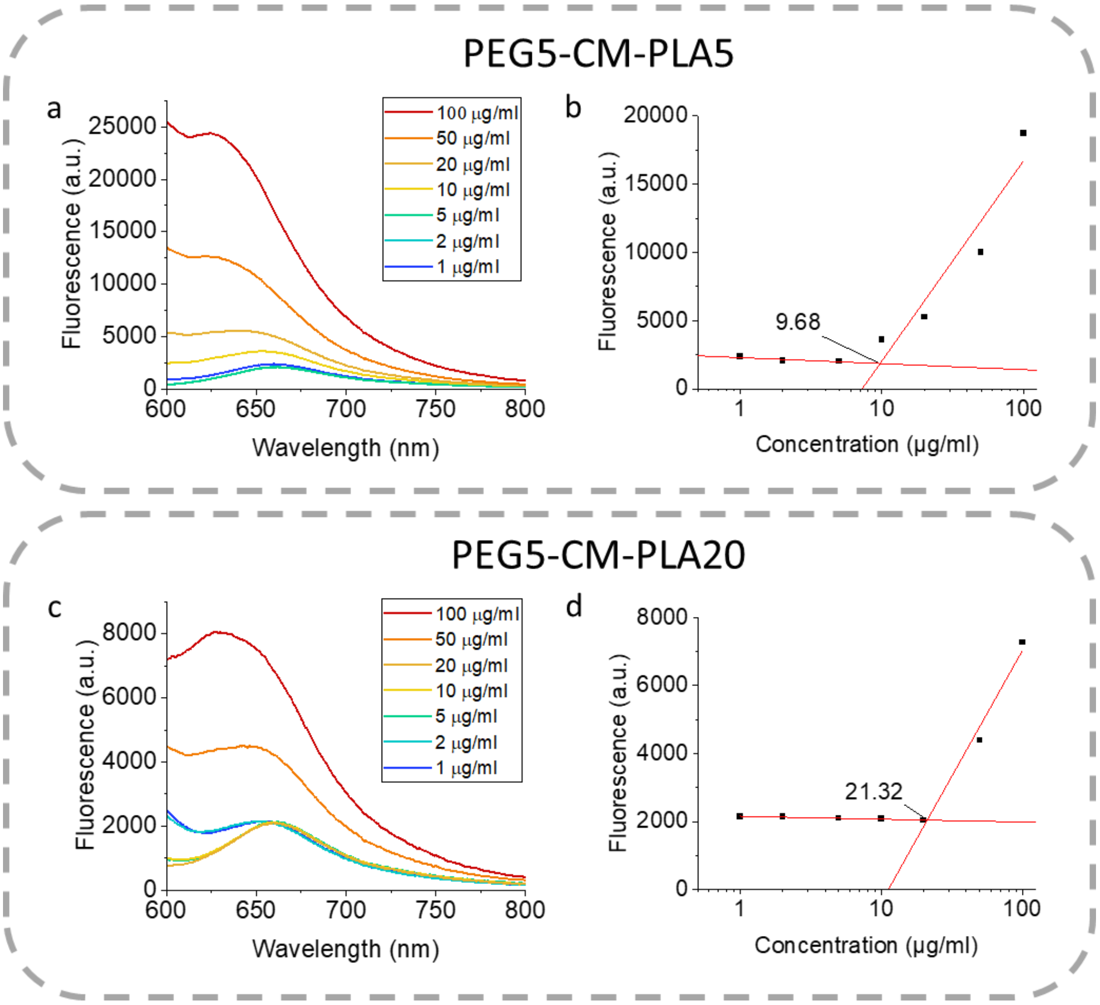

Figure 48: Fluorescence of Nile Red (520 nm excitation) at difference concentrations of polymer in H_2O along with polymer concentration dependent fluorescent of the Nile Red at 660 nm. The CMC was determined at the intersection of the fluorescence increase. A) Fluorescence spectra of Nile Red with different concentrations (1 µg/ml -100 µg/ml) of **PEG5-CM-PLA5**. B) CMC determination from fluorescence intensity of Nile Red plotted against concentrations of **PEG5-CM-PLA5**. C) Fluorescence spectra of Nile Red with different concentrations (1 µg/ml -100 µg/ml) of **PEG5-CM-PLA20**. B) CMC determination from fluorescence intensity of Nile Red plotted against concentrations of **PEG5-CM-PLA20**.

The CMC of **PEG5-CM-PLA5** and **PEG5-CM-PLA20** were 9.7 μg/ml and 21.3 μg/ml, respectively. The results agree with literature in both order of magnitude and of correlation with polymer chain length[117, 118]. As the **PEG5-CM-PLA5** polymer is 2.5 × smaller than the **PEG5-CM-PLA20** polymer, less total mass of a shorter polymer would be required achieve the spherical morphology to form nanoparticles. When considering molecular weight, i.e concentration in molarity, the CMC of **PEG5-CM-PLA5** and **PEG5-CM-PLA20** is 0.968 μM and 0.853 μM, respectively. In this case, slightly lower molarity of the longer polymer is required, likely due to the longer hydrophobic chains of the **PEG5-CM-PLA20** polymer making nanoparticle formation more energetically favourable (greater hydrophobic forces).

5.3.3 Doxorubicin Encapsulation

Doxorubicin was selected as a target cargo for loading within the nanoparticles as a well reported chemotherapy agent. Its biological pathways are well documented, and it is also frequently loaded into PEG-PLA nanoparticles and used to kill via diffusion and would therefore allow for comparison with literature [110, 116, 119]. Doxorubicin hydrochloride (Dox) was used due to its higher water solubility than doxorubicin, aiding purification of the nanoparticles and release measurements. To assess drug uptake efficiency a range of concentrations of Dox were explored with each of the polymers **PEG5-CM-PLA5** and **PEG5-CM-PLA20**. A ratio of 1:0.2 and 1:0.5 polymer:Dox *w/w* was used, and here are given as a prefix of **[0.2$_{\text{DOX}}$]** and **[0.5$_{\text{DOX}}$]** on the nanoparticle codes, respectively. In combination with the previous W/o/W nanoparticle synthesis conditions. **PEG5-CM-PLA5** yielded **[0.2$_{\text{DOX}}$]NP(5)-1**, synthesised using a 1 mg/ml concentration with a 1:0.2 ratio of polymer:Dox, as well as **[0.5$_{\text{DOX}}$]NP(5)-1**, **[0.2$_{\text{DOX}}$]NP(5)-3**, and **[0.5$_{\text{DOX}}$]NP(5)-3**. The same naming method applies for **PEG5-CM-PLA20**, yielding nanoparticle samples **[0.2$_{\text{DOX}}$]NP(20)-1**, **[0.5$_{\text{DOX}}$]NP(20)-1**, **[0.2$_{\text{DOX}}$]NP(20)-3**, **[0.5$_{\text{DOX}}$]NP(20)-3**. Nanoparticle sample names and associated fabrication concentrations can be seen in **Table 10**.

Nanoparticles were prepared as before, using the W/o/W method, with Dox dissolved in the water. Nanoparticles were washed via centrifugation twice to remove the excess Dox and resuspended in H_2O, before being resuspended in H_2O at their required concentrations and stored at 4 °C. PEG-PLA nanoparticles are well known to be stable after freeze-drying [106, 114, 118], however, here, attempting to freeze-dry the nanoparticles gave a material that could not be successfully resuspended and gave a precipitate in solution.

5.3.3.1 Drug Loading Efficiency

To evaluate Dox loading within the nanoparticles, a known mass of nanoparticles containing Dox were broken apart via dissolution in DMSO with the fluorescence measured and compared to a Dox concentration curve. The drug loading content of the nanoparticles was calculated using the mass of the Dox in the nanoparticles and the total mass of the nanoparticles as shown in **Equation 4**. The values are displayed in **Table 10**.

Equation 4: $$Drug\ loading\ content\ (\%) = \frac{mass\ of\ DOX\ in\ nanoparticles}{total\ mass\ of\ nanoparticles}\ x\ 100$$

Table 10: Drug loading content of light sensitive nanoparticles

Polymer	Polymer concentration [mg/ml]	Dox ratio (polymer: drug)	Nanoparticle Sample	Drug Loading [%]	Error (SD) [%]
PEG5-CM-PLA5	3	1:0.5	**[0.5$_{\mathrm{DOX}}$]NP(5)-3**	0.5	0.3
PEG5-CM-PLA5	3	1:0.2	**[0.2$_{\mathrm{DOX}}$]NP(5)-3**	1.9	0.4
PEG5-CM-PLA5	1	1:0.5	**[0.5$_{\mathrm{DOX}}$]NP(5)-1**	1.2	0.3
PEG5-CM-PLA5	1	1:0.2	**[0.2$_{\mathrm{DOX}}$]NP(5)-1**	0.9	0.2
PEG5-CM-PLA20	3	1:0.5	**[0.5$_{\mathrm{DOX}}$]NP(20)-3**	0.3	0.1
PEG5-CM-PLA20	3	1:0.2	**[0.2$_{\mathrm{DOX}}$]NP(20)-3**	3.4	0.4
PEG5-CM-PLA20	1	1:0.5	**[0.5$_{\mathrm{DOX}}$]NP(20)-1**	2.1	0.5
PEG5-CM-PLA20	1	1:0.2	**[0.2$_{\mathrm{DOX}}$]NP(20)-1**	1.2	0.3

The nanoparticle solutions showed drug loading of 0.3-3.4 %, which is in agreement with the experimental literature[116] [119, 120], but also agrees with the theoretical drug loading possibilities of Dox in a PEG-PLA nanoparticle system. The theoretical drug loading of a compound can be determined using its affinity of adsorption to the hydrophobic block of a diblock copolymer. A recent study utilised different simulation techniques to determine doxorubicin-PLA drug binding energy and resulting drug loading [25]. A direct correlation was found with adsorption energy and experimental drug loading, where Dox was found to have an adsorption energy of ~-40 kcal/mol and theoretical drug loading percentage of ~2.2 %. A pattern also emerged with the largest drug loading capacity occurring for both polymers in the samples at an intermediate polymer:Dox ratio, with the highest percentage drug loading occurring in the samples made using a 3 mg/ml solution of polymer with a 1:0.2 ratio of polymer:Dox in solution. This is likely due to a balance being optimal between the ratio of cargo and the polymer. Too little drug in the solution would result in Dox being less likely to be encapsulated, and too high of a concentration could potentially interfere with nanoparticle formation as the Dox could become associated with the whole surface area of the polymers and prevent the typical hydrophobic core, hydrophilic shell being formed. A higher drug loading capability was possible using **PEG5-CM-PLA20** compared to the **PEG5-CM-PLA5**. This agrees with the literature and is likely due to the larger internal core within the nanoparticles arising from the longer hydrophobic PLA chain and also from the stronger inter-nanoparticle interactions allowing for the Dox to be more strongly held within the nanoparticle's core[114, 116]. The nanoparticle synthesis was repeated three times and the pattern was consistently seen, with only a small amount of variation between samples. The fluorescence peaks observed along with the drug loading and errors are given in **Figure 49**.

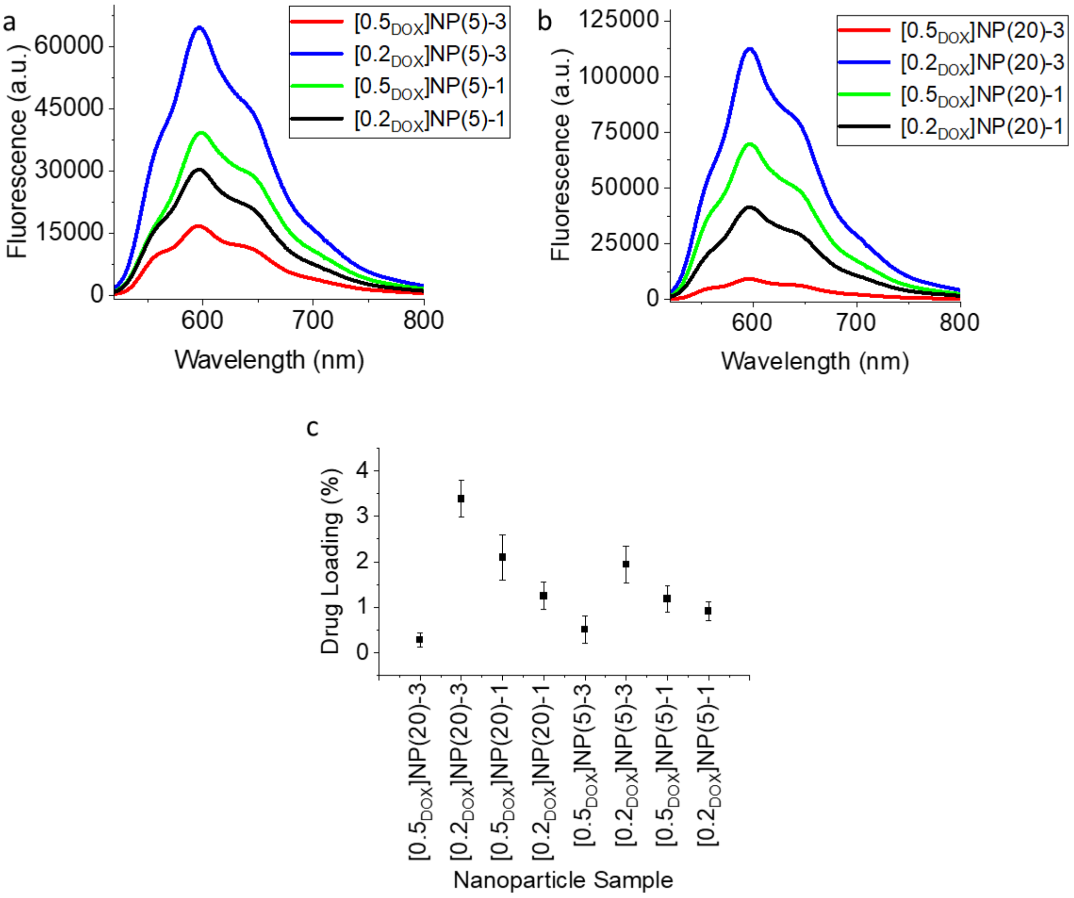

Figure 49: Fluorescence signal of Dox loaded nanoparticles when dissolved in DMSO (λ_{ex} 520 nm, λ_{em} 610 nm). Nanoparticles were fabricated using **PEG5-CM-PLA5** and **PEG5-CM-PLA20** at different polymer and Dox concentrations. A) Fluorescence of nanoparticle samples synthesised from **PEG5-CM-PLA5**. B) Fluorescence of nanoparticle samples synthesised from **PEG5-CM-PLA20**. C) The calculated drug loading (Dox) percentage of nanoparticle samples and SD errors. n = 3.

To further characterise the nanoparticles, size and zeta potential measurements as well as drug release were explored.

5.3.2.2 DLS Size and Zeta Potential Measurements

The hydrodynamic diameter of the Dox loaded nanoparticles was measured using DLS (**Figure 50**, and **51**).

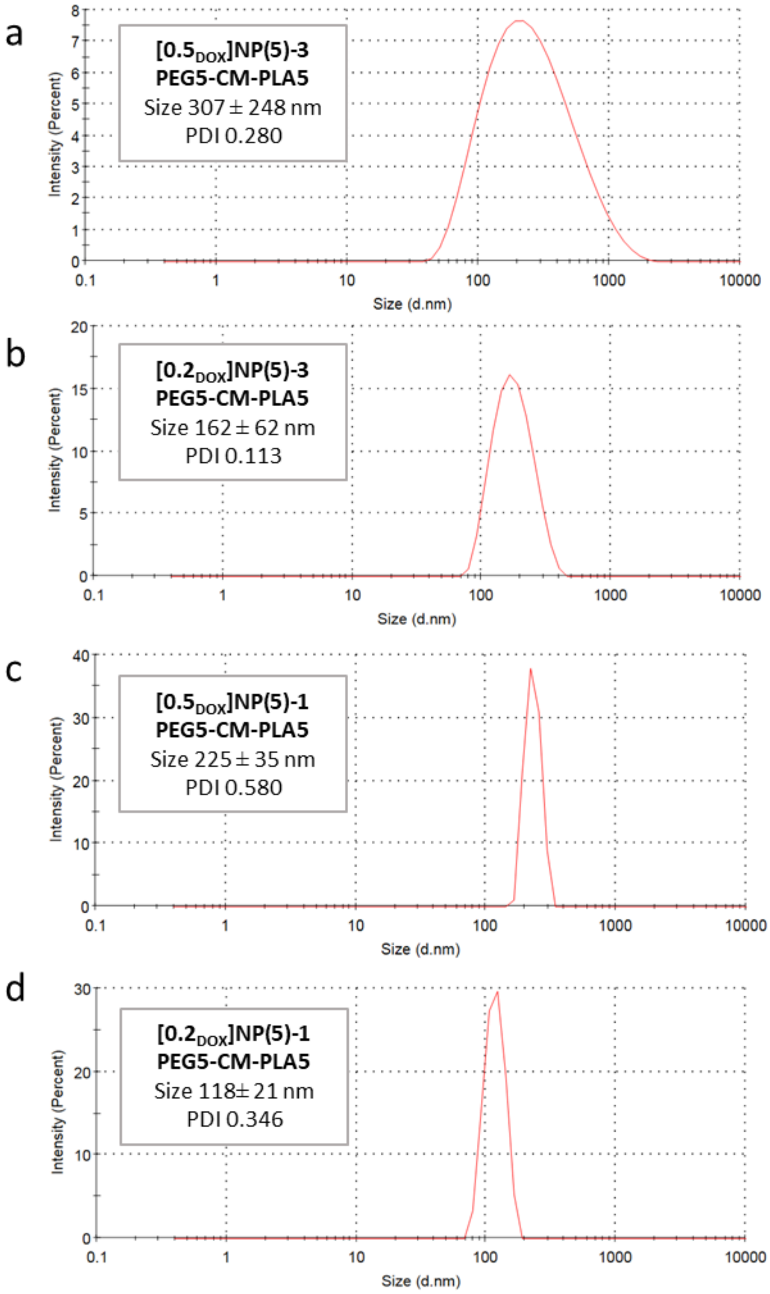

Figure 50: DLS hydrodynamic diameter of doxorubicin loaded nanoparticles fabricated using **PEG5-CM-PLA5** at different polymer and Dox concentrations.

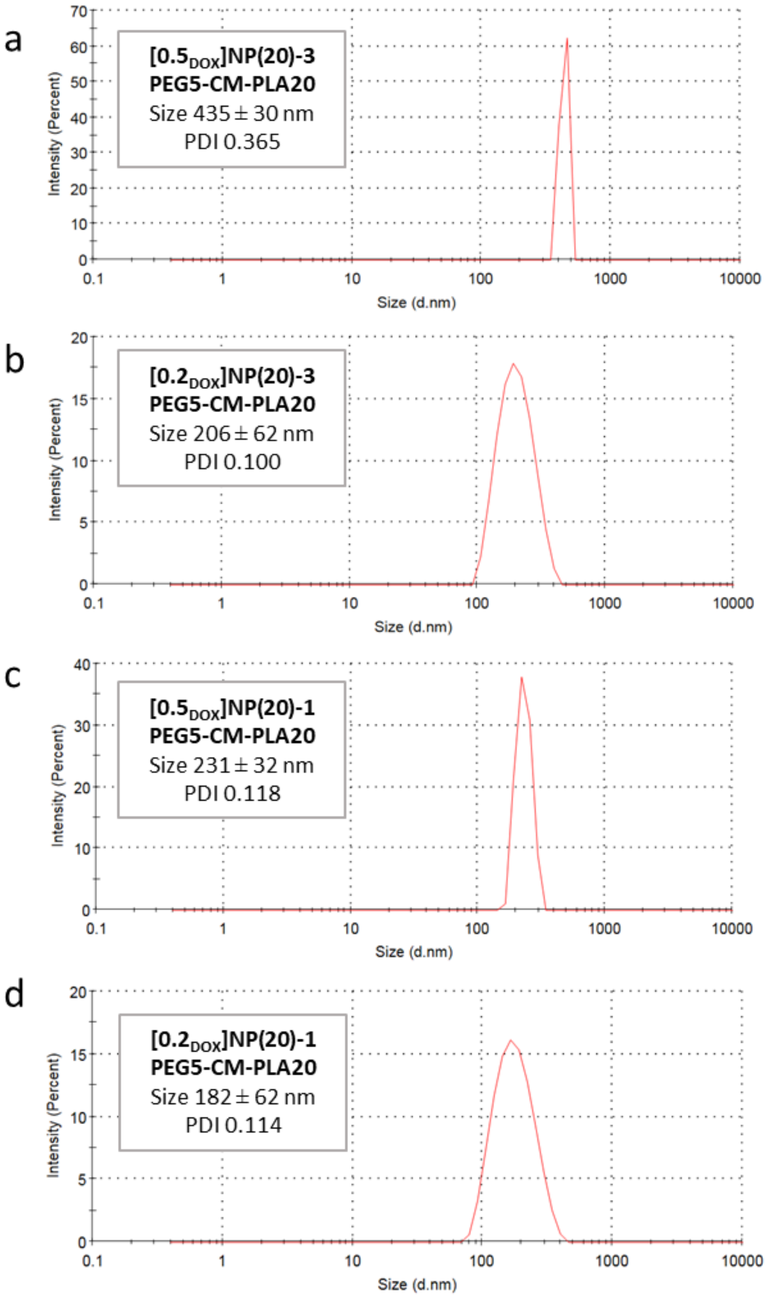

Figure 51: DLS hydrodynamic diameter of doxorubicin loaded nanoparticles fabricated using **PEG5-CM-PLA20** at different polymer and Dox concentrations.

Zeta potential measurements were also performed to measure the surface charge of the nanoparticles in water. Size and zeta potential data is shown in **Table 11**.

Table 11: Hydrodynamic diameter and zeta potential measurements of nanoparticle samples containing Dox made using the W/o/W method.

Sample	Drug Loading [%]	Zeta Potential [mV]	Zeta Potential Error [mV]	Diameter [nm]	Diameter Error [nm]	PDI
[0.5$_{\text{DOX}}$]NP(5)-3	0.5	-6.21	1.20	307	248	0.280
[0.2$_{\text{DOX}}$]NP(5)-3	1.9	-2.96	0.61	162	62	0.113
[0.5$_{\text{DOX}}$]NP(5)-1	1.2	-8.25	1.04	225	35	0.580
[0.2$_{\text{DOX}}$]NP(5)-1	0.9	-10.2	1.28	118	21	0.348
[0.5$_{\text{DOX}}$]NP(20)-3	0.3	-10.4	1.16	435	30	0.365
[0.2$_{\text{DOX}}$]NP(20)-3	3.4	-2.67	0.12	206	62	0.100
[0.5$_{\text{DOX}}$]NP(20)-1	2.1	-7.00	1.85	231	32	0.118
[0.2$_{\text{DOX}}$]NP(20)-1	1.2	-18.2	0.48	182	62	0.114

All nanoparticle samples had a similar charge following loading with Dox. The nanoparticles with the highest drug loading percentage (**[0.2$_{\text{DOX}}$]NP(5)-3** and **[0.2$_{\text{DOX}}$]NP(20)-3**) also had the highest charge. This could potentially be due to the positive charge on the amine of the doxorubicin resulting in a more relatively positive surface charge in nanoparticles containing more drug.

The nanoparticles all had a larger diameter following Dox loading, as compared to the unloaded nanoparticles. The nanoparticles will have a larger diameter when there is Dox in the core due to expansion of the nanoparticle to fit around the drug. This is also consistent within literature [106]. The sizes of the nanoparticles varied from 118 nm – 435 nm, with the larger nanoparticles occurring for the samples prepared with 3 mg/ml polymer with a 1:0.5 polymer:drug ratio. The smallest sizes and lowest PDI were observed with polymer samples that also had the highest drug loadings (**[0.2$_{\text{DOX}}$]NP(5)-3**, **[0.2$_{\text{DOX}}$]NP(20)-3**), therefore combining the low PDI, ideal size, and highest drug loading percentage, making these the target moving forward.

5.3.2.3 TEM - Size and Morphology Analysis

As DLS measurements can often overestimate the diameter of nanoparticles due to the measurement displaying the total hydrodynamic diameter of the nanoparticles, TEM was also performed to visualise the nanoparticles and examine them (**Figure 52**).

Expectedly, the nanoparticles are smaller in size than found from the DLS measurements. The unloaded nanoparticles also appear lighter in colour. After Dox loading the nanoparticles are darker with more defined borders, this is likely due to the Dox compound increasing the overall density with the nanoparticles and therefore the contrast of the images. The sizes of the nanoparticles also followed the same pattern as shown on the DLS, with the unloaded nanoparticles being smaller compared to the Dox loaded nanoparticles, and the polymers fabricated from **PEG5-CM-PLA5** (**NP(5)-3**, and **[0.2$_{\text{DOX}}$]NP(5)-3**) also being smaller than those made using **PEG5-CM-PLA20** (**NP(20)-3**, and **[0.2$_{\text{DOX}}$]NP(20)-3**).

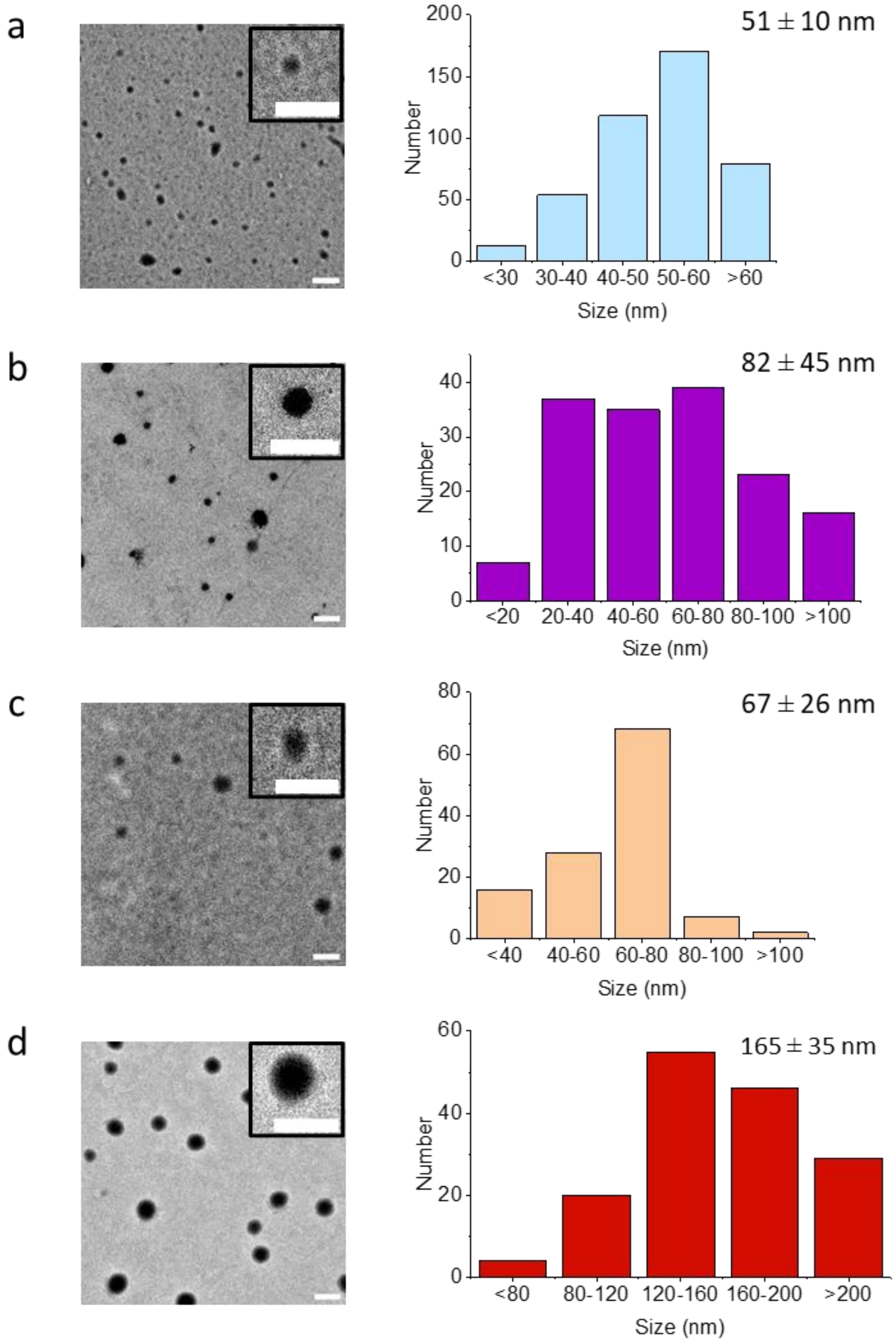

Figure 52: TEM images of nanoparticles with corresponding size profiles. a) **NP(5)-3** unloaded nanoparticles. b) **[0.2$_{\text{DOX}}$]NP(5)-3** Dox loaded nanoparticles. c) **NP(20)-3** unloaded nanoparticles. d) **[0.2$_{\text{DOX}}$]NP(20)-3** Dox loaded nanoparticles.

5.3.2.4 Drug Release Via Diffusion

To see how the nanoparticles would release drug due to osmotic pressure the nanoparticles underwent dialysis at 37 °C. Water was used instead of the more biologically imitating buffer PBS, due to the poor water solubility of Dox in PBS. Different molecular weights of PLA (5,000 Da and 20,000 Da) for **PEG5-CM-PLA5** and **PEG5-CM-PLA20**, respectively, were used along with 5,000 Da PEG due to the theoretical differences in PEG-PLA drug release profiles when the molecular weights of the chains are varied [110, 116, 118]. In theory, nanoparticles formed from **PEG5-CM-PLA5** polymers would release drugs at a faster rate than nanoparticles formed from **PEG5-CM-PLA20**, containing a higher molecular weight of PLA. This is due to the **PEG5-CM-PLA5** polymers being less tightly bound and having a 'leakier' core due to the weaker intermolecular interactions between the shorter PLA chains, meaning that Dox molecules are less strongly bound in the core. Therefore, in theory the **PEG5-CM-PLA20** polymers would be a more reliable candidate as the nanoparticle should have reduced undesirable drug leakage that would lead to off-site drug toxicity *in vivo*.

Following drug loading and morphology determination the samples **[0.2$_{\mathbf{DOX}}$]NP(5)-3** and **[0.2$_{\mathbf{DOX}}$]NP(20)-3** were selected due to their ideal properties. The drug loading efficiency was firstly be measured to be able to determine the cumulative drug release percentage as a function of time during the dialysis. The drug loading of the **[0.2$_{\mathbf{DOX}}$]NP(5)-3** and **[0.2$_{\mathbf{DOX}}$]NP(20)-3** nanoparticles were determined to be 1.8 % and 3.7 %, respectively.

To perform the dialysis Spectra-Por® Float-A-Lyzer® G2 dialysis tubes with a 20 kDa molecular weight cut off were used. The fluorescence, overtime, was found to increase, corresponding to the release of Dox from the nanoparticles (**Figure 53**). The percentage of Dox release from the nanoparticles could be determined from the concentration and drug loading of nanoparticle samples (**Figure 53b** and **d**). In both cases drug release from the nanoparticles began rapidly which then began to slow down over time. Interestingly the **[0.2$_{\mathrm{DOX}}$]NP(5)-3** nanoparticles released almost three times more Dox over 62 hours than the **[0.2$_{\mathrm{DOX}}$]NP(20)-3** (33 % and 12 %, respectively). This higher rate of release was expected from the **[0.2$_{\mathrm{DOX}}$]NP(5)-3** nanoparticles as the shorter PLA chains would cause the Dox molecules to be less strongly bound within the nanoparticles. For this reason, the **[0.2$_{\mathrm{DOX}}$]NP(20)-3** nanoparticles would likely be optimal for biological applications as the lower rate of Dox release would ensure less off-site toxicity and allow more drug to be delivered at the tumour site via light irradiation.

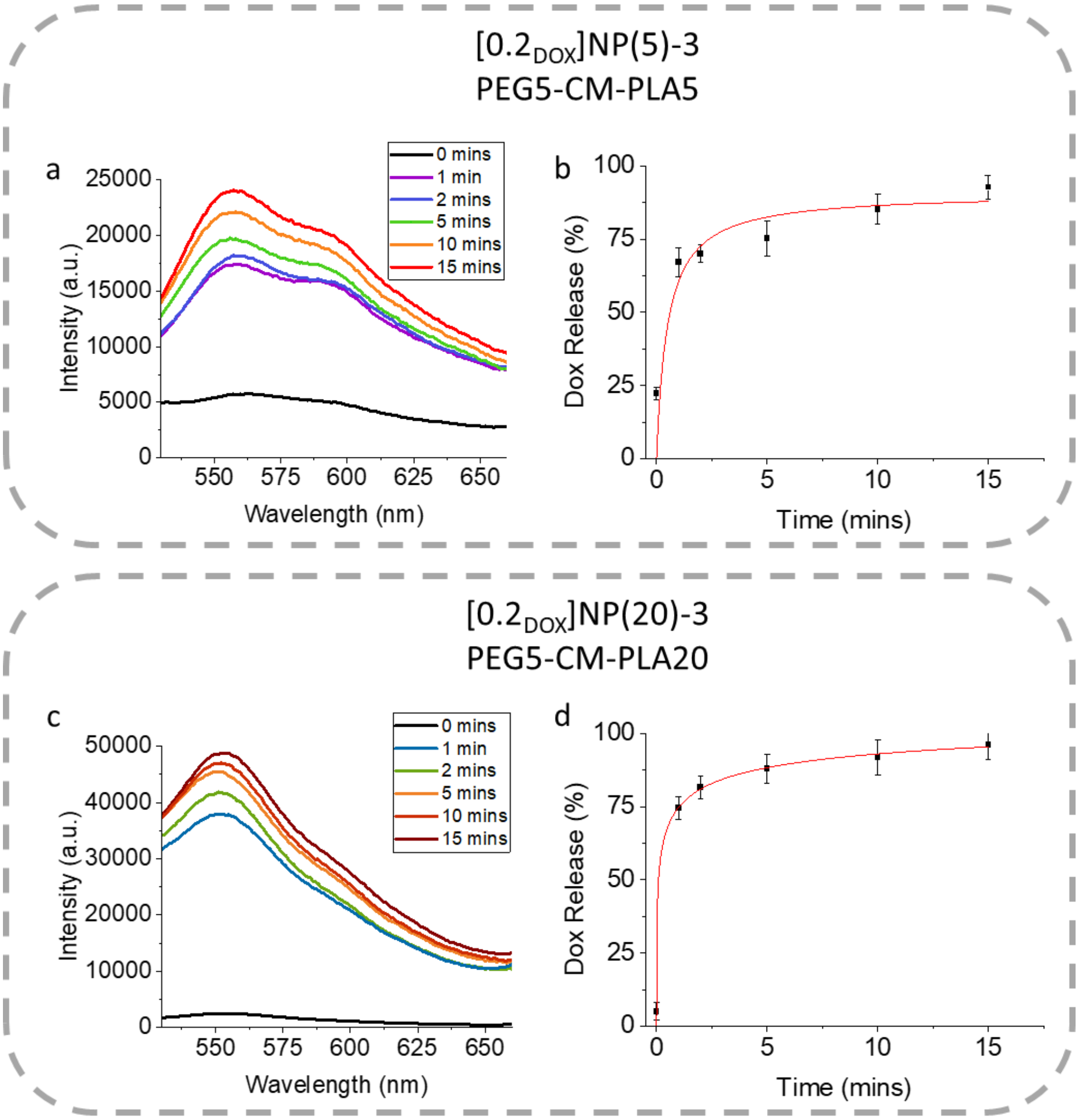

Figure 53: Dox release from nanoparticles in water at 37 °C over 62 hours, measured using fluorescence (λ_{ex} 520 nm, λ_{em} 555 nm). a) Fluorescence corresponding to Dox release from **[0.2$_{\text{DOX}}$]NP(5)-3** nanoparticles. b) Cumulative Dox release from the **[0.2$_{\text{DOX}}$]NP(5)-3** nanoparticles. Values are mean ± SD, n = 3. c) Fluorescence corresponding to Dox release from the **[0.2$_{\text{DOX}}$]NP(20)-3** nanoparticles. d) Cumulative Dox release from the **[0.2$_{\text{DOX}}$]NP(20)-3** nanoparticles. Values are mean ± SD, n = 3.

5.3.3 Light responsivity

To validate the light responsivity of the polymers and nanoparticles, irradiation experiments were performed. Following irradiation (365 nm) the diblock copolymers should be cleaved and the PEG and PLA chain should separate with the coumarin remaining on the PEG chain (**Scheme 20**).

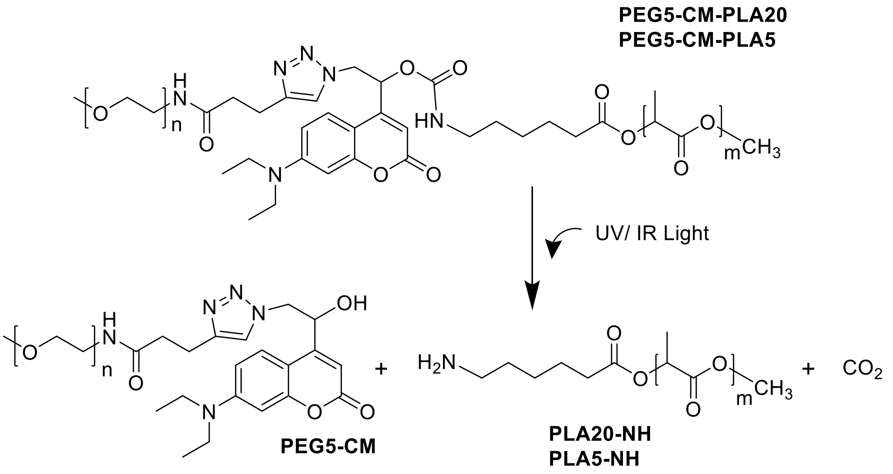

Scheme 20: Cleavage of **PEG5-CM-PLA5** and **PEG5-CM-PLA20** following irradiation with UV light (one photon) or IR light (two photon), releasing **PEG5-CM**, CO_2, and **PLA5-NH$_2$** or **PLA20-NH$_2$**, respectively.

5.3.3.2 365 nm Irradiation of Polymers in DMF

The polymers **PEG5-CM-PLA5** and **PEG5-CM-PLA20** were dissolved in DMF (0.1 % LiBr) and irradiated. Samples were throughout the irradiation analysed by GPC. The 400 nm GPC detector was used as this would only display signal arising from the absorbance of the coumarin and would therefore only show the uncleaved diblocks **PEG5-CM-PLA5** and **PEG5-CM-PLA20** or the cleaved coumarin covalently bound to the 5,000 Da Mw PEG (**PEG5-CM**). Therefore, a clear peak shift should occur following cleavage representing the molecular weight changing from 10,000 Da to 5,000 Da for **PEG5-CM-PLA5** and 25,000 Da to 5,000 Da for **PEG5-CM-PLA20**. The resulting GPC peaks were plotted and the integrations of each peak corresponding to the diblocks **PEG5-CM-PLA5** and **PEG5-CM-PLA20** and cleaved PEG-coumarin **PEG5-CM** were taken and the cleavage percentages calculated (**Figure 54**).

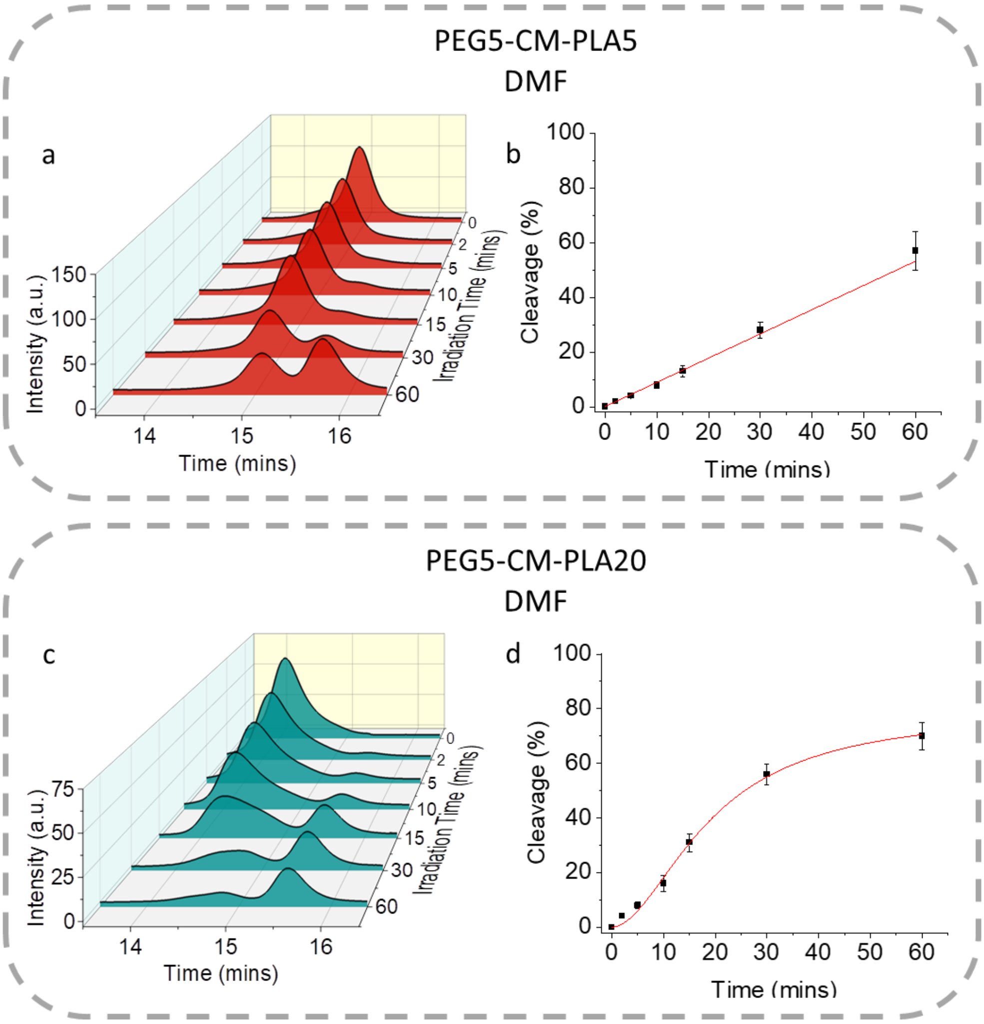

Figure 54: GPC traces and corresponding polymer cleavage percentage from **PEG5-CM-PLA5** and **PEG5-CM-PLA20** samples irradiated under 365 nm in a solution of DMF 0.1 % LiBr. GPC data shows intensity of the signal at 400 nm, retention time (mins), and irradiation time. Values are mean ± SD, n = 3. a,b) **PEG5-CM-PLA**. c,d) **PEG5-CM-PLA20**.

Both samples showed cleavage upon irradiation although at different rates. The **PEG5-CM-PLA20** cleaved more over 60 minutes, with a total cleavage of 70 % compared to 57 % in **PEG5-CM-PLA5**. The cleavage of **PEG5-CM-PLA5** also had a linear pattern, as opposed to usual kinetic curves that in which the rate starts to decrease in time (**Figure 54b**). This is likely due to the slower rate of cleavage meaning the rate was still within the linear cleavage range of a kinetics graph, this pattern would have likely evolved should the irradiation have been continued. The cleavage rate was relatively slow for both samples. This was a concern as for biological purposes as cells cannot be irradiated over long periods of time at 365 nm due to UV light resulting in cell death[121]. However only low cleavages would be needed to disrupt the nanoparticles. In addition, light responsive cleavage rates are often solvent dependent, thus, the experiment was repeated in water.

5.3.3.3 365nm Irradiation of Polymers in H_2O

As polymers **PEG5-CM-PLA5** and **PEG5-CM-PLA20** are not freely soluble in water due to their amphiphilic properties, unloaded nanoparticles samples **[0.2$_{\text{DOX}}$]NP(5)-3** and **[0.2$_{\text{DOX}}$]NP(20)-3** prepared using the W/o/W method were irradiated (365 nm) at a concentration of 3 mg/ml. Following irradiation at time points between 0 – 60 minutes, samples taken were dried using lyophilisation and analysed by GPC (in DMF 0.1 % LiBr) again using the 400 nm detector. The resulting GPC peaks were plotted and the peak areas were integrated and the cleavage was calculated (**Figure 55**).

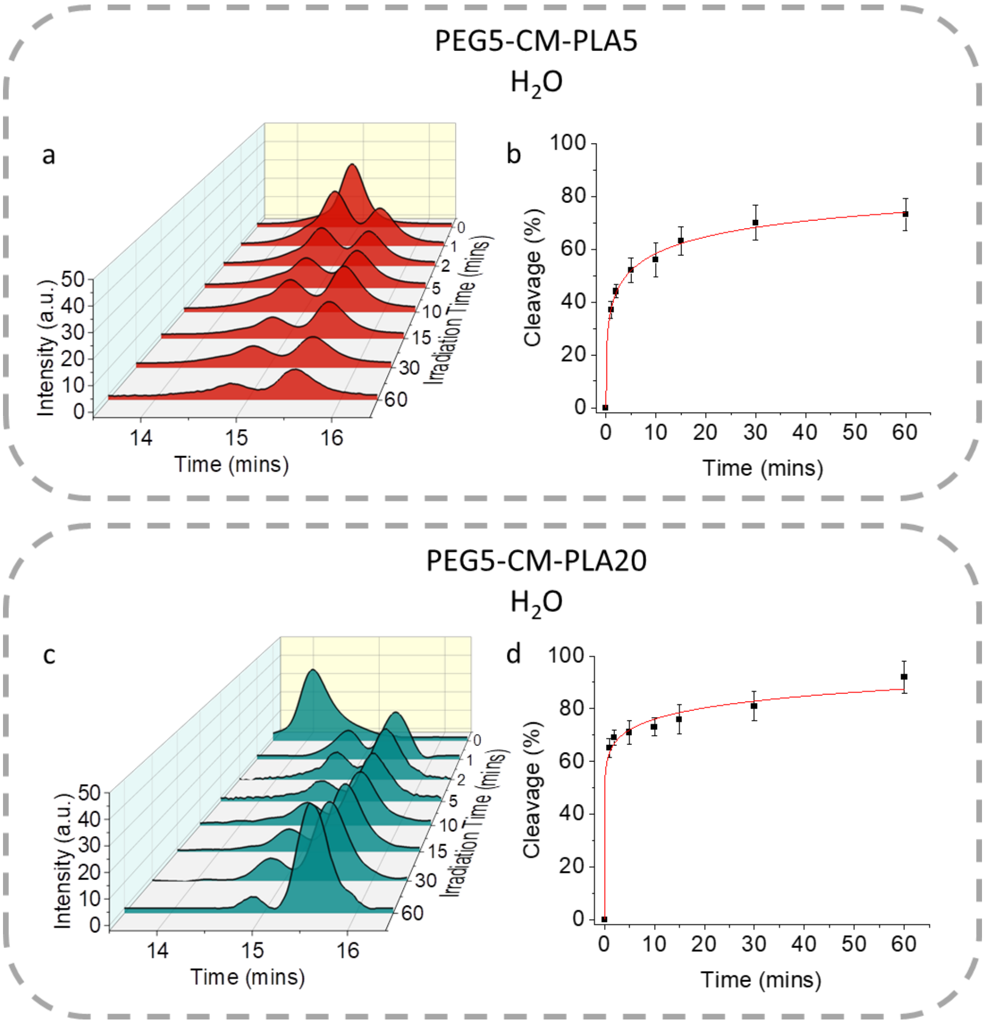

Figure 55: GPC traces and corresponding polymer cleavage percentage from **PEG5-CM-PLA5** and **PEG5-CM-PLA20** samples irradiated under 365 nm in H_2O. GPC data shows intensity of the signal at 400 nm, retention time (mins), and irradiation time. Values are mean ± SD, n = 3. a,b) **PEG5-CM-PLA**. c,d) **PEG5-CM-PLA20**.

The polymers when suspended in water as nanoparticles showed high efficiency, resulting in a faster rate of cleavage and a higher overall cleavage after 60 minutes of irradiation. The comparison of cleavage percentages is shown in **Table 12**.

The same pattern of higher cleavage rate for **PEG5-CM-PLA20** compared to the **PEG5-CM-PLA5** was observed, this could potentially be due to a lower molar concentration of the **PEG5-CM-PLA20** being used for irradiation and there being less coumarin molecules present to be cleaved. **PEG5-CM-PLA20** would also have a larger surface area and although the coumarin wouldn't change size, it could affect the conformation of the molecule when it is irradiated. Cleavage occurred much faster in water overall, likely due its presence being necessary in the cleavage mechanism. A large proportion of both the **PEG5-CM-PLA20** and **PEG5-CM-PLA5** polymer samples was cleaved (65 % and 37 %, respectively) after only 1 minute of irradiation (365 nm). This was very promising for biological applications as it would lead to high drug release rates from the nanoparticles.

Table 12: Polymer cleavage percentage in different solvents during irradiation under 365 nm.

Polymer	Cleavage Solvent	Irradiation Time (mins)							
		0	1	2	5	10	15	30	60
		Polymer Cleavage (%)[a]							
PEG5-CM-PLA5	DMF	0	-	2	4	8	13	28	57
	H_2O	0	37	44	47	56	63	70	73
PEG5-CM-PLA20	DMF	0	-	4	8	16	31	56	70
	H_2O	0	65	69	71	73	76	81	92

[a] Calculated via integration of the GPC peaks corresponding to cleaved polymer (DMF, 0.1 % LiBr).

Following this experiment, nanoparticles containing Dox were irradiated to investigate the light responsive drug release.

5.3.3.4 365nm Nanoparticle Drug Release

For the nanoparticle irradiation, the previously selected optimised samples of **[0.2$_{\mathrm{DOX}}$]NP(5)-3** and **[0.2$_{\mathrm{DOX}}$]NP(5)-3** were used. Dox loaded nanoparticles were irradiated (365 nm) for 0 – 15 minutes and samples were taken throughout and the fluorescence of the supernatant was measured to quantify Dox release. (**Figure 56**). The light responsive drug release from the nanoparticles was very efficient, with more than 70 % of drug being released after only 2 minutes of 365 nm irradiation in both nanoparticle samples (**Table 13**). The cleavage reached upwards of 90 % in both samples after 15 minutes of irradiation. A 2 minute irradiation time was selected for biological experiments to optimise drug release but minimise potential cell toxicity. The **[0.2$_{\mathrm{DOX}}$]NP(5)-3** nanoparticles released 22 % of the drug prior to the irradiation compared to 5 % from the **[0.2$_{\mathrm{DOX}}$]NP(20)-3** nanoparticles. This reaffirms the findings in section 5.3.2.4 that the **[0.2$_{\mathrm{DOX}}$]NP(5)-3** nanoparticles are ‘leakier’ due to the weaker binding of the Dox inside nanoparticle core due to the lower molecular weight PLA (5 kDa vs 20 kDa).

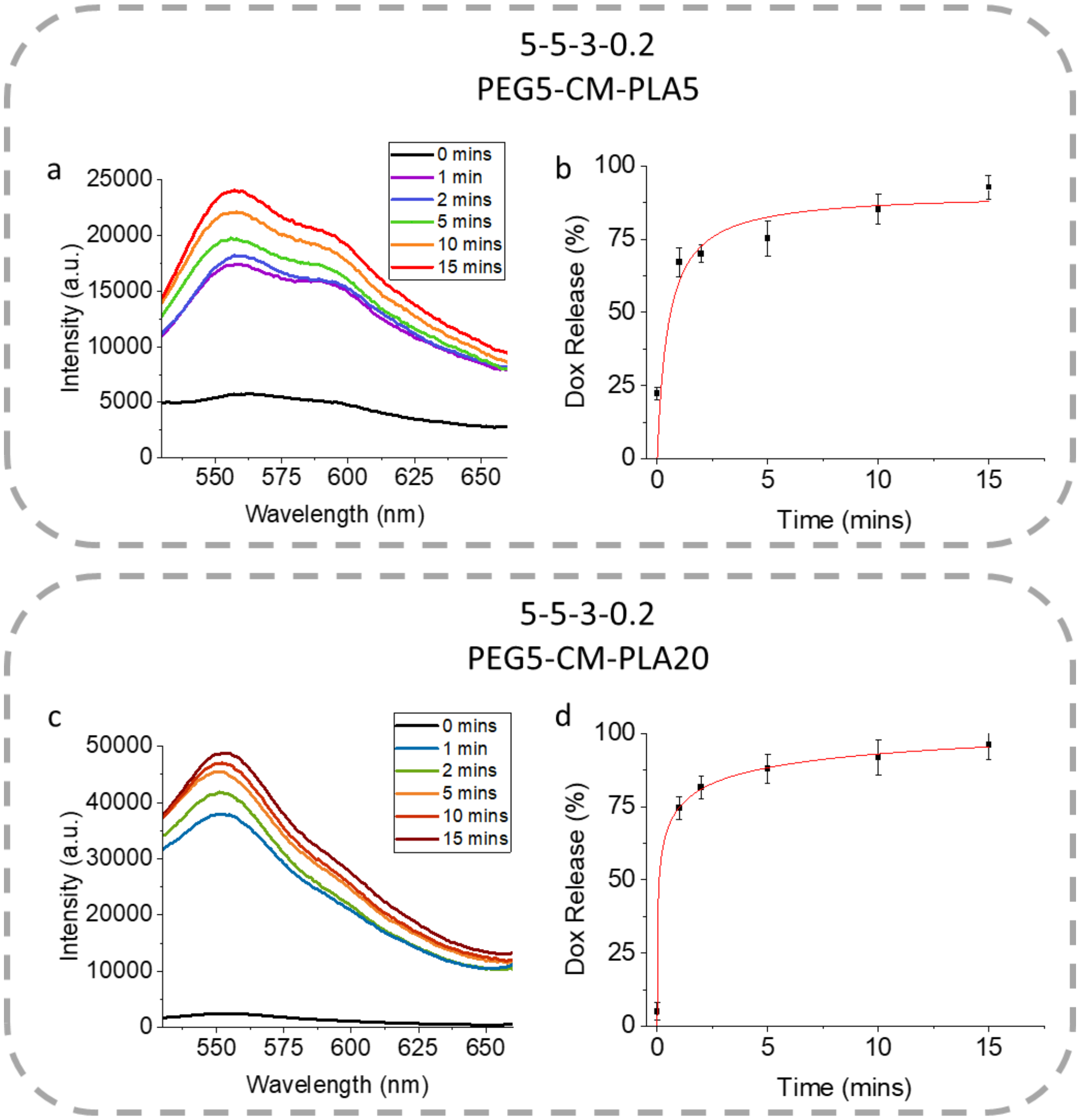

Figure 56: Fluorescence (λ_{ex} 520 nm) of Dox at 520 nm released from nanoparticles and corresponding Dox release (λ_{em} 560 nm) when irradiated for overtime (365 nm in H_2O). Values are mean ± SD, n = 3. a,b) **[0.2$_{\text{DOX}}$]NP(5)-3**. c,d) **[0.2$_{\text{DOX}}$]NP(20)-3**.

Table 13: Dox release from nanoparticle samples when irradiated at 365 nm in H_2O.

Nanoparticles	Irradiation Time (mins)					
	0	1	2	5	10	15
	Dox release (%)[a]					
[0.2$_{\text{DOX}}$]NP(5)-3	22	67	70	75	85	93
[0.2$_{\text{DOX}}$]NP(20)-3	5	75	82	88	92	96

[a] Calculated from the fluorescence at 560 nm, drug loading percentage, and mass of the nanoparticles irradiated.

Following the confirmation of the drug release from the nanoparticles, they were tested *in vitro* to investigate their selective cell-killing abilities.

5.4 *In vitro* Studies

Nanoparticle samples containing Dox **[0.2$_{\text{DOX}}$]NP(5)-3** and **[0.2$_{\text{DOX}}$]NP(20)-3** and unloaded nanoparticle samples **NP(5)-3** and **NP(20)-3** were evaluated on HeLa and MCF7 Cell lines. Both loaded and unloaded nanoparticles were tested to ensure that any cell toxicity could be attributed to the Dox release from the nanoparticles due to light irradiation and not the empty polymer nanoparticles in combination with irradiation alone. HeLa and MCF7 cell lines (cervical and breast cancer cells, respectively) were selected due to their fast proliferation rates, availability, and ease of use. Cells were incubated in phenol-red free media to prevent the absorbance of the UV light.

Cells were treated with free Dox (0.125 µg/ml - 4 µg/ml), nanoparticles **[0.2$_{\text{DOX}}$]NP(5)-3** and **[0.2$_{\text{DOX}}$]NP(20)-3** containing the equivalent amount of Dox, or unloaded nanoparticles **NP(5)-3** and **NP(20)-3**. Cells were then left to incubate for 24 hours to allow for the nanoparticles to be uptaken by the cells. The wells were then irradiated at 365 nm for 2 minutes and incubated for 24 hours. Bright field images were acquired prior to an MTT assay being performed to assess cell viability (**Figure 57**).

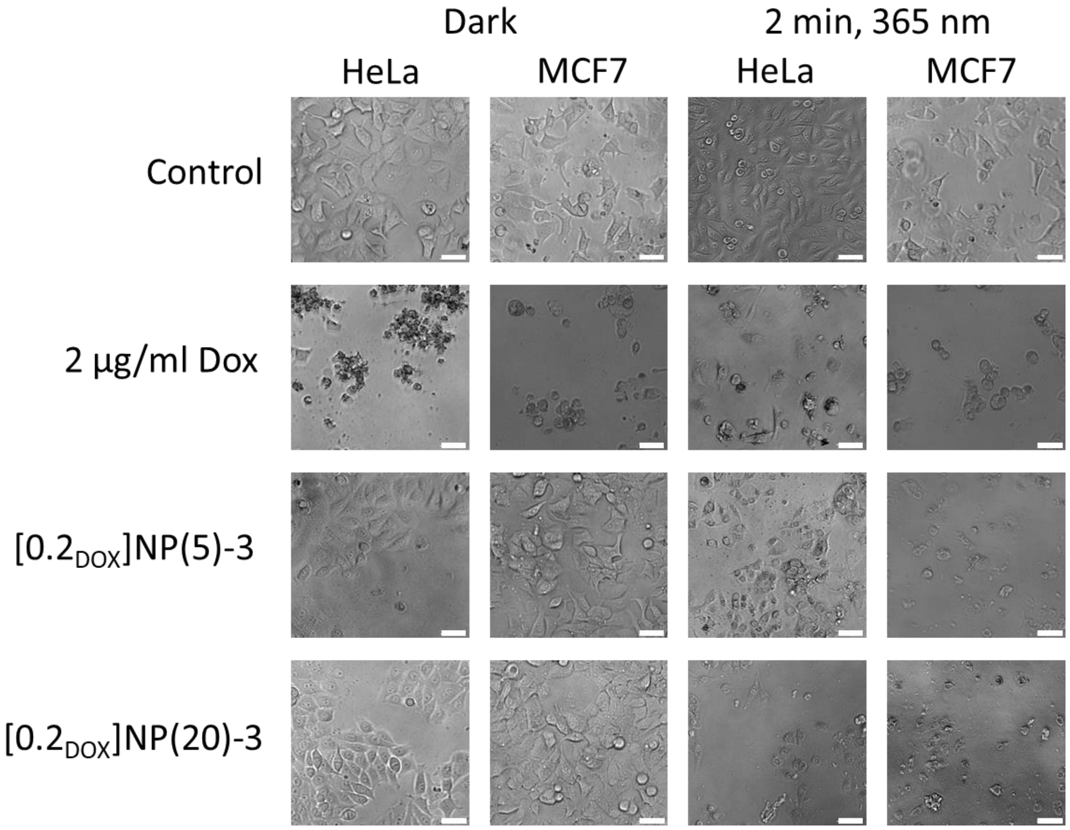

Figure 57: Bright field images of HeLa and MCF7 cells either kept in the dark or irradiated (365 nm) for 2 minutes. Control untreated cells, cells incubated with 2 µg/ml Dox, cells incubated with **[0.2$_{\text{DOX}}$]NP(5)-3** and **[0.2$_{\text{DOX}}$]NP(20)-3** at concentrations corresponding to 2 µg/ml Dox. Scale bar = 20 µm.

The cell images show promising results as the morphology of the cells for nanoparticle samples kept in the dark looked healthy and more like control cells and cells following irradiation looked more like the cells incubated with Dox. This was the case for both cell types. Control cells both have similar morphologies prior and after irradiation which demonstrates that 2 minutes under 365 nm doesn’t cause enough stress to the cells to contribute to cell death. Cell death looks to have occurred equally in cell samples containing Dox irrespective of light irradiation which would be expected. To quantify cell death MTT assays were performed (**Figure 58**).

The MTT assay showed very promising results. As the Dox was incubated with the cells for 48 hours compared to the contact that the cells had with the Dox from the nanoparticles only being 24 hours,it was to be expected that cell death would occur more in these samples. However, the difference in cell viability was not significant when considering that the cells with free Dox had twice the incubation time with the drug. The results from the Dox samples are also consistent with the reported IC50 (0.22 µg/ml for HeLa cells after 24 hours of incubation). The cells showed higher rates of cell death with higher concentrations of nanoparticles after irradiation. This is expected as more drug is being released which would lead to higher cell death. High cell viability was also recorded in the non-irradiated samples, particularly at lower concentrations of nanoparticles. Some cell death could be observed in the cells kept in the dark, particularly from the nanoparticles made with a shorter PLA chain ([0.2$_{\mathrm{DOX}}$]NP(5)-3). This is likely due to the diffusion of Dox from the nanoparticles resulting in cell death, further exacerbated by the faster diffusion times from the nanoparticles with shorter PLA chains. Overall, selective cell death was achieved upon irradiation giving these nanoparticles great promise for applications in oncology.

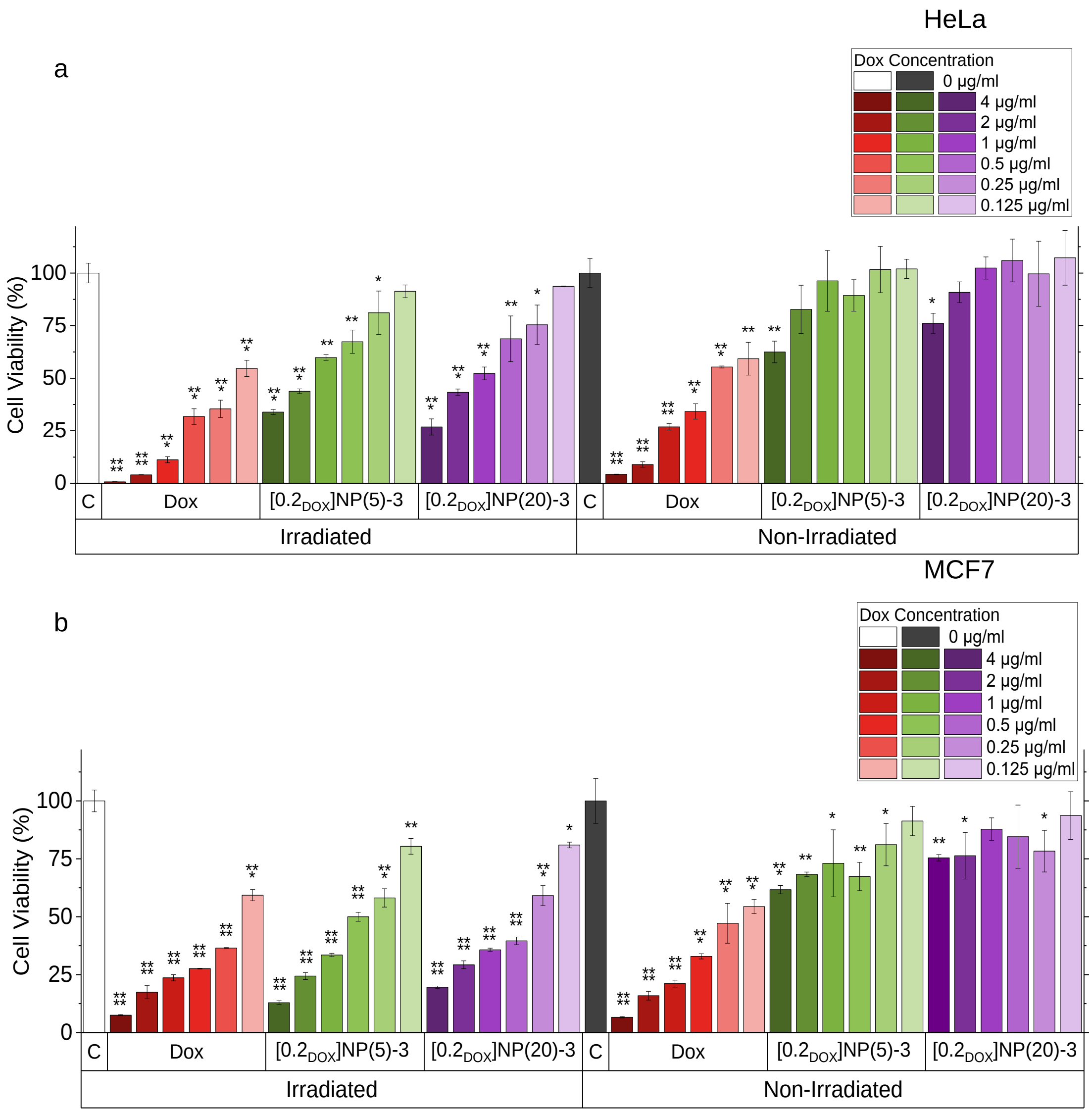

Figure 58: Cell viability (MTT assay) of control cells ‘c’, cells containing free Dox, and nanoparticles **[0.2$_{DOX}$]NP(5)-3** and **[0.2$_{DOX}$]NP(20)-3**, either after being kept in the dark or irradiated (365 nm) for 2 minutes. a) Hela Cells. b) MCF7 Cells. Values are mean ± SD, n = 3, * $p \leq 0.05$ ** = $p \leq 0.01$, *** = $p \leq 0.001$, **** = $p \leq 0.0001$

To verify the biocompatibility of the nanoparticles, an MTT assay was performed on the unloaded nanoparticles (**Figure 59**). Approximately the same concentrations of polymer were used in samples of unloaded nanoparticles as that of the Dox loaded nanoparticles (3.75 µg/ml of **NP(5)-3** and **NP(20)-3** being roughly equivalent to **[0.2DOX]NP(5)-3** and **[0.2DOX]NP(20)-3** at concentrations corresponding to 2 µg/ml Dox). The MTT assay confirmed high levels of biocompatibility of the unloaded nanoparticles, validating them as good candidates for nanoparticle formation, drug loading, drug release, and selective cell killing.

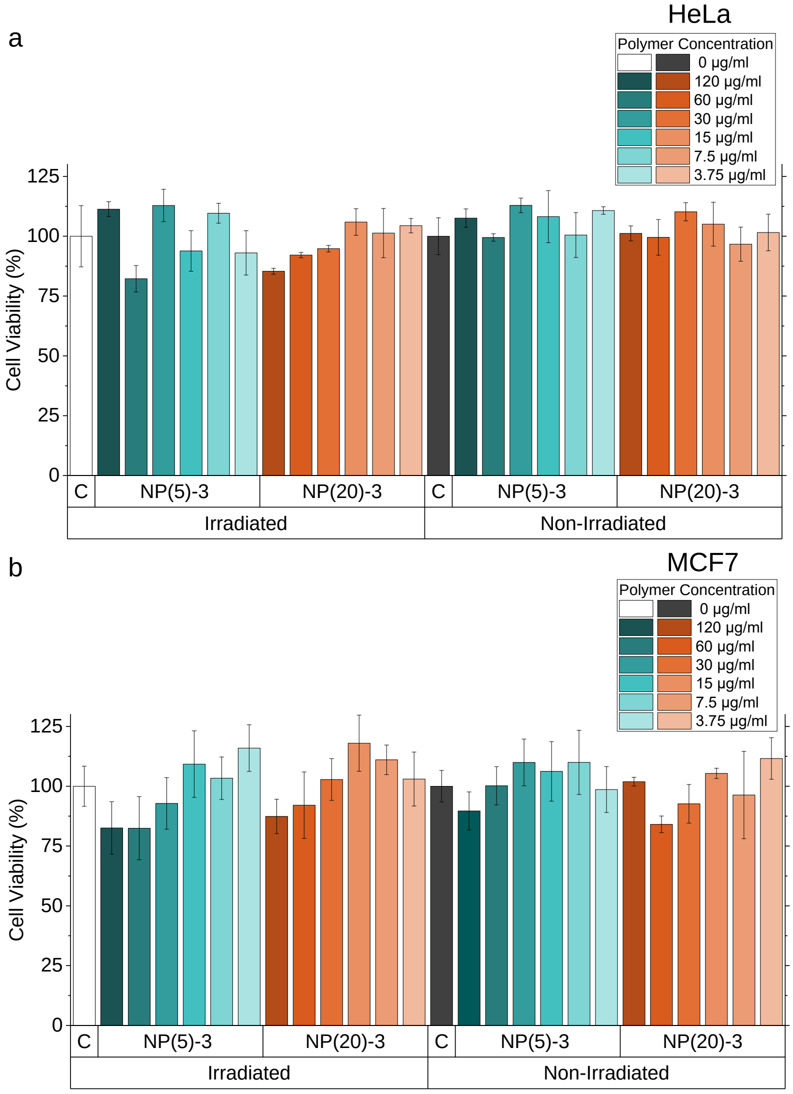

Figure 59: Cell viability confirmed by an MTT assay of control cells ‘C’, cells containing unloaded nanoparticles **NP(5)-3** and **NP(20)-3**, either after being kept in the dark or irradiated (365 nm) for 2 minutes. a) Hela Cells. b) MCF7 Cells. Values are mean ± SD, n = 3, $p > 0.05$.

5.5 Conclusion

An orthogonally difunctional coumarin was synthesised via a 4 step synthesis. The end groups of poly-L-lactides (5,000 Da and 20,000 Da Mw) were efficiently modified to yield amine-terminated polymers. The coumarin was successfully integrated between two block polymers (PEG and PLA) in a three step reaction involving click chemistry (using copper nanoparticles), *p*-nitrophenyl chloroformate activation, and the reaction with the amine terminated poly-L-lactides. Polymers were purified to yield only the diblock target. Two light sensitive diblock polymers were synthesised, **PEG5-CM-PLA5** (5 kDa PLA chain), and **PEG5-CM-PLA20** (20 kDa PLA chain). Nanoparticle synthesis methods were explored, with a water in oil in water (W/o/W) emulsion method yielding nanoparticles with low PDIs that could be collected using centrifugation. Nanoparticles were subsequently synthesised encapsulating doxorubicin hydrochloride (Dox) with drug loading efficiencies of up to 3.4 %. Light sensitivity of the polymers under 365 nm irradiation was explored using GPC in both DMF and H_2O, with a cleavage of 65 % being achieved after one minute of irradiation being achieved for **PEG5-CM-PLA20** in H_2O. Light responsive (at 365 nm) Dox release from the nanoparticles was investigated, with over 67 % of Dox being released from nanoparticles made from both polymers, after just one minute of irradiation. *In vitro* studies validated the nanoparticles light responsive selective killing efficiency in both HeLa and MCF7 cells, showing low levels of toxicity in cells kept in the dark and up to 80 % cell death in irradiated samples. Overall, the polymers provide a great tool for site-selective chemotherapy, holding great promise for light mediated drug release.

6 Summary, Conclusion, and Future Outlook

Summary

To summarise, three different novel light-responsive systems were developed to facilitate optimised drug delivery.

1. Fluorescent cell-penetrating peptide-polymers were synthesised, and their increase in cellular uptake due to the peptide length was measured and their cellular uptake route via endocytosis proven.
2. A coumarin monomer previously reported as being photo-cleavable was synthesised and its photosensitivity was disproven. Taking another approach, the coumarin monomer was conjugated to the chemotherapy agent camptothecin, making it inactive until photolytically cleaved. The monomer was integrated into water soluble polymers and then used to selectively kill cells under 365 nm irradiation.
3. A light cleavable coumarin moiety was integrated between a PEG-PLA copolymer and used to form light sensitive doxorubicin loaded nanoparticles that were used to selectively kill cells under 365 nm irradiation. Nanoparticle properties and fabrication methods were explored to optimise the system for biological applications.

Conclusion

A novel approach for measuring and comparing the cellular uptake of peptide-polymers was developed. This work includes the first report of fluorescently labelled peptide-RAFT agents, as well as demonstrating their ability to develop size-controlled polymers, with applications *in vitro*. Although previous work has shown some varieties of peptide-polymers, no report has quantifiably measured and compared the cellular uptake of different peptide-polymers conjugates. This method holds a wealth of applications with the options of developing similar systems by altering the fluorophore, peptide, and polymer to vary their application.

A report on a photo-cleavable coumarin monomer was disproven, and was instead utilised to deliver a novel, light sensitive, drug delivery polymer system to selectively kill cells. The research and validation of others' work is crucial to prevent erroneous chemistry being reported that could potentially mislead others in the field. The monomer was then used to make light-sensitive camptothecin releasing polymers that could selectively kills cells with release from along the backbone. This system could potentially be used as a therapeutic under two-photon irradiation, in which red-shifted light sources could be utilised to minimise photon-associated cell damage.

A novel photo-cleavable coumarin moiety was synthesised with orthogonal reactive groups and integrated between PEG-PLA block copolymers. This method optimised a complex coumarin to allow high yields of PEG-Coumarin-PLA light responsive polymers. By ensuring that only one coumarin per unit chain needed to be cleaved to cause the polymer to break-apart, high efficiency nanoparticle disruption could be insured with a short irradiation time. This novel synthesis approach also ensured that only simple purification needed to be performed with the solubility differences of the intermediates and by-products exploited. Polymer chain separation can often be complex but the method developed ensured that only the highly homogeneous diblocks were retrieved leading to pure and stable nanoparticled. As PEG-PLA nanoparticle systems have been FDA approved this approach provides a highly biologically compatible system for light responsive drug release that would also have applications under 2 photon irradiation.

Future Outlook

The work developed conjugation of both a peptide and fluorophore to a RAFT agent for the first time and the scope of future work is vast with applications of comparing and exploiting the influence of peptides on polymer cellular localisation and behaviour. The fluorophore could be modified to be more red-shifted in fluorescence to avoid the auto-fluorescence effects of biological tissues. An environmental fluorophore could also be substituted to have ‘switch-on’ fluorescence when the polymer enters the cellular membrane environment. The peptide could be varied to optimise intra-cellular localisation, such as nuclear targeting, or could be used to target specific cell types (e.g. RGD for cancer cells). Monomer selection could also give rise to morphology changes, toxicity, or facilitating enhanced cargo delivery.

Moving forward from the coumarin that was not light sensitive under the reported conditions, research can continue to be performed with this in mind. As the monomer synthesised was not light sensitive, it would not result in the backbone of a polymer degrading and further systems could be developed in which this would be an advantage. Light sensitive cargo releasing polymer systems could be developed using the coumarin monomer within polymers with the backbone remaining stable under irradiation, while the photoactive 4 position being utilised for cargo attachment. This could potentially be useful in biological implants and agriculture.

The light sensitive PEG-Coumarin-PLA nanoparticles hold great promise biologically. To improve these further, higher drug loading percentages in this system could be used to improve biological efficiency. As doxorubicin has a low binding efficiency with PLA, other chemotherapy agents could be used. The two photon cleavage of the nanoparticles could also be explored. This would provide the first report of two photon cleavage of drug loaded PEG-PLA nanoparticles that could hold great promise for *in vivo* applications.

7 References

1. A. Mullard, *Nat. Rev. Drug Discov.*, 2023, **22**, 83-88.
2. H. Sung, J. Ferlay, R. L. Siegel, M. Laversanne, I. Soerjomataram, A. Jemal and F. Bray, *CA Cancer J. Clin.*, 2021, **71**, 209-249.
3. M. E. O'Brien, A. Borthwick, A. Rigg, A. Leary, L. Assersohn, K. Last, S. Tan, S. Milan, D. Tait and I. E. Smith, *Br. J. Cancer*, 2006, **95**, 1632-1636.
4. R. J. Young and P. A. Lovell, *Introduction to polymers*, CRC press, Boca Raton, 2011.
5. M. Danaei, M. Dehghankhold, S. Ataei, F. Hasanzadeh Davarani, R. Javanmard, A. Dokhani, S. Khorasani and M. R. Mozafari, *Pharmaceutics*, 2018, **10**.
6. Y. Liu, Z. Wang and X. Zhang, *Chem. Soc. Rev.*, 2012, **41**, 5922-5932.
7. D. Braun, H. Cherdron, M. Rehahn, H. Ritter and B. Voit, *Polymer synthesis: Theory and practice: Fundamentals, methods, experiments*, 2005.
8. M. Zhang, S. M. June and T. E. Long, in *Polymer Science: A Comprehensive Reference*, eds. K. Matyjaszewski and M. Möller, Elsevier, Amsterdam, 2012, DOI: 10.1016/B978-0-444-53349-4.00131-X, pp. 7-47.
9. S. Ito, *Polym. J.*, 2016, **48**, 667-677.
10. S. Perrier, *Macromolecules*, 2017, **50**, 7433-7447.
11. P. Kumar, Y. S. Lakshmi, B. C, K. Golla and A. K. Kondapi, *PLoS One*, 2015, **10**, e0140399.
12. D. Pooja, H. Kulhari, M. Kuncha, S. S. Rachamalla, D. J. Adams, V. Bansal and R. Sistla, *Mol. Pharm.*, 2016, **13**, 3903-3912.
13. B. Begines, T. Ortiz, M. Pérez-Aranda, G. Martínez, M. Merinero, F. Argüelles-Arias and A. Alcudia, *Nanomaterials (Basel)*, 2020, **10**.
14. M. Hashida, *J. Control Release*, 2022, **346**, 355-357.
15. J. Lefley, C. Waldron and C. R. Becer, *Polym. Chem.*, 2020, **11**, 7124-7136.
16. P. Kesharwani, K. Jain and N. K. Jain, *Prog. Polym. Sci.*, 2014, **39**, 268-307.
17. A. Figueiras, C. Domingues, I. Jarak, A. I. Santos, A. Parra, A. Pais, C. Alvarez-Lorenzo, A. Concheiro, A. Kabanov, H. Cabral and F. Veiga, *Pharmaceutics*, 2022, **14**.
18. A. Shariff, S. Hajar, W. A. Khodir, W. Khartini, A. Hamid, S. Haris, M. S. Ismail and M. Wafiuddin, *Polymers*, 2022, **14**, 4847.
19. T. Casalini, F. Rossi, A. Castrovinci and G. Perale, *Front. Bioeng. Biotechnol.*, 2019, **7**.
20. M. Szczęch and K. Szczepanowicz, *Nanomater.*, 2020, **10**, 496.
21. J. A. Loureiro and M. C. Pereira, *Pharmaceutics*, 2020, **12**.
22. K. Priyadharsini, M. Anbuchezhiyan, N. Senguttuvan and S. Rajendran, *Mater. Technol.*, 2022, **37**, 992-1000.
23. Y. Yi, G. Lin, S. Chen, J. Liu, H. Zhang and P. Mi, *Mat. Sci. Eng. C*, 2018, **83**, 218-232.
24. J. Wang, S. Li, Y. Han, J. Guan, S. Chung, C. Wang and D. Li, *Front. Pharmacol.*, 2018, **9**, 202.
25. M. Meunier, A. Goupil and P. Lienard, *Int. J. Pharm.*, 2017, **526**, 157-166.
26. F. Qiu, T. Meng, Q. Chen, K. Zhou, Y. Shao, G. Matlock, X. Ma, W. Wu, Y. Du, X. Wang, G. Deng, J. Ma and Q. Xu, *Mol. Pharm.*, 2019, **16**, 1958-1970.
27. N. Avramović, B. Mandić, A. Savić-Radojević and T. Simić, *Pharmaceutics*, 2020, **12**, 298.

28. C. Günday, S. Anand, H. B. Gencer, S. Munafò, L. Moroni, A. Fusco, G. Donnarumma, C. Ricci, P. C. Hatir, N. G. Türeli, A. E. Türeli, C. Mota and S. Danti, *Drug Deliv. and Transl. Res.*, 2020, **10**, 706-720.
29. M. Esfandyari-Manesh, B. Darvishi, F. A. Ishkuh, E. Shahmoradi, A. Mohammadi, M. Javanbakht, R. Dinarvand and F. Atyabi, *Mater. Sci. Eng. C.*, 2016, **62**, 626-633.
30. H. Sun, Y. Dong, J. Feijen and Z. Zhong, *J. Control. Release*, 2018, **290**, 11-27.
31. S. Wu, F. Wu and X. Chen, *Adv. Mater.*, 2022, **34**, 2109210.
32. M. Dessale, G. Mengistu and H. M. Mengist, *Int. J. Nanomedicine*, 2022, **17**, 3735-3749.
33. Y. Yao, Y. Zhou, L. Liu, Y. Xu, Q. Chen, Y. Wang, S. Wu, Y. Deng, J. Zhang and A. Shao, *Front. Mol. Biosci.*, 2020, **7**.
34. M. J. Mitchell, M. M. Billingsley, R. M. Haley, M. E. Wechsler, N. A. Peppas and R. Langer, *Nat. Rev. Drug Discov.*, 2021, **20**, 101-124.
35. T. Ji and D. S. Kohane, *Nano Today*, 2019, **28**.
36. X. Lin, J. Wu, Y. Liu, N. Lin, J. Hu and B. Zhang, *Molecules*, 2022, **27**.
37. A. N. Bashkatov, E. A. Genina, V. I. Kochubey and V. V. Tuchin, *J. Phys. D.*, 2005, **38**, 2543.
38. P. A. Shaw, E. Forsyth, F. Haseeb, S. Yang, M. Bradley and M. Klausen, *Front. Chem.*, 2022, **10**, 921354.
39. T. Schweizer, H. Kubach and T. Koch, *Int. J. Automot. Technol.*, 2021, **6**, 1-13.
40. M. Y. Berezin and S. Achilefu, *Chem. Rev.*, 2010, **110**, 2641-2684.
41. V. I. Martynov, A. A. Pakhomov, N. V. Popova, I. E. Deyev and A. G. Petrenko, *Acta Nat.*, 2016, **8**, 33-46.
42. P. Klán, T. Šolomek, C. G. Bochet, A. Blanc, R. Givens, M. Rubina, V. Popik, A. Kostikov and J. Wirz, *Chem. Rev.*, 2013, **113**, 119-191.
43. R. B. Mujumdar, L. A. Ernst, S. R. Mujumdar, C. J. Lewis and A. S. Waggoner, *Bioconjug. Chem.*, 1993, **4**, 105-111.
44. J. R. Lakowicz, *Principles of Fluorescence Spectroscopy*, Springer Science + Business Media, LLC, New York, USA, 3 edn., 2006.
45. D. Magde, G. E. Rojas and P. G. Seybold, *Photochemistry and Photobiology*, 1999, **70**, 737-744.
46. M. Klausen and M. Blanchard-Desce, *J. Photochem. Photobiol. C*, 2021, **48**, 100423.
47. J. Chen, L. Liu, S. M. Motevalli, X. Wu, X. Yang, X. Li, L. Han, A. Magrini, W. Guo, J. Chang, M. Bottini and X. Liang, *Adv. Funct. Mater.*, 2018, **28**, 1707291.
48. M. M. Mahmoodi, D. Abate-Pella, T. J. Pundsack, C. C. Palsuledesai, P. C. Goff, D. A. Blank and M. D. Distefano, *J. Am. Chem. Soc.*, 2016, **138**, 5848-5859.
49. C. T. Huynh, M. K. Nguyen, G. Y. Tonga, L. Longé, V. M. Rotello and E. Alsberg, *Adv. Healthc. Mater.*, 2016, **5**, 305-310.
50. R. E. Kohman, S. S. Cha, H. Man and X. Han, *Nano Lett.*, 2016, **16**, 2781-2785.
51. L. Yang, H. Sun, Y. Liu, W. Hou, Y. Yang, R. Cai, C. Cui, P. Zhang, X. Pan, X. Li, L. Li, B. S. Sumerlin and W. Tan, *Angew. Chem. Int. Ed. Engl.*, 2018, **57**, 17048-17052.
52. Q. Lin, Q. Huang, C. Li, C. Bao, Z. Liu, F. Li and L. Zhu, *J. Am. Chem. Soc.*, 2010, **132**, 10645-10647.
53. S. S. Agasti, A. Chompoosor, C. C. You, P. Ghosh, C. K. Kim and V. M. Rotello, *J. Am. Chem. Soc.*, 2009, **131**, 5728-5729.

54. Y. Chien, Y. Chou, S. Wang, S. Hung, M. Liau, Y. Chao, C. Su and C. Yeh, *ACS Nano*, 2013, **7**, 8516-8528.
55. T. A. Theodossiou, A. R. Gonçalves, K. Yannakopoulou, E. Skarpen and K. Berg, *Angew. Chem. Int. Ed.*, 2015, **54**, 4885-4889.
56. X. Tan, B. B. Li, X. Lu, F. Jia, C. Santori, P. Menon, H. Li, B. Zhang, J. J. Zhao and K. Zhang, *J. Am. Chem. Soc.*, 2015, **137**, 6112-6115.
57. A. Brion, J. Chaud, J. Léonard, F. Bolze, S. Chassaing, B. Frisch, B. Heurtault, A. Kichler and A. Specht, *Adv. Healthc. Mater.*, 2023, **12**, 2201474.
58. Y. Dai, H. Sun, S. Pal, Y. Zhang, S. Park, C. P. Kabb, W. D. Wei and B. S. Sumerlin, *Chem. Sci.*, 2017, **8**, 1815-1821.
59. X. Wei, L. Liu, X. Guo, Y. Wang, J. Zhao and S. Zhou, *ACS Appl. Mater. Interfaces*, 2018, **10**, 17672-17684.
60. S. Uthaman, S. Pillarisetti, A. P. Mathew, Y. Kim, W. K. Bae, K. M. Huh and I. K. Park, *Biomaterials*, 2020, **232**, 119702.
61. Y. Lyu, S. He, J. Li, Y. Jiang, H. Sun, Y. Miao and K. Pu, *Angew. Chem. Int. Ed. Engl.*, 2019, **58**, 18197-18201.
62. J. Chiefari, Y. K. Chong, F. Ercole, J. Krstina, J. Jeffery, T. P. T. Le, R. T. A. Mayadunne, G. F. Meijs, C. L. Moad, G. Moad, E. Rizzardo and S. H. Thang, *Macromolecules*, 1998, **31**, 5559-5562.
63. R. T. A. Mayadunne, E. Rizzardo, J. Chiefari, Y. K. Chong, G. Moad and S. H. Thang, *Macromolecules*, 1999, **32**, 6977-6980.
64. R. T. A. Mayadunne, E. Rizzardo, J. Chiefari, J. Krstina, G. Moad, A. Postma and S. H. Thang, *Macromolecules*, 2000, **33**, 243-245.
65. R. Francis and A. Ajayaghosh, *Macromolecules*, 2000, **33**, 4699-4704.
66. R. Duncan, M. J. Vicent, F. Greco and R. I. Nicholson, *Endocr. Relat. Cancer*, 2005, **12**.
67. H. Derakhshankhah and S. Jafari, *Biomed. Pharmacother.*, 2018, **108**, 1090-1096.
68. L. E. Yandek, A. Pokorny, A. Florén, K. Knoelke, U. Langel and P. F. Almeida, *Biophysical journal*, 2007, **92**, 2434-2444.
69. D. Derossi, A. H. Joliot, G. Chassaing and A. Prochiantz, *J. Biol. Chem.*, 1994, **269**, 10444-10450.
70. A. D. Frankel and C. O. Pabo, *Cell*, 1988, **55**, 1189-1193.
71. C. Borri, S. Centi, F. Ratto and R. Pini, *J. Nanobiotechnology*, 2018, **16**, 50.
72. D. Joubert, J. van Zyl, A. Hawtrey and M. Ariatti, *Drug Deliv.*, 2003, **10**, 209-211.
73. S. Manouchehri, P. Zarrintaj, M. R. Saeb and J. D. Ramsey, *Mol. Pharm.*, 2021, **18**, 3652-3670.
74. B. Movafegh, R. Jalal, Z. Mohammadi and S. A. Aldaghi, *Anticancer Agents Med. Chem.*, 2018, **18**, 1448-1456.
75. M. A. Gauthier and H. Klok, *Chem. Commun.*, 2008, **23**, 2591-2611.
76. J. Shu, B. Panganiban and T. Xu, *Annu. Rev. Phys. Chem.*, 2013, **64**.
77. E. W. Neuse, *Met. Based Drugs*, 2008, **2008**, 469531.
78. D. Gundel, M. Allmeroth, S. Reime, R. Zentel and O. Thews, *Int. J. Nanomedicine*, 2017, **12**, 5571-5584.
79. Z. Jiang, H. He, H. Liu and S. Thayumanavan, *Biomacromolecules*, 2019, **20**, 4407-4418.
80. J. M. Rios De La Rosa, A. Spadea, R. Donno, E. Lallana, Y. Lu, S. Puri, P. Caswell, M. J. Lawrence, M. Ashford and N. Tirelli, *Sci. Rep.*, 2020, **10**, 14505.

81. J. D. Simpson, G. R. Ediriweera, C. B. Howard, N. L. Fletcher, C. A. Bell and K. J. Thurecht, *Biomater. Sci.*, 2019, **7**, 4661-4674.
82. Y. Zhang, A. Gambardella, M. Üçüncü, J. Geng, J. Clavadetscher, M. Bradley and A. Lilienkampf, *Chem. Commun.*, 2020, **56**, 13856-13859.
83. Y. Shamay, L. Shpirt, G. Ashkenasy and A. David, *Pharm. Res.*, 2014, **31**, 768-779.
84. M. Cavaco, C. Perez-Peinado, J. Valle, R. D. M. Silva, J. D. G. Correia, D. Andreu, M. Castanho and V. Neves, *Front. Bioeng. Biotechnol.*, 2020, **8**, 552035.
85. Z. Kadlecova, L. Baldi, D. Hacker, F. M. Wurm and H. A. Klok, *Biomacromolecules*, 2012, **13**, 3127-3137.
86. E. Kaiser, R. L. Colescott, C. D. Bossinger and P. I. Cook, *Anal. Biochem.*, 1970, **34**, 595-598.
87. J. J. Diaz-Mochon, L. Bialy and M. Bradley, *Org. Lett.*, 2004, **6**, 1127-1129.
88. S. Zhang, Y. Zhang, M. Üçüncü, A. Lilienkampf, J. Geng and M. Bradley, *Polymer*, 2021, **226**, 123840.
89. J. Masternak, M. Zienkiewicz-Machnik, I. Łakomska, M. Hodorowicz, K. Kazimierczuk, M. Nosek, A. Majkowska-Młynarczyk, J. Wietrzyk and B. Barszcz, *Int. J. Mol. Sci.*, 2021, **22**, 7286.
90. P. Relógio, M. Charreyre, J. S. Farinha, J. G. Martinho and C. Pichot, *Polymer*, 2004, **45**, 8639-8649.
91. H. Maeda, H. Nakamura and J. Fang, *Adv. Drug Deliv. Rev.*, 2013, **65**, 71-79.
92. R. Wolfgang, *The Column*, 2018, **14**, 9-12.
93. G. Amy, M. R. Collins, C. J. Kuo and P. H. King, *J. Am. Water Works Assoc.*, 1987, **79**, 43-49.
94. D. Held, *Journal*, 2020, 1-12.
95. H. J.-P. Ryser and W. Shen, in *Targeting of Drugs With Synthetic Systems*, eds. G. Gregoriadis, J. Senior and G. Poste, Springer US, Boston, MA, 1986, DOI: 10.1007/978-1-4684-5185-6_9, pp. 103-121.
96. T. Furuta, S. S.-H. Wang, J. L. Dantzker, T. M. Dore, W. J. Bybee, E. M. Callaway, W. Denk and R. Y. Tsien, *Proc. Natl. Acad. Sci.*, 1999, **96**, 1193-1200.
97. B. Couturaud, T. Stefanello, D. Fournier, M. Sliwa, A. Szarpack-Jankowska, R. Auzély-Velty and P. Woisel, *Polym. Chem.*, 2017, **8**, 4512-4519.
98. R. Schmidt, D. Geissler, V. Hagen and J. Bendig, *J. Phys. Chem. A*, 2007, **111**, 5768-5774.
99. J. O’Leary and F. M. Muggia, *Eur. J. Cancer*, 1998, **34**, 1500-1508.
100. A. Zare-Mirakabadi, A. Sarzaeem, S. Moradhaseli, A. Sayad and M. Negahdary, *Iran J. Cancer Prev.*, 2012, **5**, 109-116.
101. S. Mahey, R. Kumar, R. Arora, J. Mahajan, S. Arora, R. Bhardwaj and A. K. Thukral, *SpringerPlus*, 2016, **5**, 930.
102. J. Geng, C. Sun, J. Liu, L. D. Liao, Y. Yuan, N. Thakor, J. Wang and B. Liu, *Small*, 2015, **11**, 1603-1610.
103. A. Chen, S. A. Mercado and N. K. Slater, *Adv. Mat. Sci.*, 2017, **2**.
104. A. Z. Suzuki, Y. Shiraishi, H. Aoki, H. Sasaki, R. Watahiki and T. Furuta, *J. Vis. Exp.*, 2019, DOI: 10.3791/60021.
105. A. Mokhtarzadeh, A. Alibakhshi, H. Yaghoobi, M. Hashemi, M. Hejazi and M. Ramezani, *Expert Opin. Biol. Ther.*, 2016, **16**, 771-785.
106. A. Wadhawan, J. Singh, H. Sharma, S. Handa, G. Singh, R. Kumar, R. P. Barnwal, I. Pal Kaur and M. Chatterjee, *ACS Omega*, 2022, **7**, 5231-5241.

107. L. Tomar, C. Tyagi, M. Kumar, P. Kumar, H. Singh, Y. E. Choonara and V. Pillay, *Int. J. Nanomedicine*, 2013, **8**, 505-520.
108. S. Singh, V. V. Begoyan, M. Tanasova, K. Waters, M. Seel and R. Pandey, *J. Phys. Org. Chem.*, 2018, **31**, e3852.
109. J. P. Olson, H. B. Kwon, K. T. Takasaki, C. Q. Chiu, M. J. Higley, B. L. Sabatini and G. C. Ellis-Davies, *J. Am. Chem. Soc.*, 2013, **135**, 5954-5957.
110. M. Kumar, D. Gupta, G. Singh, S. Sharma, M. Bhat, C. K. Prashant, A. K. Dinda, S. Kharbanda, D. Kufe and H. Singh, *Cancer Res.*, 2014, **74**, 3271-3281.
111. E. D. Pressly, R. J. Amir and C. J. Hawker, *J. Polym. Sci. A*, 2011, **49**, 814-819.
112. P. J. Flory, *J. Am. Chem. Soc.*, 1939, **61**, 3334-3340.
113. G. Bovone, F. Steiner, E. A. Guzzi and M. W. Tibbitt, *Front. in Bioeng. Biotechnol.*, 2019, **7**.
114. A. K. Jain, A. S. Massey, H. Yusuf, D. McDonald, H. O. McCarthy and V. L. Kett, *Int. J. Nanomedicine*, 2015, **10**, 7183 - 7196.
115. R. Ghasemi, M. Abdollahi, E. Emamgholi Zadeh, K. Khodabakhshi, A. Badeli, H. Bagheri and S. Hosseinkhani, *Sci. Rep.*, 2018, **8**, 9854.
116. N. G. Sedush, Y. A. Kadina, E. V. Razuvaeva, A. A. Puchkov, E. M. Shirokova, V. I. Gomzyak, K. T. Kalinin, A. I. Kulebyakina and S. N. Chvalun, *Nanotechnol. Russia*, 2021, **16**, 421-438.
117. Q. Shuai, Y. Cai, G. Zhao and X. Sun, *Int. J. Mol. Sci.*, 2020, **21**.
118. Z. L. Yang, X. R. Li, K. W. Yang and Y. Liu, *J. Biomed. Mater. Res. A*, 2008, **85**, 539-546.
119. S. Shahrad, M. Rajabi, H. Javadi, A. A. Karimi Zarchi and M. H. Darvishi, *Sci. Rep.*, 2022, **12**, 4718.
120. C. G. Dariva, J. P. H. Figueiredo, C. Ferreira, M. Laranjo, M. F. Botelho, A. C. Fonseca, J. F. J. Coelho and A. C. Serra, *Colloids Surf. B*, 2020, **196**, 111354.
121. T. Hiramatsu, L. A. Terry, T. Kadono and T. Kawano, *Adv. Hortic. Sci.*, 2014, **28**, 133-140.
122. M. Montalti, A. Credi, L. Prodi, M. Teresa, G. Credi, A. Prodi, L. Gandolfi and M. Teresa, *Handbook of Photochemistry*, CRC Press, Boca Raton, 3rd Edition edn., 2006.

8 Experimental

8.1 General

Amino acids and the aminomethyl polystyrene resin were purchased from GL Biochem (Shanghai) Ltd and NovaBiochem, cell culture reagents from Sigma Aldrich, Corning, Life Techology and Thermo Fisher. Culture-Insert 2 Well µ-Dishes were obtained from Ibidi. PEG-alkene was purchased from Rapp Polymere. Quartz cuvettes were purchased from Hellma Analytics. All other chemicals were purchased from Sigma Aldrich and Merck. AIBN was recrystallised in MeOH and dimethyl acrylamide (DMA) was filtered through a plug of basic alumina to remove inhibitors prior to use.

Microwave reactions were performed in a Biotage® Initiator + microwave with Robot Sixty. ^{1}H and ^{13}C NMR spectra were recorded on a Bruker AVA-500 (at 500 and 125 MHz, respectively) or a Bruker AVA600 spectrometer (600 and 150 MHz, respectively) at 298 K in the deuterated solvents indicated. Shifts (δ) are given in parts per million (ppm) with respect to the residual peak of the non-deuterated solvent and coupling constant (J) are given in Hertz. Analytical HPLC was performed on an Agilent Technologies 1100 modular HPLC system coupled to a multiwavelength and PLELSD-1000 detector and equipped with a Phenomenex Kinetex® 5µm XB-C18 100 Å column (50 × 4.6 mm). Samples were eluted with a gradient of H_2O/MeCN (buffered with 0.1% formic acid) from 95/5 to 5/95, over 6 min, then holding at 95% for 3 min, followed by elution at 5% MeCN for 1 min. Preparative RP–HPLC was performed on an Agilent 1100 system equipped with a Kinetex XB-C18 column (150 × 21.2 mm, 5 µm) with a flow rate of 10 ml/min and eluting with a gradient of H_2O/MeOH (buffered with 0.1% TFA) from 50/50 to 10/90 over 30 min. GPC was performed on an Agilent 1100 GPC equipped with PLgel MIXED-C columns (2 × 102 – 2 × 106 g/mol, 5 mm) and an RI detector, eluting with DMF containing 0.1 % w/v LiBr at 60 °C and a flow rate of 1 ml/min. Electrospray ionisation mass spectrometry (ESI–MS) analyses were carried out on an Agilent Technologies LC/MSD Series 1100 quadrupole mass spectrometer (QMS) in ESI mode. MALDI-ToF mass spectra were obtained with a Bruker UltraflexExtreme MALDI TOF/TOF instrument and analysed with Bruker Daltonics flexAnalysis software with a matrix solution of sinapic acid (10 mg/ml) in H_2O/CH3CN/TFA (50/50/0.1). The absorbance and fluorescence of 96-well plates was read on a BioTek HT Synergy multimode reader at 570 nm using the Microplate manager 4.0 software. Irradiation experiments were performed using a 95-0228-02 - Long Range UV, 365 nm - UVP Crosslinker by Analytik JENA 365 ± 35 nm, 5 x 8W, 2 mW cm^{-2}. . Absorbance spectrometry was performed on an Agilent 8453 absorbance spectrometer and fluorescence spectrometry was performed on a Shimadzu RF-6000. Transmission Electron Microscope (TEM) analysis was conducted on a JEOL JEM-1400 Plus and representative images were processed using Image J. Flow cytometry analysis was carried out on a Becton Dickinson (BD) FACSAriaTM and data was analysed using FlowJo. Confocal images were taken on a Leica SP5 confocal microscope and Zeiss 510 Meta software was used for digital acquisition. HeLa and MCF7 cells were imaged using a 10x objective (Leica fluorescence microscope) under brightfield.

8.2 Functional Molecules

Control RAFT (**7**)

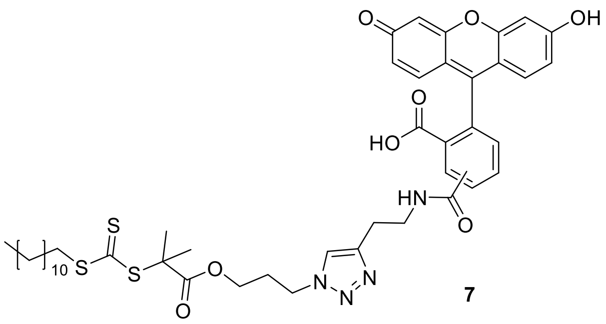

7

5,6-carboxyfluorecin (**4**) (100 mg, 0.026 mmol) and Oxyma (45 mg, 0.32 mmol) were dissolved in DMF (4 ml) and stirred for 10 min. DCC (65 mg, 0.32 mmol) was added and the mixture was stirred for 1 min. Propargylamine (44mg, 0.79 mmol) in DMF (1 ml) was slowly added and the reaction mixture was stirred at 45 °C for 4 hours (monitored by TLC). The mixture was filtered, concentrated *in vacuo* and purified by reverse phase column chromatography eluting with ACN/H_2O to give 5,6-CF-alkyne **5** as a yellow solid (70mg (60% yield)). 2-(Dodecylthiocharbonothioylthio)-2-metylpropionic acid 3-azido-1-propanol ester **6** (145.8mg, 0.326 mmol, 1.1 equiv) and **5** (122.4 mg, 0.30mmol, 1 equiv.) were dissolved in DMF (9 ml) under nitrogen. CuI (11.4 mg, 0.06 mmol) was added and the reaction mixture was stirred at 50 °C for 4 hours (monitored by TLC). The reaction mixture was centrifuged to remove excess CuI, cooled to room temperature and concentrated *in vacuo*, and the residue purified by reverse phase column chromatography with ACN/H_2O (10-100%).

Yield 27% (62 mg, orange solid). **^{1}H NMR (500 MHz, MeOD) δ (ppm)** 8.48 (s, 0.5H), 8.24 (dd, *J* = 8.0, 1.6 Hz, 0.5H), 8.16 (dd, *J* = 8.0, 1.4 Hz, 0.5H), 8.08 (d, *J* = 8.0 Hz, 0.5H), 7.92 (s, 0.5H), 7.80 (s, 0.5H), 7.68 (d, *J* = 1.4 Hz, 0.5H), 7.30 (d, *J* = 8.0 Hz, 0.5H), 6.69 (t, *J* = 2.5 Hz, 2H), 6.61 (t, *J* = 8.9 Hz, 2H), 6.53 (dt, *J* = 8.7, 2.6 Hz, 2H), 4.70 (s, 1H), 4.57 (s, 1H), 4.46 (t, *J* = 6.8 Hz, 1H), 4.38 (t, *J* = 6.9 Hz, 1H), 4.10 (t, *J* = 5.9 Hz, 1H), 4.05 (t, *J* = 5.9 Hz, 1H), 3.22 (t, *J* = 7.4 Hz, 1H), 2.25 (t, *J* = 6.3 Hz, 1H), 1.65 (s, 3H), 1.62 (s, 3H), 1.39 – 1.11 (m, 18H), 0.93 – 0.85 (m, 3H). **^{13}C**

NMR (126 MHz, MeOD) δ (ppm) 224.0, 223.90, 174.2, 174.1, 170.5, 168.1, 154.0, 142.0, 137.5, 135.6, 130.4, 130.3, 130.1, 126.1, 125.7, 124.3, 113.6, 110.8, 103.6, 79.5, 79.3, 79.0, 68.1, 66.9, 63.9, 63.8, 57.8, 57.6, 57.5, 57.3, 57.1, 57.0, 49.9, 37.71, 37.68, 36.5, 36.3, 33.1, 30.7, 30.62, 30.60, 30.49, 30.48, 30.45, 30.2, 30.13, 30.11, 30.09, 29.80, 29.78, 29.12, 29.07, 25.70, 25.68, 23.7, 17.6, 17.4, 17.3, 17.1, 17.0, 15.4, 14.5. **LCMS (ESI)** *m/z* 861.2 $(M-H)^-$. **Analytical HPLC** (220 nm) t_R 7.938 min, >99% purity.

1-((2-aminoethyl)amino)-2-methyl-1-oxopropan-2-yl dodecyl carbonotrithioate hydrochloride (**8**)

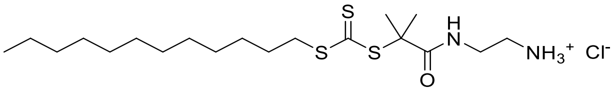

8

DDMAT (100 mg, 0.27 mmol, 1 equiv.) and Oxyma (45 mg, 0.32 mmol, 1.2 equiv.) were dissolved in DMF (4 ml) and stirred for 10 min. EDC (61 mg, 0.32 mmol, 1.2 equiv.) was added and the mixture was stirred for 1 min. *N*-Boc-1,2-diaminoethane (62 mg, 61.7 µL, 0.39 mmol, 1.4 equiv.) in DMF (1 ml) was slowly added and the reaction mixture was stirred at 45°C for 4 h. The mixture was then concentrated under reduced pressure. The residue was dissolved in Et_2O (20 ml), then washed with an aqueous solution of $NaHCO_3$ (3 × 15 ml) and with H_2O (3 × 15 ml). The organic layer was dried with $MgSO_4$, filtered and evaporated *in vacuo*. The Boc group was directly removed by dissolving the product in a solution of HCl in Et_2O (2M, 4ml) and stirring at r.t. for 24 h. The resulting precipitate was collected by filtration, washed with Et_2O, and air dried to give **5** as a light yellow solid.

Yield 78% (85 mg, light yellow powder). **^{1}H NMR (500 MHz, MeOD) δ (ppm)** 3.42 (t, *J* = 6.4 Hz, 2H), 3.33 (t, *J* = 7.4 Hz, 2H), 3.03 (t, J = 6.3 Hz, 2H), 1.68 (s, 7H), 1.72 – 1.62 (m, 2H), 1.45 – 1.22 (m, 18H), 0.90 (t, *J* = 6.9 Hz, 3H).; **^{13}C NMR (126 MHz,**

MeOD) δ (ppm) 223.7, 176.6, 57.8, 40.6, 39.1, 37.7, 33.1, 30.73, 30.65, 30.6, 30.5, 30.2, 29.9, 29.1, 25.9, 23.7, 14.4. **LCMS** *m/z* 407.2 $(M\text{-}H)^-$. **Analytical HPLC** (220 nm) t_R 5.237 min, >99% purity.

0-Lys-CF-RAFT (**9**)

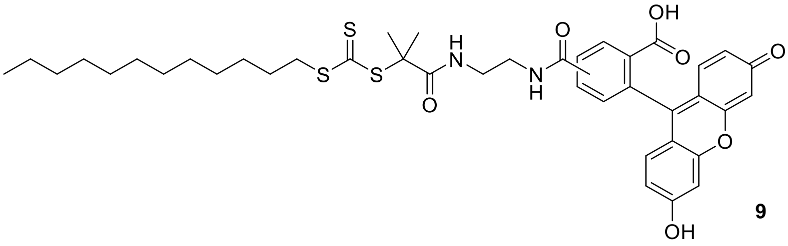

9

5,6-carboxyfluorescein (**CF**) (100 mg, 0.266 mmol, 1.1 equiv.) and Oxyma (45 mg, 0.32 mmol, 1.2 equiv.) were dissolved in DMF (4 ml) and stirred for 10 min. EDC (65 mg, 0.32 mmol, 1.2 equiv.) was added and the mixture was stirred for 1 min. A solution of **6** (90 mg, 0.22 mmol, 1 equiv.) and DIPEA (76.6 µL, 0.44 mmol, 2 equiv.) in DMF (1 ml) (previously stirred for 15 min) was slowly added and the reaction mixture was stirred at 45 °C for 4 h (monitored by TLC, eluting with DCM:MeOH, 9/1). The mixture was filtered then evaporated under reduced pressure. The residue was dissolved in EtOAc (20 ml), then and washed with H_2O (6 × 10 ml). The organic layer was dried with $MgSO_4$, filtered and dried *in vacuo*. The crude product was purified by flash column chromatography (gradient eluent: DCM/MeOH, 99:1 to 80:20), yielding **9** as a yellow solid.

Yield 16% (32 mg, orange solid). **^{1}H NMR (500 MHz, MeOD) δ (ppm)** 8.44 – 8.39 (m, 0.5H, *isomer 5*), 8.18 (dd, *J* = 8.0, 1.6 Hz, 0.5H, *isomer 5*), 8.12 (dd, *J* = 8.0, 1.4 Hz, 0.5H, *isomer 6*), 8.10 – 8.05 (m, 0.5H, *isomer 6*), 7.62 (d, *J* = 1.3 Hz, 0.5H, *isomer 6*), 7.29 (d, *J* = 8.0 Hz, 0.5H, *isomer 5*), 6.72 – 6.67 (m, 2H), 6.61 (t, *J* = 8.8 Hz, 2H), 6.54 (dt, *J* = 8.7, 2.5 Hz, 2H), 3.59 – 3.52 (m, 1H, *isomer 5*), 3.49 – 3.43 (m, 1H, *isomer 5*), 3.43 – 3.39 (m, 1H, *isomer 6*), 3.37 – 3.33 (m, 1H, *isomer 6*), 3.19 – 3.13 (m, 1H, *isomer 5*), 3.13 – 3.06 (m, 1H, *isomer 6*), 1.68 (s, 3H, *isomer 5*), 1.58 – 1.50 (m, 2H), 1.54 (s, 3H, *isomer 6*), 1.33 – 1.21 (m, 18H), 0.94 – 0.87 (m, 3H).

^{13}C NMR (126 MHz, MeOD) δ (ppm) 223.0, 222.7, 175.9, 175.71, 175.68, 175.2, 173.0, 170.6, 168.7, 168.4, 162.2, 154.3, 154.2, 141.8, 140.2, 139.3, 137.6, 135.7, 135.3, 130.9, 130.42, 130.35, 130.2, 127.09, 127.05, 126.4, 125.9, 125.5, 125.2, 124.5, 116.5, 114.2, 111.2, 111.0, 103.7, 57.9, 57.7, 41.3, 40.9, 40.8, 37.7, 37.6, 33.1, 30.9, 30.7, 30.63, 30.62, 30.51, 30.45, 30.4, 30.14, 30.09, 29.93, 29.88, 29.8, 29.7, 29.6, 29.03, 28.99, 26.10, 26.07, 26.0, 23.7, 18.4, 17.4, 17.3, 17.1, 14.5. **HRMS (ESI)** *m/z* 765.2721, calculated for $C_{40}H_{48}N_2O_7S_3$ $(M+H)^+$ 765.2696. **Analytical HPLC** (254 nm) t_R 6.177 min, 95% purity.

6-Bromo-4-(chloromethyl)-7-hydroxycoumarin (**12**)

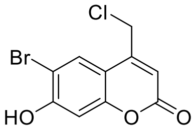

12

A solution of 4-bromoresorcinol (1 g, 5.29 mmol, 1 equiv.) and methanesulfonic acid (8 ml) was stirred for 15 minutes until the solid dissolved. Ethyl 4-chloroacetoacetate (0.92 ml, 7.94 mmol, 1.5 equiv.) was added to the solution and stirred for a further 6 hours. Iced-water (24 ml) was added to the resulting mixture and stirred for 30 minutes to yield a white precipitate. The precipitate was collected via filtration and recrystallised in hot ethanol (17 ml). The final product was collected via filtration.

Yield 72 % (1.1 g white solid).**^{1}H NMR (500 MHz, DMSO-*d*$_6$) δ (ppm):** 8.00 (1H, s), 6.92 (1H, s), 6.48 (1H, t, *J* = 1.5 Hz), 5.00 (2H, d, *J* = 0.7 Hz). **^{13}C NMR (126 MHz, DMSO-*d*$_6$) δ (ppm):** 160.1, 158.0, 154.5, 150.6, 129.5, 112.6, 111.1, 106.6, 103.8, 41. **LCMS (ESI)** *m/z* 289.0 $(M+H)^+$. **Analytical HPLC (282 nm)** t_R 4.546 min, >99 % purity.

6-Bromo-4-7-hydroxy-4-hydroxymethylcoumarin (**13**)

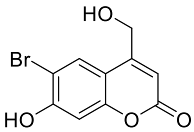

13

Compound **12** (2 g, 7.38 mmol), was dissolved in a mixture of DMF (60 ml) and 1N HCl (30 ml) and heated to 100 °C for 48 h. Following cooling, the solvent was evaporated under reduced pressure. The product was resuspended in EtOAc (100 ml) and washed in brine (3 × 50 ml) and H_2O (3 × 50 ml). The organic layer was dried with $MgSO_4$ and the product **13** was filtered and dried *in vacuo*.

Yield 67% (1.25 g light yellow solid).**^{1}H NMR (500 MHz, DMSO-*d*$_6$) δ (ppm)**: 7.84 (1H, s), 6.89 (1H, s), 6.27 (1H, t, *J* = 1.5 Hz), 5.60 (1H, t, *J* = 5.6 Hz), 4.69 (2H, dd, *J* = 5.8, 1.5 Hz). **^{13}C NMR (126 MHz, DMSO-*d*$_6$) δ (ppm):** δ 160.6, 157.6, 156.5, 154.2, 128.7, 111.5, 108.1, 106.5, 103.6, 59.6. **LCMS (ESI)** *m/z* 271.0 $(M+H)^+$. **Analytical HPLC** (282 nm) t_R 3.285 min, 98 % purity.

6-Bromo-4-hydroxymethyl-7-coumarinyl acrylate (**15**)

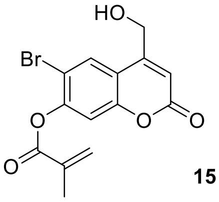

15

Compound **13** (1 g, 3.7 mmol, 1 equiv.) and triethylamine (0.5 ml, 3.7 mmol, 1 equiv.) were dissolved in THF (84 ml) under a nitrogen atmosphere. A solution of distilled methacryloyl chloride **14** (0.37 ml, 3.7 mmol, 1 equiv.) in THF (17 ml) was then added dropwise to the flask at 0 °C and left to warm to room temperature overnight. The resulting insoluble salt was removed by filtration and the solvent was evaporated under reduced pressure. The crude product **15** was purified using flash column chromatography (DCM/ EtOAc: 9/1 to 8/2).**Yield** 38 % (457 mg white solid). **^{1}H NMR (500 MHz, DMSO-*d*$_6$) δ (ppm):** 8.07 (s, 1H), 7.59 (s, 1H), 6.51 (t, *J* = 1.6 Hz, 1H), 6.39 (d, *J* = 1.0 Hz, 1H), 6.02 (d, *J* = 1.5 Hz, 1H), 5.73 (t, *J* = 5.5 Hz, 1H), 4.78 (dd, *J* = 5.5, 1.7 Hz, 2H), 2.05 (t, *J* = 1.3 Hz, 3H). **^{13}C NMR (126 MHz, DMSO-*d*$_6$) δ (ppm)**: 164.0, 159.4, 155.4, 152.8, 149.8, 134.4, 129.2, 128.34, 112.7, 111.3, 111.1, 59.1, 17.9. **HRMS (ESI)** *m/z* 338.9874, calculated for $C_{14}H_{12}Br_1O_5$ $(M+H)^+$ 338.98626. **Analytical HPLC** (282 nm) t_R 4.650, 87 % purity. R_f 0.63 DCM:EtOAc (7:3).

Coumarin Camptothecin monomer (**17**)

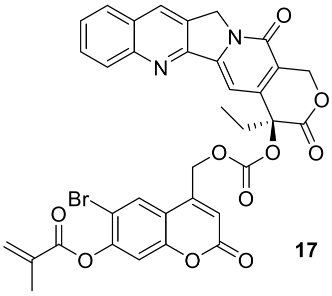

17

Camptothecin (**CPT**) (70 mg, 0.201 mmol, 1 equiv.) and DMAP (73.6 mg, 0.603 mmol, 3 equiv.) were suspended in dry CH_2Cl_2 (2 ml) under an argon atmosphere. Triphosgene (20.3 mg, 68.3 mmol, 0.34 equiv.) was then added and the mixture was stirred for 10 min at room temperature. A solution of the hydroxycoumarin monomer **15** (68.1 mg, 0.201 mmol, 1 equiv.) in dry CH_2Cl_2 (2 ml) was then added dropwise over 5 min. The reaction mixture was stirred overnight at room temperature, then directly loaded onto a column chromatography of silicagel (gradient eluent: CH_2Cl_2:EtOAc, 1:0 to 6:4) to give the pro-drug monomer as a white powder.

Yield 70% (68 mg, white powder). **^{1}H NMR (601 MHz, CDCl$_3$) δ (ppm)** 8.38 (s, 1H), 8.19 (d, *J* = 8.5 Hz, 1H), 7.91 (d, *J* = 8.1 Hz, 1H), 7.82 (ddd, *J* = 9.6, 6.4, 1.3 Hz, 1H), 7.68 – 7.63 (m, 1H), 7.62 (s, 1H), 7.29 (s, 1H), 7.16 (s, 1H), 6.54 (d, *J* = 1.4 Hz, 1H), 6.39 (d, *J* = 1.5 Hz, 1H), 5.83 (dd, *J* = 2.5, 1.3 Hz, 1H), 5.70 (d, *J* = 17.0 Hz, 1H), 5.39 (d, *J* = 17.1 Hz, 1H), 5.30 – 5.18 (m, 3H), 2.31 (dq, *J* = 14.8, 7.5 Hz, 1H), 2.19 (dq, *J* = 14.9, 7.5 Hz, 1H), 2.05 (d, J = 1.4 Hz, 2H), 1.34 – 1.19 (m, 3H), 1.04 (t, *J* = 7.5 Hz, 2H), 0.87 (t, J = 7.1 Hz, 2H). **13C NMR (151 MHz, CDCl$_3$) δ (ppm)** 167.0, 164.1, 159.1, 157.3, 153.3, 153.2, 152.2, 150.9, 149.0, 146.9, 146.3, 145.3, 134.9, 131.3, 130.9, 129.8, 129.1, 128.6, 128.32, 128.27, 128.25, 127.6, 120.4, 116.1, 114.5, 113.0, 112.1, 95.6, 79.0, 67.2, 64.8, 50.2, 34.2, 31.9, 22.4, 18.4, 18.3, 14.16, 14.15, 7.8. **HRMS (ESI):** *m/z* 735.05721, calculated for $C_{35}H_{25}BrN_2O_{10}Na$ $(M+Na)^+$ 735.05848. **Analytical HPLC (254 nm)** t_R 5.743 min.

7-(diethylamino)-4-(2-dimethylamino)vinylcoumarin (**19**)

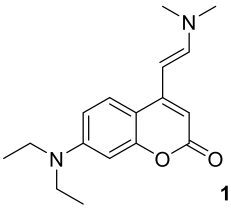

19

7-(diethylamino)-4-methylcoumarin (20 g, 86.5 mmol, 1 eq.) (**18**) was dissolved in dry DMF (10 ml) under a nitrogen atmosphere and DMFDMA (11.7ml, 86.7 mmol, 1 eq.) was added and was heated to 140 °C and stirred for 8 h. Additional DMFDMA (0.46 ml, 34.6 mmol, 0.4 eq.) was then added and heating was maintained for an additional 8 h. Solvent was removed under reduced pressure and the residue was suspended in cyclohexane (40 ml), filtered, washed with Et_2O (40 ml x 3) and dried under vacuum.

Yield 100% (24.6 g, brown solid). **^{1}H NMR (500 MHz, CDCl$_3$) δ (ppm)** 7.52 (d, *J* = 9.1 Hz, 1H), 7.22 (d, *J* = 13.0 Hz, 1H), 6.55 (dd, *J* = 9.0, 2.7 Hz, 1H), 6.49 (d, *J* = 2.6 Hz, 1H), 5.85 (s, 1H), 5.22 (d, *J* = 13.0 Hz, 1H), 3.40 (q, *J* = 7.1 Hz, 4H), 2.99 (s, 6H), 1.20 (t, *J* = 7.1 Hz, 6H). **^{13}C NMR (126 MHz, CDCl$_3$) δ (ppm)** 163.6, 156.5, 152.5, 150.2, 146.7, 124.9, 108.2, 108.0, 98.2, 93.5, 87.5, 44.8, 40.9, 12.6. **HRMS (ESI)** *m/z* 287.1760, calculated for $C_{17}H_{23}N_2O_2$ $(M+H)^+$: 287.1754.

7-diethylamino-4-formylcoumarin (**20**)

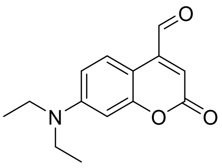

20

Compound **19** (24.6 g, 85.9 mmol, 1 eq.) was dissolved in a mixture of THF and DCM (300 ml, 5/2, v/v). A solution of $NaIO_4$ (55.1 g, 258 mmol, 3 eq.) in H_2O (250 ml) was then added, and the resulting mixture was stirred at room temperature for 2 h. Following the completion of the reaction, the mixture was filtered on Celite®, and the filtrate was partially concentrated under vacuum. The aqueous layer was then extracted with DCM (100 ml × 5), and the combined organic layers were washed with brine (200 ml × 3), dried over Na_2SO_4, filtered and evaporated. The crude was purified using column chromatography (eluent: DCM).

Yield 87% (18.3 g, dark red solid). **^{1}H NMR (500 MHz, CDCl$_3$) δ (ppm)** 10.03 (s, 1H), 8.30 (d, *J* = 9.2 Hz, 1H), 6.63 (dd, *J* = 9.2, 2.7 Hz, 1H), 6.52 (d, *J* = 2.7 Hz, 1H), 6.45 (s, 1H), 3.43 (q, *J* = 7.1 Hz, 4H), 1.22 (t, *J* = 7.1 Hz, 6H). **^{13}C NMR (126 MHz, CDCl$_3$) δ (ppm)** 192.7, 162.0, 157.5, 151.1, 144.0, 127.2, 117.5, 109.6, 103.8, 97.7, 44.9, 12.6. **LCMS (ESI):** *m/z* 246.2 $(M+H)^+$. **Analytical HPLC (254 nm)** t_R 6.454 min. R_f 0.57 DCM:EtOAc (95:5).

4-(2-chloro-1-hydroxyethyl)-7-(diethylamino)coumarin (**21**)

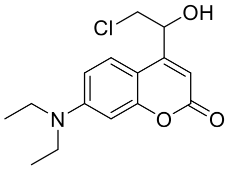

21

Chloro-iodomethane (0.32 ml, 4.40 mmol, 3 eqiv.) was dissolved in 50 ml dry THF under argon atmosphere. The mixture was then cooled down to -78°C before *i*PrMgClLiCl (1.3 M solution in THF, 1.7 ml, 2.2 mmol, 1.5 eqiv.) was added. The reaction mixture was stirred for 30 mins at -78°C and a solution of the coumarin-aldehyde (compound **20**) (360 mg, 1.43 mmol, 1 equiv.) in dry THF was added dropwise. The reaction mixture was then allowed to warm up to room temperature and stirred for 1 hr. 50 ml NH_4Cl saturated solution was then added to quench the reaction and the mixture was extracted with EtOAc (25 ml × 3). 87 %. The organic layer was dried with Na_2SO_4, filtered and concentrated to give the crude as a pale orange powder, which was pure enough to use in the following step without further purification.

Yield 78 % (180 mg, yellow solid). **^{1}H NMR (500 MHz, $CDCl_3$) δ(ppm)** 7.39 (d, *J* = 9.1 Hz, 1H), 6.61 (dd, *J* = 9.1, 2.6 Hz, 1H), 6.55 (d, *J* = 2.6 Hz, 1H), 6.34 (d, *J* = 1.1 Hz, 1H), 5.19 (dd, *J* = 10.2, 2.2 Hz, 1H), 3.92 (dd, *J* = 11.6, 2.9 Hz, 1H), 3.68 (dd, *J* = 11.6, 8.5 Hz, 1H), 3.44 (q, *J* = 7.1 Hz, 4H), 2.77 (d, *J* = 3.6 Hz, 1H), 1.23 (t, *J* = 7.1 Hz, 6H). **^{13}C NMR (126 MHz, $CDCl_3$) δ (ppm)** 162.1, 156.7, 152.8, 150.7, 124.5, 108.9, 106.8, 105.9, 98.3, 70.2, 49.4, 44.9, 12.6. **HRMS (ESI)** *m/z* 296.1043, calculated for $C_{15}H_{18}ClNO_3$ $(M+H)^+$ 296.10480. **Analytical HPLC (254 nm)** t_R 5.054 min.

4-(2-azido-1-hydroxyethyl)-7-(diethylamino)coumarin (**22**)

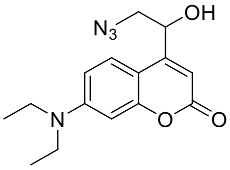

22

21 (100 mg, 0.338 mmol, 1 equiv.) was dissolved in DMSO (7 ml) and stirred at room temperature. Sodium azide (66 mg, 1.01 mmol, 3 equiv.) was then added to the reaction. The reaction was heated to 120 °C and stirred overnight. The resulting insoluble sodium chloride salt was removed by filtration, washed with acetone (20 ml) and the filtrate was concentrated under vacuum. Product **22** was purified using flash column chromotography (gradient eluent: DCM:EtOAc, 1:0 to 7:3).

Yield 34% (35 mg, brown solid). **^{1}H NMR (500 MHz, CDCl$_3$) δ ppm** 7.36 (d, *J* = 9.1 Hz, 1H), 6.60 (dd, *J* = 9.1, 2.7 Hz, 1H), 6.55 (d, *J* = 2.6 Hz, 1H), 6.34 (d, *J* = 1.0 Hz, 1H), 5.19 (dd, *J* = 10.2, 2.2 Hz, 1H), 3.61 (dd, *J* = 12.9, 3.1 Hz, 1H), 3.53 (dd, *J* = 12.9, 8.1 Hz, 1H), 3.44 (q, *J* = 7.1 Hz, 4H), 1.23 (t, *J* = 7.1 Hz, 6H). **^{13}C NMR (126 MHz, CDCl$_3$) δ (ppm)** 162.1, 156.7, 153.7, 150.6, 124.5, 109.1, 106.7, 106.0, 98.5, 69.7, 56.6, 45.1, 12.6.**HRMS (ESI)** *m/z* 303.1465, calculated for $C_{15}H_{18}N_4O_3$ $(M+H)^+$: 303.1452. **Analytical HPLC (254 nm)** t_R 5.089 min.

8.3 Peptide RAFT Agents

3-Lys-CF-RAFT (**1**)

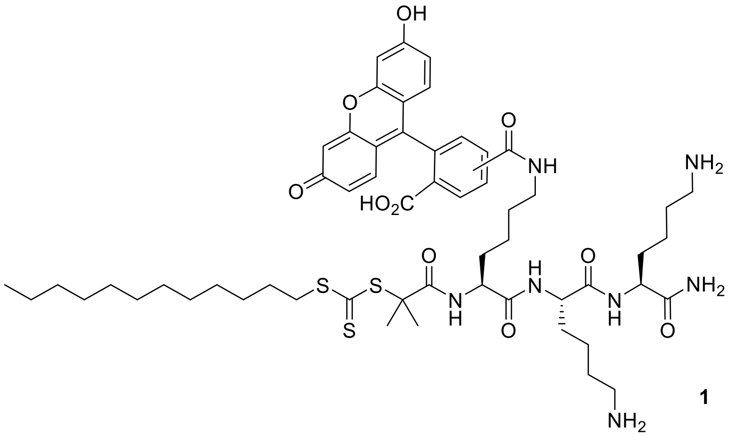

1

Yield 11% (76 mg, yellow powder). **^{1}H NMR (500 MHz, MeOD) δ (ppm)** 8.47 – 8.43 (m, 0.5H, *isomer 5*), 8.22 (dd, *J* = 8.0, 1.6 Hz, 0.5H, *isomer 5*), 8.14 (dd, *J* = 8.0, 1.4 Hz, 0.5H, *isomer 6*), 8.11 – 8.06 (m, 0.5H, *isomer 6*), 7.68 – 7.64 (m, 0.5H, *isomer 6*), 7.31 (d, *J* = 7.8 Hz, 0.5H, *isomer 5*), 6.72 – 6.65 (m, 2H), 6.65 – 6.48 (m, 4H), 4.40 – 4.27 (m, 4H), 4.19 (dd, *J* = 8.4, 5.9 Hz, 0.5H, *isomer 5*), 4.10 (dd, *J* = 8.5, 5.8 Hz, 0.5H, , *isomer 6*), 3.00 – 2.87 (m, 6H), 1.95 – 1.40 (m, 26H), 1.40 – 1.20 (m, 20H), 0.94 – 0.84 (m, 3H). **^{13}C NMR (126 MHz, MeOD) δ (ppm)** 222.9, 176.5, 175.3, 175.2, 174.6, 174.56, 173.76, 173.73, 170.53, 170.48, 168.4, 168.3, 161.7, 154.2, 154.1, 142.3, 137.9, 135.5, 130.4, 130.4, 130.4, 130.2, 130.2, 128.7, 126.3, 125.8, 125.2, 124.5, 114.0, 113.9, 111.01, 110.96, 103.7, 57.8, 57.6, 56.2, 56.1, 54.44, 54.38, 53.98, 53.96, 40.58, 40.56, 40.51, 40.49, 40.4, 37.8, 37.7, 33.05, 33.04, 32.7, 32.6, 32.20, 32.18, 32.15, 32.0, 31.8, 30.72, 30.65, 30.64, 30.57, 30.55, 30.53, 30.45, 30.19, 30.16, 30.03, 29.99, 29.92, 29.90, 29.1, 29.0, 28.01, 27.97, 26.3, 26.2, 25.7, 25.6, 24.3, 23.77, 23.75, 23.71, 23.67, 23.6, 14.44; **HRMS (MALDI-TOF**: *m/z* 1106.5109, calculated for $C_{56}H_{79}N_7O_{10}S_3$ $(M+H)^+$ 1106.5123. **Analytical HPLC (254 nm)** t_R 4.429 min, >99% purity.

5-Lys-CF-RAFT (2)

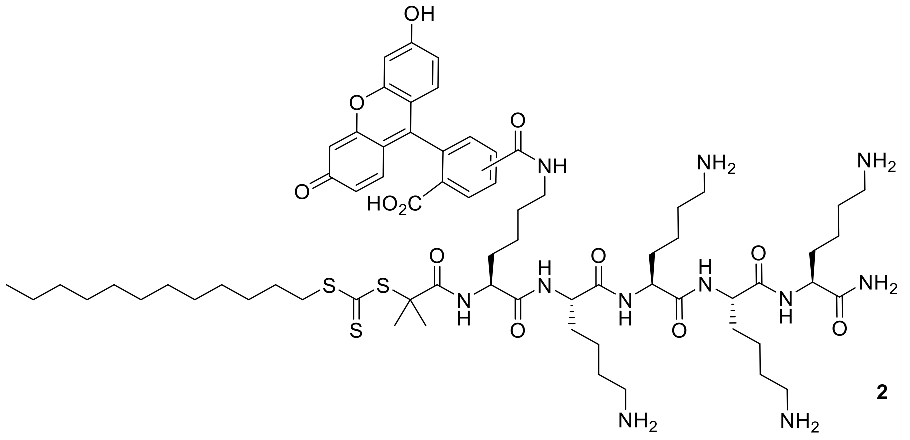

2

Yield 11% (96 mg, yellow powder). **^{1}H NMR (500 MHz, MeOD) δ (ppm)** 8.49 – 8.43 (m, 0.5H, *isomer 5*), 8.23 (dd, *J* = 8.0, 1.6 Hz, 0.5H, *isomer 5*), 8.15 (dd, *J* = 8.1, 1.2 Hz, 0.5H, *isomer 6*), 8.12 – 8.05 (m, 0.5H, *isomer 6*), 7.70 – 7.64 (m, 0.5H, *isomer 6*), 7.31 (d, *J* = 8.0 Hz, 0.5H, *isomer 5*), 6.74 – 6.66 (m, 2H), 6.65 – 6.49 (m, 4H), 4.39 – 4.22 (m, 4H), 4.16 (dd, *J* = 8.2, 6.2 Hz, 0.5H, , *isomer 5*), 4.06 (dd, *J* = 9.4, 4.9 Hz, 0.5H, , *isomer 6*), 3.01 – 2.88 (m, 8H), 1.97 – 1.40 (m, 39H), 1.39 – 1.17 (m, 20H), 0.94 – 0.83 (m, 3H); **^{13}C NMR (126 MHz, MeOD) δ (ppm)** 223.2, 223.1, 176.5, 175.53, 175.45, 174.84, 174.81, 174.24, 174.15, 174.1, 173.97, 173.96, 170.6, 170.5, 168.34, 168.26, 161.6, 154.2, 154.1, 142.3, 137.9, 135.5, 130.4, 130.4, 130.24, 130.17, 128.7, 126.2, 125.8, 125.2, 124.5, 114.0, 113.9, 113.8, 110.98, 110.95, 110.9, 103.7, 57.8, 57.6, 56.6, 56.5, 54.8, 54.74, 54.71, 54.2, 40.49, 40.46, 40.4, 37.8, 37.7, 33.04, 33.03, 32.5, 32.24, 32.18, 32.14, 32.12, 32.04, 31.99, 31.8, 31.6, 30.7, 30.64, 30.63, 30.58, 30.53, 30.52, 30.4, 30.18, 30.15, 30.0, 29.94, 29.91, 29.89, 29.03, 29.01, 27.98, 27.96, 27.9, 26.2, 26.1, 25.7, 25.6, 24.3, 24.2, 23.81, 23.79, 23.75, 23.73, 23.71, 23.70, 23.64, 23.62, 14.4. **HRMS (MALDI-TOF)** *m/z* 1362.7001 calculated for $C_{68}H_{103}N_{11}O_{12}S_3$ (M+H)$^+$ 1362.7023. **Analytical HPLC (254 nm)** t_R 3.804 min, >99% purity.

7-Lys-CF-RAFT (3)

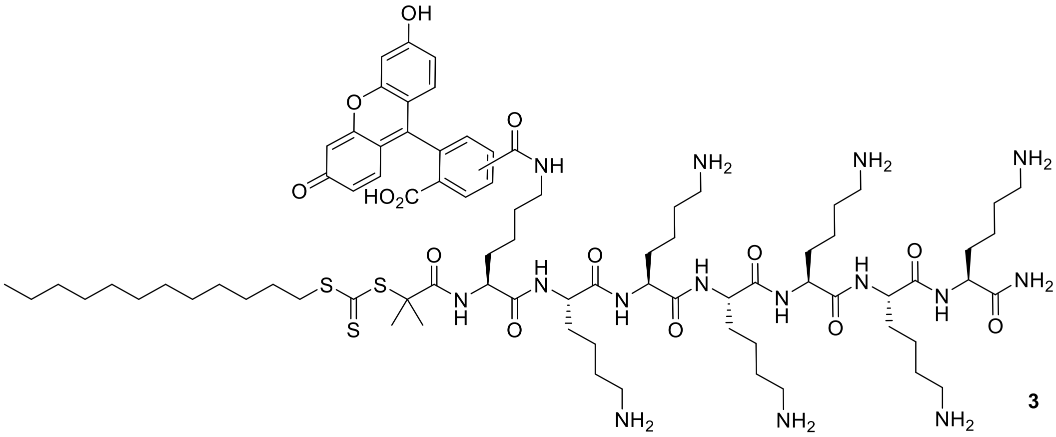

3

Yield 7% (76 mg, yellow powder). **^{1}H NMR (500 MHz, MeOD) δ (ppm)** 8.50 – 8.46 (m, 0.5H, *isomer 5*), 8.24 (dd, *J* = 8.1, 1.6 Hz, 0.5H, *isomer 5*), 8.16 (dd, *J* = 8.0, 1.4 Hz, 0.5H, *isomer 6*), 8.12 – 8.06 (m, 0.5H, *isomer 6*), 7.69 – 7.67 (m, 0.5H, *isomer 6*), 7.32 (d, *J* = 8.0 Hz, 0.5H, *isomer 5*), 6.72 – 6.69 (m, 2H), 6.64 – 6.52 (m, 4H), 4.35 – 4.22 (m, 6H), 4.14 (dd, *J* = 9.0, 5.4 Hz, 0.5H, *isomer 5*), 4.04 (dd, *J* = 9.7, 4.7 Hz, 0.5H, *isomer 6*), 3.00 – 2.92 (m, 12H), 2.02 – 1.33 (m, 61H), 1.32 – 1.22 (m, 20H), 0.92 – 0.86 (m, 3H). **^{13}C NMR (126 MHz, MeOD) δ (ppm)** 223.4, 223.3, 176.6, 175.8, 175.7, 175.2, 175.1, 174.5, 174.42, 174.37, 174.1, 170.61, 170.56, 168.34, 168.27, 163.1, 162.8, 161.6, 154.12, 154.07, 142.3, 137.9, 135.6, 130.4, 130.3, 130.3, 130.2, 128.7, 126.2, 125.7, 125.2, 124.5, 119.4, 117.0, 113.9, 113.8, 110.9, 110.9, 103.7, 57.8, 57.7, 57.5, 57.3, 57.1, 57.0, 55.3, 55.2, 55.1, 55.0, 54.9, 54.32, 40.51, 40.48, 40.39, 40.26, 37.87, 37.79, 33.05, 33.04, 32.46, 32.0, 31.91, 31.86, 31.6, 31.4, 30.72, 30.71, 30.68, 30.64, 30.55, 30.53, 30.4, 30.20, 30.17, 30.0, 29.92, 29.90, 29.04, 29.01, 28.00, 27.97, 27.9, 26.3, 26.1, 25.72, 25.66, 24.3, 24.2, 23.9, 23.8, 23.7, 17.6, 17.4, 17.3, 17.1, 17.0, 14.4. **HRMS (MALDI-TOF)** *m/z* 1618.8881, calculated for $C_{80}H_{127}N_{15}O_{14}S_3$ $(M+H)^+$ 1618.8922. **Analytical HPLC (254 nm)** t_R 3.496 min, >99% purity.

8.3.1 Peptide Synthesis

Solid-phase synthesis of fluorescein tagged Peptide-RAFT agents 1–3

Each peptide was synthesised on a 1 g scale of an aminomethyl polystyrene resin with a loading of 0.642 mmol/g (100-200 mesh). All the coupling reactions were monitored using a Kaiser test.

Rink-amide linker attachment to Polystyrene Resin. Fmoc-Rink-amide linker (1.06 g, 1.9 mmol, 3 equiv.) and Oxyma (0.27 g, 1.9 mmol, 3 equiv.) were dissolved in DMF (10 ml) and the mixture was stirred for 10 min until fully dissolved. DIC (243 µl, 1.9 mmol, 3 equiv.) was added to the solution and the mixture was stirred for a further 2 min. This mixture was added to the resin (1.0 g, 0.642 mmol/g, 1 equiv., pre-swollen in DCM) and shaken for 1 h. The resin was washed with DMF (3 × 10 ml), DCM (3 × 10 ml), MeOH (3 × 10 ml). Upon successful coupling, the Fmoc group was removed using a solution of piperidine in DMF (20%, *v/v*, 20 ml) for 2 × 20 minutes. The solution was drained and the resin was washed with DMF (3 × 20 ml), DCM (3 × 20 ml), and MeOH (3 × 20 ml).

Fmoc-Lys(Boc)-OH couplings. A solution of Fmoc-Lys(Boc)-OH (0.867 g, 1.9 mmol, 3 equiv. and Oxyma (0.27 g, 1.9 mmol, 3 equiv.) were dissolved in DMF (10 ml) and the mixture was stirred for 10 min until fully dissolved. DIC (243 µL, 1.9 mmol, 3 equiv.) was added to the solution and the mixture was stirred for a further 2 min. The mixture was added to the aforementioned resin (1.0 equiv., pre-swollen in DCM) and shaken for 1 h. The solution was drained and the resin was washed with DMF (3 × 20 ml), DCM (3 × 20 ml), MeOH (3 × 20 ml). Upon successful coupling, Fmoc groups were removed using a solution of piperidine in DMF (20%, *v/v*, 20 ml) for 2 × 20 minutes. The solution was drained and the resin was washed with DMF (3 × 20 ml), DCM (3 × 20 ml), MeOH (3 × 20 ml). The conjugation of additional Fmoc-Lys(Boc)-OH residues (2, 4, and 6) gave peptides **1**, **2**, and **3**, respectively.

Fmoc-Lys(Dde)-OH couplings and Dde deprotection. Fmoc-Lys(Dde)-OH[1] (0.743 g, 1.9 mmol, 3 equiv.) and Oxyma (0.27 g, 1.9 mmol, 3 equiv.) were dissolved in DMF (10 ml) and the mixture was stirred for 10 min until fully dissolved. DIC (243 µL, 1.9 mmol, 3 equiv.) was then added to the solution and the mixture was stirred for a further 2 min. The mixture was added to the aforementioned resin (1.0 equiv., pre-swollen in DCM) and stirred for 1 h. The solution was drained and the resin was washed with DMF (3 × 20 ml), DCM (3 × 20 ml), MeOH (3 × 20 ml). The Dde group was then

removed from the side chain by using a solution of imidazole (4.05 mmol, 0.27 M) and hydroxylamine hydrochloride (5.4 mmol, 0.36 M) in NMP (15 ml). This mixture was diluted by adding DCM (3 ml) and added to the resin, and shaken for 1.5 h. The deprotection was repeated 3 times. The solution was drained and the resin was washed with DMF (3 × 20 ml), DCM (3 × 20 ml), MeOH (3 × 20 ml).

5,6-Carboxyfluorescein coupling. 5,6-Carboxyfluorescein (0.724 g, 1.9 mmol, 3 equiv.) and Oxyma (0.27 g, 1.9 mmol, 3 equiv.) in DMF (10 ml) were stirred for 10 min until fully dissolved. DIC (243 µL, 1.9 mmol, 3 eq) was added to the solution and the mixture was stirred for a further 2 min. The mixture was added to the aforementioned resin (1.0 equiv., pre-swollen in DCM) and shaken for 4 h. The solution was drained and the resin was washed with DMF (3 × 20 ml), DCM (3 × 20 ml), MeOH (3 × 20 ml). Upon successful coupling, the Fmoc group was removed from the N-terminus using a solution of piperidine in DMF (20 %, *v/v*, 20 ml) for 2 × 20 minutes. The solution was drained and the resin was washed with DMF (3 × 20ml), DCM (3 × 20 ml), MeOH (3 × 20 ml).

RAFT agent coupling. 2-(Dodecylthiocarbonothioylthio)-2-methylpropionic acid (0.365 g, 1.9 mmol, 3 equiv.) and Oxyma (0.27 g, 1.9 mmol, 3 equiv.) were dissolved in DMF (10 ml) and the mixture was stirred for 10 min until fully dissolved. DIC (243 µl, 1.9 mmol, 3 equiv.) was added to the solution and the mixture was stirred for a further 2 min. The mixture was added to the aforementioned resin (1.0 equiv., pre-swollen in DCM) and shaken for 1 h. The solution was drained, and the resin was washed with DMF (3 × 20 ml), DCM (3 × 20 ml), MeOH (3 × 20 ml).

Cleavage off the resin, deprotection and purification. A solution of TFA/TIS/H_2O (15 ml) in a ratio of 90:5:5 (*v/v/v*) was added to the resin (pre-swollen in DCM) and the mixture was shaken for 4 h. The solution was drained and the product precipitated into ice-cold Et_2O and collected by centrifugation to give the crude peptide-RAFT agents. The peptide-RAFT agents were then dissolved (~30 mg/ml) in H_2O with 0.1% TFA and purified by reverse-phase preparative-HPLC (see materials and methods). Fractions were collected and freeze-dried to give the final peptide–RAFT agents as yellow solids.

8.4 Polymers

8.4.1 End-Group Modification

PEG5-CL

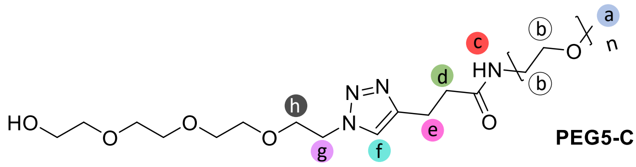

PEG5-CL

PEG5-Alkyne (100 mg, 0.02 mmol, 1 equiv.) and azido-PEG$_3$-Alcohol (**CL)** (4.54 mg, 0.026, 1.3 equiv.) were dissolved in anisole (0.6 ml) along with Copper nanopowder (16 mg, 60 - 80 nm) and sealed into a microwave tube. The reaction was heated at 160 ºC in the microwave for 15 min (‘very high absorbance’ setting). **PEG5-CL** was purified via centrifugation to remove the nanoparticles and precipitation in diethyl ether (4 × 12 ml) following resuspension in methanol.

Yield 98% (98 mg, white solid). **^{1}H NMR (601 MHz, CD_3CN) δ (ppm)** 7.74 (H_f, s, 1H), 6.67 (H_c, s, 1H), 4.49 (H_g, t , J = 5.1 Hz, 2H), 3.84 (H_h, t, J = 5.1 Hz, 2H), 3.62–3.48 (H_b, s), 3.30 (H_a, s, 3H), 2.95 (H_e, t, J = 7.3 Hz 2H), 2.51 (H_d, t, J = 7.3 Hz, 2H). **GPC (DMF)** M_n = 5.6 kDa, Đ = 1.1.

PEG5-CL-Act

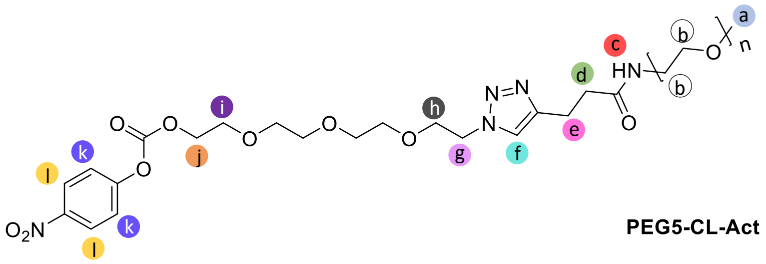

PEG5-CL-Act

PEG5-CL (50 mg, 9.7 µmol, 1 equiv.) and DMAP (2.92 mg, 24.0 µmol, 2.5 equiv.) were dissolved in fresh CD_3CN (300 µl) and DIPEA (8.4 µL, 48.0 µmol, 5 equiv.) was added. The solution was then added to an NMR tube that had been degassed under argon for 60 seconds before being capped. *p*-nitrophenyl chloroformate **23** (9.7 mg, 48.0 µmol, 5 equiv.) was dissolved in fresh CD_3CN (300 µl) that was then added to the NMR tube. The NMR tube was then further degassed using argon for 60 seconds before sealing with an NMR tube septum and parafilm, and mixed on a spinner at room temperature for 1 hour. **PEG-CL-Act** was purified via precipitation of the polymer from acetonitrile using diethyl ether (4 × 12 ml) and was then used immediately after isolation.

Yield 98 % (49 mg, white solid). **^{1}H NMR (601 MHz, CD_2Cl_2) δ (ppm)** 8.31 (H_l, d, J = 9.1 Hz, 2H), 7.55 (H_f, s, 1H), 7.45 (H_k, d, J = 9.1 Hz, 2H), 6.37 (H_c, s, 1H), 4.52 (H_g, t, J = 4.8 Hz 2H), 4.47 – 4.43 (H_j, m, 2H), 3.89 (H_h, t, J = 4.8 Hz, 2H), 3.80 – 3.77 (H_i, m, 2H), 3.73 – 3.56 (H_b), 3.38 (H_a, s, 3H), 3.02 (H_e, t, J = 7.4 Hz, 2H), 2.59 (H_d, t, J = 7.4 Hz, 2H).

PLA5-NH$_2$ and **PLA20-NH$_2$**

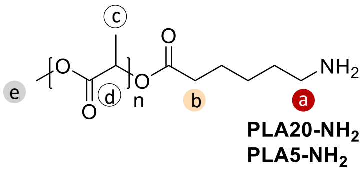

PLA20-OH (500 mg 0.025 mmol, 1 equiv.) and Boc-amino-hexanoic acid (35 mg, 0.15 mmol, 6 equiv.) were dissolved in anhydrous DCM (5 ml), along with DMAP (18.5 mg, 0.15 mmol, 6 equiv.) and DCC (31 mg, 0.15 mmol, 6 equiv.) were added to a microwave tube and sealed with a microwave Teflon cap. The mixture was degassed by bubbling with argon for 10 minutes and the seal was replaced before being heated in the microwave at 85 °C for 4 hours. The product **PLA20-NH-Boc** was purified via filtration and repeated precipitations in methanol (3 × 12 ml) and diethyl ether (3 × 12 ml). **PLA20-NH-Boc** Boc deprotection was performed in a mixture of DCM:TFA (5 ml, 1:1, *v*:*v*). **PLA20-NH$_2$** was purified by precipitation in methanol (40 ml × 3) and diethyl ether (40 ml × 3).

PLA5-NH$_2$ was synthesised according to the same procedure, adjusting the quantities of reactants used to ensure the molar ratios were respected (i.e. using 4 times more mass of other reactants) given the difference in molecular weights of the polymers.

PLA5-NH$_2$:

Yield 98 % (490 mg, white solid). **^{1}H NMR (601 MHz, CD$_2$Cl$_2$) δ (ppm)** 5.17 (H_d, q, J = 7.1 Hz), 3.72 (H_e, s, 3H), 3.02 (Ha, t, J = 7.1 Hz, 2H), 2.44 – 2.34 (H_b, m, 2H), 1.56 (H_c, d, J = 7.1 Hz). **GPC (DMF)** M_n = 5.8 kDa, Đ = 1.13.

PLA20-NH$_2$:

Yield 99 % (495 mg, white solid). **^{1}H NMR (601 MHz, CD$_2$Cl$_2$) δ (ppm)** 5.22 – 5.08 (H_d), 3.72 (H_e, 3H), 3.02 (H_a, 2H), 2.41 (H_b, 2H), 1.66 – 1.45 (H_c). **GPC (DMF)** M_n = 21.4 kDa, Đ = 1.0.

PEG5-CL-5PLA and **PEG5-CL-20PLA**

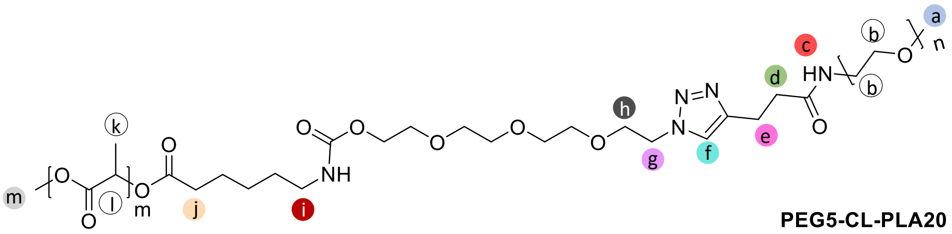

PEG5-CL-PLA20
PEG5-CL-PLA5

A solution of **PLA20-NH$_2$** (100 mg, 5.0 µmol, 0.83 equiv.) in anhydrous DCM (1 ml) and DIPEA (5 µL, 28.0 µmol, 5 equiv.) was stirred in a microwave tube for 10 minutes. **PEG5-CL-Act** (30 mg, 6.0 µmol, 1 equiv.) was separately dissolved in anhydrous DCM (0.5 ml) along with DMAP (1.5 mg, 12 µmol, 2 equiv.). This solution was added to the microwave tube and the mixture was degassed by bubbling with argon for 3 minutes. The tube was sealed with a microwave Teflon cap, and the mixture was heated in the microwave at 85 ºC for 4 hours. The product **PEG5-CL-PLA20** was purified via precipitation of the polymer from DCM using diethyl ether (12 ml × 3) and methanol (12ml × 3).

PEG5-CL-PLA5 was synthesised in according to the same procedure, adjusting the quantities of reactants used to ensure the molar ratios were respected (i.e. 4 times less **PEG5-CL-Act**) given the difference in molecular weights of the polymers.

PEG5-CL-PLA5:

^{1}H NMR (601 MHz, CD_2Cl_2) δ (ppm) 7.55 (H_f, s, 1H), 6.33 (H_c, s, 1H), 5.17 (H_l, q, *J* = 7.1 Hz), 4.47 (H_g, t, *J* = 5.1 Hz, 2H), 3.83 (H_h, t, *J* = 5.1 Hz, 2H), 3.72 (H_m, s, 3H), 3.60 (H_b, s), 3.34 (H_a, s, 3H), 3.13 (H_i, q, *J* = 6.7 Hz, 2H), 2.99 (H_e, t, *J* = 7.4 Hz, 2H), 2.58 – 2.53 (H_d, t, *J* = 7.4 Hz, 2H), 2.45 – 2.29 (H_j, m, 2H), 1.56 (H_k, d, *J* = 7.1 Hz). **GPC (DMF)** M_n = 10.1 kDa, Đ = 1.11.

PEG5-CL-PLA20:

^{1}H NMR (601 MHz, CD_2Cl_2) δ (ppm) 7.55 (H_f, s, 1H), 6.52 (H_c, s, 1H), 5.17 (H_l, q, *J* = 7.1 Hz), 4.47 (H_g, t, *J* = 5.1 Hz, 2H), 3.83 (H_h, t, *J* = 5.1 Hz, 2H), 3.72 (H_m, s, 3H), 3.60 (H_b, s), 3.34 (H_a, s, 3H), 3.13 (H_i, q, *J* = 6.8 Hz, 2H), 2.99 (H_e, t, *J* = 7.4 Hz, 2H), 2.56 (H_d, t, *J* = 7.4 Hz, 2H), 2.42 – 2.31 (H_j, m, 3H), 1.56 (H_k, d, *J* = 7.1 Hz). **GPC (DMF)** M_n = 25.3 kDa, Đ = 1.07.

PEG5-CM

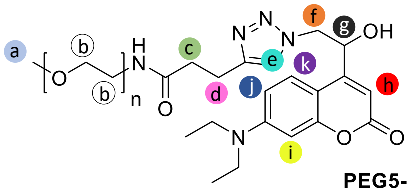

PEG5-CM

PEG5-Alkyne (100 mg, 0.020 mmol, 1 equiv.) and azido-coumarin **(25)** (7.8 mg, 0.026 mmol, 1.3 equiv.) were dissolved in anisole (0.6 ml) along with Copper nanopowder (16 mg, 60 - 80 nm) and sealed into a microwave tube. The reaction was heated at 160 °C in the microwave for 15 min (‘very high absorbance’ setting). **PEG5-CM** was purified via centrifugation to remove the nanoparticles and precipitation in diethyl ether (4 × 12 ml) following resuspension in methanol.

Yield 98% (98 mg, light brown solid). **^{1}H NMR (601 MHz, CD_3CN) δ (ppm)** 7.60 (H_e, s, 1H), 7.56 (H_k, d, *J* = 9.1 Hz, 1H), 6.71 (H_j, dd, *J* = 9.1, 2.6 Hz, 1H), 6.55 (H_i, d, *J* = 2.6 Hz, 2H), 6.03 (H_h, d, *J* = 0.9 Hz, 1H), 5.37 – 5.32 (H_g, m, 1H), 4.64 (H_f, dd, *J* = 14.3, 3.2 Hz, 1H), 4.47 (H_f, dd, *J* = 14.3, 7.5 Hz, 1H), 3.55 (H_b, s), 3.29 (H_a, s, 3H), 2.92 (H_d, t, *J* = 7, 2H), 2.45 (H_c, td, *J* = 7.4, 2.2 Hz, 2H). **GPC (DMF)** M_n = 5.6 kDa, Đ = 1.03.

PEG5-CM-Act

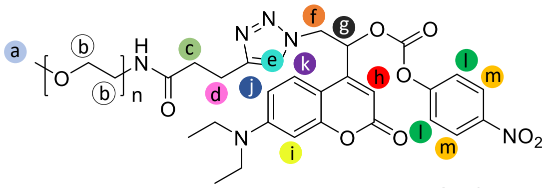

PEG5-CM-Act

PEG5-CM (50 mg, 9.7 µmol, 1 equiv.) and DMAP (2.9 mg, 24 µmol, 2.5 equiv.) were dissolved in fresh CD_3CN (300 µl) and DIPEA (8.4 µl, 48 µmol, 5 equiv.) was added. The solution was then added to an amberised NMR tube that had been degassed under argon for 60 seconds before an NMR tube septum was placed on the tube. *p*-nitrophenyl chloroformate **23** (9.7 mg, 48 µmol, 5 eqiv.) was dissolved in fresh CD_3CN (300 µl) that was then added to the NMR tube. The NMR tube was then further degassed using argon for 60 seconds before the NMR being capped. The NMR tube was sealed using parafilm and mixed on a spinner at room temperature for 1 hour. **PEG-CM-Act** was purified via precipitation of the polymer from acetonitrile using amberised falcon tubes in diethyl ether (4 × 12 ml) and was then used immediately after isolation.

^{1}H NMR (601 MHz, CD_3CN) δ (ppm) 8.27 (H_m, d, *J* = 9.2 Hz, 2H), 7.63 (H_e, s, 1H), 7.55 (H_k, d, *J* = 9.1 Hz, 1H), 7.43 (H_l, d, *J* = 9.2 Hz, 2H), 6.72 (H_j, dd, *J* = 9.1, 2.6 Hz, 1H), 6.56 (H_i, d, *J* = 2.6 Hz, 1H), 6.35 – 6.26 (H_g, m, 1H), 5.96 (H_h, d, *J* = 0.8 Hz, 1H), 4.91 – 4.88 (H_f, m, 2H), 3.55 (H_b, s). 2.95 – 2.88 (H_d, Hm, 2H) 2.45 (H_c, td, *J* = 7.4, 4.7 Hz, 2H).

PEG5-CM-PLA5 and **PEG5-CM-PLA20**

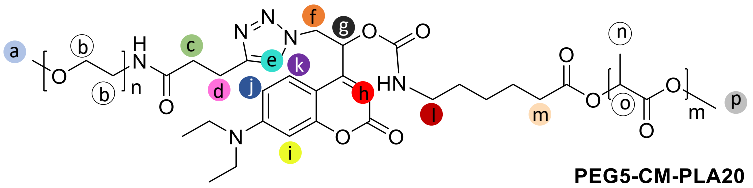

PEG5-CM-PLA20
PEG5-CM-PLA5

PLA20-NH$_2$ (100 mg, 5.0 µmol, 0.83 equiv.) was stirred in a microwave tube with 1 ml anhydrous DCM and DIPEA (5 µl, 28.0 µmol, 5 equiv.) for 10 minutes. **PEG5-CM-Act** (30 mg, 6.0 µmol, 1 equiv.) was separately dissolved in anhydrous DCM (0.5 ml) along with DMAP (1.5 mg, 12 µmol, 2 equiv.) and then added to the microwave tube. The tube was sealed and degassed by bubbling with nitrogen for 3 minutes, resealed with a Teflon cap, and reacted in the microwave at 85 ºC for 4 hours. The product **PEG5-CM-PLA20** was purified via precipitation of the polymer from DCM using diethyl ether (3 × 12 ml) and methanol (3 × 12 ml).

PEG5-CM-PLA5 was synthesised according to the same procedure, using **PLA5-NH$_2$** in place of **PLA20-NH$_2$** and adjusting the quantities of reactants used to ensure the molar ratios were respected (i.e. 4 times less **PLA-NH$_2$**) given the difference in molecular weights of the polymers.

PEG5-CM-PLA5

Yield 70 % (42 mg light brown solid). **^{1}H NMR (601 MHz, CD_2Cl_2) δ (ppm)** 7.50 (H_k, d, J = 9.1 Hz, 1H), 7.46 (H_e, s, 1H), 6.67 (H_j, dd, J = 9.1, 2.6 Hz, 1H), 6.52 (H_i, d, J = 2.6 Hz, 1H), 6.23 – 6.17 (H_g, m, 1H), 5.88 (H_h, d, J = 0.9 Hz, 1H), 5.17 (H_o, q, J = 7.1 Hz), 4.76 (H_f, dd, J = 14.7, 3.3 Hz, 1H), 4.61 (H_f, dd, J = 14.8, 7.3 Hz, 1H), 3.72 (H_p, s, 3H), 3.60 (H_b, s), 3.34 (H_a, s, 1H), 3.16 – 3.07 (H_l, m, 2H), 3.02 – 2.92 (H_d, m, 2H), 2.59 – 2.47 (H_c, m, 2H), 2.42 – 2.28 (H_m, m, 2H), 1.56 (H_n, d, J = 7.1 Hz, 86H). **GPC (DMF)** M_n = 9.9 kDa, Đ = 1.08.

PEG5-CM-PLA20

Yield 75 % (112 mg light brown solid). **^{1}H NMR (601 MHz, CD_2Cl_2) δ (ppm)** 7.52 (H_e, s, 1H), 7.51 (H_k, d, *J* = 9. Hz, 1H), 6.68 (H_j, dd, *J* = 9.1, 2.6 Hz, 1H), 6.52 (H_i, d, *J* = 2.6 Hz, 1H), 6.24 – 6.17 (H_g, m, 1H), 5.83 (H_h, d, *J* = 0.9 Hz, 1H), 5.17 (H_o, q, *J* = 7.1 Hz), 4.76 (H_f, dd, *J* = 14.7, 3.2 Hz, 1H), 4.63 (H_f, dd, *J* = 14.7, 6.9 Hz, 1H), 3.72 (H_p, s, 3H), 3.60 (H_b, s), 3.34 (H_a, s, 3H), 3.14 – 3.08 (H_l, m, 2H), 3.05 – 2.93 (H_d, m, 2H), 2.57 – 2.49 (H_c, m, 2H), 2.42 – 2.33 (H_m, m, 2H), 1.56 (H_n, d, *J* = 7.1 Hz). **GPC (DMF)** M_n = 25.9 kDa, Đ = 1.09.

8.4.2 RAFT Polymerisation

*8.4.2.1 RAFT-**1**, **2**, **3**, and **9**, Fluorescent Lysine Polymers*

Lys-PDMA Polymers

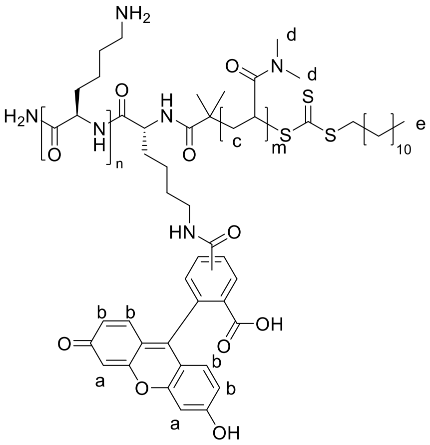

^{1}H NMR (500 MHz, MeOD) δ (ppm) 6.78 – 6.65 (Ha), 6.65 – 6.50 (m, 2H), 3.09 – 2.77 (m, 320H), 1.86 – 1.21 (m, 151H), 0.93 – 0.83 (m, 1H).

Table 14: Polymer characterisation of Lys-PDMA Polymers via NMR and GPC.

RAFT agent	Polymer	M_w [Da] (^{1}H NMR)	M_w [Da]^c (GPC)	PDI
1	**3Lys-PDMA-7.5k**	8229	7937	1.1
2	**5Lys-PDMA-7.5k**	8477	8050	1.4
3	**7Lys-PDMA-7.5k**	8761	10276	1.3
1	**3Lys-PDMA-50k**	53292	49041	1.3
2	**5Lys-PDMA-50k**	51581	47397	1.3
3	**7Lys-PDMA-50k**	52328	51943	1.3

0Lys-PDMA Polymers

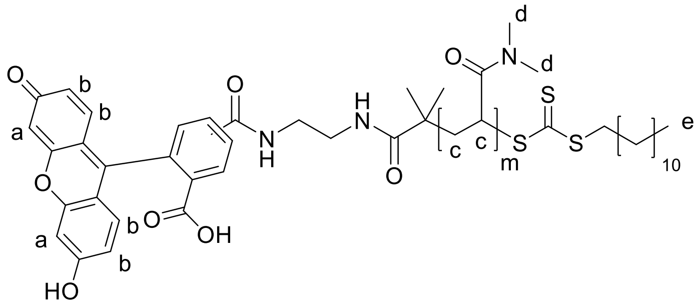

^{1}H NMR (500 MHz, MeOD) δ (ppm) 6.80 – 6.70 (H_a), 6.67 – 6.53 (H_b), 3.09 – 2.83 (H_d), 1.88 – 1.23 (H_c), 0.95 – 0.89 (H_a).

Table 15: Polymer characterisation of 0Lys-PDMA Polymers via NMR and GPC.

RAFT agent	Polymer	M_w [Da] (^{1}H NMR)	M_w [Da]^c (GPC)	PDI
9	**0Lys-PDMA-7.5k**	7663	6211	1.2
9	**0Lys-PDMA-50k**	48714	46037	1.3

Synthesis

Fluorescently-labelled PDMA polymers were synthesised using RAFT agents **1**,**2**,**3** and **9**, with a theoretical yield of ~50 mg of the resulting polymer. See **Table 16** for amount of monomer, RAFT agent, and the initiator AIBN used for each polymer.

Table 16. Quantities of starting material used for the polymerisation reactions.

Polymer	RAFT	DMA (μL)	RAFT agent (mg)	AIBN (μg)
3Lys-PDMA-7.5k	1	54	7	23
5Lys-PDMA-7.5k	2	51	9	22
7Lys –PDMA-7.5k	3	48	10	20
0Lys-PDMA-7.5k	9	49	5.5	21
3Lys-PDMA-50k	1	51	1.0	33
5Lys-PDMA-50k	2	53	1.4	34
7Lys-PDMA-50k	3	51	1.6	32
0Lys-PDMA-50k	9	52	0.8	34

Polymerisation with RAFT agents 1–**3**. DMA:RAFT:AIBN molar ratios of 75:1:0.02 and 500:1:0.02 were used to prepare the 7.5 kDa Mw and 50 kDa PDMAs, respectively. The final polymerisation concentrations of the monomers were ~0.70 M. Polymerisations were performed in a mixture of D_2O:1,4-dioxane (10:90) in a sealed tube equipped with a stirring bar. The reaction mixture was first degassed by bubbling argon for 30 min and then placed into a 70 °C oil bath for 4 h. The polymerisations were quenched with liquid nitrogen once maximum monomer conversion had been achieved (monitored using ^{1}H NMR). After defrosting in air, D_2O was added to dissolve the precipitated PDMA polymer and final monomer conversion was determined by ^{1}H NMR. Polymers were then dried *in vacuo*, precipitated in Et_2O, and consecutively dissolved in DMF (× 1) and MeOH (× 2) with precipitation in Et_2O. Finally, polymers were dialysed in water for 24 h using 1 kDa and 15 kDa molecular weight cut off dialysis tubing (Spectrum™, Spectra/Por™) for the 7.5 kDa and 50 kDA polymers, respectively. Polymers were isolated after lyophilising to dryness.

Polymerisation with RAFT agent 9 The polymerisations were performed under the same conditions as above but at 65 °C, and the reaction was quenched after 6 h (~95 % conversion, as determined by ^{1}H NMR).

8.4.2.2 *CM-DMA Copolymerisation*

CM-DMA 1-6

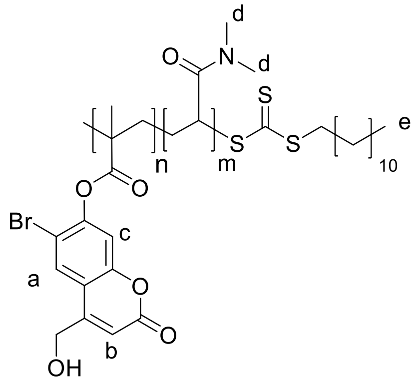

^{1}H NMR (601 MHz, D_2O) δ (ppm) 8.25 – 7.76 (H_a), 7.71 – 7.20 (H_c), 6.76 – 6.41 (H_b), 3.54 – 2.29 (H_d), 1.00 – 0.81 (H_e).

Synthesis

CM-DMA 1-3

Table 17: Polymer characterisation of **CM-DMA 1-3** polymers via GPC

Polymer	Mw [Da] (GPC)^b	PDI
CM-DMA-1	5595	1.37
CM-DMA-2	9638	1.42
CM-DMA-3	13743	1.47

Random block copolymers **CM-DMA-1**, **CM-DMA-2**, and **CM-DMA-**3 containing different ratios of coumarin monomer **18** and **DMA** were synthesised using 2-(dodecylthiocarbonothioylthio)-2-methylpropionic acid **DDMAT** as a RAFT agent and AIBN as an initiator. Three polymerisation reactions with ratios of 4:40:0.2:1, 4:80:0.2:1, and 4:120:0.2:1 of **18**:DMA:AIBN:RAFT gave polymers **CM-DMA-1**, **CM-DMA-2**, **CM-DMA-3**, respectively. **Table 18** shows the amount of each reactant used to fabricate each polymer.

Table 18. Quantities of starting material used for the **CM-DMA 1-3** polymerisation reactions.

Polymer	**18** (mg)	DMA (µL)	RAFT agent (mg)	AIBN (µg)
CM-DMA-1	17	50	3	41
CM-DMA-2	17	100	3	41
CM-DMA-3	17	150	4	41

Polymerisations were performed at 1 M concentrations in dioxane at 70 ºC under argon. The solutions were bubbled with argon prior to heating for 30 minutes to remove air from the reaction vessel. Polymerisations were quenched after 3 hours with liquid nitrogen under air. Polymers were purified by repeated precipitation in diethyl ether (3 × 12 ml) and resuspension in MeOH three times.

CM-DMA 4-6

Table 19: Polymer characterisation of **CM-DMA 4-6** polymers via GPC

Polymer	Mw [Da] (GPC)^{b}	PDI
CM-DMA-4	6146	1.36
CM-DMA-5	29957	1.64
CM-DMA-6	30563	1.60

Diblock copolymers **CM-DMA-4**, **CM-DMA-5**, and **CM-DMA-6** containing different block lengths of coumarin monomer **18** and **DMA** were synthesised. **DMA** polymer chains **P1-3** were first synthesised using 2-(dodecylthiocarbonothioylthio)-2-methylpropionic acid **DDMAT** as a RAFT agent and AIBN as an initiator. **Table 20** shows the amount of each reactant used to fabricate each polymer.

Table 20: Quantities of starting material used for PDMA polymerisation reactions to yield **P1-3**.

Polymer	DMA (µL)	RAFT agent (mg)	AIBN (mg)
P1	520	60	8.2
P2	520	12	1.6
P3	520	5	0.7

Polymerisations were performed at 1 M concentrations in dioxane at 70 ºC under argon. The solutions were bubbled with argon prior to heating for 30 minutes to remove air from the reaction vessel. Polymerisations were quenched after 3 hours with liquid nitrogen under air. Polymers were purified by repeated precipitation in diethyl ether (3 × 12 ml) and resuspension in MeOH three times. Polymers **P1-3** were then used as macro-RAFT agents to continue the polymerisation to form the **18** block. Polymerisation were performed and purified in identical conditions using the quantities in **Table 21**.

Table 21: Quantities of starting material used for the **CM-DMA 4-6** polymerisation reactions.

Polymer	**18** (mg)	Polymer-RAFT	Polymer RAFT (mg)	AIBN (µg)
CM-DMA-4	46	**P1**	30	440
CM-DMA-5	46	**P2**	28	90
CM-DMA-6	46	**P3**	150	200

8.4.2.3 *CM-CPT Copolymerisation*

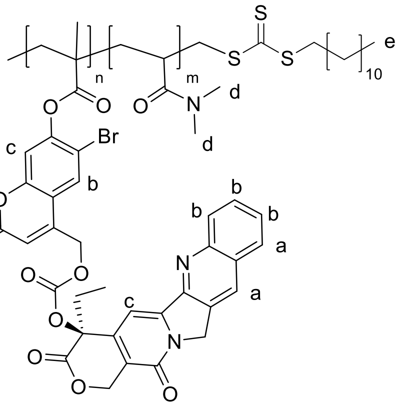

^{1}H NMR (601 MHz, MeOD) δ (ppm) 8.75 – 8.31 (H_a), 8.23 – 7.49 (H_b), 7.45 – 7.18 (H_c), 3.08 – 2.82 (H_d), 0.94 – 0.81 (H_e).

CM-CPT

Table 22: Polymer characterisation of the **CM-CPT** polymer via GPC.

Polymer	Mw [Da] (GPC)	PDI
CM-CPT	11,997	1.29

Synthesis

Random block copolymer **CM-CPT** coumarin-camptothecin monomer **20** and **DMA** were synthesised using 2-(dodecylthiocarbonothioylthio)-2-methylpropionic acid **DDMAT** as a RAFT agent and AIBN as an initiator. The polymerisation reactions was performed with a ratio of 2:100:0.2:1 **20**:DMA:AIBN:RAFT. **Table 23** shows the amount of each reactant used to fabricate each polymer.

Table 23. Quantities of starting material used for the polymerisation reactions.

Polymer	**20** (mg)	DMA (µL)	RAFT agent (mg)	AIBN (µg)
CM-DMA-1	6	42	1.5	40

Polymerisation was performed at a 1 M concentrations in dioxane:D_2O at a ratio of 90:10 at 70 ºC under argon. The solutions were bubbled with argon prior to heating for 30 minutes to remove air from the reaction vessel. The polymerisation was quenched after 3 hours with liquid nitrogen under air. **CM-CPT** was purified by repeated precipitation in diethyl ether from MeOH (3 × 12 ml).

8.5 Nanoparticle Synthesis

8.5.1 CM-DMA Nanoparticles

Unloaded

6 mg of each polymer (**CM-DMA-4**, **CM-DMA-5**, and **CM-DMA-6**) were dissolved in DMF (200 µL) and this solution was added dropwise into H_2O (800 µL) under stirring. The stirring was performed overnight to stabilise the nanoparticles. To purify, the nanoparticles were dialysed against H_2O and was performed using 20,000 Mw cut-off bags. The dialysis was performed over 24 hours with the water being replaced every 2 hours. Nanoparticles were stored in solution at 4 ºC.

Rhodamine B Loaded

Nanoparticles were fabricated using polymer **CM-DMA-4** encapsulating Rhodamine B. 6 mg **CM-DMA-4** and Rhodamine B (2 mg) were dissolved in DMF (200 µl). The solution was then added dropwise into H_2O (800 µl) while stirring, and left overnight in the dark to stabilise. Nanoparticles were purified using dialysis against deionised water using a dialysis membrane (20,000 Mw cut off). The dialysis was performed over 3 days and the water changed every 4 hours. Nanoparticles were stored in the fridge until needed.

8.5.2 PEG-Coumarin-PLA Nanoparticles

Unloaded Nanoparticles

Unloaded nanoparticle samples were prepared from **PEG5-CM-PLA5** and PEG-CM-PLA20 at concentrations of 1 mg/ml and 3 mg/ml using the nanoprecipitation and W/o/W method (**Table 24**).

Table 24: Polymer concentrations of nanoparticle samples

Polymer	Polymer conc. (mg/ml)	Nanoprecipitation Nanoparticles	W/o/W Nanoparticle s
PEG5-CM-PLA5	3	**NP’(5)-3**	**NP(5)-3**
PEG5-CM-PLA5	1	**NP’(5)-1**	**NP(5)-3**
PEG5-CM-PLA20	3	**NP’(20)-3**	**NP(20)-3**
PEG5-CM-PLA20	1	**NP’(20)-1**	**NP(20)-1**

Nanoprecipitation Method

Polymers **PEG5-CM-PLA5** and **PEG5-CM-PLA20** were dissolved in acetonitrile (200 µl). Samples were then added dropwise to 2 ml deionised water under stirring in amberised vials at either 1 mg/ml or 3 mg/ml total polymer volume concentration to yield **NP’(5)-1 and NP’(5)-3** made from **PEG5-CM-PLA5**, respectively, and **NP’(20)-1** and **NP’(20)-3**, made from **PEG5-CM-PLA20**, respectively. Flasks remained open under stirring overnight to allow for the evaporation of the acetonitrile. Nanoparticle samples were centrifuged at 20,000 rpm at 4 °C for 2 hours.

W/o/W method

Polymer samples **PEG5-CM-PLA5** and **PEG5-CM-PLA5** were dissolved in DCM (200 µl) in amberised vials. 100 µL 5% PVA w/v in dionised water was added to the DCM along with H_2O (100 µL). The samples were placed in an iced sonicator bath and sonicated for 2 minutes, until a homogenous emulsion could be seen in the vial. Then a further 800 µL H_2O was added dropwise, making a total concentration of 0.5 % PVA, and the solution was sonicated for a further 5 minutes, until homogeneity was observed. Final concentrations of 1 mg/ml and 3 mg/ml of each polymer in H_2O was used to yield nanoparticle samples **NP(5)-1**, **NP(5)-3**, **NP(20)-1**, and **NP(20)-3**. The vial was then placed into a round bottom flask, secured using cotton wool, and the DCM was evaporated under reduced pressure. The solution was then left to stir overnight to allow for the stabilisation of the nanoparticles. The nanoparticles were centrifuged to remove the PVA from the solution. This time nanoparticle could be retrieved by centrifuging at 8,000 rpm for 15 minutes, possibly indicating that the size of the nanoparticles was larger compared to the nanoprecipitation method. Nanoparticles were cleaned twice using centrifugation, and then resuspended in H_2O at their required concentrations.

Dox Loaded Nanoparticles

A ratio of 1:0.2 and 1:0.5 polymer:Dox *w/w* was used, as well as polymer concentrations of 1 mg/ml and 3 mg/ml giving 4 nanoparticle solutions for each polymer (**Table 25**).

Table 25: Polymer and Dox concentrations for nanoparticle synthesis

Polymer	Polymer conc. (mg/ml)	Dox conc. (mg/ml)	Polymer: Dox ratio (*w/w*)	Nanoparticle
PEG5-CM-PLA5	3	1.5	0.5	**[0.5$_{\mathrm{DOX}}$]NP(5)-3**
PEG5-CM-PLA5	3	0.6	0.2	**[0.2$_{\mathrm{DOX}}$]NP(5)-3**
PEG5-CM-PLA5	1	1.5	0.5	**[0.5$_{\mathrm{DOX}}$]NP(5)-1**
PEG5-CM-PLA5	1	0.6	0.2	**[0.2$_{\mathrm{DOX}}$]NP(5)-1**
PEG5-CM-PLA20	3	1.5	0.5	**[0.5$_{\mathrm{DOX}}$]NP(20)-3**
PEG5-CM-PLA20	3	0.6	0.2	**[0.2$_{\mathrm{DOX}}$]NP(20)-3**
PEG5-CM-PLA20	1	1.5	0.5	**[0.5$_{\mathrm{DOX}}$]NP(20)-1**
PEG5-CM-PLA20	1	0.6	0.2	**[0.2$_{\mathrm{DOX}}$]NP(20)-1**

1mg or 3mg of each polymer samples was dissolved in 200 µl DCM in an amberised vial, 100 µl 5% PVA in water was added along with 100 µl of either a 15 mg/ml or 6 mg/ml solution of Dox in H_2O, samples were sonicated in an iced sonicator bath until homogeneity was observed. The samples were topped up to 1.2 ml by adding a further 800 µl H_2O and further sonicated until homogeneity. Following evaporation under reduced pressure, the samples were left to stir overnight. Samples were centrifuged at 8,000 rpm for 15 minutes, the supernatant containing excess Dox was decanted, the samples were resuspended in H_2O, and washed a further 2×, before being resuspended in H_2O and stored in at 4 °C.

8.6 Other Characterisation Techniques

Fluorescence

Stock solutions of 2mg/ml of polymers **0Lys-PDMA-7.5k**, **0Lys-PDMA-50k**, **3Lys-PDMA-7.5k**, **3Lys-PDMA-50k**, **5Lys-PDMA-7.5k**, **5Lys-PDMA-50k, 7Lys-PDMA-7.5k**, **7Lys-PDMA-50k** in Dulbecco's PBS were prepared and sequentially diluted into a black Corning Costar Assay 90 well plate. ~7.5 kDa polymer samples were prepared with a concentration range of 0–200 µg/ml and ~50 kDa polymer samples with a range of 0–1000 µg/ml. A BioTek HT Synergy multi-mode reader was used to determine sample fluorescence. Samples were excited at 480 nm and fluorescence emission was recorded at 520 nm.

HPLC

Samples were dissolved in mixtures of acetonitrile and water (containing 0.1 % FA) and filtered through PTFE.

GPC

Polymer solutions unless specified otherwise were dissolved at concentrations of 5 mg/ml in DMF containing 0.1 % LiBr. Samples were run at 60 °C for 30 minutes at flow rate of 1 ml/min.

Critical Micelle Concentration

A 1 mg/ml solution of Nile Red in DCM was prepared of which 32 µl was taken and diluted into 968 µl of DCM for a final concentration of 100 µM. 15 µl of the solution was added into 14 separate amber vials (1.5 ml) where the solution was allowed to dry. 500 µl of **NP(5)-3** and **NP(20)-3** at concentrations of 1 µg/ml - 100 µg/ml were added to the vials, and left to stir in the dark overnight. 100 µl of each solution was taken and the fluorescence 655 nm was measured (520 nm excitation).

Drug Loading Efficiency

To evaluate Dox loading within the nanoparticles, Eppendorfs were preweighed and 500 µl of each nanoparticle sample (**[0.5$_{DOX}$]NP(5)-3**, **[0.2$_{DOX}$]NP(5)-3**, **[0.5$_{DOX}$]NP(5)-1**, **[0.2$_{DOX}$]NP(5)-1**, **[0.5$_{DOX}$]NP(20)-3**, **[0.2$_{DOX}$]NP(20)-3**, **[0.5$_{DOX}$]NP(20)-1**, and **[0.2$_{DOX}$]NP(20)-1**) was added, frozen, and lyophilised. The mass of the nanoparticles was then determined and nanoparticles were resuspended in DMSO at 1 mg/ml concentrations until fully dissolved. Samples were centrifuged at 13,000 rpm for 15 minutes and then fluorescence spectrometry was performed. The fluorescence at 610 nm was measured from 520 nm excitation and compared to a Dox concentration curve prepared in DMSO to determine the mass of Dox in the nanoparticle sample.

Drug Release Via Diffusion

Spectra-Por® Float-A-Lyzers® G2 (20 kDa molecular weight cut off) were first pre-soaked, as per the manufacturer’s instructions and emptied. 1 ml deionised H_2O was added to the dialysis tube along with 110 µl of each of the **[0.2$_{DOX}$]NP(5)-3** and **[0.2$_{DOX}$]NP(20)-3** nanoparticles and the tube was submerged in the outer casing and dialysed against in 5 ml H_2O. The Float-A-Lyzer was then suspended in a water bath at 37 °C. 200 µL was taken from the water reservoir at time points between 1 hours and 62 hours and the fluorescence of the sample was measured at 555 nm emission (520 nm excitation). 200 µl fresh H_2O was added to maintain the osmotic gradient.

8.7 Light Cleavage Experiments

All light cleavage experiments were performed at room temperature using a UVP CL-1000 Crosslinker (Analytik Jena GmbH, Jena, Germany) equipped with five 8W UV-A tubes (F8T5/BL368; λ_{max} = 365 nm; Analytik Jena GmbH, Jena, Germany). Samples were placed within the crosslinker and therefore all had a consistent set distance from the light source.

Coumarin Monomer (15)

15 was dissolved at a concentration of 2 mg/ml in DMSO-d_6. A ^{1}H-NMR spectra was aquired before and after the irradiation. The sample was irradiated under 365 nm in a quartz cuvette while stirring for 30 minutes.

Camptothecin-Coumarin Monomer (17)

A 1.4 mM solution of **17** was prepared by diluting compound **17** (1 mg) in acetonitrile (1 ml). 214 µl of this solution was made up to a 3 ml solution with a final 1:1 *v/v* ratio of H_2O:acetonitrile to give a concentration of 100 µM. The solution was added to a quartz cuvette and the solution was irradiated for 60 seconds and 50 µl samples were taken at each time point.

Quantum Yield Measurement

Potassium Ferrioxalate (295 mg) was dissolved in 90 ml deionised water and 10 ml H_2SO_4 (solution 1). 7.35 g $NaOAc \cdot 3H_2O$, 30 mg 1,10-phenanthroline$\cdot H_2O$ was dissolved in a solution of 20 ml deionised water and 0.9 ml conc. H_2SO_4 (solution 2). 2 ml solution 1 was added to two quartz cuvettes (optical path l = 1 cm). One cuvette was irradiated for 5 seconds under 365 nm and the other was kept in the dark. 330 µl solution 2 was added to the cuvettes and the absorbance was measured at 510 nm. **Equation 4** was used to calculate the number of moles of generated Fe^{2++} ions per unit time of irradiation (nFe^{2+} in $mol \cdot s^{-1}$).

Equation 5: $$nFe^{2+} = ((V_1 + V_2) \times \Delta A_{510})(t \times l \times \varepsilon_{510})^{-1}$$

Where $V_1 + V_2$ is the volume (l) of solution 1 and 2, respectively, ΔA_{510} is the change in absorbance at 510 nm before and after irradiation, t is the time of irradiation of the potassium ferrioxalate solution (s), l is the optical path length (cm), and ε_{510} is the molar absorptivity of the Fe^{2+}-phen complex at 510 nm ($l \cdot mol^{-1} cm^{-1}$). Values of $V_1 + V_2 = 2.33 \times 10^{-3}$, $l = 1$, t = 5, and $\varepsilon_{510} = 1.1 \times 10^4$ were used.

The irradiation intensity, I (einstein·$cm^{-2} \cdot s^{-1}$), of the 365 nm light supply was then calculated using **Equation 6**. This number was then used in **Equation 3** to find the quantum yield.

Equation 6: $$I = nFe^{2+}/\Phi^{365}$$

Where Φ^{365} is the quantum efficiency of photoreduction of ferrioxalate at 365 nm, given as 1.21 in literature[122].

CM-DMA-2 Polymer

A 2 mg/ml sample of **CM-DMA-2** in D_2O was prepared and an NMR spectrum was acquired. The solution was transferred to a quartz cuvette, irradiated under 365 nm for 30 minutes, before another NMR spectra was acquired.

A 1 mg/ml solution of **CM-DMA-2** was prepared in PBS and an absorbance spectrum was acquired. The solution irradiated at 365 nm for 30 minutes and a second absorbance spectra was acquired.

CM-DMA-4 Nanoparticles

A 1 ml solution of **CM-DMA-4** nanoparticles was prepared by diluting 100 µl of the nanoparticle stock solution with 900 µl H_2O (0.6 mg/ml total polymer concentration). The solution was added to a quartz cuvette and irradiated at 365 nm under stirring. 200 µL samples of the nanoparticles were taken at intervals between 0 - 30 minutes of irradiation and placed into an Eppendorf and centrifuged at 20,000 rpm, at 5°C, for 30 minutes. Following centrifugation, a 100 µL sample of the supernatant was taken and the fluorescence signal of released Rhodamine B was measured (λ_{ex} = 540 nm, λ_{em} = 570 nm).

CM-CPT-DMA Polymer

A 2 mg/ml solution of **CM-CPT-DMA** was prepared in a 50:50 mixture of H_2O (0.1 % FA) and Acetonitrile (0.1 % FA) and was irradiated in a quartz cuvette while stirring under 365 nm for 5 minutes. Samples were taken following 0 seconds, 15 seconds, 30 seconds, 45 seconds, 60 seconds, 120 seconds, 180 seconds, 300 seconds of cleavage. HPLC and LCMS was performed on the samples. The peak height at t_R 5.33 and 4.75 minutes on the HPLC was recorded. Calculations of cleavage were based on the assumption that the concentration of camptothecin within the polymer sample (at the 2 mg/ml concentration irradiated) was approximately 0.120 mM based on the composition of the polymer.

PEG5-CM-PLA5 and PEG5-CM-PLA20

Photolysis in DMF

The polymers **PEG5-CM-PLA5** and **PEG5-CM-PLA20** were suspended in DMF containing 0.1 % LiBr at a concentration of 4 mg/ml and placed a quarts cuvettes containing a stirrer bar. Samples were taken at time points between 0 mins - 60 mins of 365 nm irradiation and ran through the GPC in DMF with 0.1 % LiBr, monitoring the cleavage using the 400 nm detector on the GPC.

Photolysis in H_2O

[0.2$_{DOX}$]NP(5)-3 and **[0.2$_{DOX}$]NP(20)-3** were irradiated under 365 nm at concentrations of 3 mg/ml. 100 µl samples were taken between 0 – 60 minutes of irradiation, placed into amberised Eppendorfs, frozen, and dried using lyophilisation. Samples were resuspended in DMF with 0.1 % LiBr, and ran on the GPC in the same solvent mixture using the 400 nm detector.

[0.2$_{DOX}$]NP(5)-3 and [0.2$_{DOX}$]NP(20)-3 Nanoparticles

[0.2$_{DOX}$]NP(5)-3 and **[0.2$_{DOX}$]NP(20)-3** nanoparticles were diluted to 0.1 mg/ml and irradiated under 365 nm while stirring. 100 µl samples were taken after 0 - 15 mins of irradiation and centrifuged at 13,000 rpm for 30 minutes. The peak of the fluorescence emission of the supernatant at 560 nm (λ_{ex} = 520 nm), was measured

8.8 Biological Studies

8.8.1 Cell Culture

HeLa and MCF7 cells were cultured in ‘complete media’ consisting of Dulbecco’s modified Eagle medium (DMEM) supplemented with L-glutamine (4 mM), 10 % fetal bovine serum (FBS), and antibiotics (penicillin and streptomycin, 100 units/ml). Phenol red-free media was also prepared using Fluorobrite™ DMEM using the same supplements. Cell cultures were performed in a SteriCult 200 (Hucoa-Erloss) incubator at 5 % CO_2 atmosphere at 37 °C. To culture and plate the cells, the cells were washed with PBS, detached with trypsin/EDTA (0.25 % trypsin, 1 mM in PBS), diluted in DMEM, counted, then further diluted with DMEM to the appropriate concentration.

8.8.2 Cell Viability Assay

Cell viability was assessed using the MTT assay. The cell media was replaced with 100 µL of 3-(4,5-dimethylthiazol-2-yl)-2,5-diphenyltetrazolium bromide (MTT) solution (1 mg/ml) in PBS and the cells incubated for a further 3 h at 37 °C. After incubation, the resulting formazan crystals were dissolved by adding 100 µL of MTT solubilisation solution (10 % Triton-X 100 in 0.1 N HCI in isopropanol). The absorbance was measured at a wavelength of 570 nm (BioTek HT Synergy multi-mode reader) and the results compared to untreated (control) cells.

Poly-L-Lysine RAFT Agent Polymers

HeLa cells were plated in a 96-well plate at 5 × 10^3 cells per well and allowed to grow to ~70% confluency overnight. Cells were incubated for 24 h with solutions at desired concentrations of **0Lys-PDMA-7.5k**, **3Lys-PDMA-7.5k**, **5Lys-PDMA-7.5k**, **7Lys-PDMA-7.5k** (5, 50, and 400 µg/ml), or **0Lys-PDMA-50k**, **3Lys-PDMA-50k**, **5Lys-PDMA-50k**, **7Lys-PDMA-50k** (5, 50, 400, and 1000 µg/ml) in complete media. After incubation, cells were washed twice using PBS and the MTT assay was performed.

Intra-Cellular Drug Release Studies

CM-CPT-DMA Polymers

Cells were plated in 96 well plates (10,000 cell per well density), and allowed to grow to ~60 % confluency overnight. Cells were then incubated with the polymer **CM-CPT-DMA** in 200 µl complete media for 24 hours at concentrations of 6.25 µg/ml, 12.5 µg/ml, 25 µg/ml, 50 µg/ml, 100 µg/ml, and 250 µg/ml (corresponding to concentrations of camptothecin of 0.375 µM, 0.75 µM, 1.5 µM, 3 µM, 6 µM, and 15 µM, respectively). The polymer solutions were then removed, the cells were washed with phenol red-free media and 200 µl of phenol red-free media was added to each well. Cells were then either placed in the dark or irradiated for 2 minutes under 365 nm irradiation. 4 hours later an MTT assay was performed.

[0.2$_{DOX}$]NP(5)-3 and [0.2$_{DOX}$]NP(20)-3

To perform to experiment HeLa and MCF7 cells were plated at 10,000 per well and allowed to adhere and reach ~60 % confluency overnight. Media was removed and replaced with phenol-red free media containing either free Dox (0.125 µg/ml - 4 µg/ml), or samples of **[0.2$_{DOX}$]NP(5)-3** and **[0.2$_{DOX}$]NP(20)-3** containing the equivalent amount of Dox (based on their individual drug loading), or unloaded nanoparticles **NP(5)-3** and **NP(20)-3**. Unloaded nanoparticles were to cells at concentrations of polymer corresponding to that of the loaded nanoparticles (0.125 µg/ml, 0.250 µg/ml, 0.500 µg/ml, 1 µg/ml, 2 µg/ml, and 4 µg/ml Dox loaded nanoparticle samples (total Dox concentration) corresponded to 3.75 µg/ml, 7.5 µg/ml, 15 µg/ml, 30 µg/ml, 60 µg/ml, and 120 µg/ml unloaded nanoparticle samples (total polymer concentration)). Cells were left to incubate for 24 hours, media was removed and replenished with 200 µl fresh phenol-red free media. The plates were then either placed in tinfoil and left in a cupboard for 2 minutes or irradiated at 365 nm for 2 minutes, plates were then placed back into the incubator for a further 24 hours before the MTT assay was performed.

8.8.3 Cellular Uptake Studies

HeLa cells were plated on a 24-wellplate at a density of 2×10^4 cells/well and grown to 70% confluency overnight at 37°C. The media was replaced with a 50 µg/ml solution of the polymers of **0Lys-PDMA-7.5k**, **3Lys-PDMA-7.5k**, **5Lys-PDMA-7.5k**, **7Lys-PDMA-7.5k**, or **0Lys-PDMA-50k**, **3Lys-PDMA-50k**, **5Lys-PDMA-50k**, **7Lys-PDMA-50k** in complete DMEM media and the cells were incubated for 24 h. After incubation, the cells were washed twice with PBS and harvested with 500 µL trypsin/EDTA (0.25 % trypsin, 1 mM in PBS), transferred to falcon tubes, and the trypsin/EDTA deactivated by adding fresh 500 µL complete DMEM. The cells were washed twice via centrifugation with complete DMEM and resuspended in FACS buffer (PBS, 10% FBS, 0.1% NaN_3) and analysed by flow cytometry.

Live Cell Microscopy

Brightfield

HeLa and MCF7 cells incubated with CM-CPT-DMA or **[0.2$_{\text{DOX}}$]NP(5)-3** and **[0.2$_{\text{DOX}}$]NP(20)-3** were prepared the same as for the cell viability experiments and were imaged using the brightfield of a Leica microscope under a 10x objective.

Confocal

HeLa cells were plated on an 8-well µ-Slide (ibidi GmbH, Germany) with 10×10^4 cells/well and grown to 40 % confluency for 24 h at 37 °C. The media was removed and replaced with ~7.5 kDa polymer solutions in DMEM (200 µg/ml), and CellLight® early Endosomes-RFP, BacMam 2.0 (ThermoFisher) solution was added according to the manufacturer's instructions, and the cells incubated for 24 h at 37 °C. After incubation, cells were washed twice with media, stained with Hoechst 33342 for 20 min and imaged in supplemented FluoroBrite$^{\mathrm{TM}}$ DMEM with a Leica SP5 confocal microscope. Microscope lasers settings were: excitation laser lines at 405 nm, 488 nm, and 595 nm with emission filters of 385–470 nm for Hoechst 33342 (nuclei stain), 505–530 nm for CF labelled polymers, and 595–615 nm for RFP (CellLight® early Endosomes-RFP).

9 Appendices

frontiers | Frontiers in Chemistry

REVIEW
published: 24 June 2022
doi: 10.3389/fchem.2022.921354

Two-Photon Absorption: An Open Door to the NIR-II Biological Window?

*Paige A. Shaw, Ewan Forsyth, Fizza Haseeb, Shufan Yang, Mark Bradley and Maxime Klausen**

EaStCHEM School of Chemistry, University of Edinburgh, Edinburgh, United Kingdom

The way in which photons travel through biological tissues and subsequently become scattered or absorbed is a key limitation for traditional optical medical imaging techniques using visible light. In contrast, near-infrared wavelengths, in particular those above 1000 nm, penetrate deeper in tissues and undergo less scattering and cause less photo-damage, which describes the so-called "second biological transparency window". Unfortunately, current dyes and imaging probes have severely limited absorption profiles at such long wavelengths, and molecular engineering of novel NIR-II dyes can be a tedious and unpredictable process, which limits access to this optical window and impedes further developments. Two-photon (2P) absorption not only provides convenient access to this window by doubling the absorption wavelength of dyes, but also increases the possible resolution. This review aims to provide an update on the available 2P instrumentation and 2P luminescent materials available for optical imaging in the NIR-II window.

Keywords: two-photon absorption, infrared dyes, fluorescent imaging, near-infrared II, two-photon microscopy, tissue penetration, pulsed lasers

Edited by:
Junsheng Chen,
University of Copenhagen, Denmark

Reviewed by:
Yuncong Chen,
Nanjing University, China
Fabiao Yu,
Hainan Medical University, China

****Correspondence:***
Maxime Klausen
mklausen@ed.ac.uk

Specialty section:
This article was submitted to Physical Chemistry and Chemical Physics,
a section of the journal Frontiers in Chemistry

Received: *15 April 2022*
Accepted: *04 May 2022*
Published: *24 June 2022*

Citation:
Shaw PA, Forsyth E, Haseeb F, Yang S, Bradley M and Klausen M (2022) Two-Photon Absorption: An Open Door to the NIR-II Biological Window?
Front. Chem. 10:921354.
doi: 10.3389/fchem.2022.921354

1 INTRODUCTION

Optical molecular imaging (OMI) technologies such as fluorescence imaging, Raman imaging, and optical coherence tomography, have emerged as safe and non-invasive tools to screen and monitor and diagnose disease in real-time, and follow treatment progress (Nicolson et al., 2021; Cao et al., 2019). Fluorescence-based OMI offers the ability to investigate biological systems with high spatio-temporal resolution and is now commonly applied to allow bio-molecular detection, drug distribution monitoring, image-guided surgery, and clinical diagnosis and therapy (Diao et al., 2015). The majority of *in vivo* fluorescence imaging approaches are performed using visible (400 nm–700 nm) and near-infrared I (NIR-I, 700 nm–900 nm) light due to the availability of light sources and detectors operating in this regime. However, the optical properties of tissues in this range of wavelengths intrinsically generate two challenges: a loss of signal due to poor penetration of light, and a low signal to background ratio (SBR) resulting from tissue auto-fluorescence (Zhang et al., 2016). The poor penetration of light *in vivo* arises due to the strong attenuation coefficients of tissue components, which causes photons to be scattered or absorbed by endogenous chromophores as they travel through tissues (**Figure 1**) (Keiser and Keiser, 2016). Tissue auto-fluorescence also represents a major limitation when imaging at shorter wavelengths. This loss in signal along with low SBR both contribute to the reduction in the resolution of the output image with increased depth, thereby limiting the optical imaging to micrometre depths.

Favorably, the spectral properties of biological tissues are strongly wavelength-dependent, which opens two windows of "biological optical transparency" that enable higher resolution fluorescence

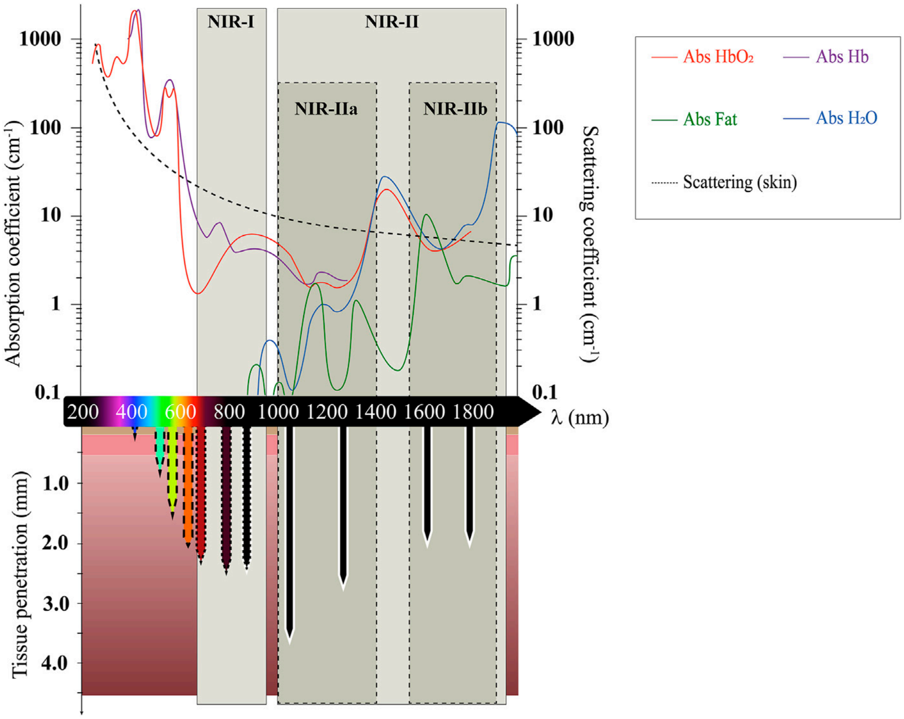

FIGURE 1 | Absorption and scattering coefficients of endogenous chromophores, tissues, and water over the visible and SWIR wavelengths (200–2000 nm). The downwards arrows represent the tissue penetration of light at these wavelengths, according to the values reported for human skin in ref. (Bashkatov et al., 2005). Dashed, dotted and solid outlines on penetration arrows represent the increase in imaging resolution with increased wavelengths. Adapted from values reported in ref (Jacques, 2015). and references therein.

imaging (Nicolson et al., 2021; Cao et al., 2019; Sordillo et al., 2014a; Kenry et al., 2018; Chen et al., 2021; Hassan and Klaunberg, 2004; Li and Wang, 2018). Firstly, the absorption coefficients of tissue components such as whole blood (oxygenated HbO_2 or deoxygenated Hb), or fat (**Figure 1**) strongly decrease when reaching red/NIR wavelengths, which constitutes a first "NIR-I″ transparency window (Bashkatov et al., 2005). Secondly, and more significantly, as the scattering coefficient of light is inversely proportional to the fourth power of its wavelength, photons of even longer wavelengths are more likely to continue on their intended linear trajectory rather than being scattered away due to their interactions within the tissue (Sordillo et al., 2014a; Wang et al., 2020a; Lockwood and Luo, 2016). For this reason, the use of low-energy light in the so-called "near-infrared II" (NIR-II) window (1000 nm–2000 nm), also known as the short-wave infrared region (SWIR), can not only help achieve higher penetration in biological tissue (**Figure 1**), but also aid in enhanced spatio-temporal resolution at fixed tissue depths, as well as reduce risks of photo-toxicity (Wang et al., 2020a; Ding et al., 2018). Moreover, tissue auto-fluorescence generated by endogenous molecules such as flavins, NADH, porphyrins, and collagens decreases significantly at longer wavelengths where these fluorophores do not absorb. Substantially diminished background auto-fluorescence is observed with NIR-II excitation, especially at wavelengths greater than 1500 nm; with this reduction in auto-fluorescence contributing to enhanced spatio-temporal resolution and fidelity in 3D images (Li and Wang, 2018; Ding et al., 2018; Tian et al., 2020). The NIR-II window can be further sub-divided into two wavelength ranges spanning across a peak in water absorption at 1450 nm (**Figure 1**), i.e. the NIR-IIa (1000–1400 nm), and the NIR-IIb (1500–1800 nm) (Ma et al., 2021a; Feng et al., 2021). In spite of a higher endogenous absorption re-emerging at such wavelengths, several studies have revealed that the higher absorption coefficient of water can be beneficial in depleting the amount of scattered photons, thereby allowing "ballistic" photons to travel deeper into the tissue. This effect is known as "absorption-induced resolution enhancement" and can therefore produce clearer fluorescence images (Yoo et al., 1991; Sordillo et al., 2014b; Carr et al., 2018a; Feng et al., 2021).

The advancement from the NIR-I to the NIR-II optical window in fluorescence imaging has been facilitated by the development of NIR-II-absorbing probes suitable for biological imaging and by the increased availability of photodetectors sensitive enough in this spectral range (Hong et al., 2017). Currently, a variety of NIR-II imaging probes, including single-walled carbon nanotubes (SWCNTs), quantum dots (QDs), rare-earth doped nanoparticles (NPs), organic dyes, and semiconductor polymer NPs have been reported but these often have poor water solubility and limited physiological stability. Most significantly, as emitted photons are of lower

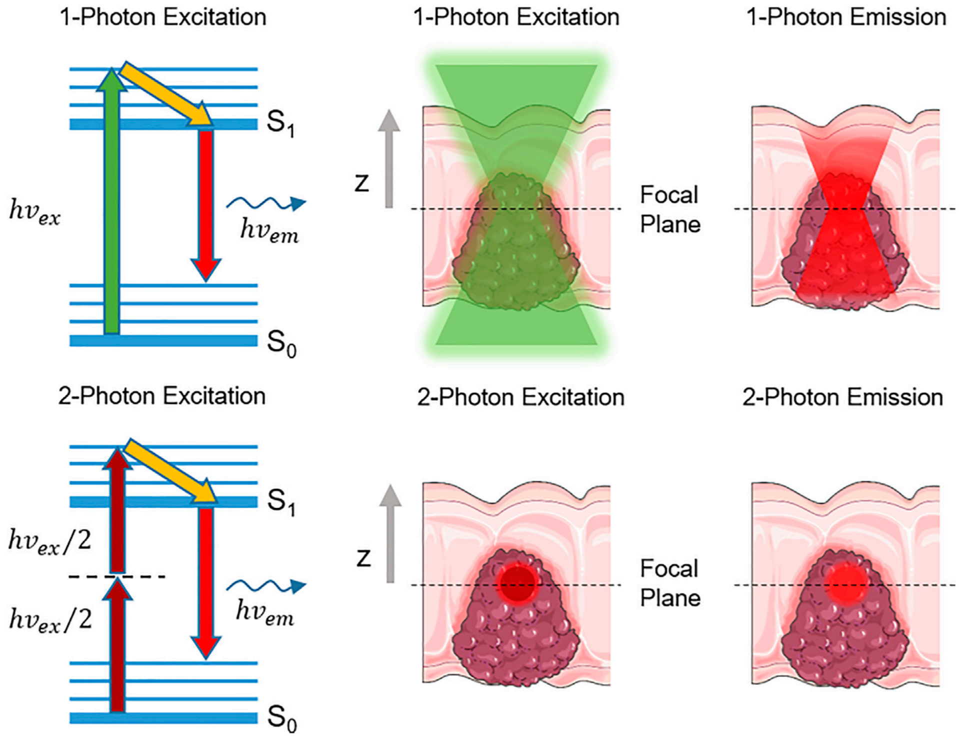

FIGURE 2 | (Left) Simplified Jablonski diagram illustrating the double-photon absorption and single-photon emission involved in 1PA vs. 2PA excitation (Middle) Demonstrates the quadratic excitation that arises in 2PA vs. 1PA, due to the requirement of two photons having to arrive simultaneously at a sample to result in excitation (Right) The resulting tissue is capable of producing fluorescence emission due to the location of the excitation photons in 2PA vs. 1PA, resulting in more focused, high-resolution images in 2PA fluorescence imaging.

energy than standard single-photon (1P) excitation, NIR-II-emitting fluorophores usually suffer from poor emission quantum yields (Φ_f). Risks are also associated with the use of inorganic nano-systems including possible toxicity and lack of tissue specificity (Ding et al., 2018; Cao et al., 2019; Zhang et al., 2021a; Chen et al., 2021; Wang et al., 2021). The specific design of NIR-II-absorbing organic probes for bio-imaging has become a key challenge in the discipline, involving the multi-step synthesis of bulky water insoluble structures which often require complex purification (Sordillo et al., 2014a; Hong et al., 2017; Wanderi and Cui, 2022). On the other hand, a number of visible and NIR-I-absorbing fluorophores exhibiting high quantum yields are commercially available, and have the ability to target a wide range of biological substrates (Carr et al., 2018b). Such dyes are comparatively easy to synthesise and are routinely used for bio-imaging using one-photon absorption (1PA) (Escobedo et al., 2010). The use of two-photon (2P) fluorescence microscopy can facilitate the imaging in the NIR-II window by targeting 1P-absorbing visible/NIR-I dyes but with the added advantage of deep tissue penetration, exceptional feature clarity and high SBR (Carr et al., 2018b).

First predicted theoretically by Maria Göppert-Mayer in 1929 (Göppert, 1929; Göppert-Mayer, 1931), 2P absorption (2PA) is a third-order, resonant non-linear optical (NLO) process (Vivas et al., 2018; Ewart and Guenther, 2005) using the combined energy of two photons to generate an electronic transition from the ground state (S_0) to a singlet excited state (S_n) (**Figure 2**, left) (He et al., 2008; Pawlicki et al., 2009; Klausen and Blanchard-Desce, 2021; Pascal et al., 2021). Contrary to 1P excitation (1PE), 2P excitation (2PE) therefore requires near-simultaneous absorption of two photons of the same frequency ν (degenerate 2PA) or different frequencies ν_1 and ν_2 (non-degenerate 2PA). The excitation occurs as a two-step process, firstly involving a transition to a short-lived (sub-femtosecond) non-resonant excited state, called the "virtual state" (dashed line, **Figure 2**, left). Assuming that each chromophore is exposed to the same laser cross-section, photons must arrive on the attosecond timescale to further promote electron excitation to a singlet excited state. Furthermore, as with all non-linear processes, the relationship between the excitation light intensity and fluorescence intensity is non-linear (quadratic) and therefore excitation can only occur when the photon flux of the excitation light is in the range of 10^{20}–10^{30} photons/(cm^2·s) (Ewart and Guenther, 2005). This high energy density can be achieved by using an ultra-short (~100 fs) pulsed (~80 MHz) laser system (Ávila et al., 2019). In such non-linear conditions, the capacity of a dye to absorb 2P light differs from standard 1PE. The 2PA capacity of a dye is defined as its 2PA cross-section (e.g. the effective "photon-catching area" of the molecule), noted as σ_2 and expressed in Göppert–Mayer unit (1 GM = 10^{-50} cm^4·s·photon^{-1}), as a tribute to Maria Göppert-Mayer's work (He et al., 2008; Pawlicki et al., 2009; Klausen and Blanchard-Desce, 2021; Pascal et al., 2021).

After excitation and internal conversion, the electron relaxes to the lowest singlet excited state (Kasha's rule), from where all radiative and non-radiative decays occur, regardless of the type of excitation. With regards to biomedical imaging applications, this is essential, as the fluorescence generated (emission wavelength and efficiency) during radiative decay is the same after either 1PE or 2PE (Denk et al., 1990; Ewart and Guenther, 2005; Benninger and Piston, 2013). The efficiency of the radiative decay process is quantified by the fluorescence quantum yield Φ_f, representing the number of photons emitted per photon absorbed. In microscopy applications, the overall brightness of a fluorescent imaging agent at a given wavelength is therefore defined as the product of its absorption capacity ($\varepsilon^{(\lambda)}$ in 1PA, or $\sigma_2^{(\lambda)}$ in 2PA) and its emission quantum yield Φ_f. In 2P applications, the 2P brightness $\sigma_2\Phi_f$ thus allows direct comparison between fluorophores (Kim and Cho, 2015).

Further adding to the imaging benefits, as the quadratic nature of the 2P process confines the excitation to a femtoliter-sized volume where the light intensity is the highest, 2PE avoids photon absorption and fluorescence both above and below the focal point (**Figure 2**, middle and right). As the fluorescence only originates from the focal point without out-of-focus emission of light, 2P microscopy provides inherent "confocality", which allows high-resolution and high contrast imaging of thick living samples (Denk et al., 1990; Piston, 2005). This also prevents extensive photo-bleaching and photo-toxicity in live samples (Looney et al., 2011; Lu et al., 2020). Thanks to such unparalleled advantages over linear 1PE, 2PA has not only been extensively employed in bio-imaging and cell signal monitoring (Benninger and Piston, 2013; Kim and Cho, 2015; Kucikas et al., 2021; Helmchen and Denk, 2005; Ricard et al., 2018), but also in photodynamic therapy (PDT) (Sun et al., 2017a) and drug delivery (Klausen and Blanchard-Desce, 2021). In the context of NIR-II bio-imaging in particular, 2PE provides alternative solutions to the challenges met with standard 1PE. While the development of 1P-absorbing NIR-II-emitting OMI probes intrinsically leads to a high loss in brightness, 2PA directly exploits the emissive properties of 1P dyes at shorter wavelengths, which circumvents any loss of fluorescence quantum yield. The detection of fluorescence is also maximized with the use of common visible/NIR detectors with high sensitivities compared to their NIR-II counterparts, and by the increased distance between excitation and emission wavelengths preventing loss of signal due to spectral overlap. In addition, while standard single-photon confocal can only image samples of up to 200 µm in thickness, 2P microscopy improves imaging penetration depth by at least 2-fold relative to confocal imaging (Wang et al., 2017; Rubart, 2004). Several studies have also shown improved biocompatibility of 2P imaging as compared to 1P confocal imaging (Wokosin et al., 1996a). Squirrel *et al.* demonstrated that 8h of confocal imaging at 514 nm resulted in the inhibition of hamster embryo development (Squirrell et al., 1999), even without staining. In contrast, embryo viability was maintained when imaged using a 1047 nm ultrashort pulsed laser with the same microscope system for a 24-hour period. Importantly, similar experiments have also demonstrated that even NIR-I femtosecond irradiation could impair cell division at low power, and even lead to complete cell destruction (König et al., 1997). Therefore, the development of 2P microscopy in the NIR-II optical window represents an opportunity for higher-resolution and safer cellular imaging and would also facilitate a wider range of biological imaging applications such as image-guided surgery, diagnostics, gene expression monitoring, and chemical sensing (**Figure 3**). Such advanced applications have not yet been fully explored *in vivo* with NIR-II 2PA, but have shown great promise in *ex vivo* examples or utilizing shorter wavelengths for 2PE (Paoli et al., 2009; Grienberger and Konnerth, 2012; Cao et al., 2013; Fan et al., 2018).

In order to visualise, characterise and quantify biological entities, bright molecular imaging probes are needed (Yang et al., 2020a). To generate bright 2P microscopy images without causing considerable photo-damage to the sample at laser intensities required ($1\ \mathrm{GW{\cdot}cm^{-2}}$ at the focal plane; or ~5 mW at the objective lens), it is estimated that the 2P brightness $\sigma_2\Phi_f$ of the imaging agent should be more than 50 GM (Kim and Cho, 2015; Osmialowski et al., 2020). As such, breaking down the barriers to exploit NIR-II wavelengths in 2P bio-imaging involves three main challenges: (i) shifting the 2PA band of the imaging agent beyond 1000 nm, which typically involves 1PA above 500 nm; (ii) improving the 2PA cross-section σ_2 above this wavelength, typically to values >50–100 GM; and (iii) retaining a high enough fluorescence quantum yield Φ_f to image tissues with high contrast. High water solubility, *in vivo*- and photo-stability, target specificity, and low toxicity are other general key criteria to develop ideal, clinically translatable OMI probes (Kim and Cho, 2015; Yang et al., 2020a; Rao et al., 2007; Yao and Belfield, 20122012). Small organic fluorophores (Wang et al., 2020a; Wu et al., 2022), aggregation induced emission (AIE) dyes (Lu et al., 2020; Zhu et al., 2018), inorganic and hybrid nanomaterials (Yao et al., 2014) and fluorescent proteins (FPs) are key types of materials that have been used in the development of OMI probes to date, and have shown high potential in the field of 2P in the NIR-II region (**Figure 3**). NIR-II-absorbing 2P-responsive dyes find applications in several additional areas beyond the scope of this review, such as optical power limiting (Pascal et al., 2021), chemical and ion sensing (Ricard et al., 2018), or targeted photo-therapies (Sun et al., 2017a; Zhao et al., 2019). In this review, we aim to present the current state of available luminescent 2P probes in a biological imaging and microscopy context, and highlight the recent progress and tremendous potential in this field. In the first subsection, we present the different classes of materials available for such applications and summarise their key optical properties in **Table 1**. We then present the available pulsed excitation sources used for such applications and discuss examples of 2P *in vivo* imaging in this "second optical window" by exploring imaging and lasing systems (**Table 2**), and tissue penetration depths (**Table 3**).

2 NIR-II-ABSORBING LUMINESCENT MATERIALS FOR 2P BIO-IMAGING

2.1 Organic Fluorophores

Reaching the NIR-II window with 2P excitation typically involves using dyes with 1PA maxima ranging from orange to NIR-I wavelengths. The design of 2P-responsive organic fluorophores

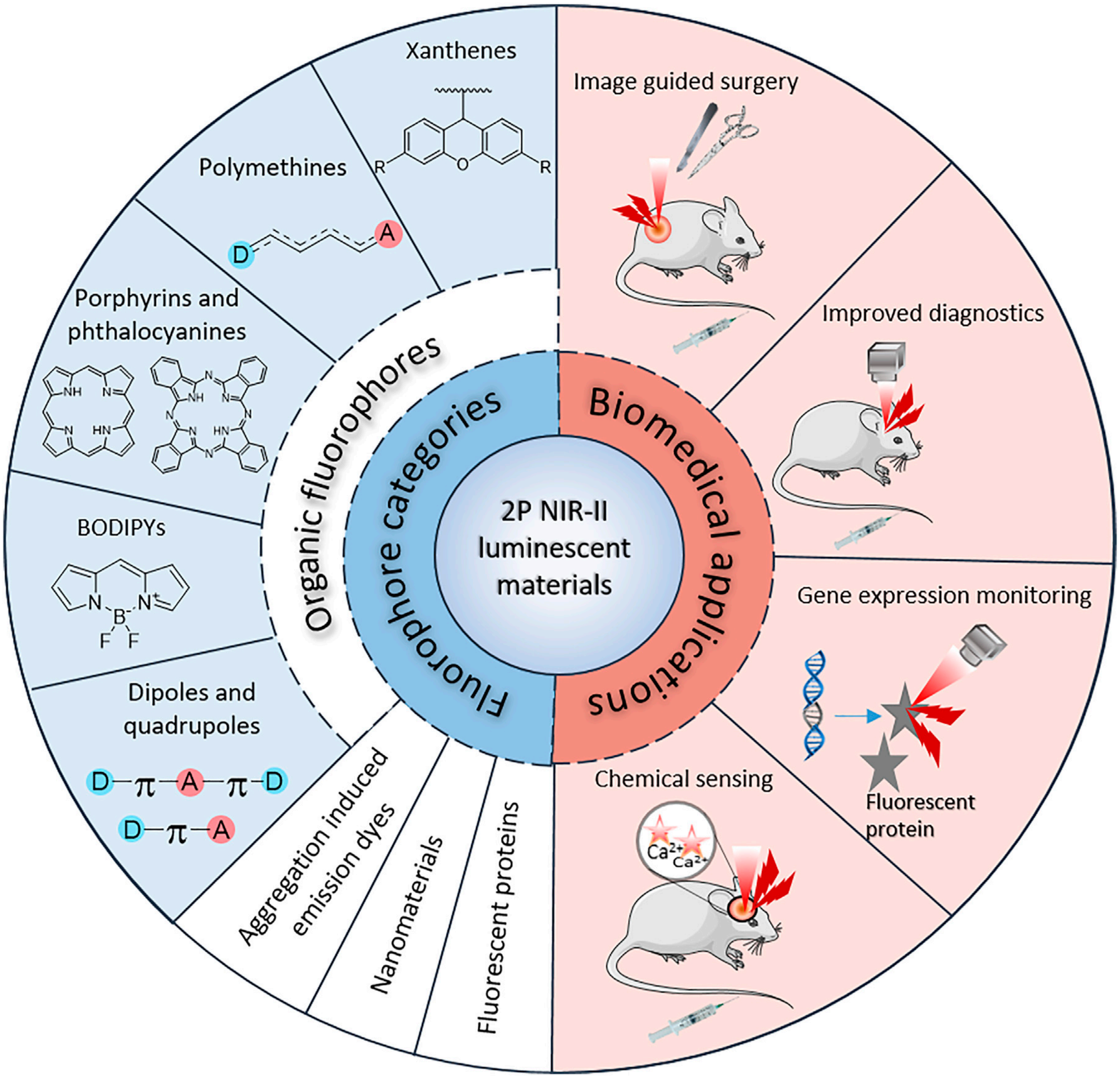

FIGURE 3 | Overview of fluorophore categories and potential biomedical applications with 2PA NIR-II imaging.

has been covered extensively in several reviews and falls beyond the immediate scope of this review (He et al., 2008; Pawlicki et al., 2009; Klausen and Blanchard-Desce, 2021; Pascal et al., 2021; Kim and Cho, 2015). However, to achieve such results the following parameters must be taken into account. Even more so than in the context of standard 1PE, the size/length of the π-conjugated system and the magnitude of intramolecular charge transfer (ICT) are major driving forces for the 2PA capacity of a chromophore. Therefore, selecting strong electron-donating (ED) and electron-withdrawing (EW) moieties or extending the π-conjugated backbone in a push–pull compound are typical strategies to cause both ICT-induced bathochromic shifts in absorption wavelengths and increase in 2PA cross-sections. Nonetheless, to achieve NIR-II absorption, the selection rules of 2PA should be considered due to their direct effect on allowed electronic transitions within the molecule, which in turn affects its maximum absorption wavelength. Symmetry-based selection rules state that 2P electronic transitions at 2 × λ_{1PA}^{max} wavelengths are forbidden in centrosymmetric chromophores. As a result, 2PA bands in symmetrical dyes are usually more intense, but shifted to higher energies, which can be a limitation in the design of NIR-II-absorbing dyes. Dipolar dyes present no such restriction as the transition to the first excited state is generally both 1P- and 2P-allowed. Therefore, 2P-absorbers with dipolar (D-π-A) or symmetrical (quadrupolar D-π-A-π-D, A-π-D-π-A; or octupolar D-(π-A)$_3$, A-(π-D)$_3$) structures, sometimes belonging to well-known classes of dyes, have been investigated in recent years and will be reviewed below. With the development and increased accessibility of SWIR pulsed laser technologies (**Section 3**, **Tables 2** and **3**), several studies have shown that remarkable potential resides in the pool of current

TABLE 1 | 1PA, 2PA and emission properties of NIR-II chromophores reported in literature. Solvent and method of 2P properties are also noted for comparison.

Probe	Chemical structure	Solvent	λ_{1PA}^{max} (nm)	λ_{em}^{max} (nm)	Φ_f	$2\lambda_{1PA}^{max}$ (nm)	λ_{2PA} (nm)	$\sigma_2^{(\lambda)}$ (GM)^a	$\sigma_2^{(\lambda)}\Phi_f$ (GM)^a	Ref.
Xanthenes										
Disodium fluorescein **(1)**	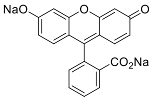	pH11	497	518^c	0.90^c	994	1000	2.7	2.4^b	(Makarov et al., 2008; Mütze et al., 2012)
PhenGreen FL (diacetate, uncomplexed) **(2)**	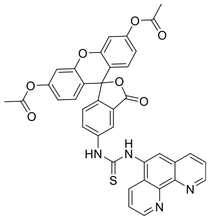	PBS	492^c	517^c	0.80^c	984	1074	n.d.	n.d.	(Bestvater et al., 2002)
Rhodamine 6G **(3)**	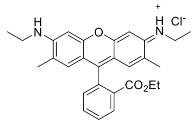	MeOH	519^c	546^c	0.95^c	1038	1060	10	9.5^b	(Makarov et al., 2008)
Rhodamine B **(4)**	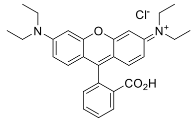	MeOH	553^c	627^c	0.70^c	1106	1040	39	27^b	Makarov et al., 2008
Rhodamine 101 **(5)**	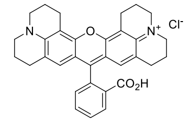	EtOH	570^c	591^c	1.0^c	1140	1060	20	20^b	(Li and She, 2010; Mütze et al., 2012)
Rhodamine 123 **(6)**	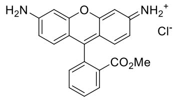	PBS	507	529^c	0.90^c (EtOH)	1014	1090	n.d.	n.d.	(Bestvater et al., 2002)
Alexa Fluor 488 **(7)**	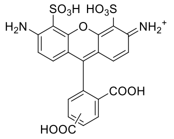	NaPhos	491	519^c	0.92^c	980	1000	21^b	19	(Bestvater et al., 2002; Anderson and Webb, 2011; Mütze et al., 2012)
Alexa Fluor 546 **(8)**	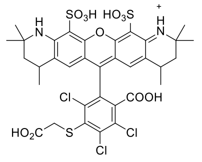	PBS	553	573^c	0.79^c	1112	1028	n.d.	n.d.	(Bestvater et al., 2002; Mütze et al., 2012)
Alexa Fluor 568 **(9)**	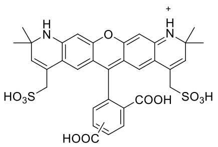	PBS	578^c	603^c	0.69^c	1156	1060	n.d.	n.d.	(Mütze et al., 2012)
Alexa Fluor 594 **(10)**	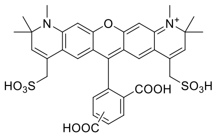	PBS	594^c	617^c	0.66^c	1180	1074	n.d.	n.d.	(Bestvater et al., 2002; Mütze et al., 2012)

(Continued on following page)

TABLE 1 | (*Continued*) 1PA, 2PA and emission properties of NIR-II chromophores reported in literature. Solvent and method of 2P properties are also noted for comparison.

Probe	Chemical structure	Solvent	λ_{1PA}^{max} (nm)	λ_{em}^{max} (nm)	Φ_f	$2\lambda_{1PA}^{max}$ (nm)	λ_{2PA} (nm)	$\sigma_2^{(\lambda)}$ (GM)[a]	$\sigma_2^{(\lambda)}\Phi_f$ (GM)[a]	Ref.
Alexa Fluor 610 **(11)**	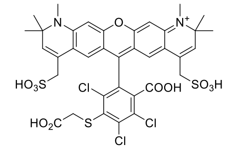	PBS	612[c]	628[c]	–	1224	1010	n.d.	n.d.	(Mütze et al., 2012)
Alexa Fluor 633 **(12)**	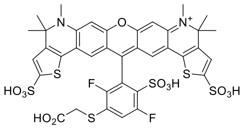	H_2O	632[c]	647[c]	–	1264	1260	n.d.	<5	(Kobat et al., 2009; Mütze et al., 2012)
MitoTracker Red **(13)**	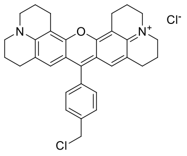	PBS	579[c]	599[c]	0.15 [187]	1158	1133	n.d.	n.d.	(Bestvater et al., 2002)
CellTracker Red **(14)**	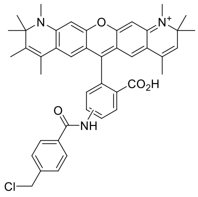	*In vitro*	585[c]	602[c]	n.d.	1170	1080	n.d.	n.d.	(Rakhymzhan et al., 2017)
Lissamine Rhodamine-IgG **(15)**	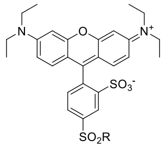	PBS	570[c]	590[c]	0.33 [188]	1140	1116	n.d.	n.d.	(Bestvater et al., 2002)
Texas Red-IgG **(16)**	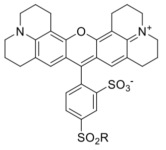	PBS	596[c]	615[c]	0.90[c]	1192	1150	n.d.	n.d.	(Bestvater et al., 2002)
ATTO 680 **(17)**		*In vitro*	681[c]	698[c]	0.30[c]	1362	1260	n.d.	n.d.	(Rakhymzhan et al., 2017)
Nile Red **(18)**	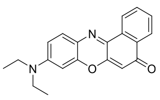	MeOH	550	636	0.40	1100	1057	104	42	(Hornum et al., 2020)
19	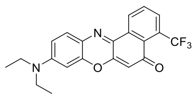	MeOH	554	631	0.43	1108	1055	183	79	(Hornum et al., 2020)
20	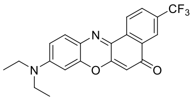	MeOH	569	632	0.45	1065	1050	123	55	(Hornum et al., 2020)
21	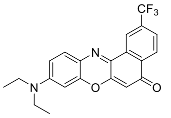	MeOH	565	638	0.35	1130	1057	232	81	(Hornum et al., 2020)

(Continued on following page)

TABLE 1 | (*Continued*) 1PA, 2PA and emission properties of NIR-II chromophores reported in literature. Solvent and method of 2P properties are also noted for comparison.

Probe	Chemical structure	Solvent	λ_{1PA}^{max} (nm)	λ_{em}^{max} (nm)	Φ_f	$2\lambda_{1PA}^{max}$ (nm)	λ_{2PA} (nm)	$\sigma_2^{(\lambda)}$ (GM)[a]	$\sigma_2^{(\lambda)}\Phi_f$ (GM)[a]	Ref.
			Polymethines							
Cy3-IgG (**22**)	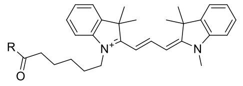	PBS	548[c]	563[c]	0.1[c]	1096	1032	n.d.	n.d.	(Bestvater et al., 2002)
Cy5 (**23**)	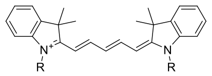	H_2O	646[c]	662[c]	0.28[c]	1292	1220	143[b]	≈40	(Kobat et al., 2009)
Cy5.5 (**24**)	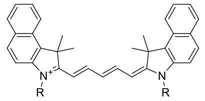	H_2O	673[c]	691[c]	0.21[c]	1346	1280	286[b]	≈60	(Kobat et al., 2009)
Cy7 (**25**)	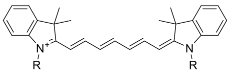	H_2O	750[c]	773[c]	0.30[c]	1500	1320	200[b]	≈60	(Kobat et al., 2009)
26	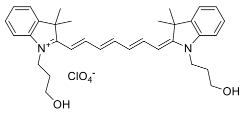	DMSO	753	780	0.17	1506	1552	240	41[b]	(Berezin et al., 2011)
ICG (**27**)	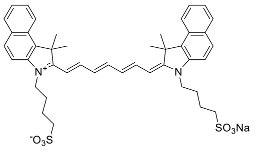	DMSO	794	817	0.12	1588	1552	590	71[b]	(Berezin et al., 2011)
Cypate (**28**)	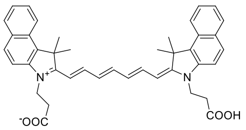	DMSO	796	817	0.13	1592	1552	520	68[b]	(Berezin et al., 2011)
29	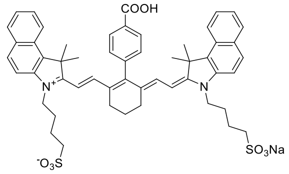	DMSO	809	829	0.07	1618	1552	900	63[b]	(Berezin et al., 2011)
DTTC (**30**)	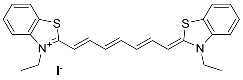	DMSO	771[c]	800[c]	0.80[c]	1542	1552	160	128[b]	(Berezin et al., 2011)
DODCI (**31**)	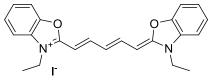	EtOH	582[c]	610[c]	0.87[c] (DMSO)	1164	1060	38	n.d.	(Li and She, 2010)
IR-140 (**32**)	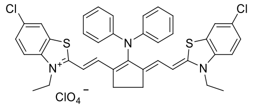	DMSO	825	≈840	0.06	1640	1552	950	57[b]	(Berezin et al., 2011)
33	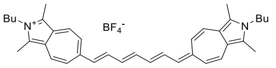	CH_2Cl_2 CH_3CN	1064 1043	≈1080 ≈1065	0.05 0.05	2128 2086	1800 1800	2250 1050	113[b] 53[b]	(Hu et al., 2013)
34	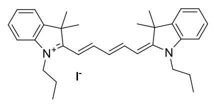	EtOH	650	665	n.d.	1300	1180	140	n.d.	(Fu et al., 2007)

(Continued on following page)

TABLE 1 | (*Continued*) 1PA, 2PA and emission properties of NIR-II chromophores reported in literature. Solvent and method of 2P properties are also noted for comparison.

Probe	Chemical structure	Solvent	λ_{1PA}^{max} (nm)	λ_{em}^{max} (nm)	Φ_f	$2\lambda_{1PA}^{max}$ (nm)	λ_{2PA} (nm)	$\sigma_2^{(\lambda)}$ (GM)[a]	$\sigma_2^{(\lambda)}\Phi_f$ (GM)[a]	Ref.
35	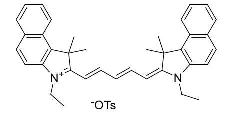	EtOH	690	704	n.d.	1380	1260	150	n.d.	(Fu et al., 2007)
36	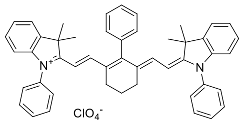	EtOH	770	n.d.	n.d.	1540	1340	60	n.d.	(Fu et al., 2007)
37	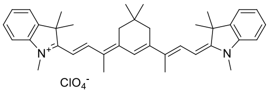	EtOH	824	n.d.	n.d.	1648	1480	600	n.d.	(Fu et al., 2007)
Alexa Fluor 647 (**38**)	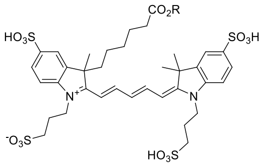	H_2O	650[c]	665[c]	0.33[c]	1300	1240	133[b]	≈44	(Kobat et al., 2009; Mütze et al., 2012)
Alexa Fluor 680 (**39**)	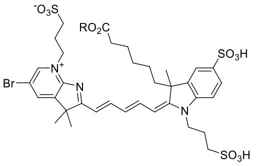	H_2O	679[c]	702[c]	0.36[c]	1358	1280	203[b]	≈73	(Kobat et al., 2009)
Alexa Fluor 700 (**40**)	–[d]	H_2O	702[c]	723[c]	0.25[c]	1404	1320	208[b]	≈52	(Kobat et al., 2009)
Alexa Fluor 750 (**41**)	–[d]	H_2O	753[c]	778[c]	0.12[c]	1506	1320	292[b]	≈35	(Kobat et al., 2009)
42	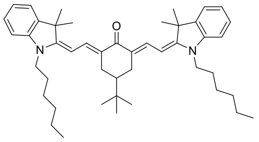	MeOH	532	636	0.44	1064	1064 (900)	23 (570)	10[b]	(Pascal et al., 2017)
43	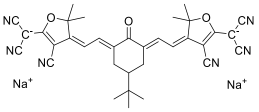	MeOH	573	708	0.33	1146	1146	225	74[b]	(Pascal et al., 2017)
44	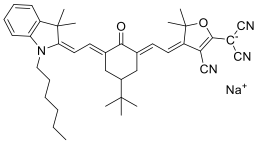	MeOH	549	673	0.54	1098	1098	137	74[b]	(Pascal et al., 2017)
45	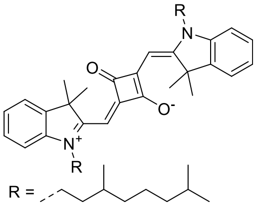	Toluene	643	654	0.62	1286	1198	133	82[b]	(Ceymann et al., 2016)

(Continued on following page)

TABLE 1 | (*Continued*) 1PA, 2PA and emission properties of NIR-II chromophores reported in literature. Solvent and method of 2P properties are also noted for comparison.

Probe	Chemical structure	Solvent	λ_{1PA}^{max} (nm)	λ_{em}^{max} (nm)	Φ_f	$2\lambda_{1PA}^{max}$ (nm)	λ_{2PA} (nm)	$\sigma_2^{(\lambda)}$ (GM)^a	$\sigma_2^{(\lambda)}\Phi_f$ (GM)^a	Ref.
46	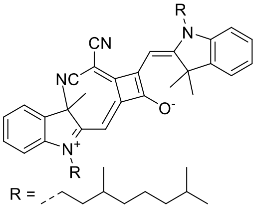	Toluene	700	714	0.75	1400	1274	100	75^b	(Ceymann et al., 2016)
Styryl 9M (**47**)	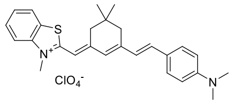	$CHCl_3$	≈625	≈790	0.10 [189]	≈1250	1240	780	78	(Makarov et al., 2008)
FM4-64 (**48**)	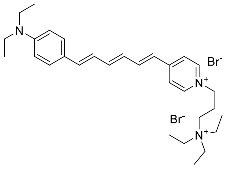	PBS $CHCl_3$ (López-Duarte et al., 2015)	471 564	691 761	n.d. 0.35	942 1128	1047	n.d.	n.d.	(Wokosin et al., 1996a; Nuriya et al., 2016)
TO-PRO-3 (**49**)	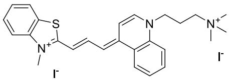	H_2O	641^c	657^c	n.d.	1284	1110	n.d.	n.d.	(Smith et al., 2012)
50	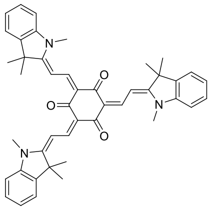	THF	562	598	0.07	1124	1070	167	12^b	(Poronik et al., 2012)
51	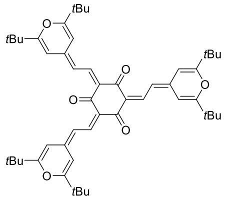	THF	615	655	0.02	1230	1150	214	4^b	(Poronik et al., 2012)
			Porphyrins							
52	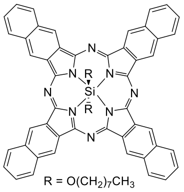	CCl_4	≈770	≈780	n.d.	≈1540	1020 1270	470 48	n.d.	(Makarov et al., 2008)
53	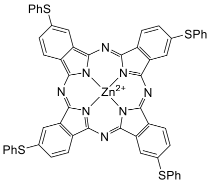	CCl_4	≈685	≈700	n.d.	≈1370	1270	13	n.d.	(Makarov et al., 2008)

(Continued on following page)

TABLE 1 | (*Continued*) 1PA, 2PA and emission properties of NIR-II chromophores reported in literature. Solvent and method of 2P properties are also noted for comparison.

Probe	Chemical structure	Solvent	λ_{1PA}^{max} (nm)	λ_{em}^{max} (nm)	Φ_f	$2\lambda_{1PA}^{max}$ (nm)	λ_{2PA} (nm)	$\sigma_2^{(\lambda)}$ (GM)^a	$\sigma_2^{(\lambda)}\Phi_f$ (GM)^a	Ref.
54	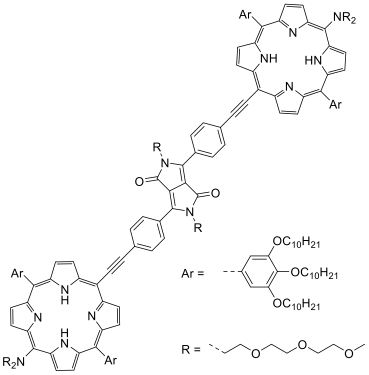	$CHCl_3$	≈525 ≈605 ≈680	710	n.d.	≈1050 ≈1210 ≈1360	≈1040 ≈1220 ≈1360	≈2000 ≈500 ≈200	n.d.	(Nowak-Król et al., 2013)
			BODIPYs							
LysoTracker Red (**55**)	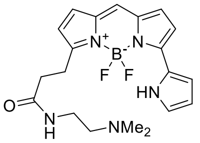	PBS	577^c	590^c	0.07	1154	1100	n.d.	n.d.	(Bestvater et al., 2002)
BODIPY-TR (**56**)	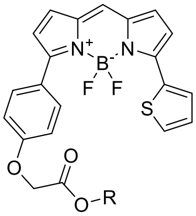	MOPS	589^c	616^c	0.90^c	1178	1060	269^b	242	(Bestvater et al., 2002; Mütze et al., 2012)
IR-07 (**57**)	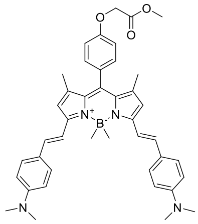	CH_2Cl_2	~700	750	0.30	~1400	1310	101	30^b	(Zheng et al., 2009)
58	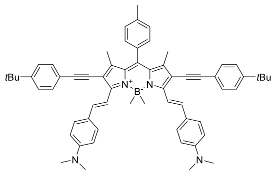	THF	755	830	0.09	1560	1064	n.d	n.d	(Hu et al., 2020)
			Dipoles – Quadrupoles – Miscellaneous							
59	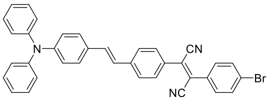	NPs (Aq.)	480	678	0.17	960	1040	5.6 × 10^5	9520	(Alifu et al., 2017)
60	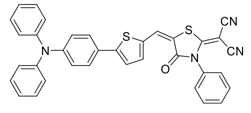	H_2O (0.1% DMSO)	530	740	n.d.	1060	1100	n.d.	n.d.	(Zhou et al., 2021)

(Continued on following page)

TABLE 1 | (*Continued*) 1PA, 2PA and emission properties of NIR-II chromophores reported in literature. Solvent and method of 2P properties are also noted for comparison.

Probe	Chemical structure	Solvent	λ_{1PA}^{max} (nm)	λ_{em}^{max} (nm)	Φ_f	$2\lambda_{1PA}^{max}$ (nm)	λ_{2PA} (nm)	$\sigma_2^{(\lambda)}$ (GM)[a]	$\sigma_2^{(\lambda)}\Phi_f$ (GM)[a]	Ref.
61	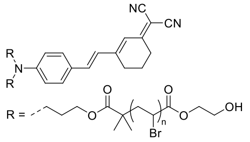	H_2O	510	676	0.22	1020	1040	440	97[b]	(Massin et al., 2013)
62	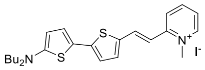	CH_2Cl_2	660	785	0.005	1320	1300	500	2.5[b]	(Ricci et al., 2017)
63	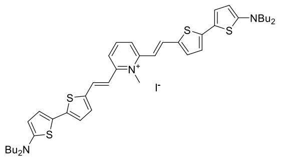	CH_2Cl_2	678	782	0.0005	1356	1300	1400	0.7[b]	(Ricci et al., 2017)
64	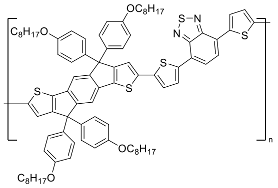	H_2O	≈600	≈725	0.21	≈1200	1200	1.21×10^3	242[b]	(Wang et al., 2019b)
65	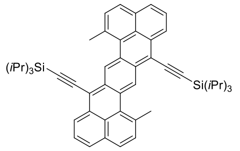	$CHCl_3$	634	704	0.16	1268	1250	920	147[b]	(Li et al., 2012)
66	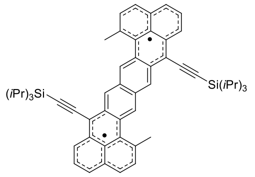	$CHCl_3$	668	807	0.02	1336	1250	1200	24[b]	(Li et al., 2012)
67	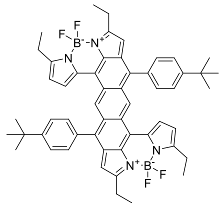	$CHCl_3$	1088	1120	0.002	2176	2200	1300	2.6[b]	(Ni et al., 2016)
68	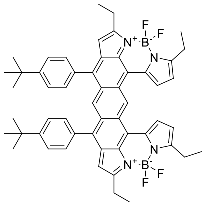	$CHCl_3$	1136	1193	0.0002	2272	2300	1500	0.3[b]	(Ni et al., 2016)
Propidium iodide (**69**)	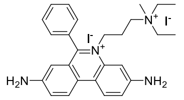	PBS	536[c]	617[c]	0.20[c] (dsDNA bound)	1072	1015	n.d.	n.d.	(Bestvater et al., 2002)

(Continued on following page)

TABLE 1 | (*Continued*) 1PA, 2PA and emission properties of NIR-II chromophores reported in literature. Solvent and method of 2P properties are also noted for comparison.

Probe	Chemical structure	Solvent	λ_{1PA}^{max} (nm)	λ_{em}^{max} (nm)	Φ_f	$2\lambda_{1PA}^{max}$ (nm)	λ_{2PA} (nm)	$\sigma_2^{(\lambda)}$ (GM)[a]	$\sigma_2^{(\lambda)}\Phi_f$ (GM)[a]	Ref.
AIEgens and AIEDots										
70	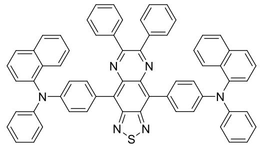	NP (aq.)	613	790-810	0.14	1226	1040 1300	16100 1220	2240[b] 170[b]	(Qi et al., 2018; Liu et al., 2021)
71	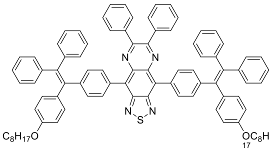	NP (aq.) THF	454 ≈451	≈700 ≈699	0.19 n.d.	908	1200 n.d.	76300 n.d.	14500[b] n.d.	(Wang et al., 2019c)
72	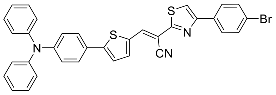	NP (aq.) H_2O/ DMSO	≈479 ≈488	≈627 >627	0.06 n.d.	≈960	1040 n.d.	3200 n.d.	192[b] n.d.	(Samanta et al., 2021)
73	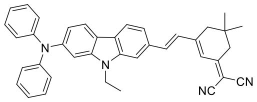	NP (aq.) Toluene	510 491	709 ≈635	0.14 (solid state)	1020	1000 n.d.	≈520 n.d.	73[b] n.d.	(Zheng et al., 2018)
74	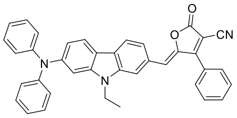	NP (aq.) Toluene	538 528	755 ≈636	0.02 (solid state)	1076	1020 n.d.	887 n.d.	18[b] n.d.	(Zheng et al., 2018)
75	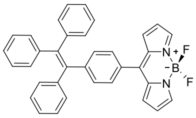	NP (aq.) THF	522 511	620 532	0.05 n.d.	1044	1040 n.d.	2.9×10^6 n.d.	1.5×10^5 n.d.	(Wang et al., 2015)
Carbon, hybrid and inorganic materials										
76	SWCNT-based dopamine sensor	H_2O	600–1000	1000–1265[e]	0.0023	–	1560	216000	497[b]	(Bonis-O'Donnell et al., 2017)
77	Aptamer-modified graphene oxide	H_2O	440–720	500–650[f]	0.34	–	1120	36000	12240[b]	(Pramanik et al., 2014)
78	CDs prepared from urea and citric acid	H_2O	540	624	0.06	1080	1200	n.d.	n.d.	(Li et al., 2018)
79	Carbon quantum dots prepared from tris(4-aminophenyl)amine	H_2O	592	615	0.84	1184	1100	n.d.	n.d.	(Liu et al., 2020)
80	AuNP with SWCNT	H_2O	500–1100	775	n.d.	–	1100	n.d.	n.d.	(Olesiak-Banska et al., 2019)
81	Au25 cluster	H_2O	675	830	<0.001	1350	1290	2700	n.d.	(Ramakrishna et al., 2008)
82	PEG-dithiolane AuNC	H_2O	355, 670	820	0.08	1370	1100	300	24[b]	(Oh et al., 2013)
83	Mn^{2+}-ZnS QD	H_2O	318	586	0.65	636	1180	265	172[b]	(Subha et al., 2013)
84	PbS/CdS QD	H_2O	665	1270	0.18	1330	1550	530	95[b]	(Ni et al., 2022)
QD605 (**85**)	polymer-encapsulated CdSe-ZnS QD	H_2O	350–475	605	0.71	–	1000	66200[b]	47000	(Larson et al., 2003)
Fluorescent proteins										
tdTomato (**86**)	–	H_2O	554[g]	581	0.72[b]	1108	1050	278	200	(Drobizhev et al. 2011)
tdKatushka2 (**87**)	–	H_2O	588[g]	633	0.44[b]	1176	1100	143	63	(Drobizhev et al. 2011)
dsRed2 (**88**)	–	H_2O	561[g]	587	0.71[b]	1126	1050	103	73	(Drobizhev et al. 2011)
HcRFP (**89**)	–	PBS	592[g]	645[g]	0.05[g]	1184	1160	720[b]	36	(Tsai et al., 2006)
mCherry (**90**)	–	H_2O	587[g]	610	0.24[b]	1174	1080	27	6.4	(Drobizhev et al. 2011)
mBanana (**91**)	–	H_2O	540[g]	553	0.69[b]	1080	1070	64	44	(Drobizhev et al. 2011)
mStrawberry (**92**)	–	H_2O	574[g]	596	0.34[b]	1148	1070	20	6.8	(Drobizhev et al. 2011)

(Continued on following page)

TABLE 1 | (*Continued*) 1PA, 2PA and emission properties of NIR-II chromophores reported in literature. Solvent and method of 2P properties are also noted for comparison.

Probe	Chemical structure	Solvent	λ_{1PA}^{max} (nm)	λ_{em}^{max} (nm)	Φ_f	$2\lambda_{1PA}^{max}$ (nm)	λ_{2PA} (nm)	$\sigma_2^{(\lambda)}$ (GM)[a]	$\sigma_2^{(\lambda)}\Phi_f$ (GM)[a]	Ref.
mRFP (**93**)	–	H_2O	584[g]	611	0.30[b]	1168	1080	44	13	(Drobizhev et al. 2011)
TagRFP (**94**)	–	H_2O	555[g]	584	0.44[b]	1110	1050	95	42	(Drobizhev et al. 2011)
mOrange (**95**)	–	H_2O	548[g]	565	0.70[b]	1096	1080	67	47	(Drobizhev et al. 2011)
eqFP650 (**96**)	–	H_2O	592[g]	646	0.19[b]	1184	1112	45	8.5	(Drobizhev et al. 2011)
Katushka (**97**)	–	H_2O	588[g]	635	0.35[b]	1176	1080	66	23	(Drobizhev et al. 2011)
Katushka2 (**98**)	–	H_2O	588[g]	633	0.44[b]	1176	1140	62	27	(Drobizhev et al. 2011)
mKate (**99**)	–	pH8	588[g]	635	0.27[b]	1176	1118	52	14	(Drobizhev et al. 2011)
mKate2 (**100**)	–	H_2O	588[g]	633	0.42[b]	1176	1140	72	30	(Drobizhev et al. 2011)
mNeptune (**101**)	–	H_2O	600[g]	651	0.17[b]	1200	1104	70	12	(Drobizhev et al. 2011)
mRaspberry (**102**)	–	H_2O	598[g]	625	0.19[b]	1196	1118	31	5.8	(Drobizhev et al. 2011)
Neptune (**103**)	–	H_2O	600[g]	647	0.22[b]	1200	1104	72	16	(Drobizhev et al. 2011)
tdRFP (**104**)	–	Aq. buffer	584 (Campbell et al., 2002)	579	0.68	1168	1110	20	13.7	(Drobizhev et al. 2011)

[ab] *Two-photon absorption cross-section value taken at the excitation wavelength λ_{2PA} reported by the authors in the NIR-II window; note that this may differ from the maximum of the 2PA band. Value extrapolated from the data available and from the formula of the 2P brightness (= $\sigma_2^{(\lambda)} \times \Phi_F$).*

[c] *1P properties as reported by commercial suppliers, reported in water unless indicated otherwise.*

[d] *Chemical structures are propriety and undisclosed.*

[e] *Chirality-dependant.*

[f] *Excitation-dependant.*

[g] *Properties extracted from the fluorescent protein database (Available at https://www.fpbase.org/, Accessed on 11/04/2022).*

biological stains and FDA approved fluorophores that offer such 1PA properties (Wokosin et al., 1996b; Bestvater et al., 2002; Fu et al., 2007; Makarov et al., 2008; Kobat et al., 2009) (**Table 1**).

2.1.1 Xanthene Derivatives

Thanks to their exceptional structural diversity, xanthene-type dyes are among the most widely used biological imaging agents. The highly versatile xanthene backbone allows for extensive structural modification, with the possibility to induce dramatic bathochromic shifts in absorption and emission through dye design. As a result, the 1PE bands of such fluorophores can range from green to NIR-II wavelengths (Liu and Scott, 2021), leading to the majority of current research being focused on the design of NIR-I to NIR-II 1P-absorbing xanthene dyes. To the best of our knowledge, only a small number of xanthene dyes have been specifically designed for 2PA in the NIR-II, but the vast number of commercially available probes in this family facilitates their use as a model for 2P measurements. This in turn has led to several seminal reports on their 2P properties at NIR-II wavelengths since the first examples in 1972 (Bradley et al., 1972).

The 2PA properties of several commercial fluorescein- and rhodamine-based probes have been studied thoroughly and are well reported (Bestvater et al., 2002; Makarov et al., 2008; Bradley et al., 1972; Li and She, 2010; Hermann and Ducuing, 1972). Fluoresceins, being the most blue-shifted xanthene dyes, possess almost no 2P response in the NIR-II window (**Table 1**), as evidenced by the negligible σ_2 of disodium fluorescein (**1**) at 1060 nm (0.069 GM) (Makarov et al., 2008). However, the heavy metal indicator PhenGreen FL^{TM} (**2**), a fluorescein derivative, was reported to show fluorescence when excited under 2PA at 1074 nm (Bestvater et al., 2002). Thanks to their higher internal charge transfer (ICT) and superior structural variety, Rhodamines possess a higher potential for 2PE in the NIR-II. Rhodamines 6G (**3**), B (**4**), 101 (**5**) and 123 (**6**) all present 2PA beyond 1000 nm (**Table 1**). Among them, Rhodamine B was reported with the highest 2PA cross-section in the early NIR-II window, with a second 2PA band at 1040 nm in MeOH (38 GM) (Makarov et al., 2008). Highly photo-stable Alexa Fluor^{TM} dyes 488 to 633 (**7–12**) were also reported with 2PA bands between 985 nm and 1264 nm respectively (Bestvater et al., 2002; Kobat et al., 2009; Anderson and Webb, 2011; Mütze et al., 2012). Alexa Fluor^{TM} 488 (**7**) responded moderately to 2PE at 1000 nm (Anderson and Webb, 2011), which corresponds to the tail of its absorption band. No quantification was performed on the other rhodamine-type Alexa Fluor^{TM} dyes, however, several other accessible cell-labelling and bioconjugatable rhodamine derivatives were investigated, such as MitoTracker Red (**13**), or Lissamine Rhodamine (**15**) and TexasRed (**16**) conjugates (Bestvater et al., 2002).

Phenoxazines are nitrogen-containing xanthene derivatives that also demonstrated 2PA properties in the NIR-II. Rakhymzhan *et al.* demonstrated the use of extended phenoxazine ATTO680 (**17**) in live cells under 2PE at 1260 nm (Rakhymzhan et al., 2017). Nile Red (**18**) is another well-known member of this class of dyes, and is commonly used as a reference for cross-section measurements using the 2P-excited fluorescence (2PEF) technique. In an effort to optimise the 2PA properties of Nile Red, Hornum *et al.* prepared and optically characterised a nu mber of halo-substituted Nile Red derivatives (Hornum et al., 2020). On this occasion, they measured a σ_2 of 104 GM for Nile Red at 1057 nm. The σ_2 of the reported derivatives were also measured between 1000 and 1200 nm, showing a substantial increase upon introduction of a trifluoromethyl group (compounds **19**, **20** and **21**). Interestingly, regio-isomer 2- (**21**) showed the highest gain in σ_2 compared to isomers 3- and 4- (**19** and **20**). Nile Red derivatives are notably solvatochromic, which increased both their 2PA wavelengths and cross-sections by up to 313% with increasing polarity.

2.1.2 Polymethine Derivatives

Polymethine dyes consist of an alternating single and double-bond backbone, which connects two aromatic moieties. Cyanine (Cy) dyes are a member of this family of dyes, with the polymethine conjugated chain separating two nitrogen-containing heterocycles (i.e. indolenine, benzindole). These core structures can tolerate numerous structural changes including: i) lateral groups (i.e. sulfo, carboxyl) on the heterocycles to increase solubility; ii) cycloalkane-rings within longer polymethine chains (Cy7, Cy7.5, squarines) for structural rigidity and photo-property tuning; iii) flexible chains terminating in functional groups (i.e. carboxylic acid, alkyne, azide, NHS ester) for attachment to drug probes (Lee et al., 2008; Pham et al., 2008; Henary et al., 2009; Sun et al., 2019). The most recently reported NIR-II polymethines have been designed for 1P-excited fluorescence (1PEF), including BTC1070 which employed a pentamethine chain, benzothiopyrylium heterocycles and diethylamino ED moieties to achieve emission above 1000 nm (Wang et al., 2019a). Selection rules will affect differently polymethines bearing identical or different substituents on each side of the poly-ene chain, which will therefore modify the nature of their dominant 2P transition. Largely blue-shifted transitions can be observed in certain environments in the case of symmetrical polymethines.

The polymethine family includes several commercially available and FDA-approved derivatives that have been evaluated under 2PE (**Table 1**). In 2002, Bestvater *et al.* reported the 2PA spectrum of Cy3 (**22**), showing a response at 1032 nm (Bestvater et al., 2002), and modest 2P brightnesses were then measured by Fu *et al.* and Kobat *et al.* for the original Cy5 (**23**), Cy5.5 (**24**) and Cy7 (**25**) fluorophores in the 1200–1300 nm range (Fu et al., 2007; Kobat et al., 2009). While there is much reported about the structure-1P property relationships in custom-made polymethine dyes, even towards the NIR-I and -II regime, less is known about their 2P properties. Berezin *et al.* studied the 2P properties of several cyanine derivatives with comparable conjugation under 1552 nm excitation, by varying the central and hetero-aromatic moieties (Lee et al., 2008; Berezin et al., 2011). Strong absorption was reported at this wavelength for compound **26**, a direct Cy7 analogue (240 GM).

Replacing the indolenine units with π-extended benzoindolenines causes an increase in ICT and oscillator strength leading to red-shifted optical properties and higher σ_2. This is evidenced by the commercially available and FDA-approved dye indocyanine green (ICG, **27**) whose σ_2 is more than doubled compared to **26**. Interestingly, ICG (**27**) was also used as a contrast agent for 2P fluorescence imaging at 790 nm (Kumari and Gupta, 2019), which leads to excitation in its blue-shifted $S_0 \rightarrow S_2$ band. The fluorophore thus presented an Anti-Kasha fluorescence at 570 nm, emitting directly from the S_2 excited state, which provided it with an excitation-dependent 2PEF. ICG is now used in a clinical context for diagnostic purposes (Schaafsma et al., 2011; Hackethal et al., 2018), and therefore possesses a strong potential to develop 2P imaging past 1500 nm. Cypate (**28**), a bio-conjugatable version of ICG replacing both side sulfonate groups with carboxylic acids was also prepared and characterised, leading to similar optical properties (Berezin et al., 2011). Restriction of the polymethine chain with a phenylcyclohexene moiety (**29**) led to a 70% increase in cross-section but similar brightness. DTTC and DODCI (**30** and **31**), two benzothiazolyl and benzoxazolyl analogues of Cy7 and Cy5, were also used in studies at 1552 nm (Berezin et al., 2011) and 1060 nm (Li and She, 2010) respectively. The reported cross-section for DODCI was measured at a wavelength significantly different from the $2\lambda_{1PA}$ value, but was still considerably lower than for DTTC which contains an extra double bond in its π-conjugated system. Introducing aromatic units at the 4-position of the heptamethine chain led to increased cross-sections, but halved the quantum yield. IR-140 (**32**) therefore has the largest cross-section in this class of dyes thanks to a diphenylamine unit attached to the central cyclopentene-heptamethine chain; however, this does not yield a high brightness due to a poor Φ_f. In this study, the best 2P brightness was calculated for DTTC, which was then selected for *ex vivo* 2PEF imaging of kidney tissue (**Section 3**) (Berezin et al., 2011). Additionally, the 2P properties of 2-azaazulene polymethine dye **33** were extensively studied theoretically and experimentally to elucidate their symmetrical character (Hu et al., 2013). By comparing the 2PA spectra of **33** in apolar dichloromethane and polar acetonitrile, the authors demonstrated a symmetry-breaking character in high polarity media leading to a restriction lifting of their forbidden transition at $2\lambda_{1PA}{}^{max}$, which is a crucial observation for the development of NIR-II responsive polymethines. A set of structure-property relationships was also constructed by Fu *et al.* in a seminal report on the 2PA properties of polymethine dyes (Fu et al., 2007). Cross-sections ranging from 60 to 600 GM were measured in the NIR-II on different extended, locked and substituted cyanines (dyes **34–37**), which is consistent with other reports on similar dyes. This demonstrated similar effects of conjugation lengths and ICT on the 2PA spectra and cross-sections. A strong increase in σ_2 was noted in particular for cyanine **37**, which presented the most constrained conformation. Alexa Fluor™ 647 and 680 (**38–39**) are other commercially available polymethine analogues reported with moderate 2P brightnesses (Kobat et al., 2009; Mütze et al., 2012).

Adding ketones to the central polymethine chain was found to produce fluorescent dyes **42–44** that show significant red-shifting and quantum yield increase in protic solvents (Pascal et al., 2017). Because of their pseudo-quadrupolar character, these dyes exhibit strong blue-shifted 2PA bands in the NIR-I, with σ_2 values ranging from 570 to 1400 GM at 900–970 nm. However, their transition at $2\lambda_{1PA}$ remains partially allowed, which leads to a second weaker 2PA peak in the 1100 nm region, reaching 250 GM in the case of bis-acceptor dye **44**. These dyes were modified to include hydrophilic, hydrophobic and water-solubilizing polymers, and were successfully used in 1P and 2P microscopy.

Squaraines are a particular example of keto-polymethine dyes combining two ED groups connected to a four strongly electron-deficient 4-membered ring system derived from squaric acid. This class of dyes is known for their potential to reach considerable 2PA cross-section values with relatively simple structures, which provides them with a high σ_2 to molecular weight ratio (Chung et al., 2006; Sun et al., 2017b). Only a few examples of squaraine fluorophores were investigated in the NIR-II range; yet the simplest examples of squaraines, built from indolenine subunits, show intense 2PEF upon excitation past 1000 nm (Ceymann et al., 2016). Squaraine **45** and its malononitrile derivative **46** were described as bright red/NIR fluorophores (λ_{em} = 654 nm and 714 nm), with quantum yields of 0.62 and 0.75 respectively. Both dyes showed moderate 2P response (σ_2 > 100 GM) around 1250 nm. Compound **45** was used for *in vitro* and *in vivo* for 2P imaging at 1200 nm (Yi et al., 2019). The authors demonstrated that the 2PEF of this small dye was enhanced 17.7 times in the presence of bovine serum albumin (BSA). Moreover, squaraine showed excellent photostability and low cytotoxicity. Interestingly, more advanced squaraine oligomers and branched structures were also investigated, showing high 2PA in the NIR-II (Scherer et al., 2002; Ceymann et al., 2016).

Other heptamethine cyanine dyes carrying different terminal heteroaromatic moieties (benzoindolenine, thiazole, oxazoles, azaindoles, flavyliums) have been developed and widely used as 1P contrast agents. Dimethylamino flavylium polymethine dyes have been shown to exhibit significant bathochromic shifts compared to their analogous Cy dyes, thus taking their 1PE up to 1026 nm (Cosco et al., 2017). Funabiki *et al.* also showed the importance of the counter-ion in benzo [cd] indolenyl-substituted heptamethine cyanine dyes (Funabiki et al., 2019). Already reaching the NIR-II window for *in vivo* 1PEF microscopy, these would be excellent candidates to have their 2P properties investigated.

A common trait of cyanine-type dyes is their pseudo-centrosymmetric character that can make the 2PA transition at $2\lambda_{1PA}$ partially forbidden (Hu et al., 2013), and therefore reduce their 2P brightness in the NIR-II. Non-symmetrical polymethines are another important sub-class of dyes that adopt a dipolar character and therefore overcome this feature. The 2PA spectrum of the commercially available dye Styryl 9M (**47**) was reported by Makarov *et al.*, which highlighted a high 2PA cross-section (750 GM), in the 1150–1250 nm region (Makarov et al., 2008). Styryl 9M was notably used for the detection of lysozyme amyloid fibrils with 2PE (Udayan et al., 2020). The nonpolar and viscous environment generated by the hydrophobic channels of lysozyme fibrils led to a strong bathochromic shift in the absorption spectrum of the dye, accompanied by an increase in quantum yield. FM4-64 (**48**) (Wokosin et al., 1996a) and To-Pro-3 (**49**) (Smith et al., 2012), two other non-symmetrical dipolar polymethines, were reportedly used in 2P imaging past 1064 nm. FM4-64 is also commonly used in second-harmonic generation experiments, which makes it a multi-modal imaging agent (Nuriya et al., 2016).

Merocyanines are a sub-group of dipolar polymethine chromophores constituted specifically of an amine (D) and a carbonyl (A) moiety, connected to each end of the poly-ene π-conjugated system. Merocyanines are typically sensitive to their local environment, with optical properties varying in contact with cell membranes, metal ions, or DNA; and 2PE was shown to be even more sensitive than 1PE to such variations in the local environment (Pascal et al., 2017). Fewer examples of 2P-responsive merocyanines have been reported in the NIR-II. However, in their investigation of keto-polymethines, Pascal *et al.* also reported a merocyanine-like dye **43** that showed a 2PA maximum at 1098 nm. Its moderate cross-section was compensated by a good Φ_f, which led to a brightness value of 74 GM in MeOH. An interesting example of advanced merocyanine design was also achieved by incorporating the polymethine system onto a cyclohexanetrione moiety (Poronik et al., 2012). The resulting octupolar $(D\text{-}\pi)_3\text{-}A$ structures **50** and **51** showed moderate 2PA response in the NIR-II transition ranging between 98 and 214 GM in THF.

2.1.3 Porphyrin and Phthalocyanine Derivatives

Porphyrins, phthalocyanines and other types of polypyrrole derivatives are commonly used as contrast agents or photosensitizers in biomedical applications (Josefsen and Boyle, 2012). The particular properties of such compounds make it possible to tune multiple parameters such as the lifetime of the excited state, and therefore their emissive character, by metalation. The 2PA properties of Zn-tetrakis-(phenylthio)-phthalocyanine (**52**) and Si-naphthalocyanine dioctyloxide (**53**), both commercially available, were investigated by Makarov *et al.* (Makarov et al., 2008). Both dyes showed 2PA bands at 1270 nm in CCl_4 with moderate cross-sections (**Table 1**). The silicon derivative however showed significant 2PA capacity in its higher energy band (470 GM at 1020 nm). In contrast, tetraphenylporphyrin showed virtually no absorption past 1000 nm, which is in accordance with the limited 1PA capacity associated with its red Q-band. Porphyrin derivatives can however exhibit large cross-sections, as fused-systems show an increase in both cross-section and λ_{ex2PA} with the increasing number of rings (Yoon et al., 2007), although this can lead to preferential non-radiative behaviour. Only a few examples of polypyrrole design have led to NIR-II responsive fluorescent dyes specifically for 2P imaging applications. *Meso* substitution is nonetheless a typical design strategy to amplify the 2P response of porphyrin dyes (Nowak-Król et al., 2012), and porphyrin dimers bridged by a diketopyrrolopyrrole unit at this position were prepared to form highly absorbing D-π-A-π-D dyes (Nowak-Król et al., 2013). Although no quantification was performed in this study, the authors claim that their porphyrin dimer (**54**) remained fluorescent at 710 nm. A band structure characteristic of porphyrin dyes was observed on the 2PA spectrum, which leads to broad absorption between 1000 and 1450 nm. However, while these structures are of interest, their ability to be utilised in a bio-medical setting is limited due to poor solubility in aqueous environments, and the requirement of controlled self-assembly *in vitro*.

2.1.4 BODIPY Derivatives

BODIPY dyes are often used as fluorescent trackers for imaging thanks to their high brightness, narrow fluorescence peaks and low sensitivity to changes in pH and polarity. BODIPY structures are highly tunable, and extensions of the π-conjugated system in positions 3- and 5- can lead to strong bathochromic shifts that can be exploited in 2PA. Several commercially available cell stains belong to this class of dyes, such as LysoTracker Red (**55**) which shows 2PA at 1032 nm (Bestvater et al., 2002). BODIPY TR (**56**) is a π-extended derivative with high photostability that was reported with superior 2P brightness (>200 GM) at 1060 nm (Mütze et al., 2012). Extension at the 3- and 5- positions was also the strategy used by Zheng *et al.* to design the compound IR07 (**57**) in 2009 (Zheng et al., 2009). Albeit initially developed for optical power limiting applications, the dye still had a fluorescence quantum yield of 30% and a 2PA cross-section of 101 GM at 1310 nm in CH_2Cl_2, which makes it an interesting candidate for further developments in bio-imaging. Interestingly, Prasad and co-workers further extended this aminostyryl-BODIPY with phenylacetylenes, and used compound **58** under 2PE at 1064 nm (Hu et al., 2020). As this dye had a relatively low fluorescence quantum yield of 9% (in THF), the authors investigated its application in 2P photo-acoustic imaging instead of traditional 2P fluorescence.

Theoretical reports have also shown the potential of BODIPY derivatives as 2P and 3P imaging agents (Zhang et al., 2015), which opens the way towards the rational design of NIR-II fluorophores. More advanced dye-design strategies have also been applied to optimise the 2PA properties of BODIPY fluorophores beyond 1000 nm (see **Section 2.1.5**).

2.1.5 Dipoles, Quadrupoles and Advanced Design Strategies

By taking advantage of strong ICT, relatively simple D-π-A structures can sometimes lead to strongly red-shifted optical properties and important 2PA cross-sections. Importantly, in contrast to symmetrical dyes, their transitions at $2\lambda_{1PA}^{max}$ are usually allowed, which is an important factor to reach the NIR-II window in 2PA. Triphenylamines are an important ED building block of 2P-responsive dipoles. Examples of triphenylamine dipoles include dye **59** that was incorporated within a poly (styrene-co-maleic anhydride) (PSMA) polymer, thus forming fluorescent nanoparticles (NPs) with high chemical and optical stability across a broad pH range (Alifu et al., 2017). The dipole emits in the NIR-I region, and interestingly shows a bathochromic shift of λ_{em} in the solid state. When excited at 1040 nm (2PA) the PSMA NPs of **59** emit over a wide range of wavelengths (500–950 nm) with a maximum at 678 nm. A large cross-section was measured for these NPs (5.6×10^5 GM), and the fluorescence quantum yield could be tuned from 1.7% to 16.9% by modifying the weight ratio of dye to polymer. These NPs were used as contrast agents to facilitate the 2PA NIR-II imaging of mouse brain blood vessels at the deepest tissue penetration reported to date (**Section 3.2**, **Table 3**). Similar to **59**, a second NIR-II absorbing triphenylamine dipole **60** was also utilised for imaging *in vivo* (**Section 3.2**, **Table 3**) while acting as a lysosomal photosensitizer for PDT (Zhou et al., 2021). Tuning the EW moiety shifted the 1PA properties of this dipole to the red compared to **59**, allowing 2P imaging to be performed at 1100 nm, i.e. near the $2\lambda_{1PA}$ value (530 nm).

Some other amino-substituted D-π-A dyes have been shown to exhibit strong solvochromatic or fluorogenic behaviour (Klymchenko, 2017). A reported water-soluble dipolar fluorophore (**61**) exhibited a large 2PA cross-section value at 1040 nm (440 GM) (Massin et al., 2013). Strong solvato-fluorogenic properties were demonstrated for this dye, with a fluorescence quantum yield of 0.22 in water, and therefore a 2P brightness close to 100 GM. Similar relatively simple structures have led to highly red-shifted 2P active dyes, which constitutes efficient dye design examples. Using a dialkylamino ED group and a pyridinium acceptor in a D-π-A structure led to dipole **62** that was reported with a σ_2 of 500 GM at 1300 nm (Ricci et al., 2017). Interestingly, the corresponding D-π-A-π-D counterpart **63** was also prepared by the authors. With a C_{2v} symmetry leading to a "bis-dipolar" character, this compound showed an enhanced cross-section at 1300 nm compared to dipole **62**, but the emission quantum yield was reduced by an order of magnitude. With limited quantum yields, both dipole **62** and bis-dipole **63** showed limited 2P brightness. Benzothiadiazole (BTZ) and related derivatives are other typical moieties that have been used in the design of NIR-absorbing chromophores for 1P and 2P bio-imaging, in particular when incorporated as a strongly EW core in a D-π-A-π-D structure. This has led to a strong 2P response with the ability to extend beyond 1000 nm (Yao et al., 2016). However, these pseudo-centrosymmetrical chromophores, with forbidden transitions, can be counterproductive in NIR-II dye design. Moreover, water solubility can be a limitation for these molecules, and they tend to be used more commonly as AIE building blocks (**Section 2.1.6**), or incorporated in different types of NPs. For this purpose, Liu and co-workers prepared conjugated polymers from BTZ and thiophene derivatives (**64**) that proved highly NIR-emissive once incorporated in phospholipid-type NPs (Wang et al., 2019b). These polymer dots showed significant 2PA between 1000 and 1200 nm, with cross-sections in the 1000–2000 GM range. A 2P brightness of 242 GM was reported, along with impressive *in vivo* results (**Section 3.2**, **Table 3**).

Other advanced strategies have been applied to design NIR-II-absorbing 2P dyes with optimised 2PA cross-sections in the NIR-II, without focusing on emissive properties or imaging applications, which has been reviewed recently (Pascal et al., 2021). This includes the preparation of stable π-radical and diradical structures (Hisamune et al., 2015), macrocyclic dyes with controlled topology (Mobius dyes, *meso-meso*-linked porphyrin oligomers amongst others) (Tanaka et al., 2008), or multi-chromophoric systems with hybrid electronic transitions (Webster et al., 2009). During their investigation

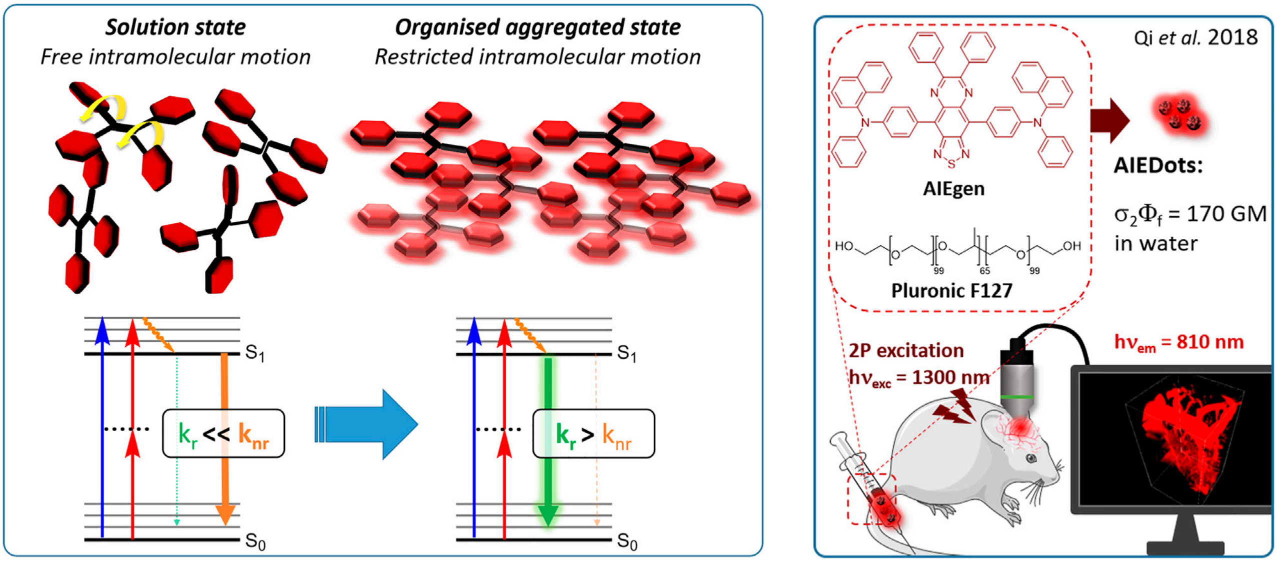

FIGURE 4 | (Left) Illustration of AIEgen molecules in solution and aggregated state, and their corresponding simplified Jablonski diagrams showing the effect of motion restriction on the radiative (k_r) and non-radiative (k_{nr}) relaxation pathways after 1PE or 2PE. (Right) Example of *in vivo* application of 2P microscopy with NIR-II-responsive AIEDots used to reconstruct images of a mouse brain. The 3D reconstruction of mouse brain vasculature is reprinted with permission from ref. (Qi et al., 2018). Copyright 2018 American Chemical Society.

of singlet biradical dyes, Li *et al.* reported the preparation of zethrene derivatives (**65** and **66**) with strong 2PA properties at 1250 nm (Li et al., 2012). The compounds retained fluorescent properties, however, measurements were only performed in chloroform because of their lipophilic nature. Ni *et al.* reported quinodimethane-bridged BODIPY dimers (**67** and **68**) that showed up to 26% diradical character, which provided strong 1PA at the beginning of the NIR-II window at 1100 nm (Ni et al., 2016). The corresponding 2PA band was, therefore, shifted beyond 2000 nm (up to 1500 GM at 2300 nm). Although no application in imaging was envisioned, the authors report that their BODIPY derivatives remain fluorescent in chloroform solutions, with up to a 0.2% quantum yield of infrared emission. This low Φ_f value leads to very poor 2P brightness (up to 2.6 GM). The quinodimethane dimerization strategy was also used by Zeng *et al.* to prepare porphyrin dimers with intense 2PA cross-section at 1800 nm (Zeng et al., 2013). In this report, the Zinc and Magnesium porphyrin dimers showed emission bands in the 900 nm range (CH_2Cl_2). Self-assembly of porphyrin-oligomers and 4,4′-bipyridine has also led to record cross-sections (up to 2.3×10^5 GM) and strongly red-shifted 2PE (up to 1300 nm) by restricting rotation and enhancing electron transfer through the metal bridge (Drobizhev et al., 2006). Such strategies have led to σ_2 of several thousands of GM above 1200 nm, but often lead to non-emissive compounds, typically because of preferential vibrational decay or very short excited state lifetimes (Cho et al., 2009). They are also susceptible to poor stability and lack of biocompatibility.

Other families of dyes have also been investigated with the goal of improving 2PA capacity in the NIR-II (Pascal et al., 2021), including for optical imaging applications. The classical dead cell stain propidium iodide (**69**) shows 2PA response at 1015 nm (Bestvater et al., 2002). Polyaromatic fluorophores such as diketopyrrolopyrroles have also been proposed as potential multi-photon imaging agents in theoretical reports (Ye et al., 2017).

2.1.6 Aggregation Induced Emission Dyes and Dots

Dye design strategies for 2P-responsive NIR-II fluorophores can lead to highly lipophilic aromatic structures prone to forming irregular aggregates in aqueous environments. Fluorescence quantum yields can thus be dramatically reduced as a result of a reduction in the rate of radiative decay (k_r), either by significant bathochromic shifts leading to favoured non-radiative vibrational decay (k_{nr}) processes, by fluorescence quenching by water molecules, or by intermolecular π–π stacking, which is known as "aggregation-caused quenching". Counteracting this effect, certain lipophilic organic dyes generate an organised solid-state arrangement of chromophores with a local lipophilic environment within nano-aggregates. While the dye molecules move freely in diluted solution form, the restriction of intramolecular motions (i.e. vibrations, rotations etc.) in this organised aggregated state causes a strong decrease in the probability of non-radiative decay, and therefore a strong increase in fluorescence (**Figure 4A**, left). The concept of "aggregation-induced emission" (AIE) was first described in 2001 by Tang and co-workers (Luo et al., 2001), and has since become a popular approach to the design of 1P and 2P theranostic agents (Zhu et al., 2018; Yang et al., 2020b; Lu et al., 2020; Han et al., 2021) and circumvent the limitations of standard NIR-dye design strategies. In contrast to traditional organic fluorophores, AIE luminogens (AIEgens) typically exhibit low fluorescence in dilute solutions, but both high Φ_f and photostability in the aggregated state, which are key requirements for high-resolution imaging.

In the context of 2P-imaging using NIR-II wavelengths, AIEgens provide a way to prepare highly NIR-shifted chromophores maintaining strong 2P brightness in water. The BTZ derivative **70** has been shown to exhibit AIE behaviour in two different studies, emitting NIR light after 2PE at 1200 nm (aqueous media) and 1300 nm (organic media) respectively (Qi et al., 2018; Liu et al., 2021). Significant cross-section values (1.6 × 10^4 GM at 1040 nm and 1220 GM at 1300 nm) were reported in the NIR-II for these AIEdots. The emission peak was measured at 810 nm with 14% quantum yield. This AIEgen was used to image mouse brain tissues with high resolution (**Figure 4B**, right), demonstrating the imaging benefits of NIR-II 2PA over NIR-I 1PA (**Section 3.2**, **Table 3**). The use of AIEgen dye **70** was then extended to 2P fluorescent lifetime imaging (2PFLIM) by the same research group (Liu et al., 2021). Replacing the arylamine EDG of this molecule with a propeller-shaped tetraphenylethene moiety (Wang et al., 2019c), a structure commonly used in the design of AIEgens, led to D-π-A-π-D dye **71** that was co-nanoprecipitated with a pegylated phospholipid. The 2PA spectrum of the resulting AIEdots showed a σ_2 close to 1 × 10^5 GM both at the maximum of the low energy band (1150 nm) and in the tail of the high-energy band (1000 nm). With a fluorescence quantum yield of 19% in aqueous media and high photo-stability, these AIE dots showed high potential for *in vivo* imaging, which was demonstrated in tumour tissues and blood vessels (**Section 3.2** and **Table 3**).

Outside of the BTZ class of dyes, a 2PA fluorescent nanoprobe made of a triphenylamine-based brominated AIEgen (dye **72**) (Samanta et al., 2021), showing a similar structure to dipole **59** (**Section 2.1.5**), was reported. The triphenylamine ED group provides a good balance between strong twisted ICT in the molecule and unrestricted rotation to ensure possible AIE. These NPs showed large 2PA cross-section of 3 × 10^3 GM at 1040 nm and a Φ_f of 6%, which also allowed 2D and 3D imaging of brain vasculature (**Section 3.2**, **Table 3**). Similarly, four push–pull AIEgens based on a diphenylamine donor attached to different EW moieties (Zheng et al., 2018) were prepared. All 2PA bands extended somewhat past 1000 nm, but the highest cross-sections were obtained with the isophorone and furanone dipoles **73** and **74** (887 GM at 1020 nm for the latter) which showed great promise in *ex vivo* cell and tissue studies. Finally, the tetraphenylethene propeller-shaped moiety was attached to a BODIPY dye to prepare AIEgen **75**. The NPs prepared from this dye showed a record absorption capacity past 1000 nm (2.9 × 10^6 GM at 1040 nm) (Wang et al., 2015), which is among the highest cross-section values in the NIR-II region all classes of materials combined. Therefore, AIEgens allow the combination of massive cross-sections, arising from the combined cross-section contribution of each dye in the NP, and of a fluorescence strongly switched-on in water. Both these factors combine to give unprecedented 2P brightness values (>10^4 GM), which makes them high-potential materials for 2P imaging in the NIR-II (**Section 3.2**, **Table 3**).

2.2 Carbon, Hybrid and Inorganic Nanomaterials

Carbon and metal-containing nanomaterials have been investigated for decades as a source of 2P-reponsive imaging agents thanks to unique electronic, physical and morphological properties. Such materials also tend to show higher brightness and photo-stability than organic dyes, and thanks to their surface functionalisation, they provide huge versatility to expand into multimodal and theranostic applications. The potential toxicity of metal and carbon nanomaterials is arguably the main limitation to their use for *in vivo* imaging.

Carbon nanomaterials have been a key focus of research in bio-imaging over the past decade owing to their unique optical properties, large surface area, and robust photostability allowing long-term imaging. Carbon dots (CDs), single-wall carbon nanotubes (SWCNTs), graphene derivatives and nanodiamonds have all been reported as luminescent 2P-active

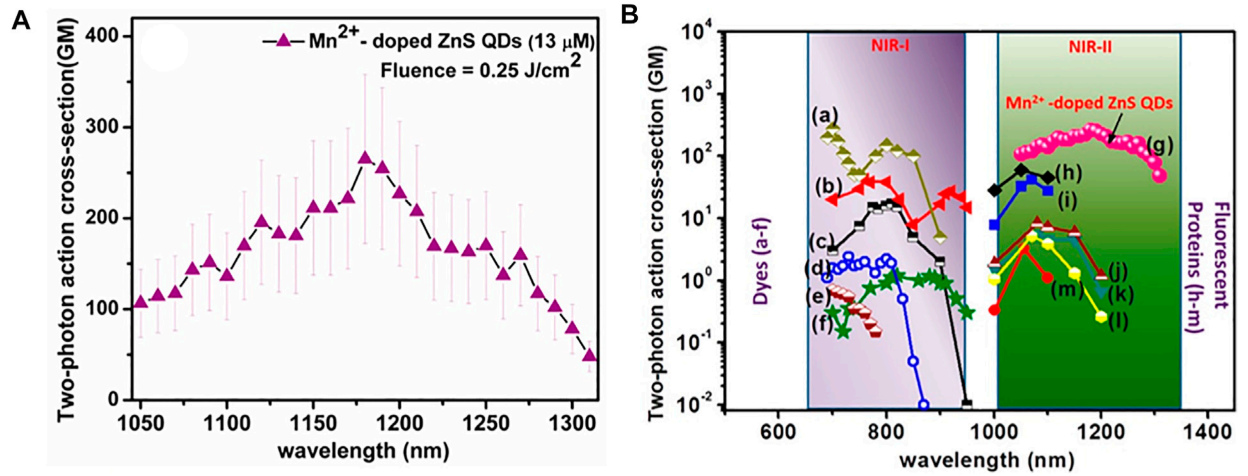

FIGURE 5 | (A) 2PA spectrum of Mn^{2+}-doped ZnS QDs in the range from 1050 to 1300 nm reported by Subha *et al.* **(B)** Comparison of σ_2 values in Mn^{2+}-doped ZnS QDs (curve g) with other standard chromophores (curves a–f) and fluorescent proteins (curves h–m): (a) Rhodamine B, (b) Fluorescein, (c) Coumarin 307, (d) Cascade blue, (e) Dansyl and (f) Lucifer Yellow), and (h) tdTomato, (i) mBanana (j) mRFP (k) mCherry (l) mStrawberry (m) mTangerine). Reprinted with permission from ref. (Subha et al., 2013). Copyright 2013 American Chemical Society.

materials with imaging potential (Hong et al., 2015). In the NIR-II window, semiconducting SWCNTs have demonstrated strong potential, both because of their strong 2P response, and their NIR emission. In the context of optoneurology and neurotransmitter sensing, a dopamine-sensitive nanosensor was developed using SWCNT (**76**), and provided chirality-dependent fluorescent turn-on responses varying between 20% and 350% in the presence of the analyte (Bonis-O'Donnell et al., 2017). Sensing was performed at 1560 nm under 2PE with a σ_2 estimated at 2.16 $\times 10^5$ GM, but the fluorescence quantum yield of **76** remained limited ($\Phi_f = 0.0023$). These nanosensors were embedded 2 mm into strongly scattering tissue phantoms mimicking brain tissues, which demonstrated that the light scattering decreased from 42% to 4% using NIR-II 2PE compared to traditional 1PE. In 2014 an aptamer-modified graphene oxide material (**77**) was used to show excitation dependant luminescence outputs and develop multi-channel and multi-colour imaging of multi-drug resistant bacteria (Pramanik et al., 2014). In particular, 2PE of the material at 1120 nm led to bright red-light emission, which allowed imaging of methicilin-resistant *Staphylococcus Aureus* (MRSA) with a σ_2 above 3.6 $\times 10^4$ GM in aqueous solution. Recently, nitrogen-doped graphene quantum dots were also reported with high luminescence and photosensitizing properties for antimicrobial applications (Kuo et al., 2022). Although the 2P properties of these graphene-based nano-objects were only measured up to 970 nm, they likely still possess 2P responses beyond 1000 nm. Finally, sulfoxide- and carbonyl-enriched CDs (**78**) were prepared by solvothermal treatment of readily available citric acid and urea. These CDs were brightly fluorescent at 760 nm under 1PE at 714 nm, with efficient NIR-II absorption upon 2P and three-photon (3P) excitation at 1200 and 1400 nm (Li et al., 2018). Carbon quantum dots prepared from tris(4-aminophenyl)amine (**79**) also led to ultra-narrow emission at 615 nm with high photoluminescence quantum yield (84%) (Liu et al., 2020). These CDs were used for *in vitro* for 2P imaging of tumor spheroids at 1100 nm, with a penetration depth reaching 200 µm. Further 2P *in vivo* imaging was carried out in zebrafish larvae, in which a maximum penetration depth of 500 µm was achieved (**Section 3.2**, **Table 3**).

Noble metal nano-objects are known to interact strongly with high-intensity light pulses, which is the source of interesting NLO properties (Olesiak-Banska et al., 2019). In recent reports, gold nanoparticles (AuNPs) have been used to develop a hybrid theranostic platform (**80**) combining anti-GD2 antibodies and SWCNTs for selective 2P imaging and efficient photothermal therapy of human melanoma cancer cells at 1100 nm (Tchounwou et al., 2015). Although no σ_2 or Φ_f values were explicitly mentioned in the article, the authors measured the 2P-induced photoluminescence of the hybrid nanomaterial and evidenced that the strong plasmon-coupling generated by the gold increased the emission by 6 orders of magnitudes compared to the AuNPs or SWCNTs alone. The plasmon coupling also acted as a local nano-antenna to enhance the photothermal efficiency of this theranostic system. Recently, hybrid Au-Si NPs functionalised with a NIR-resonant cyanine dye were also exploited for tissue imaging with surface-enhanced resonance hyper-Raman scattering (SERHRS) (Olson et al., 2022), a vibrational 2P spectroscopy technique.

Gold nano-clusters (AuNCs) are ultrasmall nano-materials constituted of as little as a dozen atoms of gold. Due to the proximity of their size to the de Broglie wavelength of an electron, they do not exhibit the typical plasmon resonance observed in larger AuNPs, but instead show strong quantum confinement effects, leading to molecule-like electronic transitions and fluorescence properties. AuNCs with a number of gold atoms varying from 25 to 2406 had their 2P fluorescence properties measured in the NIR-I and -II regions (Ramakrishna et al., 2008). In the NIR-I (800 nm), 2PA cross-sections ranging from 5 $\times 10^5$ to a 3 $\times 10^6$ GM were reported; but interestingly, the σ_2 value per gold atom decreased drastically with the size of the AuNC, eventually showing saturation when transitioning to standard AuNP behaviour. In the NIR-II, the Au25 clusters (**81**) showed a cross-section of 2700 GM at 1290 nm with emission of light at 830 nm, however the quantum yield value of such systems is said to be in the 10^{-7} range which limits their brightness. PEG-lipoic acid functionalised AuNCs (**82**) of 1.5 nm in size have also been discussed for cellular imaging (Oh et al., 2013). The 2PA cross-section of these AuNCs was above 300 GM at 1100 nm, and remained >100 GM at 1300 nm where the measurement ended. Fluorescence at 820 nm with a Φ_f of 4–8% was reported depending on the surface functional group, and the objects were stable for months and generally non-toxic.

Quantum dots (QDs) are crystalline semiconductor materials that also display quantum confinement effects due to their nanometer size (Wegner and Hildebrandt, 2015; Barroso, 2011). The dependency of the confinement energy on the QD's diameter leads to size-dependent absorption and emission, with smaller NPs resulting in larger band gaps–and therefore blue-shifted emission, and larger NPs having more red-shifted emission. Their highly tunable size and properties, high stability, limited photobleaching, and reported 2PA cross-sections (>5.0 $\times 10^4$ GM at ≥1000 nm) make them great candidates for OMI applications (Gui et al., 2017; Nyk et al., 2012). Due to their unique semiconducting energy profile, they also feature broad absorption bands which would make them ideal for 2PA NIR-II imaging where excitation wavelength can be laser-dependent (**Section 3.1**). The main drawbacks of QDs arise due to reports on potential toxicity related to their heavy metal components (Tsoi et al., 2013). Examples of 2P-responsive QDs in the NIR-II include Mn^{2+}-doped ZnS QDs (**83**) reported in 2013 by Subha *et al.* (Subha et al., 2013), which presented 2P- and 3P-induced photoluminescence at 586 nm resulting from the electronic transitions of the manganese ions. A maximum 2PA cross-section of 265 GM was measured at 1180 nm, with an absorption band extending beyond 1250 nm (**Figure 5A**), which was higher than most standard dyes and fluorescent proteins (**Section 2.3**) reported at the time (**Figure 5B**). These QDs also possessed long photoluminescence lifetime (millisecond range).

Pioneering work combining 2P fluorescence and 2PFLIM using PbS/CdS QDs (**84**) as water-dispersible contrast agents was recently reported (Ni et al., 2022). These QDs allowed "NIR-to-NIR" imaging under 2PE at 1550 nm with a σ_2 of 530 GM in water. Importantly, the QDs maintained bright fluorescence properties at

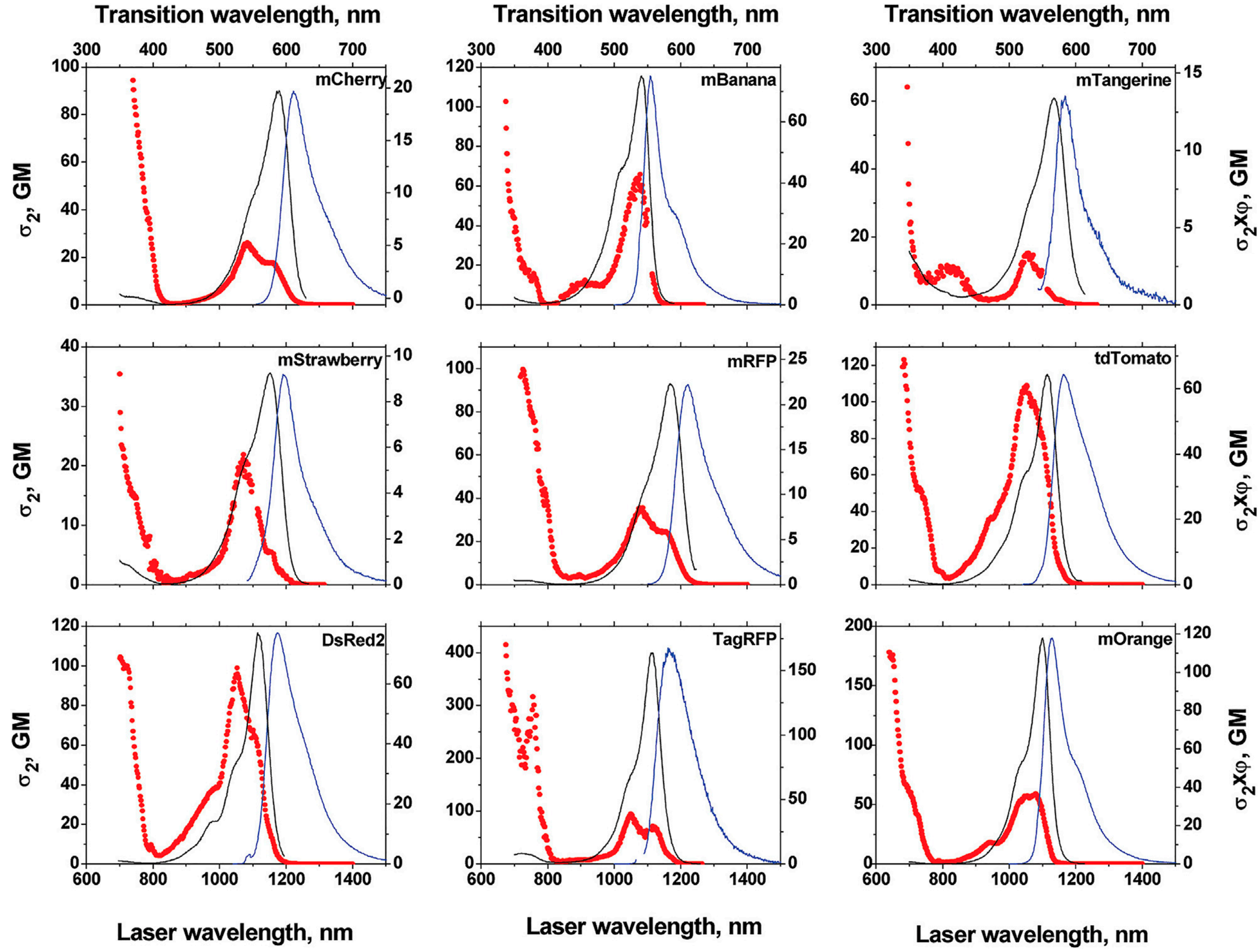

FIGURE 6 | 1PA and 2PA spectra of fluorescent proteins of the "fruit series". Left axis shows the 2PA cross-section $\sigma_2^{(\lambda)}$ per mature chromophore, right axis shows corresponding $\sigma_2^{(\lambda)}\Phi_f$ values. Adapted with permission from ref. (Drobizhev et al., 2009). Copyright 2009 American Chemical Society.

1270 nm, with a quantum yield of 18% in water, which is higher than most organic dyes at such long wavelengths. The high fluorescence lifetime ($\tau = 501$ ns) of these QDs allowed the authors to implement a 2PFLIM system to complement 2P fluorescence imaging, and *in vivo* images of mouse brain blood vessels were obtained for the first time. As well as this, it is worth mentioning that Larson *et al.* reported polymer-encapsulated CdSe-ZnS QDs with 2P brightness of up to 4.7×10^4 GM, which is orders of magnitude higher than organic fluorescent probes (Larson et al., 2003). Although the measurements were only performed between 700 and 1000 nm at the time, brightness values proved relatively constant all over this range of wavelength thanks to their large absorption band; and QD605 (**85**), the brightest NP in their study, would likely still respond in the NIR-II regime.

2.3 Fluorescent Proteins

FPs are a class of proteins that contain chromophores that arise from specific amino-acid sequences in their polypeptide sequence undergoing a series of atypical transformations (Tsien, 1998; Shaner et al., 2004). Unlike the aforementioned examples that require injection or incubation with a contrast agent, FPs can be genetically encoded, and they can therefore generate luminescence with high target specificity. The 2P properties of NIR-II-responsive FPs have been well documented in the seminal work by Drobizhev et al. (2011). Several proteins absorbed efficiently above 1000 nm, and we limited our selection to the ones showing brightness values above 5 GM in **Table 1** (compounds **86–104**). Among them, the so-called "fruit proteins" have been reported with medium to strong 2P brightness in the 1000–1200 nm region (**Figure 6**) (Drobizhev et al., 2011; Drobizhev et al., 2009). With a maximum 2PA cross-section of 278 GM at 1050 nm, as well as an absorption band extending beyond 1200 nm, tdTomato (**86**) was reported as the brightest in the series (Shaner et al., 2004; Drobizhev et al., 2009). Proteins tdKatushka2 (**87**) and dsRed2 (**88**) follow with brightness values in the 50–100 GM range. As shown in **Figure 6**, the $\sigma_2\Phi_f$ values per mature chromophore of FPs are comparable to those of organic fluorophores, and orders of magnitude lower than those of nanomaterials and AIEgens. Still, as highlighted by Drobizhev et al. (2011), these 2PA

TABLE 2 | Benefits associated with Fibre lasers over traditional solid-state and OPO lasers (adapted from ref (RPMC, 2020))

Solid-State/OPO-Based Lasers	Femtosecond Fibre Lasers
Large cumbersome design	Lightweight, up to 10x smaller
Expensive	Affordable
Less consistent pulse duration	Pulse duration always maintained
Lower power at long wavelengths (crystal-based amplifiers)	Maintains high power at long wavelengths (up to 4W at 920 nm)
Water-cooled	Air-cooled
High cost of ownership	Low maintenance and engineer fees (fast return on investment potential)

properties match well with current widespread NIR-II laser technologies such as Ti:Sapphire with optical parametric oscillators, neodymium (Nd)- and ytterbium (Yb)-doped fibre and glass lasers and chromium-forsterite (Cr-Mg_2SiO_4) lasers (**Section 3.1**) (Shaner et al., 2004; Drobizhev et al., 2009). FPs were therefore among the first luminescent trackers to be used successfully to perform 2P imaging of biological systems in the NIR-II window, and to develop new adapted multi-photon technologies. Gene expression in transgenic zebrafish embryo, tagged with a red FP (Hc-RFP, **89**), was investigated by Tsai *et al.* using 2P imaging (Tsai et al., 2005; Tsai et al., 2006). Heart-specific regulatory elements of a zebrafish cardiac gene fused with the encoding element for Hc-RFP were injected into zebrafish embryos. This generated a zebrafish line that showed strong 2P red fluorescence in cardiac cells (Tsai et al., 2005). This red FP allowed imaging with a 1230 nm fs light source, providing superior imaging resolution compared with traditional green FP-based 2P microscopy. In addition, the properties of HcRFP were measured under 2PE by the same group, showing an excitation maximum around 1200 nm and an absorption cross-section of the same order as the green FP (GFP) (Tsai et al., 2006). The use of red FPs and mCherry (**90**) under OPO excitation has also been demonstrated (Herz et al., 2010) and compared against NIR-I activated GFP. The authors report that, in the cortex of fluorescent-protein-expressing mice, a maximal imaging depth of 508 μm was possible when imaging with tandem dimer RFP (TdRFP, **104**) at 1110 nm, which represents an 80% enhancement compared to GFP-expressing mice imaged at 850 nm. The depth-dependent deterioration of the spatial resolution was also significantly lower at 1110 nm. Yang *et al.* induced the expression of the tdTomato protein in excitatory neurons of mice (Yang et al., 2013). The authors used this model to validate the development of their multi-colour OPO-based laser set up which was used successfully at 1070 nm for 2P imaging of the intact brain cortex (**Section 3**). Voigt *et al.* recently validated the design of a novel semiconductor-disk laser (SDL) by performing *in vivo* 2P imaging of FP-containing *Drosophila* larvae (Voigt et al., 2017).

3 *IN VIVO* 2P-NIR-II BIO-IMAGING: INSTRUMENTATION AND EXAMPLES

Two-photon absorption is a third-order NLO phenomenon. As such, 2PA can be observed in many types of materials provided

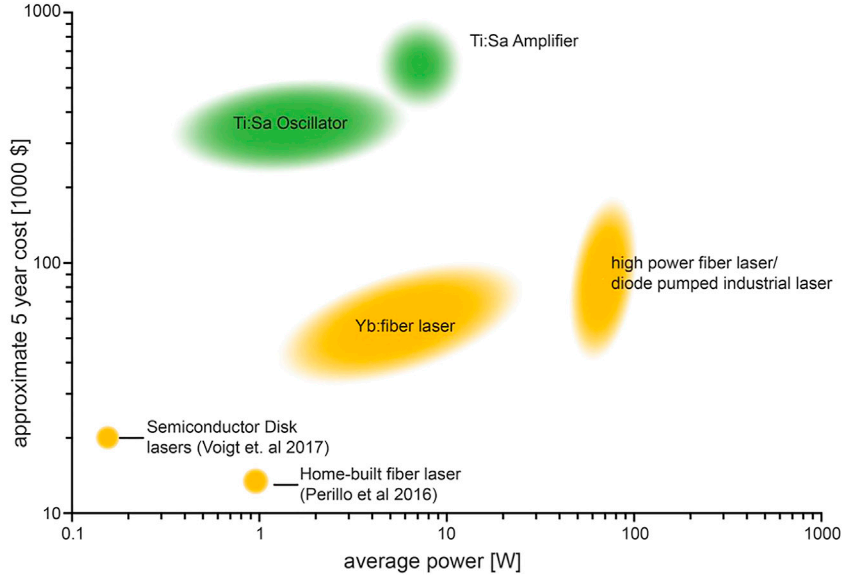

FIGURE 7 | The approximate 5-years costs of traditional tunable 2PA lasers (green) and alternative fixed wavelengths lasers (yellow), demonstrating the economical benefits of fixed wavelength fibre lasers. Reproduced from the supplementary material of ref (Mohr et al., 2020) with permission from the authors.

that the intensity of the electric field in the light source is strong enough to generate a non-linear polarisation in the material (He et al., 2008).

For 2PA imaging applications, high photon densities are required to ensure sufficient fluorophore excitation; requiring around one million times more photon flux compared to 1PA events (Le Bot, 2009). This involves the use of high intensity pulsed (mode-locked) lasers. Such systems provide brief but intense light pulses which results in high photon fluxes arriving at a sample to promote 2PE, while also keeping the average power low enough to prevent tissue damage. By reducing the average excitation power, the number of 1PA events are minimised, which is known to be the source of heating and resultant photo-damage. Laser requirements for 2P imaging are typically met with output powers of >1 W, pulse durations of <100 fs, repetition rates of typically between 80-100 MHz, and high peak powers (>100 kW). Lasers capable of producing pulses of light of durations shorter than picoseconds (10^{-12}) do so using a method known as ‘mode locking’.

Recent years have shown an increase in successful 2PA NIR-II imaging with imaging depths of up to 1200 μm into tissue being claimed (Alifu et al., 2017). However, most lasers explored in current literature have their output wavelengths in the NIR-IIa region, with most reports showing imaging performed at lasing wavelengths of <1300 nm (**Section 3.2**, **Table 3**). This is likely due to the limited capacities of current lasers struggling to reach the power, portability and flexibility requirements at such long wavelengths.

Traditional systems for 2P imaging involve the use of solid-state lasers (Drobizhev et al., 2011; Ustione and Piston, 2011). However, due to their drawbacks, such lasers have limited applications in the NIR-II window. As such, lasing systems involving the use of optical parametric oscillators (OPOs), optical parametric amplifiers (OPAs), and fibre lasers, are more commonly used for 2P NIR-II imaging.

3.1 NIR-II Laser Technologies

3.1.1 NIR-II Solid-State Pulsed Lasers

The first paper demonstrating 2P imaging applications was demonstrated by Denk et al. (1990) in which a 25 mW colliding pulse, mode-locked dye laser with an emission of 630 nm was used. Historically, dye lasers dominated the field of tuneable lasers but were then replaced by solid-state lasers (often based on Ti:Sapphire crystal) due to their bulky structures, complex liquid handling systems, and the involvement of toxic and volatile dyes (Ferguson et al., 1993).

Solid-state ‘mode-locked’ lasers compatible with 2P imaging produce high-power light pulses on a femtosecond time-scale. Solid-state lasers typically consist of a solid gain media typically doped with rare-earth ions, such as ytterbium, chromium, and neodymium, and optically pumped by a diode laser (Chénais and Forget, 2012; Arbuzov et al., 2013). Solid-state ‘mode-locked’ lasers have been historically used in imaging applications for their convenience, high potential output powers, and low cost. However, their applications in the NIR-II is restricted due to their shorter emission wavelengths or limited wavelength tunability (Zhang et al., 2021b). Ti:Sapphire lasers have a range of advantages such as a wide tuning range, high output power, and femtosecond pulsing capability, however, they are not suited for 2P NIR-II imaging applications due to their emission wavelength (700–1000 nm) not reaching the NIR-II optical window.

Solid-state lasers based on crystals such as Cr:Forsterite are of particular interest as they can produce emission wavelengths between 1220 nm and 1270 nm and have been successfully applied in 2P NIR-II imaging applications with wavelengths of around 1230 nm (Shen et al., 2015; Tsai et al., 2005). Nd:YLF lasers are a common composition that produces a fixed lasing wavelength of 1047 nm (Squirrell et al., 1999; Wokosin et al., 1996b). As demonstrated in **Section 2**, the 2PE wavelength at 1047 nm overlaps with the absorption band of several bio-imaging dyes. However, both Cr:Forsterite and Nd:YLF mode-locked lasers lack a wide wavelength tuning range (Trägårdh et al., 2016), which implies that fluorescent probes must be carefully chosen in order to match the small bandwidths, therefore this tends to limit biological imaging to just one colour. An example of a solid-state laser being used for *in vivo* applications involve a Nd:YLF laser being used to perform 2P NIR-II imaging of a stained zebrafish embryo (Wokosin et al., 1996a) (**Section 3.2**, **Table 3**). To overcome the drawback of limited excitation wavelengths of such solid-state lasers, multi-colour 2P imaging can instead be achieved by using two tunable lasers in tandem, although this is a relatively high-cost solution. Other solutions have been found in utilising the second Stokes shift to extend output wavelengths in Ti:Sapphire laser systems, or in methods such as phase-shaping (Brenner et al., 2013; Trägårdh et al., 2016).

3.1.2 NIR-II OPO/OPA Systems

OPOs based on the second-order NLO interactions can convert the output wavelength of an input laser (pump) into two longer wavelengths with lower energy output waves, known as signal and idler (Trovatello et al., 2021). Both continuous wave (CW) and pulsed OPOs can be realised depending on requirements and applications (Sowade et al., 2013). In phase-matching conditions, parametric amplification occurs within a NLO crystal where all three waves are interacting (Trovatello et al., 2021). Wavelengths of the amplified signal can be tuned to access the near-, mid-, and far-infrared regions–which is often much harder to achieve in traditional laser systems. OPO systems have great potential in biological imaging applications as a wide range of wavelengths from a single laser allows multicolour imaging across the whole NIR spectrum, overcoming the limitations of standard solid-state systems. Such systems have only been commercially available within the last few decades, and have now extended lasing applications into the deep IR (up to 2500 nm) (Pascal et al., 2021), which has enabled the discovery of new 2P-absorbing organic molecules within this spectral range where other associated tools for optical investigation exist.

Traditional ‘mode-locked’ lasers in combination with OPO techniques now appear to be the laser system of choice for 2P NIR-II imaging applications (**Table 3**). Common 2P microscopes include a high-peak-power Ti:Sapphire laser used in combination with a compatible OPO, which can significantly extend the wavelength range. For example, the Blaze laser from Radiantis offers a “one box” Ti:Sapphire/OPO system with three output ports (pump, signal and idler). The pump laser (Ti:Sapphire) provides a tunable wavelength range of 730–1020 nm, the signal output provides a tunable wavelength range of 1000–1550 nm, and the idler output provides a tunable range of 1620–4000 nm. Unfortunately, the output power of the tunable OPO laser decreases dramatically when tuned to longer wavelengths due to the lower conversion efficiency and higher intrinsic loss. Here, the power drops from 2.2 W to 250 mW with increasing wavelength, thus limiting its imaging applications. Due to the difficulties in developing long-wavelength lasers that also match the power requirements for 2P imaging, most current examples in the NIR-II window are demonstrated with wavelengths between 1000-1300 nm. An example of the benefits of OPOs was demonstrated by Herz *et al.* who showed the increased tissue penetration performance by using an OPO laser compared to a traditional Ti:Sapphire laser (Herz et al., 2010). Recent advancement has led to the commercialisation of systems capable of 2P NIR-II imaging with the integration of OPO based lasers. The Olympus FVMPE-RS Multiphoton Microscope appears to be a popular system of choice for current 2P NIR-II *in vivo* imaging purposes, achieving impressive resolution and penetration depths (**Section 3.2**, **Table 3**) (Zhou et al., 2021; Wang et al., 2019b; Wang et al., 2019c; Liu et al., 2020). This microscope can image at wavelengths of up to 1300 nm and also contains detectors and other equipment required for plug-in bench top imaging. This is achieved by combining two lasers within the microscope, namely the MAi Tai DeepSee One Box ultra-fast laser (Ti: Sapphire-based for excitation up to 1040 nm), and an InSight® DS+™ OPO (up to 1348 nm). Also worth noting is the Leica TCS SP8 DIVE upright multiphoton/confocal microscope that claims to be the first multiphoton microscope with spectrally tunable detection. This microscope utilises an OPO laser source to realise a tunable output wavelength between 680-1300 nm and has also demonstrated 2P NIR-II imaging applications *in vivo* (**Section 3.2**, **Table 3**) (Liu et al., 2020).

Limitations of OPO lasers arise due to the requirements of a pump source with high spatial coherence and optical intensity, often requiring a diode-pumped solid-state laser. Furthermore, complex procedures have to be undertaken that require variation in the crystal’s temperature, orientation, and poling period in order to realise phase matching. Careful free-space alignment and temporal synchronisation are also required for the OPO cavity, which makes the system sensitive to external perturbation and hence a high-level of maintenance is needed. Power restraints, requirements of water cooling, bulkiness, high cost, and expensive maintenance requirements are further limitations for desirable “turn-key” 2P microscopy. To overcome these downfalls, other systems have been developed, such as OPAs. Although OPA systems have similar principles of converting the short-wavelength input pump to the output signal with wavelength in the NIR-II regime, they do not need cavity and temporal synchronisation which can result in a simpler structure and has a smaller footprint (Chen et al., 2020).

Yang *et al.* demonstrated 2P NIR-II imaging by using a multi-colour ultrafast OPO source (Yang et al., 2013), where brain tissues of a tdTomato-expressing mouse were imaged with 2PE at 1070 nm (**Section 3.2**, **Table 3**). Xu *et al.* have developed a periodically poled lithium niobate OPA system operating at 2-ps pulse duration (Xu et al., 2021). In their work, imaging at a depth of 40 µm was achieved in both label-free coherent anti-Stokes Raman scattering (CARS) and 2PE based imaging of mitochondrial flavin adenine dinucleotide autofluorescence in tissue samples.

3.1.3 Fibre Lasers

Fibre lasers were first demonstrated in the mid-1980s, followed by the development of high energy Q-switched fibre lasers and mode-locked fibre lasers (Rose, 2019). Fibre lasers consist of an optical fibre doped with rare-earth ions such as Erbium, Neodymium, or Ytterbium, similar to the elements used in their solid-state counterparts (Kim et al., 2012; Mohr et al., 2020). Light from a pump source is guided through this robust waveguide that provides a long gain medium length, resulting in a high optical gain (Rose, 2019).

Fibre lasers present unique optical and practical benefits for 2P NIR-II imaging by removing the requirement of bulk optics and free-space alignment, which offers the benefits of compactness, high stability, reduced initial and maintenance cost (**Figure 7**), and increased reliability compared to OPO lasers (**Table 2**). Simple air-cooling of fibre lasers is possible, due to the large surface-area of the fibre, compared to expensive and cumbersome water-cooling that traditional solid-state lasers require. This all results in greater flexibility for the end-user, with many in the near-future looking likely to replace the bulky and complex laser systems and provide a more ‘plug and play’ approach to 2P microscopy imaging.

Importantly, unlike solid-state lasers and OPO lasers that tend to decrease output power at longer wavelengths, fibre lasers can maintain high output powers at the wavelengths required for 2P imaging. This was demonstrated by Jung *et al.*, whose initial attempts of the 2PE of Chrimson-expressing neurons with a conventional femtosecond Ti:Sapphire laser did not result in reliable activation of the target neurons (Jung et al., 2020). On the contrary, activation was observed upon 2P NIR-II excitation at 1070 nm (2W) by using a Yb-doped fibre laser which provided 5–10 times higher power output than the Ti:Sapphire laser. Another example of 2P NIR-II imaging was demonstrated by Kim *et al.*, showing tridimensional 2P imaging of *ex vivo* nerve cells at 1060 nm using a Yb-doped fiber lasers (Kim et al., 2012).

The major challenge of developing high-power short-pulsed fibre lasers is to prevent the distortion of pulse shapes by nonlinear effects such as self-phase modulation and stimulated Raman scattering, which can consequently degrade peak power and 2PE efficiency (Liu and Yang, 2012). This could reduce the fluorescence signal and cause unwanted heating within the sample, and as such, certain technical approaches such as temporally stretching the pulse (Eisele, 2020) can be implemented to resolve this limitation. The tuning range of common fibre lasers for 2P imaging is below 100 nm due to the limited gain bandwidth. Current commercially available fibre lasers using common doping agents

TABLE 3 | Current examples of 2PA *in vivo* experiments performed using NIR-II absorbing fluorophores.

λ_{2PA} (nm)	Imaging System	Laser used	λ_{em} (nm)	Contrast media	Depth (μm)	Animal model	Biological media imaged	Administration Method	Toxic. Test *in vivo* (Y/N)	Year	Ref
1550	Home-built system	PolarOnyx Mercury **Fibre laser**	800	DTTC dye (**30**)	180	Mouse	Resected kidney vasculature	Intravenous injection	N	2011	Berezin et al. (2011)
1200	Commercial Leica TCS SP8 MP	Laser with **OPO**	630	Squaraine **45**	40	Mouse	Ear vasculature	Ear blood vessel injection	N	2019	Yi et al. (2019)
1057	Home-built with BioRad MRC 600 confocal microscope	Nd:YLF **solid state laser**	~590	FM4-64 dye (**48**)	45	Zebrafish embryo	Body	Pre-stained	N	1996	Wokosin et al. (1996a)
1040	Home built with Olympus, BX61 FV1200 microscope	Yb-doped photonic crystal **fibre laser**	~700	Triphenylamine dipole **59** encapsulated in PSMA NPs	1200	Mouse	Ear vasculature Brain vasculature Resected tumour vasculature	Tail vein injection	Y	2017	Alifu et al. (2017)
1100	Commercial Olympus FVMPE-RS	InSight® DS with **OPO**	740	PDT-imaging agent 60	210	Mouse	Resected tumour vasculature	Intravenous injection	Y	2021	Zhou et al. (2021)
1200	Commercial Olympus FVMPE-RS	InSight® DS with **OPO**	~700	BTZ SNPs (**64**)	1010	Mouse	Brain vasculature	Rectoorbital injection	N	2019	Wang et al. (2019b)
1300	1. Home built with Olympus, BX61W1-FV1200 microscope 2. Home-Built system	1. PHAROS-10W with **OPA** 2. Laser from an **OPA**	810	AIEDots of BTZ dye **70** (~35 nm)	1065	Mouse	Ear vasculature Brain vasculature	Tail vein injection	Y	2018	Qi et al. (2018)
1040	Home built with Olympus, BX61 FV1200 microscope	Mira HP and Mira **OPA**	790	AIEDots of BTZ dye **70**	750	Mouse	Brain vasculature	Tail vein injection	N	2021	Liu et al. (2021)
1200	Commercial Olympus FVMPE-RS	InSight® DS with **OPO**	~700	AIEDots of BTZ dye **71**	800	Mouse	Brain/Ear tumour vasculature	Rectoorbital injection	Y	2019	Wang et al. (2019c)
1040	Nikon A1 Confocal Microscope	Laser with **OPO**	~650	AIEDots of triphenylamine dye **72**	800	Mouse	Brain vasculature	Retro orbital injection	Y	2021	Samanta et al. (2021)
1040	Home built with Olympus, BX61W1-FV1000	Yb-doped photonic crystal **fibre laser**	~620	AIEDots of BODIPY dye **75**	700	Mouse	Brain vasculature	Intravenous injection	Y	2015	Wang et al. (2015)
1100	Commercial Leica SP8 DIVE	Laser with **OPO**	615	Carbon quantum dots **79**	500	1. Zebrafish larvae 2. Mouse	1. Zebrafish Body (2PA) 2. Mouse (1PA)	1. Dots added to media 2. Intravenous injection	1. N 2. Y	2020	Liu et al. (2020)
1550	Home built with Olympus, BX61 FV1200 microscope	FLCPA-01C Calmar **fibre laser**	1270	PbS/CdS quantum dots **84**	220		Brain vasculature	Intravenous injection	N	2022	Ni et al. (2022)
1070	Home built system	Ti:Sapphire laser with **OPO**	~580	Red Fluorescent Protein (tdTomato **86**)	300–500	Mouse	Brain neurons	Gene Expression (Six3 gene)	N	2013	Yang et al. (2013)

only provide distinct wavelengths of around 780 nm, 920 nm, 1050 nm, and 1550 nm (Eisele, 2020). Commonly used Yb-doped fibre lasers for 2P NIR-II imaging have a tunability range of around 1020–1080 nm (Liu and Yang, 2012). However, although difficult, methods for expanding the tunability range of fibre lasers are being explored by implementing nonlinear effects as well as temperature and magnetic field control (Wei et al., 2021). Zhang *et al.* also recently developed a CW fibre laser with an output wavelength tunable from 1000 to 1900 nm by utilising a random distributed feedback Raman fibre laser.

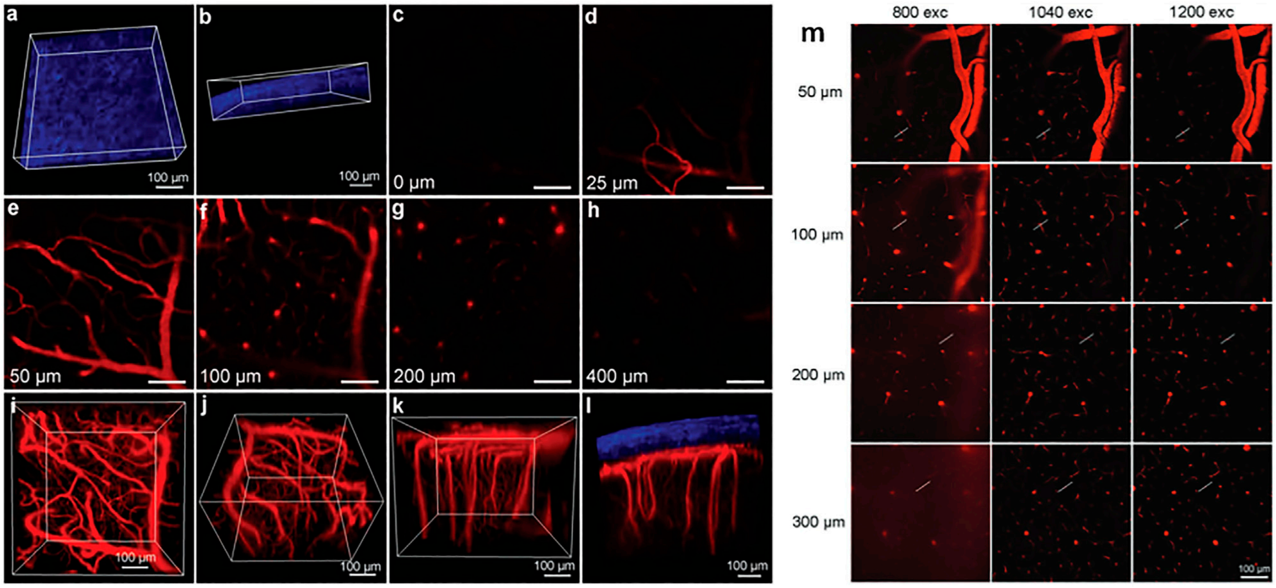

FIGURE 8 | 2PA images of brain blood vessels in a mouse injected with CP dots. **(a,b)** 3D reconstructed second-harmonic generation images of mouse skull. **(c–h)** 2PA images at various vertical depths (0–400 μm) at 1200 nm excitation, 660–750 nm emission. **(i–l)** 3D reconstructed 2PA images of brain blood vessels. **(m)** comparison of 2PA images at excitation wavelengths of 800, 1040, and 1200 nm, of brain vasculature in a mouse injected with polymer dots. 2PA line intensity profiles with the different wavelengths across the blood vessels on the right were also acquired for the corresponding depths. Emission at 660–750 nm. Reprinted from ref (Wang et al., 2019b). with permission from John Wiley and Sons.

So far only a limited number of biological 2P NIR-II studies have been reported with fibre lasers despite their portability, ease-of-use, access to longer wavelengths, and high power features, possibly due to the lack of commercially available microscopes that integrates such lasers. However, *in vivo* studies using in-house built fibre lasers have demonstrated their high potential, both by performing 2P NIR-II imaging at 1550 nm–the longest wavelength so far reported (Berezin et al., 2011; Ni et al., 2022), and by reaching the deepest *in vivo* penetration (1040 nm) (Alifu et al., 2017) (**Section 3.2**, **Table 3**). In addition, the components of fibre lasers are much cheaper than OPO sources, as evidenced by Perillo *et al.* who developed a 2P NIR-II microscope using a mode-locked Yb-doped fibre laser for ~$13000 and applied it to image FPs at 1060 nm with penetration depths of up to 900 μm (Perillo et al., 2016). In contrast, the cost of a OPO-based imaging system commonly used for similar 2P NIR-II applications, such as the Olympus FVMPE-RS (**Section 3.2**, **Table 3**) can be up to 10–100 times higher. Modern solutions will hopefully arise in time with the development of affordable commercial benchtop fibre lasers suitable for 2P NIR-II clinical applications.

3.2 *In vivo* Examples of 2P NIR-II Imaging

Clinically relevant examples of 2P NIR-II imaging have been reported using commercially available biological stains, FPs, and custom-made AIEgens. This section aims to discuss the probes presented in **Section 2** in a photo-biological context, with a focus on *in vivo* examples.

The main aim of 2P NIR-II imaging is to improve resolution and depth perception when imaging. The latest examples of 2P NIR-II emitting materials being used *in vivo* ("*in vivo*" here indicating agents being administered in a living creature; including examples of imaging post-resection) can be seen in **Table 3**. As well as having outstanding applications for bio-imaging, recent advances in NIR-II 2PE have led to developments in other biological applications such as PDT and photoacoustic imaging (Wang et al., 2020b; Hu et al., 2020; Ma et al., 2021b).

In 1996, Wokosin *et al.* demonstrated the improved 2P NIR-II imaging resolution at a penetration depth of 55 μm into stained zebrafish embryos compared to traditional 1P confocal microscopy (Wokosin et al., 1996d). In this case, a traditional solid-state Nd:YLF mode-locked laser operating at 1057 nm was used to image safranin-stained embryos (a biological stain typically used for histology and cytology with an absorption and emission of ~500 nm and ~590 nm respectively) (Krumschnabel et al., 2014). Zebrafish have a history of being used for biological imaging due to their transparency resulting in limited photon scattering. In the more recent work of Liu *et al.*, a penetration depth of 500 μm was reached in zebrafish larvae using red-emitting CDs **79** excited at 1100 nm using a commercial microscope (Leica SP8 DIVE) fitted with an OPO system for 2PE (Liu et al., 2020). DTTC (**30**) is another example of a commercial stain used for 2P NIR-II imaging, where a fibre laser was used to achieve an imaging depth of up to 210 μm at 1550 nm in a resected mouse kidney post-injection (Berezin et al., 2011).

Out of all *in vivo* studies reported in this range of wavelengths, AIEgen NPs and other NP-based systems appear to be the most popular choice to demonstrate superior penetration depth compared to other systems (**Table 3**). In the context of *in vivo* 2P imaging, NPs bypass the solubility limitation of organic dyes. They also show increased stability and cumulative size-related increase in

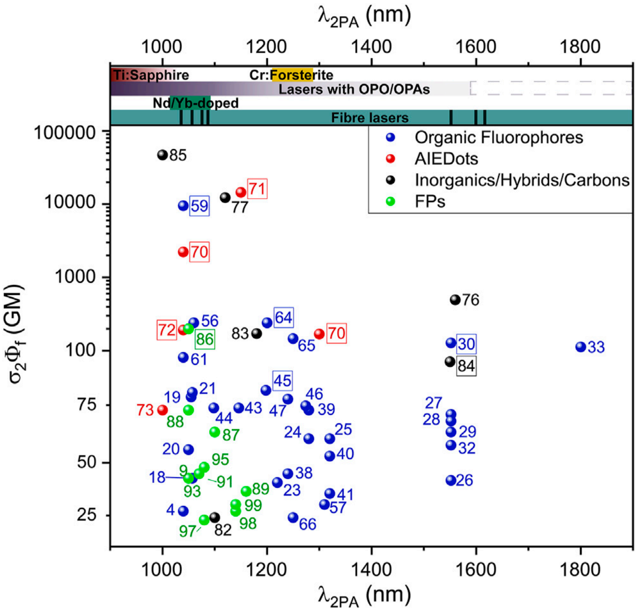

FIGURE 9 | Plot of the 2P brightness and corresponding NIR-II wavelengths of the contrast agents presented in this review ($\sigma_2\Phi_f > 24$ GM). The 2P contrast agents used *in vivo* are represented with a framed number. For clarity, a linear scale for brightnesses between 0 and 100 GM, and a logarithmic scale above 100 GM. The typical range of wavelengths covered by common SWIR lasers is shown for reference (power attenuation is represented by the fading colour; note that OPOs and OPAs can extend past 2000 nm).

2PA cross-section; all of which make them promising imaging agents. The current record of tissue penetration was thus reported by Alifu *et al.* (Nowak-Król et al., 2013) using triphenylamine dipole **59** incorporated within PSMA-based NPs, which led to 2P imaging at a depth of 1200 µm into mouse brain vasculature. Using the BTZ-based AIEgen **70**, 2P imaging of mouse brain tissues was achieved with high resolution and showed significant improvements, reaching a depth of 1064 µm at 1300 nm compared to 700 µm under 1PA (**Table 3**) (Qi et al., 2018). This highlights the sequential increased depth penetration of medical imaging using NIR-II wavelengths compared to shorter wavelengths, and the advantage of 2P over 1P microscopy. On a separate occasion, the same group used similar AIE NPs on a home built OPO laser-based system to demonstrate penetration depths of up to 750 µm at a shorter 2P wavelength (1040 nm) (**Table 3**) (Liu et al., 2021). Here, mouse brain vessels as small as 3.17 µm were imaged. The AIEdots prepared from compound **72** by Samanta *et al.* also allowed 800 µm brain tissue penetration under 2PE at 1040 nm (**Table 3**) (Samanta et al., 2021). Interestingly, record absorption capacity and unprecedented 2P brightness values (>10^4 GM) were measured for the tetraphenylethene-BODIPY (**75**) AIEDots made by Wang *et al.*, but the reported penetration depth was not higher than in more recent studies (700 µm vs. 1200 µm) (Wang et al., 2015). As this is one of the older reports from these studies (2015) it is worth noting that newer technologies with optimum imaging systems could assist in taking this value to similar levels. The potential development of non-invasive imaging techniques using 2P NIR-II excitation was demonstrated by Wang *et al.* using polymer dots **64** as contrast agents (Wang et al., 2019b). The imaging of mice brains was achieved at an impressive penetration depth of 400 µm without craniotomy (intact skull) (**Figure 8**, a-l). The authors also showed the distinct resolution improvement using NIR-II light for 2P imaging when imaging at depths, when compared to light of shorter wavelengths (**Figure 8**, m). Among other classes of luminescent materials, *in vivo* 2P NIR-II imaging was shown for the first time using QDs as a contrast agent by Ni *et al.* with the PbS/CdS QDs **84** (Ni et al., 2022). Imaging depths of 220 µm were achieved in the mouse brain vasculature with a fibre laser operating at 1550 nm. Zhou *et al.* also demonstrated the potential of dual-functional dye **60** that combined 2PEF and ROS generation. 2P imaging of the probe was demonstrated using NIR-II irradiation and a white light laser was used to induce ROS generation in tumours of living mice, allowing for image-guided PDT (Zhou et al., 2021). A triphenylamine dipole was thus used as a theranostic agent to combine 2P imaging and cancer treatment in mice (**Table 3**).

Unsurprisingly, commercially available OPO laser-based microscopes are popular systems for imaging experiments; with most examples performed in the early NIR-II range (1000–1300 nm) (**Table 3**) although imaging at wavelengths above 1200 nm could show the optimum optical benefits. This highlights the limitation of a lack of commercial imaging systems in the NIR-IIb range.

4 DISCUSSION AND PERSPECTIVES

The design of OMI probes usable in the "biological transparency windows" is arguably one of the most prevalent challenges in optobiology today. Shifting the 1PE band of dyes to the NIR-II is possible, but highly challenging as massive bathochromic shifts often come at the cost of fluorescence quantum yield and brightness. To circumvent this problem, 2P NIR-II imaging shows outstanding potential for expanding the applications of fluorescence-based medical imaging. By reducing auto-fluorescence and scattering while confining the excitation to a femtoliter-sized volume, this technique allows for dramatic resolution improvement and enhanced deep tissue imaging which would help the applications of image-guided surgery, point-by-point chemical detection, and image-based diagnostics reach their full potential. A wide range of probe design strategies have been implemented recently to achieve sufficient 2P brightness (>25 GM) in this wavelength range (**Figure 9**). Organic fluorophores have the benefit of low toxicity and easy functionalisation to change their optical and biological properties. Among them, xanthene and polymethine dyes hold great potential for 2P NIR-II imaging due to their versatility allowing bathochromic shifts in their optical properties while retaining a highly emissive character. However, in designing such contrast agents, dye design rules and choice of fluorophore should be considered carefully as centrosymmetric molecules can easily fail to reach the NIR-II range because of selection rules. In contrast, significantly higher $\sigma_2\Phi_f$ values are witnessed when 2P absorbers are integrated into nanoparticle structures, including AIE systems, achieving unprecedented 2P brightnesses of up to 5.6×10^5 GM in the NIR-II. 2P NIR-II luminescent materials have the potential to expand into image guided surgery, diagnostics and chemical sensing due to the high resolution and penetration depths that can be reached, which can also expand to controlled photo-release in therapy applications (Sun et al., 2017a; Zhao et al., 2019). For *in vivo* imaging, unsurprisingly, AIEgens have proven to be the 2P dyes of choice. Such nanosystems also show good biocompatibility and high brightnesses and facilitate mouse brain vascular imaging at depths of up to 1200 μm, and even showed the potential for through-skull brain imaging. Nonetheless, such imaging agents require a certain amount of design and preparation, and more user-friendly solutions can be found in commercially available biological stains. Indeed, there is still to this day a significant gap in the availability and measurement of 2P properties of such dyes, even though many potential 2P dyes can be found in common cell stains (ICG, Alexa dyes etc.). Easily accessible and biologically compatible probes, and their custom-made derivatives, hold great potential in the development of 2P imaging in the NIR-II.

Such compounds, as well as synthetic fluorophores with higher NIR absorption capacities, have likely not yet been categorised due to the difficulty in taking such measurements in this optical window due to the lack of commercial 2P solutions. Nevertheless, more recently, commercially available OPO-based laser imaging systems have facilitated greater access to 2P NIR-II measurements and 2P imaging. These new systems have led to a dramatic rise in publications of *in vivo* studies emerging from 2015 and beyond, and will likely continue to be developed to push the field. Fibre lasers offer huge promise in this sense, by facilitating the necessary power requirements to encourage imaging at wavelengths above 1300 nm, and to give rise to a new generation of imaging agents and biological applications. In this highly favourable context, we now hope that this review will serve as a motivation for researchers to explore the vast possibilities of multiphoton-excited luminescence in the NIR-II transparency windows.

AUTHOR CONTRIBUTIONS

PS, EF, FH, SY, and MK; investigation, writing and original draft preparation. PS, MK; validation and formal analysis. PS, EF, MB, MK; review and editing. MB, MK, EF; supervision. MK; conceptualisation and project administration. All authors have read and agreed to the published version of the manuscript.

FUNDING

We acknowledge the Engineering and Physical Sciences Research Council (EPSRC, United Kingdom) for funding of the programme grant EP/T020997, and for support of the Interdisciplinary Research Collaborations (EP/R018669/1 and EP/R005257) and of the CDT OPTIMA (EP/L016559).

ACKNOWLEDGMENTS

The authors would like to thank Dr. Lin Xu (University of Southampton) for his input on laser systems and proofreading of **Section 3.1** of the manuscript.

REFERENCES

Alifu, N., Yan, L., Zhang, H., Zebibula, A., Zhu, Z., Xi, W., et al. (2017). Organic Dye Doped Nanoparticles with NIR Emission and Biocompatibility for Ultra-deep *In Vivo* Two-Photon Microscopy under 1040 Nm Femtosecond Excitation. *Dyes Pigments* 143, 76–85. doi:10.1016/j.dyepig.2017.04.017

Anderson, V. L., and Webb, W. W. (2011). Transmission Electron Microscopy Characterization of Fluorescently Labelled Amyloid β 1-40 and α-synuclein Aggregates. *BMC Biotechnol.* 11, 125. doi:10.1186/1472-6750-11-125

Arbuzov, V. I., and Nikonorov, N. V. (2013). "Neodymium, Erbium and Ytterbium Laser Glasses," in *Handbook of Solid-State Lasers*. Editors B. Denker and E. Shklovsky (Cambridge: Woodhead Publishing), 110–138. doi:10.1533/9780857097507.1.110

Ávila, F. J., Gambín, A., Artal, P., and Bueno, J. M. (2019). *In Vivo* two-photon Microscopy of the Human Eye. *Sci. Rep.* 9, 10121.

Barroso, M. M. (2011). Quantum Dots in Cell Biology. *J. Histochem Cytochem.* 59, 237–251. doi:10.1369/0022155411398487

Bashkatov, A. N., Genina, E. A., Kochubey, V. I., and Tuchin, V. V. (2005). Optical Properties of Human Skin, Subcutaneous and Mucous Tissues in the Wavelength Range from 400 to 2000 Nm. *J. Phys. D. Appl. Phys.* 38, 2543–2555. doi:10.1088/0022-3727/38/15/004

Benninger, R. K., and Piston, D. W. (2013). Two-photon Excitation Microscopy for the Study of Living Cells and Tissues. *Curr. Protoc. Cell Biol.* Chapter 4, Unit–24. doi:10.1002/0471143030.cb0411s59

Berezin, M. Y., Zhan, C., Lee, H., Joo, C., Akers, W. J., Yazdanfar, S., et al. (2011). Two-Photon Optical Properties of Near-Infrared Dyes at 1.55 μm Excitation. *J. Phys. Chem. B* 115, 11530–11535. doi:10.1021/jp207618e

Bestvater, F., Spiess, E., Stobrawa, G., Hacker, M., Feurer, T., Porwol, T., et al. (2002). Two-photon Fluorescence Absorption and Emission Spectra of Dyes Relevant for Cell Imaging. *J. Microsc.* 208, 108–115. doi:10.1046/j.1365-2818.2002.01074.x

Bonis-O'Donnell, J. T. D., Page, R. H., Beyene, A. G., Tindall, E. G., McFarlane, I. R., and Landry, M. P. (2017). Dual Near-Infrared Two-Photon Microscopy for Deep-Tissue Dopamine Nanosensor Imaging. *Adv. Funct. Mat.* 27, 1702112. doi:10.1002/adfm.201702112

Bradley, D. J., Hutchinson, M. H. R., Koetser, H., and Tolansky, S. (1972). Interactions of Picosecond Laser Pulses with Organic Molecules II. Two-Photon Absorption Cross-Sections. *Proc. R. Soc. A Math. Phys. Eng. Sci.* 329, 105–119.

Brenner, M. H., Cai, D., Swanson, J. A., and Ogilvie, J. P. (2013). Two-photon Imaging of Multiple Fluorescent Proteins by Phase-Shaping and Linear Unmixing with a Single Broadband Laser. *Opt. Express* 21, 17256–17264. doi:10.1364/oe.21.017256

Campbell, R. E., Tour, O., Palmer, A. E., Steinbach, P. A., Baird, G. S., Zacharias, D. A., et al. (2002). A Monomeric Red Fluorescent Protein. *Proc. Natl. Acad. Sci. U.S.A.* 99, 7877–7882. doi:10.1073/pnas.082243699

Cao, J., Zhu, B., Zheng, K., He, S., Meng, L., Song, J., et al. (2019). Recent Progress in NIR-II Contrast Agent for Biological Imaging. *Front. Bioeng. Biotechnol.* 7, 487. doi:10.3389/fbioe.2019.00487

Cao, V. Y., Ye, Y., Mastwal, S. S., Lovinger, D. M., Costa, R. M., and Wang, K. H. (2013). *In Vivo* two-photon Imaging of Experience-dependent Molecular Changes in Cortical Neurons. *J. Vis. Exp.* 71, 50148. doi:10.3791/50148

Carr, J. A., Aellen, M., Franke, D., So, P. T. C., Bruns, O. T., and Bawendi, M. G. (2018). Absorption by Water Increases Fluorescence Image Contrast of Biological Tissue in the Shortwave Infrared. *Proc. Natl. Acad. Sci. U.S.A.* 115, 9080–9085. doi:10.1073/pnas.1803210115

Carr, J. A., Franke, D., Caram, J. R., Perkinson, C. F., Saif, M., Askoxylakis, V., et al. (2018). Shortwave Infrared Fluorescence Imaging with the Clinically Approved Near-Infrared Dye Indocyanine Green. *Proc. Natl. Acad. Sci. U.S.A.* 115, 4465–4470. doi:10.1073/pnas.1718917115

Ceymann, H., Rosspeintner, A., Schreck, M. H., Mützel, C., Stoy, A., Vauthey, E., et al. (2016). Cooperative Enhancement versus Additivity of Two-Photon-Absorption Cross Sections in Linear and Branched Squaraine Superchromophores. *Phys. Chem. Chem. Phys.* 18, 16404–16413. doi:10.1039/c6cp02312f

Chen, B.-Y., Wu, S., Yu, Y.-J., Wu, C.-T., Wang, Y.-H., and Jin, G.-Y. (2020). 3.8 μm Mid-infrared Optical Parametric Amplifier Based on MgO:PPLN Crystal. *Infrared Phys. Technol.* 111, 103448. doi:10.1016/j.infrared.2020.103448

Chen, Y., Xue, L., Zhu, Q., Feng, Y., and Wu, M. (2021). Recent Advances in Second Near-Infrared Region (NIR-II) Fluorophores and Biomedical Applications. *Front. Chem.* 9, 750404. doi:10.3389/fchem.2021.750404

Chénais, S., and Forget, S. (2012). Recent Advances in Solid-State Organic Lasers. *Polym. Int.* 61, 390–406.

Cho, S., Lim, J. M., Hiroto, S., Kim, P., Shinokubo, H., Osuka, A., et al. (2009). Unusual Interchromophoric Interactions in β,β′ Directly and Doubly Linked Corrole Dimers: Prohibited Electronic Communication and Abnormal Singlet Ground States. *J. Am. Chem. Soc.* 131, 6412–6420. doi:10.1021/ja900220y

Chung, S.-J., Zheng, S., Odani, T., Beverina, L., Fu, J., Padilha, L. A., et al. (2006). Extended Squaraine Dyes with Large Two-Photon Absorption Cross-Sections. *J. Am. Chem. Soc.* 128, 14444–14445. doi:10.1021/ja065556m

Cosco, E. D., Caram, J. R., Bruns, O. T., Franke, D., Day, R. A., Farr, E. P., et al. (2017). Flavylium Polymethine Fluorophores for Near- and Shortwave Infrared Imaging. *Angew. Chem. Int. Ed.* 56, 13126–13129. doi:10.1002/anie.201706974

Denk, W., Strickler, J. H., and Webb, W. W. (1990). Two-photon Laser Scanning Fluorescence Microscopy. *Science* 248, 73–76. doi:10.1126/science.2321027

Diao, S., Blackburn, J. L., Hong, G., Antaris, A. L., Chang, J., Wu, J. Z., et al. (2015). Fluorescence Imaging *In Vivo* at Wavelengths beyond 1500 Nm. *Angew. Chem. Int. Ed.* 54, 14758–14762. doi:10.1002/anie.201507473

Ding, F., Zhan, Y., Lu, X., and Sun, Y. (2018). Recent Advances in Near-Infrared II Fluorophores for Multifunctional Biomedical Imaging. *Chem. Sci.* 9, 4370–4380. doi:10.1039/c8sc01153b

Drobizhev, M., Makarov, N. S., Tillo, S. E., Hughes, T. E., and Rebane, A. (2011). Two-photon Absorption Properties of Fluorescent Proteins. *Nat. Methods* 8, 393–399. doi:10.1038/nmeth.1596

Drobizhev, M., Stepanenko, Y., Rebane, A., Wilson, C. J., Screen, T. E. O., and Anderson, H. L. (2006). Strong Cooperative Enhancement of Two-Photon Absorption in Double-Strand Conjugated Porphyrin Ladder Arrays. *J. Am. Chem. Soc.* 128, 12432–12433. doi:10.1021/ja0649623

Drobizhev, M., Tillo, S., Makarov, N. S., Hughes, T. E., and Rebane, A. (2009). Absolute Two-Photon Absorption Spectra and Two-Photon Brightness of Orange and Red Fluorescent Proteins. *J. Phys. Chem. B* 113, 855–859. doi:10.1021/jp8087379

Eisele, M. (2020). *Simplifying Two-Photon Microscopy*. Wiley Analytical Science.

Escobedo, J. O., Rusin, O., Lim, S., and Strongin, R. M. (2010). NIR Dyes for Bioimaging Applications. *Curr. Opin. Chem. Biol.* 14, 64–70. doi:10.1016/j.cbpa.2009.10.022

Ewart, P. (2005). "Spectroscopy | Nonlinear Laser Spectroscopy," in *Encyclopedia of Modern Optics*. Editor R.D. Guenther (Oxford: Elsevier), 109–119. doi:10.1016/b0-12-369395-0/00897-6

Fan, Y., Sun, Y., Chang, W., Zhang, X., Tang, J., Zhang, L., et al. (2018). Bioluminescence Imaging and Two-Photon Microscopy Guided Laser Ablation of GBM Decreases Tumor Burden. *Theranostics* 8, 4072–4085. doi:10.7150/thno.25357

Feng, Z., Tang, T., Wu, T., Yu, X., Zhang, Y., Wang, M., et al. (2021). Perfecting and Extending the Near-Infrared Imaging Window. *Light Sci. Appl.* 10, 197. doi:10.1038/s41377-021-00628-0

Ferguson, A. I., and Malcolm, G. P. A. (1993). "Mode-Locked Solid State Lasers," in *Solid State Lasers: New Developments and Applications*. Editors M. Inguscio and R. Wallenstein (Boston, MA: Springer US), 29–44. doi:10.1007/978-1-4615-2998-9_3

Fu, J., Padilha, L. A., Hagan, D. J., Van Stryland, E. W., Przhonska, O. V., Bondar, M. V., et al. (2007). Molecular Structure-Two-Photon Absorption Property Relations in Polymethine Dyes. *J. Opt. Soc. Am. B* 24, 56–66. doi:10.1364/josab.24.000056

Funabiki, K., Yanagawa, R., Kubota, Y., and Inuzuka, T. (2019). Thermo- and Photo-Stable Symmetrical Benzo[cd]indolenyl-Substituted Heptamethine Cyanine Dye Carrying a Tetrakis(pentafluorophenyl)borate that Absorbs Only Near-Infrared Light over 1000 Nm. *New J. Chem.* 43, 7491–7501. doi:10.1039/c9nj00867e

Göppert, M. (1929). Über die Wahrscheinlichkeit des Zusammenwirkens zweier Lichtquanten in einem Elementarakt. *Sci. Nat.* 17, 932.

Göppert-Mayer, M. (1931). Über Elementarakte mit zwei Quantensprüngen. *Ann. Phys.* 401, 273–294.

Grienberger, C., and Konnerth, A. (2012). Imaging Calcium in Neurons. *Neuron* 73, 862–885. doi:10.1016/j.neuron.2012.02.011

Gui, R., Jin, H., Wang, Z., and Tan, L. (2017). Recent Advances in Optical Properties and Applications of Colloidal Quantum Dots under Two-Photon Excitation. *Coord. Chem. Rev.* 338, 141–185. doi:10.1016/j.ccr.2017.02.007

Hackethal, A., Hirschburger, M., Eicker, S., Mücke, T., Lindner, C., and Buchweitz, O. (2018). Role of Indocyanine Green in Fluorescence Imaging with Near-Infrared Light to Identify Sentinel Lymph Nodes, Lymphatic Vessels and Pathways Prior to Surgery - A Critical Evaluation of Options. *Geburtshilfe Frauenheilkd* 78, 54–62. doi:10.1055/s-0043-123937

Han, X., Ge, F., Xu, J. L., and Bu, X. H. (2021). Aggregation-induced Emission Materials for Nonlinear Optics. *Aggregate* 2, e28. doi:10.1002/agt2.28

Hassan, M., and Klaunberg, B. A. (2004). Biomedical Applications of Fluorescence Imaging *In Vivo*. *Comp. Med.* 54, 635–644.

He, G. S., Tan, L.-S., Zheng, Q., and Prasad, P. N. (2008). Multiphoton Absorbing Materials: Molecular Designs, Characterizations, and Applications. *Chem. Rev.* 108, 1245–1330. doi:10.1021/cr050054x

Helmchen, F., and Denk, W. (2005). Deep Tissue Two-Photon Microscopy. *Nat. Methods* 2, 932–940. doi:10.1038/nmeth818

Henary, M., Mojzych, M., Say, M., and Strekowski, L. (2009). Functionalization of Benzo[c,d]indole System for the Synthesis of Visible and Near-Infrared Dyes. *J. Heterocycl. Chem.* 46, 84–87. doi:10.1002/jhet.39

Hermann, J. P., and Ducuing, J. (1972). Dispersion of the Two-Photon Cross Section in Rhodamine Dyes. *Opt. Commun.* 6, 101–105. doi:10.1016/0030-4018(72)90204-0

Herz, J., Siffrin, V., Hauser, A. E., Brandt, A. U., Leuenberger, T., Radbruch, H., et al. (2010). Expanding Two-Photon Intravital Microscopy to the Infrared by Means of Optical Parametric Oscillator. *Biophys. J.* 98, 715–723. doi:10.1016/j.bpj.2009.10.035

Hisamune, Y., Nishimura, K., Isakari, K., Ishida, M., Mori, S., Karasawa, S., et al. (2015). Stable π Radical from a Contracted Doubly N-Confused Hexaphyrin by Double Palladium Metalation. *Angew. Chem. Int. Ed.* 54, 7323–7327. doi:10.1002/anie.201502285

Hong, G., Diao, S., Antaris, A. L., and Dai, H. (2015). Carbon Nanomaterials for Biological Imaging and Nanomedicinal Therapy. *Chem. Rev.* 115, 10816–10906. doi:10.1021/acs.chemrev.5b00008

Hong, G. S., Antaris, A. L., and Dai, H. J. (2017). Near-infrared Fluorophores for Biomedical Imaging. *Nat. Biomed. Eng.* 1, 0010. doi:10.1038/s41551-016-0010

Hornum, M., Reinholdt, P., Zaręba, J. K., Jensen, B. B., Wüstner, D., Samoć, M., et al. (2020). One- and Two-Photon Solvatochromism of the Fluorescent Dye Nile Red and its CF3, F and Br-Substituted Analogues. *Photochem. Photobiol. Sci.* 19, 1382–1391. doi:10.1039/d0pp00076k

Hu, H., Przhonska, O. V., Terenziani, F., Painelli, A., Fishman, D., Ensley, T. R., et al. (2013). Two-photon Absorption Spectra of a Near-Infrared 2-azaazulene Polymethine Dye: Solvation and Ground-State Symmetry Breaking. *Phys. Chem. Chem. Phys.* 15, 7666–7678. doi:10.1039/c3cp50811k

Hu, W., Zhang, H., He, G. S., Baev, A., Xia, J., Huang, W., et al. (2020). Organic NIR-II Photoacoustic Agent Utilizing Combined Two-Photon and Excited State Absorption at 1064 Nm. *ACS Photonics* 7, 3161–3165. doi:10.1021/acsphotonics.0c01227

Jacques, S. L. (2015). Generic Tissue Optical Properties. Available at: https://omlc.org/news/feb15/generic_optics/index.html.

Josefsen, L. B., and Boyle, R. W. (2012). Unique Diagnostic and Therapeutic Roles of Porphyrins and Phthalocyanines in Photodynamic Therapy, Imaging and Theranostics. *Theranostics* 2, 916–966. doi:10.7150/thno.4571

Jung, Y., Kennedy, A., Chiu, H., Mohammad, F., Claridge-Chang, A., and Anderson, D. J. (2020). Neurons that Function within an Integrator to Promote a Persistent Behavioral State in Drosophila. *Neuron* 105, 322–333. doi:10.1016/j.neuron.2019.10.028

Keiser, G. (2016). "Light-Tissue Interactions," in *Biophotonics: Concepts to Applications*. Editor G. Keiser (Singapore: Springer Singapore), 147–196. doi:10.1007/978-981-10-0945-7_6

Kenry, Y., Duan, Y., and Liu, B. (2018). Recent Advances of Optical Imaging in the Second Near-Infrared Window. *Adv. Mat.* 30, e1802394. doi:10.1002/adma.201802394

Kim, D. U., Song, H., Song, W., Kwon, H.-S., Sung, M., and Kim, D. Y. (2012). Two-photon Microscopy Using an Yb̂3+-Doped Fiber Laser with Variable Pulse Widths. *Opt. Express* 20, 12341–12349. doi:10.1364/oe.20.012341

Kim, H. M., and Cho, B. R. (2015). Small-molecule Two-Photon Probes for Bioimaging Applications. *Chem. Rev.* 115, 5014–5055. doi:10.1021/cr5004425

Klausen, M., and Blanchard-Desce, M. (2021). Two-photon Uncaging of Bioactive Compounds: Starter Guide to an Efficient IR Light Switch. *J. Photochem. Photobiol. C Photochem. Rev.* 48, 100423. doi:10.1016/j.jphotochemrev.2021.100423

Klymchenko, A. S. (2017). Solvatochromic and Fluorogenic Dyes as Environment-Sensitive Probes: Design and Biological Applications. *Acc. Chem. Res.* 50, 366–375. doi:10.1021/acs.accounts.6b00517

Kobat, D., Durst, M. E., Nishimura, N., Wong, A. W., Schaffer, C. B., and Xu, C. (2009). Deep Tissue Multiphoton Microscopy Using Longer Wavelength Excitation. *Opt. Express* 17, 13354–13364. doi:10.1364/oe.17.013354

König, K., So, P. T. C., Mantulin, W. W., and Gratton, E. (1997). Cellular Response to Near-Infrared Femtosecond Laser Pulses in Two-Photon Microscopes. *Opt. Lett.* 22, 135–136. doi:10.1364/ol.22.000135

Krumschnabel, G., Eigentler, A., Fasching, M., and Gnaiger, E. (2014). "Use of Safranin for the Assessment of Mitochondrial Membrane Potential by High-Resolution Respirometry and Fluorometry," in *Methods in Enzymology*. Editors L. Galluzzi and G. Kroemer (Academic Press), 163–181. doi:10.1016/b978-0-12-416618-9.00009-1

Kucikas, V., Werner, M. P., Schmitz-Rode, T., Louradour, F., and van Zandvoort, M. (2021). Two-Photon Endoscopy: State of the Art and Perspectives. *Mol. Imaging Biol.* 2021, 1.

Kumari, A., and Gupta, S. (2019). Two-photon Excitation and Direct Emission from S2 State of U.S. Food and Drug Administration Approved Near-Infrared Dye: Application of Anti-kasha's Rule for Two-Photon Fluorescence Imaging. *J. Biophot.* 12, e201800086. doi:10.1002/jbio.201800086

Kuo, W.-S., Wu, P.-C., Chang, C.-Y., Wang, J.-Y., Chen, P.-C., Hsieh, M.-H., et al. (2022). Graphene Near Infrared-I/II Probe in Two-Photon Excitation-wavelength-independent Photoluminescence and Photoinactivation. *Carbon* 193, 205–215. doi:10.1016/j.carbon.2022.03.019

Larson, D. R., Zipfel, W. R., Williams, R. M., Clark, S. W., Bruchez, M. P., Wise, F. W., et al. (2003). Water-soluble Quantum Dots for Multiphoton Fluorescence Imaging *In Vivo*. *Science* 300, 1434–1436. doi:10.1126/science.1083780

Le Bot, N. (2009). It Takes Two Photons to Tango. *Nat. Cell Biol.* 11, S17–S18. doi:10.1038/ncb1950

Lee, H., Berezin, M. Y., Henary, M., Strekowski, L., and Achilefu, S. (2008). Fluorescence Lifetime Properties of Near-Infrared Cyanine Dyes in Relation to Their Structures. *J. Photochem. Photobiol. A Chem.* 200, 438–444. doi:10.1016/j.jphotochem.2008.09.008

Li, C., and Wang, Q. (2018). Challenges and Opportunities for Intravital Near-Infrared Fluorescence Imaging Technology in the Second Transparency Window. *ACS Nano* 12, 9654–9659. doi:10.1021/acsnano.8b07536

Li, D., Jing, P., Sun, L., An, Y., Shan, X., Lu, X., et al. (2018). Near-Infrared Excitation/Emission and Multiphoton-Induced Fluorescence of Carbon Dots. *Adv. Mat.* 30, e1705913. doi:10.1002/adma.201705913

Li, S., and She, C. Y. (2010). Two-photon Absorption Cross-Section Measurements in Common Laser Dyes at 1·06 μm. *Opt. Acta Int. J. Opt.* 29, 281–287. doi:10.1080/713820851

Li, Y., Heng, W.-K., Lee, B. S., Aratani, N., Zafra, J. L., Bao, N., et al. (2012). Kinetically Blocked Stable Heptazethrene and Octazethrene: Closed-Shell or Open-Shell in the Ground State? *J. Am. Chem. Soc.* 134, 14913–14922. doi:10.1021/ja304618v

Liu, C., and Scott, C. N. (2021). Design Strategies to Rhodamine Analogue Fluorophores for Near-Infrared II Biological Imaging Applications. *Dyes Pigments* 196, 109792. doi:10.1016/j.dyepig.2021.109792

Liu, J., and Yang, L. (2012). *Femtosecond Fiber Lasers for Biomedical Solutions*. SPIE.

Liu, W., Zhang, Y., Qi, J., Qian, J., and Tang, B. Z. (2021). NIR-II Excitation and NIR-I Emission Based Two-Photon Fluorescence Lifetime Microscopic Imaging Using Aggregation-Induced Emission Dots. *Chem. Res. Chin. Univ.* 37, 171–176. doi:10.1007/s40242-021-0405-2

Liu, Y., Gou, H., Huang, X., Zhang, G., Xi, K., and Jia, X. (2020). Rational Synthesis of Highly Efficient Ultra-narrow Red-Emitting Carbon Quantum Dots for NIR-II Two-Photon Bioimaging. *Nanoscale* 12, 1589–1601. doi:10.1039/c9nr09524a

Lockwood, D. J. (2016). "Rayleigh and Mie Scattering," in *Encyclopedia of Color Science and Technology*. Editor M.R. Luo (New York, NY: Springer New York), 1097–1107. doi:10.1007/978-1-4419-8071-7_218

Looney, M. R., Thornton, E. E., Sen, D., Lamm, W. J., Glenny, R. W., and Krummel, M. F. (2011). Stabilized Imaging of Immune Surveillance in the Mouse Lung. *Nat. Methods* 8, 91–96. doi:10.1038/nmeth.1543

López-Duarte, I., Chairatana, P., Wu, Y., Pérez-Moreno, J., Bennett, P. M., Reeve, J. E., et al. (2015). Thiophene-based Dyes for Probing Membranes. *Org. Biomol. Chem.* 13, 3792–3802. doi:10.1039/c4ob02507e

Lu, Q., Wu, C. J., Liu, Z., Niu, G., and Yu, X. (2020). Fluorescent AIE-Active Materials for Two-Photon Bioimaging Applications. *Front. Chem.* 8, 617463. doi:10.3389/fchem.2020.617463

Luo, J., Xie, Z., Lam, J. W. Y., Cheng, L., Tang, B. Z., Chen, H., et al. (2001). Aggregation-induced Emission of 1-Methyl-1,2,3,4,5-Pentaphenylsilole. *Chem. Commun.* 2001, 1740–1741. doi:10.1039/b105159h

Ma, H., Zhao, C., Meng, H., Li, R., Mao, L., Hu, D., et al. (2021). Multifunctional Organic Fluorescent Probe with Aggregation-Induced Emission Characteristics: Ultrafast Tumor Monitoring, Two-Photon Imaging, and Image-Guide Photodynamic Therapy. *ACS Appl. Mat. Interfaces* 13, 7987–7996. doi:10.1021/acsami.0c21309

Ma, Z., Wang, F., Wang, W., Zhong, Y., and Dai, H. (2021). Deep Learning for *In Vivo* Near-Infrared Imaging. *Proc. Natl. Acad. Sci. U. S. A.* 118, e2021446118. doi:10.1073/pnas.2021446118

Makarov, N. S., Drobizhev, M., and Rebane, A. (2008). Two-photon Absorption Standards in the 550-1600 Nm Excitation Wavelength Range. *Opt. Express* 16, 4029–4047. doi:10.1364/oe.16.004029

Massin, J., Charaf-Eddin, A., Appaix, F., Bretonnière, Y., Jacquemin, D., van der Sanden, B., et al. (2013). A Water Soluble Probe with Near Infrared Two-Photon Absorption and Polarity-Induced Fluorescence for Cerebral Vascular Imaging. *Chem. Sci.* 4, 2833–2843. doi:10.1039/c3sc22325f

Meng, F., Liu, Y., Niu, J., and Lin, W. (2017). A Novel Fluorescent Probe with a Large Stokes Shift for Real-Time Imaging Mitochondria in Different Living Cell Lines. *Tetrahedron Lett.* 58, 3287–3293. doi:10.1016/j.tetlet.2017.07.030

Mohr, M. A., Bushey, D., Aggarwal, A., Marvin, J. S., Kim, J. J., Marquez, E. J., et al. (2020). jYCaMP: an Optimized Calcium Indicator for Two-Photon Imaging at Fiber Laser Wavelengths. *Nat. Methods* 17, 694–697. doi:10.1038/s41592-020-0835-7

Mütze, J., Iyer, V., Macklin, J. J., Colonell, J., Karsh, B., Petrášek, Z., et al. (2012). Excitation Spectra and Brightness Optimization of Two-Photon Excited Probes. *Biophysical J.* 102, 934–944. doi:10.1016/j.bpj.2011.12.056

Ni, H., Wang, Y., Tang, T., Yu, W., Li, D., He, M., et al. (2022). Quantum Dots Assisted *In Vivo* Two-Photon Microscopy with NIR-II Emission. *Phot. Res.* 10, 189–196. doi:10.1364/prj.441471

Ni, Y., Lee, S., Son, M., Aratani, N., Ishida, M., Samanta, A., et al. (2016). A Diradical Approach towards BODIPY-Based Dyes with Intense Near-Infrared Absorption Around λ =1100 Nm. *Angew. Chem. Int. Ed.* 55, 2815–2819. doi:10.1002/anie.201511151

Nicolson, F., and Kircher, M. F. (2021). "Theranostics: Agents for Diagnosis and Therapy," in *Molecular Imaging*. Editors B.D. Ross and S.S. Gambhir (Academic Press), 655–677. doi:10.1016/b978-0-12-816386-3.00040-5

Nowak-Król, A., Grzybowski, M., Romiszewski, J., Drobizhev, M., Wicks, G., Chotkowski, M., et al. (2013). Strong Two-Photon Absorption Enhancement in a Unique Bis-Porphyrin Bearing a Diketopyrrolopyrrole Unit. *Chem. Commun.* 49, 8368–8370. doi:10.1039/c3cc44728f

Nowak-Król, A., Wilson, C. J., Drobizhev, M., Kondratuk, D. V., Rebane, A., Anderson, H. L., et al. (2012). Amplified Two-Photon Absorption inTrans-A2b2-Porphyrins Bearing Nitrophenylethynyl Substituents. *ChemPhysChem* 13, 3966–3972. doi:10.1002/cphc.201200507

Nuriya, M., Fukushima, S., Momotake, A., Shinotsuka, T., Yasui, M., and Arai, T. (2016). Multimodal Two-Photon Imaging Using a Second Harmonic Generation-specific Dye. *Nat. Commun.* 7, 11557. doi:10.1038/ncomms11557

Nyk, M., Wawrzynczyk, D., Szeremeta, J., and Samoc, M. (2012). Spectrally Resolved Size-dependent Third-Order Nonlinear Optical Properties of Colloidal CdSe Quantum Dots. *Appl. Phys. Lett.* 100, 041102. doi:10.1063/1.3679381

Oh, E., Fatemi, F. K., Currie, M., Delehanty, J. B., Pons, T., Fragola, A., et al. (2013). PEGylated Luminescent Gold Nanoclusters: Synthesis, Characterization, Bioconjugation, and Application to One- and Two-Photon Cellular Imaging. *Part. Part. Syst. Charact.* 30, 453–466.

Olesiak-Banska, J., Waszkielewicz, M., Obstarczyk, P., and Samoc, M. (2019). Two-photon Absorption and Photoluminescence of Colloidal Gold Nanoparticles and Nanoclusters. *Chem. Soc. Rev.* 48, 4087–4117. doi:10.1039/c8cs00849c

Olson, J. E., Yu, J. H., Thimes, R. L., and Camden, J. P. (2022). Vibrational Two-Photon Microscopy for Tissue Imaging: Short-Wave Infrared Surface-Enhanced Resonance Hyper-Raman Scattering. *J. Biophot.* 15, e202100158. doi:10.1002/jbio.202100158

Osmialowski, B., Petrusevich, E. F., Antoniak, M. A., Grela, I., Bin Jassar, M. A., Nyk, M., et al. (2020). Controlling Two-Photon Action Cross Section by Changing a Single Heteroatom Position in Fluorescent Dyes. *J. Phys. Chem. Lett.* 11, 5920–5925.

Palit, D. K., Singh, A. K., Bhasikuttan, A. C., and Mittal, J. P. (2001). Relaxation Dynamics in the Excited States of LDS-821 in Solution. *J. Phys. Chem. A* 105, 6294–6304. doi:10.1021/jp004142r

Paoli, J., Smedh, M., and Ericson, M. B. (2009). Multiphoton Laser Scanning Microscopy-A Novel Diagnostic Method for Superficial Skin Cancers. *Seminars Cutan. Med. Surg.* 28, 190–195. doi:10.1016/j.sder.2009.06.007

Pascal, S., David, S., Andraud, C., and Maury, O. (2021). Near-infrared Dyes for Two-Photon Absorption in the Short-Wavelength Infrared: Strategies towards Optical Power Limiting. *Chem. Soc. Rev.* 50, 6613–6658. doi:10.1039/d0cs01221a

Pascal, S., Denis-Quanquin, S., Appaix, F., Duperray, A., Grichine, A., Le Guennic, B., et al. (2017). Keto-polymethines: a Versatile Class of Dyes with Outstanding Spectroscopic Properties for in Cellulo and *In Vivo* Two-Photon Microscopy Imaging. *Chem. Sci.* 8, 381–394. doi:10.1039/c6sc02488b

Pawlicki, M., Collins, H. A., Denning, R. G., and Anderson, H. L. (2009). Two-photon Absorption and the Design of Two-Photon Dyes. *Angew. Chem. Int. Ed.* 48, 3244–3266. doi:10.1002/anie.200805257

Perillo, E. P., McCracken, J. E., Fernée, D. C., Goldak, J. R., Medina, F. A., Miller, D. R., et al. (2016). Deep *In Vivo* Two-Photon Microscopy with a Low Cost Custom Built Mode-Locked 1060 Nm Fiber Laser. *Biomed. Opt. Express* 7, 324–334. doi:10.1364/boe.7.000324

Pham, W., Cassell, L., Gillman, A., Koktysh, D., and Gore, J. C. (2008). A Near-Infrared Dye for Multichannel Imaging. *Chem. Commun.* 2008, 1895–1897. doi:10.1039/b719028j

Piston, D. W. (2005). When Two Is Better Than One: Elements of Intravital Microscopy. *PLoS Biol.* 3, e207. doi:10.1371/journal.pbio.0030207

Poronik, Y. M., Hugues, V., Blanchard-Desce, M., and Gryko, D. T. (2012). Octupolar Merocyanine Dyes: a New Class of Nonlinear Optical Chromophores. *Chem. Eur. J.* 18, 9258–9266. doi:10.1002/chem.201200718

Pramanik, A., Fan, Z., Chavva, S. R., Sinha, S. S., and Ray, P. C. (2014). Highly Efficient and Excitation Tunable Two-Photon Luminescence Platform for Targeted Multi-Color MDRB Imaging Using Graphene Oxide. *Sci. Rep.* 4, 6090. doi:10.1038/srep06090

Qi, J., Sun, C., Li, D., Zhang, H., Yu, W., Zebibula, A., et al. (2018). Aggregation-Induced Emission Luminogen with Near-Infrared-II Excitation and Near-Infrared-I Emission for Ultradeep Intravital Two-Photon Microscopy. *ACS Nano* 12, 7936–7945. doi:10.1021/acsnano.8b02452

Rakhymzhan, A., Leben, R., Zimmermann, H., Günther, R., Mex, P., Reismann, D., et al. (2017). Synergistic Strategy for Multicolor Two-Photon Microscopy: Application to the Analysis of Germinal Center Reactions *In Vivo*. *Sci. Rep.* 7, 7101. doi:10.1038/s41598-017-07165-0

Ramakrishna, G., Varnavski, O., Kim, J., Lee, D., and Goodson, T. (2008). Quantum-sized Gold Clusters as Efficient Two-Photon Absorbers. *J. Am. Chem. Soc.* 130, 5032–5033. doi:10.1021/ja800341v

Rao, J., Dragulescu-Andrasi, A., and Yao, H. (2007). Fluorescence Imaging *In Vivo*: Recent Advances. *Curr. Opin. Biotechnol.* 18, 17–25. doi:10.1016/j.copbio.2007.01.003

Ricard, C., Arroyo, E. D., He, C. X., Portera-Cailliau, C., Lepousez, G., Canepari, M., et al. (2018). Two-photon Probes for *In Vivo* Multicolor Microscopy of the Structure and Signals of Brain Cells. *Brain Struct. Funct.* 223, 3011–3043. doi:10.1007/s00429-018-1678-1

Ricci, F., Carlotti, B., Keller, B., Bonaccorso, C., Fortuna, C. G., Goodson, T., et al. (2017). Enhancement of Two-Photon Absorption Parallels Intramolecular Charge-Transfer Efficiency in Quadrupolar versus Dipolar Cationic Chromophores. *J. Phys. Chem. C* 121, 3987–4001. doi:10.1021/acs.jpcc.6b10629

Rose, M. H. H. (2019). *A History of the Laser: 1960 - 2019, Photonics Spectra*. Photonics Media.

RPMC (2020). *Advantages of Two-Photon Microscopy Utilizing Femtosecond Fiber Lasers, Pulsed Lasers Blog Posts*. RPMC Lasers.

Rubart, M. (2004). Two-photon Microscopy of Cells and Tissue. *Circulation Res.* 95, 1154–1166. doi:10.1161/01.res.0000150593.30324.42

Samanta, S., Huang, M., Li, S., Yang, Z., He, Y., Gu, Z., et al. (2021). AIE-active Two-Photon Fluorescent Nanoprobe with NIR-II Light Excitability for Highly Efficient Deep Brain Vasculature Imaging. *Theranostics* 11, 2137–2148. doi:10.7150/thno.53780

Schaafsma, B. E., Mieog, J. S. D., Hutteman, M., van der Vorst, J. R., Kuppen, P. J. K., Löwik, C. W. G. M., et al. (2011). The Clinical Use of Indocyanine Green as a Near-Infrared Fluorescent Contrast Agent for Image-Guided Oncologic Surgery. *J. Surg. Oncol.* 104, 323–332. doi:10.1002/jso.21943

Scherer, D., Dörfler, R., Feldner, A., Vogtmann, T., Schwoerer, M., Lawrentz, U., et al. (2002). Two-photon States in Squaraine Monomers and Oligomers. *Chem. Phys.* 279, 179–207. doi:10.1016/s0301-0104(02)00384-1

Shaner, N. C., Campbell, R. E., Steinbach, P. A., Giepmans, B. N. G., Palmer, A. E., and Tsien, R. Y. (2004). Improved Monomeric Red, Orange and Yellow Fluorescent Proteins Derived from Discosoma Sp. Red Fluorescent Protein. *Nat. Biotechnol.* 22, 1567–1572. doi:10.1038/nbt1037

Shen, Y.-F., Tsai, M.-R., Chen, S.-C., Leung, Y.-S., Hsieh, C.-T., Chen, Y.-S., et al. (2015). Imaging Endogenous Bilirubins with Two-Photon Fluorescence of Bilirubin Dimers. *Anal. Chem.* 87, 7575–7582. doi:10.1021/acs.analchem.5b01903

Smith, P. G., Baldacchini, T., Carter, J., and Zadoyan, R. (2012). *Two-Photon Microscopy/Multimodal Imaging: Femtosecond Laser Developments Advance Two-Photon Imaging*. Spectra Physics: BioOptics World.

Smith, S. N., and Steer, R. P. (2001). The Photophysics of Lissamine Rhodamine-B Sulphonyl Chloride in Aqueous Solution: Implications for Fluorescent Protein-Dye Conjugates. *J. Photochem. Photobiol. A Chem.* 139, 151–156. doi:10.1016/s1010-6030(01)00372-0

Sordillo, L. A., Pratavieira, S., Pu, Y., Salas-Ramirez, K., Shi, L. Y., Zhang, L., et al. (2014). Third Therapeutic Spectral Window for Deep Tissue Imaging. *Opt. Biopsy Xii* 2014, 8940. doi:10.1117/12.2040604

Sordillo, L. A., Pu, Y., Pratavieira, S., Budansky, Y., and Alfano, R. R. (2014). Deep Optical Imaging of Tissue Using the Second and Third Near-Infrared Spectral Windows. *J. Biomed. Opt.* 19, 056004. doi:10.1117/1.jbo.19.5.056004

Sowade, R., Kiessling, J., and Breunig, I. (2013). *CW Laser Light Tunable from Blue to Red: OPOs Pave the Way*. Germany: Photonik International.

Squirrell, J. M., Wokosin, D. L., White, J. G., and Bavister, B. D. (1999). Long-term Two-Photon Fluorescence Imaging of Mammalian Embryos without Compromising Viability. *Nat. Biotechnol.* 17, 763–767. doi:10.1038/11698

Subha, R., Nalla, V., Yu, J. H., Jun, S. W., Shin, K., Hyeon, T., et al. (2013). Efficient Photoluminescence of Mn2+-Doped ZnS Quantum Dots Excited by Two-Photon Absorption in Near-Infrared Window II. *J. Phys. Chem. C* 117, 20905–20911. doi:10.1021/jp404124c

Sun, C.-L., Lv, S.-K., Liu, Y.-P., Liao, Q., Zhang, H.-L., Fu, H., et al. (2017). Benzoindolic Squaraine Dyes with a Large Two-Photon Absorption Cross-Section. *J. Mat. Chem. C* 5, 1224–1230. doi:10.1039/c6tc04129a

Sun, C., Li, B., Zhao, M., Wang, S., Lei, Z., Lu, L., et al. (2019). J-aggregates of Cyanine Dye for NIR-II *In Vivo* Dynamic Vascular Imaging beyond 1500 Nm. *J. Am. Chem. Soc.* 141, 19221–19225. doi:10.1021/jacs.9b10043

Sun, Z., Zhang, L.-P., Wu, F., and Zhao, Y. (2017). Photosensitizers for Two-Photon Excited Photodynamic Therapy. *Adv. Funct. Mat.* 27, 1704079. doi:10.1002/adfm.201704079

Tanaka, Y., Saito, S., Mori, S., Aratani, N., Shinokubo, H., Shibata, N., et al. (2008). Metalation of Expanded Porphyrins: A Chemical Trigger Used to Produce

Molecular Twisting and Möbius Aromaticity. *Angew. Chem. Int. Ed.* 47, 681–684. doi:10.1002/anie.200704407

Tchounwou, C., Sinha, S. S., Viraka Nellore, B. P., Pramanik, A., Kanchanapally, R., Jones, S., et al. (2015). Hybrid Theranostic Platform for Second Near-IR Window Light Triggered Selective Two-Photon Imaging and Photothermal Killing of Targeted Melanoma Cells. *ACS Appl. Mat. Interfaces* 7, 20649–20656. doi:10.1021/acsami.5b05225

Tian, R., Ma, H., Zhu, S., Lau, J., Ma, R., Liu, Y., et al. (2020). Multiplexed NIR-II Probes for Lymph Node-Invaded Cancer Detection and Imaging-Guided Surgery. *Adv. Mat.* 32, e1907365. doi:10.1002/adma.201907365

Trägårdh, J., Murtagh, M., Robb, G., Parsons, M., Lin, J., Spence, D. J., et al. (2016). Two-Color, Two-Photon Imaging at Long Excitation Wavelengths Using a Diamond Raman Laser. *Microsc. Microanal.* 22, 803–807. doi:10.1017/s143192761601151x

Trovatello, C., Marini, A., Xu, X., Lee, C., Liu, F., Curreli, N., et al. (2021). Optical Parametric Amplification by Monolayer Transition Metal Dichalcogenides. *Nat. Photonics* 15, 6–10. doi:10.1038/s41566-020-00728-0

Tsai, T.-H., Chen, S.-Y., Tai, S.-P., Lin, C.-Y., Tsai, H.-J., and Sun, C.-K. (2005). in In Vivo *Two-Photon Fluorescence Imaging with Cr: Forsterite Lasers Using Transgenic Lines Tagged by HcRed*. Editors A. Periasamy and P.T.C. So (Biomedical Optics), 265. doi:10.1117/12.585732

Tsai, T.-H., Lin, C.-Y., Tsai, H.-J., Chen, S.-Y., Tai, S.-P., Lin, K.-H., et al. (2006). Biomolecular Imaging Based on Far-Red Fluorescent Protein with a High Two-Photon Excitation Action Cross Section. *Opt. Lett.* 31, 930–932. doi:10.1364/ol.31.000930

Tsien, R. Y. (1998). The Green Fluorescent Protein. *Annu. Rev. Biochem.* 67, 509–544. doi:10.1146/annurev.biochem.67.1.509

Tsoi, K. M., Dai, Q., Alman, B. A., and Chan, W. C. W. (2013). Are Quantum Dots Toxic? Exploring the Discrepancy between Cell Culture and Animal Studies. *Acc. Chem. Res.* 46, 662–671. doi:10.1021/ar300040z

Udayan, S., Sherin, D. R., Vijaykumar, S., Manojkumar, T. K., Nampoori, V. P. N., and Thomas, S. (2020). Exploring the LDS 821 Dye as a Potential NIR Probe for the Two Photon Imaging of Amyloid Fibrils. *Biomater. Sci.* 8, 6082–6092. doi:10.1039/d0bm00548g

Ustione, A., and Piston, D. W. (2011). A Simple Introduction to Multiphoton Microscopy. *J. Microsc.* 243, 221–226. doi:10.1111/j.1365-2818.2011.03532.x

Vivas, M. G., De Boni, L., and Mendonça, C. R. (2018). "Two-Photon Spectroscopy of Organic Materials," in *Molecular and Laser Spectroscopy*. Editor V.P. Gupta (Elsevier), 165–191.

Voigt, F. F., Emaury, F., Bethge, P., Waldburger, D., Link, S. M., Carta, S., et al. (2017). Multiphoton *In Vivo* Imaging with a Femtosecond Semiconductor Disk Laser. *Biomed. Opt. Express* 8, 3213–3231. doi:10.1364/boe.8.003213

Wanderi, K., and Cui, Z. (2022). Organic Fluorescent Nanoprobes with NIR-IIb Characteristics for Deep Learning. *Exploration* 2, 20210097. doi:10.1002/exp.20210097

Wang, S., Liu, J., Goh, C. C., Ng, L. G., and Liu, B. (2019). NIR-II-Excited Intravital Two-Photon Microscopy Distinguishes Deep Cerebral and Tumor Vasculatures with an Ultrabright NIR-I AIE Luminogen. *Adv. Mat.* 31, e1904447. doi:10.1002/adma.201904447

Wang, S., Chen, H., Liu, J., Chen, C., and Liu, B. (2020). NIR-II Light Activated Photosensitizer with Aggregation-Induced Emission for Precise and Efficient Two-Photon Photodynamic Cancer Cell Ablation. *Adv. Funct. Mat.* 30, 2002546. doi:10.1002/adfm.202002546

Wang, S., Fan, Y., Li, D., Sun, C., Lei, Z., Lu, L., et al. (2019). Anti-quenching NIR-II Molecular Fluorophores for *In Vivo* High-Contrast Imaging and pH Sensing. *Nat. Commun.* 10, 1058. doi:10.1038/s41467-019-09043-x

Wang, S., and Larina, I. V. (2017). "High-resolution Imaging Techniques in Tissue Engineering," in *Monitoring and Evaluation of Biomaterials and Their Performance* in Vivo. Editor R. J. Narayan (Cambridge: Woodhead Publishing), 151–180. doi:10.1016/b978-0-08-100603-0.00008-0

Wang, S., Li, B., and Zhang, F. (2020). Molecular Fluorophores for Deep-Tissue Bioimaging. *ACS Cent. Sci.* 6, 1302–1316. doi:10.1021/acscentsci.0c00544

Wang, S., Liu, J., Feng, G., Ng, L. G., and Liu, B. (2019). NIR-II Excitable Conjugated Polymer Dots with Bright NIR-I Emission for Deep *In Vivo* Two-Photon Brain Imaging through Intact Skull. *Adv. Funct. Mat.* 29, 1808365. doi:10.1002/adfm.201808365

Wang, Y., Hu, R., Xi, W., Cai, F., Wang, S., Zhu, Z., et al. (2015). Red Emissive AIE Nanodots with High Two-Photon Absorption Efficiency at 1040 Nm for Deep-Tissue *In Vivo* Imaging. *Biomed. Opt. Express* 6, 3783–3794. doi:10.1364/boe.6.003783

Wang, Z., Wang, X., Wan, J. B., Xu, F., Zhao, N., and Chen, M. (2021). Optical Imaging in the Second Near Infrared Window for Vascular Bioimaging. *Small* 17, e2103780. doi:10.1002/smll.202103780

Webster, S., Odom, S. A., Padilha, L. A., Przhonska, O. V., Peceli, D., Hu, H., et al. (2009). Linear and Nonlinear Spectroscopy of a Porphyrin−Squaraine−Porphyrin Conjugated System. *J. Phys. Chem. B* 113, 14854–14867. doi:10.1021/jp904460f

Wegner, K. D., and Hildebrandt, N. (2015). Quantum Dots: Bright and Versatile *In Vitro* and *In Vivo* Fluorescence Imaging Biosensors. *Chem. Soc. Rev.* 44, 4792–4834. doi:10.1039/c4cs00532e

Wei, Z., Chen, S., Ding, J., Sun, B., Qi, X., Lu, B., et al. (2021). Recent Advance in Tunable Single-Frequency Fiber Laser Based on Two-Dimensional Materials. *Front. Phys.* 8.

Wokosin, D. L., Centonze, V. E., Crittenden, S., and White, J. (1996). Three-photon Excitation Fluorescence Imaging of Biological Specimens Using an All-Solid-State Laser. *Bioimaging* 4, 208–214. doi:10.1002/1361-6374(199609)4:3%3C208::AID-BIO11%3E3.0.CO;2-J

Wokosin, D. L., Centonze, V. E., White, J. G., Hird, S. N., Sepsenwol, S., Malcolm, G. P., et al. (1996). "Multiple-photon Excitation Imaging with an All-Solid-State Laser," in *Proceedings of SPIE - the International Society for Optical Engineering* (United States: SPIE), 38–49.

Wokosin, D. L., Centonze, V., White, J. G., Armstrong, D., Robertson, G., and Ferguson, A. I. (1996). All-solid-state Ultrafast Lasers Facilitate Multiphoton Excitation Fluorescence Imaging. *IEEE J. Sel. Top. Quantum Electron.* 2 (4), 1051–1065. doi:10.1109/2944.577337

Wu, J., Shi, Z., Zhu, L., Li, J., Han, X., Xu, M., et al. (2022). The Design and Bioimaging Applications of NIR Fluorescent Organic Dyes with High Brightness. *Adv. Opt. Mater.* 10, 2102514. doi:10.1002/adom.202102514

Xu, D., Liang, S., Xu, L., Bourdakos, K. N., Johnson, P., Read, J., et al. (2021). Widely-tunable Synchronisation-free Picosecond Laser Source for Multimodal CARS, SHG, and Two-Photon Microscopy. *Biomed. Opt. Express* 12, 1010–1019. doi:10.1364/boe.411620

Yang, J., Fang, M., and Li, Z. (2020). Organic Luminescent Materials: The Concentration on Aggregates from Aggregation-Induced Emission. *Aggregate* 1, 6–18. doi:10.1002/agt2.2

Yang, S., Adhikari, S., Dobbala, M., Adusumilli, S., Rowley, J. D., Ganikhanov, F., et al. (2013). Multi-color Ultrafast Laser Platform for Nonlinear Optical Imaging Based on Independently Tunable Optical Parametric Oscillators. *Appl. Phys. B* 111, 617–625. doi:10.1007/s00340-013-5381-x

Yang, X., Lovell, J. F., Murthy, N., and Zhang, Y. (2020). "Organic Fluorescent Probes for Diagnostics and Bio-Imaging," in *Fluorescent Imaging in Medicinal Chemistry*. Editor Z. Cheng (Cham: Springer International Publishing), 33–53. doi:10.1007/7355_2019_88

Yao, J., Yang, M., and Duan, Y. (2014). Chemistry, Biology, and Medicine of Fluorescent Nanomaterials and Related Systems: New Insights into Biosensing, Bioimaging, Genomics, Diagnostics, and Therapy. *Chem. Rev.* 114, 6130–6178. doi:10.1021/cr200359p

Yao, S., and Belfield, K. D. (20122012). Two-Photon Fluorescent Probes for Bioimaging. *Eur. J. Org. Chem.* 2012, 3199–3217. doi:10.1002/ejoc.201200281

Yao, S., Kim, B., Yue, X., Colon Gomez, M. Y., Bondar, M. V., and Belfield, K. D. (2016). Synthesis of Near-Infrared Fluorescent Two-Photon-Absorbing Fluorenyl Benzothiadiazole and Benzoselenadiazole Derivatives. *ACS Omega* 1, 1149–1156. doi:10.1021/acsomega.6b00289

Ye, C.-x., Zhang, J.-m., Lin, X.-d., Zhang, T., Wang, B., and He, T.-c. (2017). Multiphoton Absorption of Three Chiral Diketopyrrolopyrrole Derivatives in Near-Infrared Window I and II. *Opt. Mat. Express* 7, 3529–3537. doi:10.1364/ome.7.003529

Yi, R., Das, P., Lin, F., Shen, B., Yang, Z., Zhao, Y., et al. (2019). Fluorescence Enhancement of Small Squaraine Dye and its Two-Photon Excited Fluorescence in Long-Term Near-Infrared I&II Bioimaging. *Opt. Express* 27, 12360–12372. doi:10.1364/oe.27.012360

Yoo, K. M., Liu, F., and Alfano, R. R. (1991). Imaging through a Scattering Wall Using Absorption. *Opt. Lett.* 16, 1068–1070. doi:10.1364/ol.16.001068

Yoon, M.-C., Noh, S. B., Tsuda, A., Nakamura, Y., Osuka, A., and Kim, D. (2007). Photophysics of Meso-β Doubly Linked Ni(II) Porphyrin Arrays: Large Two-Photon Absorption Cross-Section and Fast Energy Relaxation Dynamics. *J. Am. Chem. Soc.* 129, 10080–10081. doi:10.1021/ja0735655

Zeng, W., Ishida, M., Lee, S., Sung, Y. M., Zeng, Z., Ni, Y., et al. (2013). A P -Quinodimethane-Bridged Porphyrin Dimer. *Chem. Eur. J.* 19, 16814–16824. doi:10.1002/chem.201302023

Zhang, H., Salo, D., Kim, D. M., Komarov, S., Tai, Y.-C., and Berezin, M. Y. (2016). Penetration Depth of Photons in Biological Tissues from Hyperspectral Imaging in Shortwave Infrared in Transmission and Reflection Geometries. *J. Biomed. Opt.* 21, 126006. doi:10.1117/1.jbo.21.12.126006

Zhang, L., Zou, L.-Y., Guo, J.-F., Wang, D., and Ren, A.-M. (2015). A Theoretical Study of a Series of Novel Two-Photon Nitric Oxide (NO) Fluorescent Probes Based on BODIPY. *New J. Chem.* 39, 8342–8355. doi:10.1039/c5nj01023c

Zhang, N.-n., Lu, C.-y., Chen, M.-j., Xu, X.-l., Shu, G.-f., Du, Y.-z., et al. (2021). Recent Advances in Near-Infrared II Imaging Technology for Biological Detection. *J. Nanobiotechnol* 19, 132. doi:10.1186/s12951-021-00870-z

Zhang, N.-N., Lu, C.-Y., Chen, M.-J., Xu, X.-L., Shu, G.-F., Du, Y.-Z., et al. (2021). Recent Advances in Near-Infrared II Imaging Technology for Biological Detection. *J. Nanobiotechnol* 19, 132. doi:10.1186/s12951-021-00870-z

Zhao, W., Zhao, Y., Wang, Q., Liu, T., Sun, J., and Zhang, R. (2019). Remote Light-Responsive Nanocarriers for Controlled Drug Delivery: Advances and Perspectives. *Small* 15, 1903060. doi:10.1002/smll.201903060

Zheng, Q., He, G. S., and Prasad, P. N. (2009). A Novel Near IR Two-Photon Absorbing Chromophore: Optical Limiting and Stabilization Performances at an Optical Communication Wavelength. *Chem. Phys. Lett.* 475, 250–255. doi:10.1016/j.cplett.2009.05.040

Zheng, Z., Zhang, T., Liu, H., Chen, Y., Kwok, R. T. K., Ma, C., et al. (2018). Bright Near-Infrared Aggregation-Induced Emission Luminogens with Strong Two-Photon Absorption, Excellent Organelle Specificity, and Efficient Photodynamic Therapy Potential. *ACS Nano* 12, 8145–8159. doi:10.1021/acsnano.8b03138

Zhou, Y., Zhang, D., He, G., Liu, C., Tu, Y., Li, X., et al. (2021). A Lysosomal Targeted NIR Photosensitizer for Photodynamic Therapy and Two-Photon Fluorescence Imaging. *J. Mat. Chem. B* 9, 1009–1017. doi:10.1039/d0tb02692a

Zhu, C., Kwok, R. T. K., Lam, J. W. Y., and Tang, B. Z. (2018). Aggregation-Induced Emission: A Trailblazing Journey to the Field of Biomedicine. *ACS Appl. Bio. Mat.* 1, 1768–1786. doi:10.1021/acsabm.8b00600

Conflict of Interest: The authors declare that the research was conducted in the absence of any commercial or financial relationships that could be construed as a potential conflict of interest.